Regulation of PP1 activity by binding and p97-mediated dissociation of SDS22 and Inhibitor-3

Dissertation
for
the doctoral degree of
Dr. rer. nat.

from the Faculty of Biology
University of Duisburg-Essen
Germany

Submitted by

Anja Friederike Kück

Born in Langenfeld

May 2024

DOI: 10.17185/duepublico/82494
URN: urn:nbn:de:hbz:465-20241016-082607-1

The experiments underlying the present work were conducted at the Center of Medical Biotechnology (ZMB) at the University of Duisburg-Essen.

1. Examiner: Prof. Dr. Hemmo Meyer
2. Examiner: Prof. Dr. Stefan Westermann

Chair of the Board of Examiners: Prof. Dr. Dominik Boos

Date of the oral examination: October 2nd 2024

In the context of this doctoral work, the following articles were submitted for publication:

Kueck A. F., van den Boom J., Koska S., Ron D., Meyer H. Alternating binding and p97-mediated dissociation of SDS22 and I3 recycles active PP1 between holophosphatases. May 2024 *PNAS* (in review)

In the context of this doctoral work, the following articles were published:

van den Boom, J., Kueck, A. F., Kravic, B., Muschenborn, H., Giesing, M., Pan, D., Kaschani, F., Kaiser, M., Musacchio, A., & Meyer, H. (2021). Targeted substrate loop insertion by VCP/p97 during PP1 complex disassembly. *Nat Struct Mol Biol*, *28*(12), 964-971. https://doi.org/10.1038/s41594-021-00684-5

‘It's a dangerous business, Frodo, going out your door. You step onto the road, and if you don't keep your feet, there's no knowing where you might be swept off to.'

J.R.R. Tolkien, The Fellowship of the Ring

Contents

Contents I

List of Figures V

List of Tables VII

Summary IX

Zusammenfassung XI

1. Introduction 1

1.1 Protein-phosphatase-1 1

1.1.1 PP1 catalytic mechanism and cellular functions 2

1.1.2 PP1 interaction mechanisms and substrate specifiers 4

1.1.3 Function of PP1 in the integrated stress response 8

1.2 PP1 interactors SDS22 and Inhibitor-3 11

1.2.1 Structure of PP1:I3 15

1.2.2 Structure of SDS22:PP1 17

1.2.3 The SDS22:PP1:I3 complex 19

1.3 The AAA-ATPase p97 21

1.3.1 Cellular functions of p97 22

1.3.2 p97 structure and mechanism 25

1.3.3 SEP-domain adapters 29

1.4 Ubiquitin-independent disassembly of SPI by p97:p37 30

1.5 Aims of the thesis 33

2. Results 37

2.1 A FRET-based assay to determine SPI disassembly kinetics 37

2.1.1 Establishing a FRET-based assay to monitor SPI disassembly through binding of NIPP1 40

2.1.2 Optimization and validation of FRET-based assay conditions 44

2.1.3 Determination of kinetic parameters of the SPI disassembly reaction48

2.2 Characterization of SDS22 and I3 interplay during SPI complex disassembly 51

2.2.1 Establishing FRET-based assays to monitor SDS22 and I3 interactions with PP1 52

2.2.2 Validation of FRET-based assays conditions monitoring SDS22 and I3 interactions with PP1 55

2.2.3 SDS22 and I3 disassembly occurs simultaneously 59

2.2.4 SDS22 and I3 are both necessary for efficient SPI disassembly....... 61

2.2.5 SDS22 and PP1 interaction is improved by the presence of I3 62

2.3 Exploring SPI complex reassembly and stability........ 64

2.3.1 The SPI complex reassembles upon inhibition of p97 activity........... 64

2.3.2 The SPI complex is stable in the presence of a PP1-binding competitor 69

2.3.3 SDS22 and I3 can displace a PP1-binding competitor........ 70

2.4 Investigation of PP1 activity after SPI disassembly by p97:p37............... 71

2.4.1 PP1 dephosphorylates a synthetic substrate after SPI disassembly. 72

2.4.2 PP1 dephosphorylates an endogenous substrate after SPI disassembly 74

3. Discussion 79

3.1 p97 efficiently targets SPI and poly-ubiquitinated substrates........ 80

3.2 Interplay of SDS22 and I3 in SPI disassembly........ 82

3.2.1 SDS22 and I3 are both essential for efficient SPI disassembly......... 82

3.2.2 SDS22 dissociation is linked to I3 dissociation from PP1........ 84

3.2.3 A possible role for I3 in PP1 metal ion binding........ 85

3.3 SPI re-forms after initial disassembly........ 87

3.4 Cycles of SDS22 and I3 binding and p97-mediated disassembly regulate PP1 activity 89

3.5 p97-mediated SPI disassembly results in the formation of an active PP1 holoenzyme........ 92

4. Methods 95
4.1 Molecular Cloning 95
4.1.1 Polymerase Chain Reaction (PCR) 95
4.1.2 Gibson assembly 95
4.1.3 Site-directed mutagenesis 96
4.1.4 DNA transformation, isolation, and sequencing 96
4.1.5 Plasmids, Peptides, and Viruses 96
4.2 Protein expression 98
4.2.1 Expression in *E. coli* BL21 98
4.2.2 Expression in *E. coli* ArcticExpress 98
4.2.3 Expression in insect cells (Baculovirus system) 99
4.3 Protein purification 100
4.4 Protein labeling 103
4.5 In vitro eIF2α phosphorylation with PERK 103
4.6 Fluorescence spectra 103
4.7 FRET-based assays 104
4.7.1 Initial conditions for SPI disassembly reaction with NIPP1^{TAMRA} 104
4.7.2 Optimal conditions of the SPI disassembly reaction 104
4.7.3 TEV experiments 105
4.7.4 Association experiments 105
4.7.5 Dissociation experiments 105
4.7.6 SP and PI disassembly experiments 106
4.8 Fluorometric OMFP dephosphorylation assay 106
4.9 eIF2a-P dephosphorylation assay and PhosTag gel analysis 106
4.10 Quantification and statistical analysis 107
4.11 *In vitro* co-immunoprecipitations 108
4.12 Immunoblotting 108
5. References 109

Abbreviations .... **cxxv**

Acknowledgements .... Fehler! Textmarke nicht definiert.

Curriculum vitae .... Fehler! Textmarke nicht definiert.

Declarations .... **cxxix**

List of Figures

Figure 1.1: Surface depiction of the PP1α catalytic subunit crystal structure. 5
Figure 1.2: The integrated stress response (ISR)..9
Figure 1.3: Evolutionary emergence of PP1 and its earliest interactors in eukaryotic evolution. 12
Figure 1.4: Crystal structure of the PP1$α_{7-300}$:$I3_{27-68}$-complex. 16
Figure 1.5: Crystal structure of SDS22. 17
Figure 1.6: Crystal structure of the $SDS22_{56-360}$:PP1$α_{1-300}$ complex. 18
Figure 1.7: Crystal structure of the $SDS22_{56-360}$:PP1$α_{1-330}$:$I3_{1-126}$ complex. 20
Figure 1.8: p97-dependent pathways and associated adapter proteins. 23
Figure 1.9: Domain arrangement and substrate translocation mechanism of p97.....26
Figure 1.10: Targeting of a ubiquitinated substrate for unfolding by Cdc48:Ufd1:Npl4. 27
Figure 1.11: Domain strucutres of all four human SEP-domain adapters..................29
Figure 1.12: Cryo-EM structure of p97:p37:SDS22:PP1:I3. 31
Figure 2.1: Tagging strategy for the creation of FRET substrates to monitor SPI complex disassembly coupled to binding of the alternative PP1 interaction partner NIPP1. 39
Figure 2.2: Monitoring the development of FRET upon $NIPP1^{TAMRA}$ binding to $PP1^{Clover}$ after SPI disassembly...41
Figure 2.3: Example of FRET-based assay data analysis of an SPI disassembly reaction with subsequent binding of NIPP1. 43
Figure 2.4: Titration of all assay components to determine optimal assay conditions. 45
Figure 2.5: Validation of FRET-based assay, which monitors $NIPP1^{TAMRA}$ binding to $PP1^{Clover}$ after SPI disassembly. 47
Figure 2.6: Determination of kinetic parameters of NIPP1 binding to PP1 upon SPI disassembly...50
Figure 2.7: Creating FRET substrates with two fluorescently labeled SPI components. 52
Figure 2.8: Two different FRET assays monitoring the disassembly of either SDS22 or I3 from PP1 through p97:p37. 54
Figure 2.9: Titrations of FRET-based assay components for monitoring the disassembly of SDS22 and I3 from PP1 through p97:p37. 56

Figure 2.10: TEV-protease experiments with TEVc-FRET substrates to determine full SPI disassembly levels. 58
Figure 2.11: FRET assays show simultaneous disassembly of SDS22 and I3. 60
Figure 2.12: SDS22 and I3 are both necessary for efficient SPI disassembly by p97:p37. 61
Figure 2.13: Association experiment with PP1 and SDS22 in the presence or absence of I3. 63
Figure 2.14: SPI reassembles upon p97 inhibition, after initial disassembly by p97:p37. 65
Figure 2.15: CoIP experiment of SPI reassembly induced by the addition of ATP hydrolyzing enzyme apyrase. 67
Figure 2.16: SDS22 association with PP1 upon p97 inhibition with CB-5083 in the presence of an excess amount of Mn^{2+} ions. 69
Figure 2.17: The SPI complex is stable in the presence of high concentrations of the competitor NIPP1. 70
Figure 2.18 SDS22 and I3 displace another PP1 interaction partner....................... 71
Figure 2.19: PP1 dephosphorylates synthetic substrate OMFP after SPI disassembly. 73
Figure 2.20: MBP-GADD34$^{513\text{-}636}$ displaces I3 from PP1 after disassembly by p97:p37. 75
Figure 2.21: PP1 dephosphorylates an endogenous substrate *in vitro* after SPI disassembly, dependent on p97 activity. 76
Figure 3.1: Summary of the main results achieved in this thesis. 80
Figure 3.2: Cycles of SDS22 and I3 binding and displacement of PP1 regulatory subunits by mass action, as well as p97-catalyzed disassembly regulate PP1 holophosphatase formation, which can result in PP1 substrate dephosphorylation.. 91

List of Tables

Table 1: PCR program used for generation of Gibson fragments and site-directed mutagenesis. 95
Table 2: Plasmids, peptides and virus V2-generations used in this study. 96
Table 3: Primary and secondary antibodies used for western blot signal detection.108

Summary

Protein-phosphatase-1 (PP1) catalyzes a major fraction of all dephosphorylation reactions in eukaryotic cells, regulating numerous cellular pathways. To achieve substrate specificity, PP1 interacts with a myriad of interaction partners, which have inhibiting, substrate targeting and substrate specifying properties. During PP1 biogenesis, two of these interaction partners, SDS22 and Inhibitor-3 (I3), bind to PP1. The three proteins form a ternary complex (SPI complex), in which PP1 is inactive. The SPI complex was shown to be recognized by the AAA-ATPase p97, together with its adapter protein p37. Upon recognition, I3 is translocated through the p97 pore, resulting in I3 unfolding and dissociation from PP1. SDS22 also dissociates from PP1 during this process, though the mechanism of dissociation is unknown. Further, the process of SPI disassembly by p97 is uniquely ubiquitin-independent, in contrast to other known p97-dependent pathways. The role of SPI and its individual components in cells is controversial. Both SDS22 and I3 have demonstrated involvement in PP1 inhibition and stability, yet they are also shown to be crucial for PP1 functions during mitosis. This study aimed to elucidate molecular details of the SPI disassembly reaction and explore how SPI formation and p97-mediated SPI disassembly contribute to PP1 regulation beyond PP1 biogenesis.

High resolution FRET-based assays were established to determined kinetic parameters of the SPI disassembly reaction catalyzed by p97. To overcome FRET detection limits, the parameters were determined through the association of the PP1 interacting protein NIPP1 to PP1 after SPI disassembly. Kinetic parameters at 37 °C were K_M = 342 *÷ 1.37 nM and k_{cat} = 2.70 *÷ 1.25 min^{-1}, demonstrating that the reaction achieved half its maximal velocity at a concentration of 342 nM SPI, with approximately 2.7 SPI molecules per p97 molecule being catalyzed per minute at 37 °C. The values reveal that SPI as a substrate of p97 is efficiently disassembled, displaying even more effective targeting than poly-ubiquitinated substrates, based on published data.

FRET assays monitoring the dissociation and association of SDS22 and I3 to PP1 revealed that both proteins dissociate simultaneously, while NIPP1 binds with a delay. The delayed binding of NIPP1 reveals that SDS22 is not displaced by a third PP1 interacting protein. Instead, experiments performed with a complex of SDS22 and PP1, lacking I3, demonstrated that I3 was essential for SDS22 dissociation and also aided in the association of SDS22 to PP1. These results indicate direct involvement of I3 in the SDS22-PP1 interaction, possibly with a role in PP1 metal ion exchange. Further, SDS22 was also necessary for efficient I3 disassembly, suggesting a role in SPI targeting to p97 and p37.

This study establishes that SPI disassembly releases active PP1. This was shown through dephosphorylation assays with purified components. Both, a synthetic (OMFP) and an endogenous PP1 substrate (eIF2α) were effectively dephosphorylated following SPI disassembly, and dependent on p97 activity. Activity could only be observed under conditions where re-association of SDS22 and I3 was prevented. To show SPI reassembly directly, p97 was inhibited with CB-5083 at the end of the SPI disassembly reaction. Under p97 inhibition, constant SPI disassembly ceases, which resulted in re-binding of SDS22 and I3 to PP1, as shown by FRET. Demonstrating SPI reassembly indicates a post-biogenesis relevance for the formation of the SPI complex.

Re-association of SDS22 and I3 caused the displacement of other regulatory PP1 subunits. Even in the absence of p97 and p37, SDS22 and I3 displaced NIPP1 from PP1 in a cooperative manner. While NIPP1 could be displaced by SDS22 and I3, SPI disassembly and NIPP1 binding to PP1 was strictly dependent on p97 activity. This was highlighted by the observation that SPI was stable in the presence of high concentrations of NIPP1 over long time periods. These results indicate that PP1 availability for holophosphatase formation and activity is governed by alternating binding of SDS22 and I3, and p97-mediated SPI disassembly. The purpose of PP1 regulation by p97 and SPI could be to prevent PP1 from existing free in the cell, as the PP1 catalytic domain is highly indiscriminate towards substrates, which would cause signaling problems in the cell. Another hypothesis is that the ability of SDS22 and I3 to take apart PP1 holoenzymes contributes to exchange of PP1 holoenzyme subunits. Together with p97-mediated SPI disassembly, this would maintain of a pool of free PP1, available for holoenzyme formation, as well as regulate dynamic PP1 subunit exchange. This study contributed insights into the convergence of two major, evolutionarily conserved cellular regulators, PP1 and p97. Future studies may build upon the concepts presented here to elucidate precisely how these mechanisms contribute to cellular health and disease.

Zusammenfassung

Protein-Phosphatase-1 (PP1) katalysiert einen Großteil aller Dephosphorylierungsreaktionen in eukaryontischen Zellen und reguliert zahlreiche zelluläre Prozesse. Um Substratspezifität zu erreichen, interagiert PP1 mit einer Vielzahl von Interaktionspartnern, die hemmende und substratspezifizierende Eigenschaften haben. Während der PP1-Biogenese binden zwei dieser Interaktionspartner, SDS22 und Inhibitor-3 (I3), an PP1. Die drei Proteine bilden einen ternären Komplex (SPI-Komplex), in dem PP1 inaktiv ist. Es wurde gezeigt, dass der SPI-Komplex von der AAA-ATPase p97 zusammen mit ihrem Adapterprotein p37 erkannt wird. Nach der Erkennung wird I3 unter Energieaufwand durch die p97-Pore gezogen, was zur Entfaltung von I3 und zu seiner Dissoziation von PP1 führt. Während dieses Prozesses dissoziiert auch SDS22 von PP1, obwohl der Mechanismus der Dissoziation unbekannt ist. Darüber hinaus ist der Prozess der SPI-Disassemblierung durch p97 Ubiquitin-unabhängig, im Gegensatz zu anderen bekannten p97-abhängigen Wegen. Die Rolle von SPI und seiner einzelnen Komponenten in Zellen ist umstritten. Sowohl SDS22 als auch I3 haben gezeigt, dass sie an der Hemmung und Stabilität von PP1 beteiligt sind, aber auch, dass sie für die Funktionen von PP1 während der Mitose entscheidend sind. Ziel dieser Studie war es, die molekularen Details der SPI-Disassemblierungsreaktion aufzuklären und zu untersuchen, wie die SPI-Bildung und die durch p97 vermittelte SPI-Disassemblierung zur PP1-Regulierung über die PP1-Biogenese hinaus beitragen.

Hochauflösende FRET-basierte Assays wurden entwickelt, um die kinetischen Parameter der von p97 katalysierten SPI-Disassemblierungsreaktion zu bestimmen. Um die FRET-Detektionsgrenzen zu überwinden, wurden die Parameter durch die Assoziation des mit PP1 interagierenden Proteins NIPP1 mit PP1 nach der SPI-Disassemblierung bestimmt. Die kinetischen Parameter bei 37 °C waren $K_M = 342$ *÷ 1,37 nM und $k_{cat} = 2{,}70$ *÷ 1,25 min^{-1}, was zeigt, dass die Reaktion die Hälfte ihrer maximalen Geschwindigkeit bei einer Konzentration von 342 nM SPI erreicht, wobei bei 37 °C etwa 2,7 SPI-Moleküle pro p97-Molekül pro Minute katalysiert werden. Die Werte zeigen, dass SPI als p97-Substrat effizient auseinander gebaut wird, sogar noch effektiver als poly-ubiquitinierte Substrate, wie aus veröffentlichten Daten hervorgeht.

FRET-Assays zur Überprüfung der Dissoziation und Assoziation von SDS22 und I3 mit PP1 ergaben, dass beide Proteine gleichzeitig dissoziieren, während NIPP1 mit

einer Verzögerung bindet. Die verzögerte Bindung von NIPP1 zeigt, dass SDS22 nicht durch ein drittes mit PP1 interagierendes Protein verdrängt wird. Stattdessen zeigten Experimente mit einem Komplex aus SDS22 und PP1 ohne I3, dass I3 für die Dissoziation von SDS22 unerlässlich ist und auch die Assoziation von SDS22 mit PP1 unterstützt. Diese Ergebnisse deuten auf eine direkte Beteiligung von I3 an der Interaktion zwischen SDS22 und PP1 hin, möglicherweise mit einer Rolle beim Metallionenaustausch von PP1. Darüber hinaus war SDS22 auch für eine effiziente Dissoziation von I3 notwendig, was auf eine Rolle bei der Bindung von SPI an p97 und p37 hindeutet.

Diese Studie belegt, dass die Disassemblierung von SPI aktives PP1 freisetzt. Dies wurde durch Dephosphorylierungsversuche mit gereinigten Komponenten nachgewiesen. Sowohl ein synthetisches (OMFP) als auch ein endogenes PP1-Substrat (eIF2α) wurden nach der Disassemblierung von SPI effektiv dephosphoryliert, und zwar in Abhängigkeit von der Aktivität von p97. PP1 Aktivität konnte nur unter Bedingungen beobachtet werden, bei denen die Re-assoziation von SDS22 und I3 verhindert wurde. Um die SPI-Re-assemblierung direkt zu zeigen, wurde p97 am Ende der SPI-Disassemblierung mit CB-5083 gehemmt. Durch die Hemmung von p97 wird die konstante SPI-Disassemblierung gestoppt, was zu einer erneuten Bindung von SDS22 und I3 an PP1 führt, wie durch FRET gezeigt wurde. Der Nachweis der SPI-Reassemblierung weist auf eine Bedeutung für die Bildung des SPI-Komplexes hin, die über die PP1-Biogenese hinausgeht.

Die erneute Assoziation von SDS22 und I3 verursachte die Verdrängung anderer regulatorischer PP1-Untereinheiten. Selbst in Abwesenheit von p97 und p37 verdrängten SDS22 und I3 NIPP1 von PP1, auf kooperative Weise. Während NIPP1 durch SDS22 und I3 verdrängt werden konnte, waren die Disassemblierung von SPI und die Bindung von NIPP1 an PP1 streng von der Aktivität von p97 abhängig. Dies wurde durch die Beobachtung belegt, dass SPI in Gegenwart hoher Konzentrationen von NIPP1 über lange Zeiträume stabil war. Diese Ergebnisse deuten darauf hin, dass die Aktivität und Verfügbarkeit von PP1 für Holoenzymbildung durch die alternierende Bindung von SDS22 und I3 und die durch p97 vermittelten Disassemblierung von SPI bestimmt wird. Der Zweck der PP1-Regulierung durch p97 und SPI könnte darin bestehen, zu verhindern, dass PP1 frei in der Zelle existiert, da die katalytische Domäne von PP1 weitestgehend unspezifisch Substrate dephosphoryliert, was zu Signalisierungsproblemen in der Zelle führen würde. Eine andere Hypothese ist, dass die Fähigkeit von SDS22 und I3, PP1-Holoenzyme zu zerlegen, zum Austausch von PP1-Holoenzym-Untereinheiten beiträgt. Zusammen mit der p97-vermittelten SPI-Disassemblierung würde dies ein Reservoir von freiem PP1 aufrechterhalten, das für die Holoenzymbildung zur Verfügung steht, und den dynamischen Austausch von PP1-Untereinheiten regulieren. Diese Studie hat Einblicke in die Konvergenz von zwei wichtigen, evolutionär konservierten zellulären Regulatoren, PP1 und p97, geliefert. Künftige Studien könnten auf den hier vorgestellten Konzepten aufbauen, um genau zu klären, wie diese Mechanismen zu zellulärer Gesundheit und Krankheit beitragen.

1. Introduction

1.1 Protein-phosphatase-1

The function of a protein derives from its three-dimensional structure, which is determined by its linear sequence of amino acids. A variety of physical forces and interactions among the amino acid chain determines how the protein will fold into its native conformation and three-dimensional structure. The resulting shape of the protein is essential for protein functions. An important example of protein function is the enzymatic catalysis of specific biochemical reactions in the cell, accelerating the reactions by lowering the required activation energy. These chemical processes include reactions essential for metabolism, energy production, and other principal cellular function. For these processes to proceed efficiently in cells, they undergo tight regulation through multiple mechanisms like transcriptional control, binding to interaction partners, or post-translational modification.

Post-translational modification is a process by which proteins are covalently modified after their synthesis from amino acids during translation. These covalent modifications include attachment of small chemical groups, carbohydrates, lipids, or other proteins like ubiquitin or SUMO (small ubiquitin-like modifier). These modifications serve a spectrum of functions, including the regulation of protein activity and interactions, ensuring proper protein folding and intercellular trafficking, and anchoring proteins to membrane structures (Bononi et al., 2011; Moremen et al., 2012; Resh, 2012). Protein phosphorylation, the covalent attachment of a phosphate group to the amino acid residues serine, threonine, or tyrosine, is one of the most common post-translational modifications and regulatory mechanisms in eukaryotic cells. Through mass spectrometry and computational analysis, phosphorylation was predicted to occur on 90 % of the expressed human proteome (Sharma et al., 2014). The attachment of a phosphate group adds an additional negative charge to the respective protein, which alters the protein’s biophysical properties. The consequences of these alterations are conformational changes, which influence protein activity, subcellular localization, and protein-protein interactions (Cohen, 2002).

Protein phosphorylation is a reversable modification catalyzed by protein kinases and phosphatases. At least 518 human genes have been identified to code for protein kinases, which catalyze the transfer of the ATPγ-phosphate to their target proteins

(Manning et al., 2002). Counteracting these reactions are 189 known phosphatases, catalyzing the cleavage of the phosphate group and restoring the protein to its dephosphorylated form (Chen et al., 2017). PPPs are serine/threonine phosphatases comprising PP1-7 and their respective isoforms. The discrepancy between the larger number of kinases compared to phosphatases is compensated by the family of phosphoprotein phosphatases (PPPs), which form holoenzymes with non-catalytic, regulatory subunits. Importantly, all PPPs, with the exception of PP5, achieve substrate specificity through association with interaction partners, resulting in a multitude of phosphatase variants with the ability to perform unique regulatory functions (Bertolotti, 2018; Shi, 2009). An important member of the PPP family, responsible for a large amount of serine/threonine dephosphorylations is protein-phosphatase-1 (PP1).

1.1.1 PP1 catalytic mechanism and cellular functions

PP1 is a widely expressed enzyme that has undergone minimal changes over the course of more than 1 billion years of eukaryotic evolution (Lundberg et al., 2010; Nagaraj et al., 2011). This stability is reflected in the 80 % sequence identity shared between yeast and human PP1. Notably, human PP1 can rescue the lethality associated with PP1 loss in yeast, highlighting its functional conservation (Gibbons et al., 2007). While the yeast *Saccharomyces cerevisiae* expresses only one PP1 isoform, Glc7, mammals possess four principle isoforms of the catalytic subunit: PP1α, PP1β, PP1γ, and the tissue-specific splice variant PP1γ^2 (Cohen, 2002). The amino acid sequences of these PP1 isoforms share over 85 % identity with noteworthy variations especially in the C-terminal 30 amino acid residues, contributing to isoform-specific interactions (Bollen et al., 2010; Terrak et al., 2004). However, these closely related PP1 isoforms emerged relatively recently in evolutionary history and cannot be discerned based on their enzymatic characteristics (Chen et al., 2017). The conservation of the PP1 isoforms in mammals emphasizes their potential functional significance.

Determination of the PP1 crystal structure provided insights into the PP1 catalytic mechanism, shared throughout the PPP family. X-ray crystallography as well as X-ray emission spectroscopy revealed that the PP1 active site consists of six conserved amino acids, which coordinate two divalent metal ions (Egloff et al., 1995; Goldberg et al., 1995). PP1 derived from skeletal muscle contains iron and zinc, as identified through total reflection X-ray fluorescence (Heroes et al., 2015). In contrast, PP1 expressed in bacteria has been documented to be associated with two manganese ions within its catalytic site (Dancheck et al., 2011). Dephosphorylation catalyzed by PP1 is dependent on the presence of two metal ions and achieved in a single step, through an activated water molecule (Egloff et al., 1995). Stabilized by the two metal ions, metal-activated water performs a nucleophilic attack on the phosphate, leading to dephosphorylation of the PP1-bound substrate. The PP1 active site is shallow, which means that it is principally able to bind and dephosphorylate a wide range of substrates. The PP1 crystal structure also revealed three surface grooves radiating from the active site with the potential to bind further interaction partners, in addition to the dephosphorylation substrate (Goldberg et al., 1995). Screening cDNA libraries for overexpression lethality revealed that overexpression of the Glc7 catalytic subunit in yeast is lethal (Liu et al., 1992). Additionally, a synthetic, cell permeable peptide, which occludes one of the main PP1 binding sites, was shown to be cytotoxic in human U2OS cells (Chatterjee et al., 2012). These results indicate that a tight control of the PP1 catalytic activity by interacting proteins is necessary in cells. Indeed, over 200 PP1 interaction partners and regulatory subunits, also referred to as substrate specifiers, are predicted (Hendrickx et al., 2009).

The regulatory mechanism of substrate specifiers requires the study of PP1 functions alongside its regulators, adding complexity to the elucidation of PP1-dependent pathways. Consequently, the specific substrates of many holoenzymes remain to be fully identified, with phosphoproteomics studies starting to provide further information about protein interaction landscapes of phosphatases and their function in cellular pathways (Yadav et al., 2017). Extensive cell-biological and biochemical studies have found PP1 as an important regulator in an increasing number of cellular processes including glycogen-metabolism (Brady & Saltiel, 2001), entry into mitosis and cell cycle progression (Lesage et al., 2011; Rebelo et al., 2015; Saurin, 2018), apoptosis (Garcia et al., 2003), viral infection (Corda et al., 2024), DNA-damage signaling (Kuntziger et al., 2011), learning and memory (Foley et al., 2021; Genoux et al., 2002), and response to diverse cellular stresses (Hicks et al., 2023), among many others. The significance of PP1 within these pathways renders it an intriguing potential target for drug development. While a number of PP1 inhibitors were discovered, which inhibit PP1 activity independent of other interactors, identification of small molecules capable of targeting specific regulatory subunits bound to PP1 highlight the potential to modify particular PP1 pathways associated with diseases (Tsaytler & Bertolotti, 2013; Tsaytler et al., 2011). Further research into how PP1 interaction with its interacting subunits is regulated in cells will contribute to this endeavor.

1.1.2 PP1 interaction mechanisms and substrate specifiers

Through extensive research over the past decades, ~200 PP1-interacting proteins (PIPs) were discovered (Casamayor & Arino, 2020; Heroes et al., 2013). PIPs are found in molar excess to the PP1 catalytic subunit, so that it is believed that PP1 is consistently regulated by its regulatory subunits (Heroes et al., 2013; Verbinnen et al., 2017). The significance of these PIPs stems from the observation that the PP1 catalytic subunit alone has the ability to dephosphorylate a broad range of proteins, peptides, and synthetic molecules (Bertolotti, 2018; Pinna & Donella-Deana, 1994; Swingle & Honkanen, 2014). Recruitment of regulatory subunits has the capability to limit the inherently wide substrate range of PP1 by restricting activity against certain substrates, or obstructing the active site entirely (Bollen et al., 2010; Cohen, 2002). In addition to PP1-binding domains, substrate specifying subunits can also contain substrate-targeting domains, which increase the affinity to a particular substrate, as shown for the substrate specifiers GADD34 and CReP and the PP1 substrate translation initiation factor eIF2α (Carrara et al., 2017). The broad substrate specificity of PP1 *in vitro*, as well as the existence of only few PP1 isoforms with high sequence identity reinforce the idea that the specificity and vast diversity of PP1 function are determined by the regulatory subunits with which the PP1 catalytic subunit interacts, together counteracting the effects of hundreds of protein serine and threonine kinases.

PIPs have been shown to serve as substrate specifiers, act as substrates, function as inhibitors, or govern the subcellular localization of PP1 (Eto, 2009; Helps et al., 2000; Katayose et al., 2000; Liu & Brautigan, 2000). The targeting of PP1 to specific substrates enhances their local concentration, which significantly elevates the dephosphorylation rate, often by several orders of magnitude (Zeke et al., 2009). While there is no obvious structural relation among known PIPs, most have an intrinsically disordered domain with which they bind to PP1 with high affinity (Choy et al., 2014; Choy et al., 2015; Kumar et al., 2016; O'Connell et al., 2012; Ragusa et al., 2010; Terrak et al., 2004). How the small ~35 kDa protein PP1 can interact with such a large number of diverse interactors was determined through the discovery of several short sequence motifs that serve as interaction sites in a combinatorial manner.

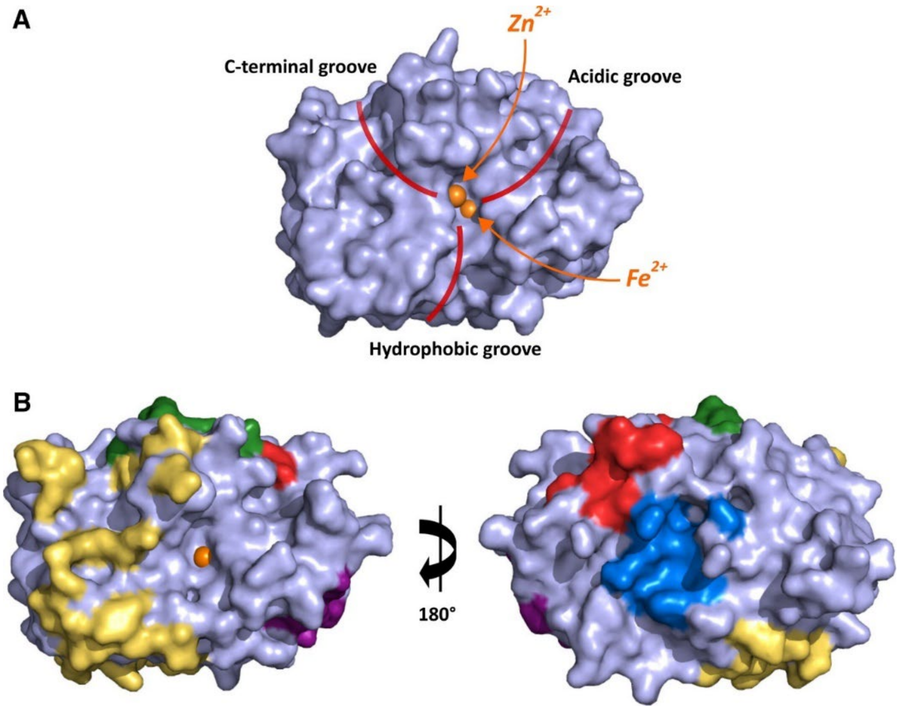

Figure 1.1: Surface depiction of the PP1α catalytic subunit crystal structure. A) Highlighted are the two metal ions bound in the PP1 active site (orange) and the three grooves that are involved in binding of substrates and interaction partners of PP1. **B)** Highlighted are residues that interact with common PP1 interaction motifs: RVXF (red), SILK (blue), MyPhoNE (purple), ΦΦ (green), and residues interacting with SDS22 (yellow) (Cao et al., 2022).

Extensive investigation by numerous research groups demonstrated that PP1 regulatory subunits commonly bind via short 4-6 residue interaction motifs, lacking particular or collective properties. Additionally, some of these interaction sites are shared among the PIPs and PIPs can bind more than one interaction motif at the same time. The interaction motifs, also called short linear motifs (SLiMs), interact with PP1 residues including the C-terminal, acidic and hydrophobic grooves that emanate from the PP1 active site (**Figure 1.1A**), as well as interaction sites for the RVXF (red), SILK (blue), MyPhoNE (purple) and ΦΦ (two consecutive hydrophobic residues, green) motifs, and the SDS22 binding residues (yellow) (**Figure 1.1B**). Most subunits interact with PP1 through a variation of the RVXF sequence, with 143 PIPs having been validated to carry the RVXF motif (Hendrickx et al., 2009). The RVXF motif binds strongly to a hydrophobic channel on PP1, possibly promoting the interaction with other, lower affinity binding sites (Wakula et al., 2003). The SILK interaction residues opposite of the active site fulfill a similar function to RVXF, and SILK motifs were discovered in seven PIPs (Hendrickx et al., 2009; Hurley et al., 2007; Wakula et al., 2003). The MyPhoNE motif binds N-terminal of the RVXF binding site and six PIPs are knows to carry this motif (Hendrickx et al., 2009). The ΦΦ is engaged by multiple PP1 interaction partners through two sequential hydrophobic amino acids, conserved throughout many eukaryotic species (O'Connell et al., 2012). In addition to the PP1 interaction motifs shown in Figure 1.1, myosin phosphatase target subunit 1 (MYPT1) interacts strongly with PP1 by wrapping its ankyrin repeats around the C-terminus of PP1, highlighting that many more interaction modes may exist (Terrak et al., 2004). Therefore, despite the restricted interaction surface available for regulatory subunits, PIPs can engage with PP1 in numerous configurations, resulting in a diverse array of holoenzymes characterized by distinct activities and substrate specificities.

The binding of most PIPs leads to a reduced PP1 activity against certain substrates. Therefore, it is crucial to differentiate between designated inhibitors and substrate targeting or specifying subunits. This can be achieved by evaluating whether the PIP blocks the active site of the PP1, and therefore suppresses all activity of the phosphatase. Examples of inhibitory PP1 subunits include Inhibitor-2 (I2) and the protein kinase-C potentiated inhibitor CPI-17. As a PP1 inhibitor, I2 is a suppressor of memory formation and has been shown to dissociate from PP1 upon DNA damage produced by ionizing irradiation, restoring PP1 activity (Tang et al., 2008; Yang et al., 2015). I2 binds PP1 via its SILK and RVXF motifs, as well as a kinked α-helix, which interacts with the hydrophobic and acidic grooves. This interaction induces the loss of one of the active site metals and occludes the active site, leading to PP1 inhibition (Hurley et al., 2007). Another mode of inhibition is exhibited by CPI-17, which inhibits PP1 only in its phosphorylated form. CPI-17 is an inhibitor of the myosin phosphatase, which is composed of myosin phosphatase target subunit 1 (MYPT1) and PP1. The MYPT1:PP1 complex dephosphorylates myosin light chain, leading to smooth muscle relaxation (Ito et al., 2004). When phosphorylated, CPI-17 attaches to PP1 via a phosphorylated peptide, mimicking a substrate. This pseudo-substrate configuration shields CPI-17 from dephosphorylation by PP1, effectively inhibiting the enzyme (Eto, 2009).

In contrast to PP1 inhibitors, substrate targeting and specifying subunits only restrict PP1 activity against certain substrates, while increasing specific dephosphorylation rates (Zeke et al., 2009). An example is spinophilin, an abundant protein in neuronal synapses where it is involved in the dephosphorylation of glutamate receptors (Cao et al., 2022). The spinophilin:PP1 complex structure reveals that spinophilin obstructs the C-terminal substrate-binding groove. Restricting interaction with the C-terminal groove allows PP1 to dephosphorylate specific substrates while preventing dephosphorylation of others (Ragusa et al., 2010). This form of negative selection of substrates is contrasted by proteins like MYPT1. MYPT1 harbors binding sites for PP1 and additionally for various proteins like the cytoskeletal protein merlin and protein polo-like kinase-1 involved in mitosis (Jin et al., 2006; Yamashiro et al., 2008). Since these proteins are also substrates of PP1, MYPT1 confers a positive selection of PP1 substrates by recruiting PP1 to the relevant site of dephosphorylation (Terrak et al., 2004). Similar mechanisms were observed for nuclear inhibitor of PP1 (NIPP1) and the growth arrest and DNA damage-inducible protein (GADD34) and its paralogue constitutive repressor of eIF2α phosphorylation (CReP). NIPP1, formerly known as a PP1 inhibitor (Beullens et al., 1999) has a role in pre-mRNA splicing, serving as a PP1 substrate specifier for Sap155, among others (Tanuma et al., 2008). As such it possesses a multifunctional targeting domain that is involved in recruitment of multiple substrates (Nuytten et al., 2008; Tanuma et al., 2008). GADD34 and CReP are PP1 regulatory subunits involved in the restoration of cap-dependent translation after cellular stress responses, by dephosphorylation of translation initiation factor eIF2α (Connor et al., 2001; Jousse et al., 2003; Novoa et al., 2001). It was found that the carboxy-terminal regions of the two proteins bind to PP1 with high affinity but are not functional on its own. The amino-terminal region provides a high-affinity binding site for the substrate eIF2α (Carrara et al., 2017). In combination with the finding that PP1 activity is simultaneously inhibited towards its substrate phosphorylase a, these interactions explain the selectivity of regulatory subunits, which can function as both inhibitors of PP1c towards some substrates and enhancers of dephosphorylation towards other substrates (Connor et al., 2001).

In addition to PP1 regulation through binding of PIPs, PP1-interacting proteins can also be subject to cellular regulation themselves. These mechanisms can influence protein availability, PIP affinity to PP1, and PP1 activity. As such, some PP1 regulatory subunits are regulated through ubiquitination and rapid degradation through the proteasome, as was shown for GADD34 and MYPT1 (Brush & Shenolikar, 2008; Twomey et al., 2010). Additionally, PIP expression differs in different cell types, making certain interactors more available for PP1 than others (Ceulemans & Bollen, 2004; Moorhead et al., 2007). Another form of PIP regulation is covalent post-translational modification. Signaling pathways can interfere with PP1 activity, by mediating the phosphorylation of PIPs in or near their RVXF motif and therefore blocking interaction with PP1. This was shown for PIPs phosphorylated by mitotic kinase Aurora B, which regulates cell cycle progression (Nasa et al., 2018). Conversely, during mitosis PP1 auto-dephosphorylates itself in response to certain cellular signals, which catalyzes the dephosphorylation of the bound I2 subunit, ultimately leading to PP1 activity and mitotic exit (Wu et al., 2009). Further, PIPs can also be regulated through interactions with other proteins like the allosteric regulation of PP1 by phosphorylase a, leading to conformational changes in PP1 and resulting in the suppression of glycogen synthesis (Kelsall et al., 2009). Another mode of interaction-based PIP regulation is the energy-dependent dissociation of the inhibitory subunits Suppressor-of-Dis2-number 2 (SDS22) and Inhibitor-3 (I3) from PP1 through the AAA-ATPase p97, which will be discussed in detail in the following chapters. In conclusion, PIP interaction with PP1 is thought to be determined by PIP concentration and affinities, as well as their interaction with other regulatory proteins, while the exact mechanisms of holoenzyme formation and exchange are still subject of investigation.

1.1.3 Function of PP1 in the integrated stress response

PP1 performs numerous functions within a cell, mediated by its varied interaction partners. A well-studied substrate of PP1 is the α subunit of the eukaryotic translation initiation factor (eIF2α). eIF2α is the core element of a process called the integrated stress response (ISR), which is a response to various cellular stresses, adapting gene expression to restore homeostasis. The ISR is divided into several stages, comprising the reception of an initial stress signal, activation of regulatory kinases, phosphorylation of eIF2α, attenuation of protein synthesis through phospho-eIF2α signaling, and finally the termination of phospho-eIF2α signaling through dephosphorylation of eIF2α by PP1 and its interaction partners GADD34 and CReP (**Figure 1.2**). Four kinases phosphorylate eIF2α in mammals: PKR-like ER kinase (PERK), general control nonderepressible 2 (GCN2), heme-regulated eIF2α kinase (HRI), and double-stranded RNA-dependent protein kinase (PKR). While all four kinases share a catalytic mechanism, they respond to different environmental stimuli. PERK is activated upon ER stress, induced by accumulation of unfolded proteins in the ER (Kaufman, 2002), GCN2 responds to low levels of amino acids (Kilberg et al., 2005), HRI phosphorylates eIF2α under conditions of low heme (Chen, 2007), and PKR senses viral dsRNA during viral infection of the cell, all leading to phosphorylation of eIF2α (Sadler & Williams, 2007).

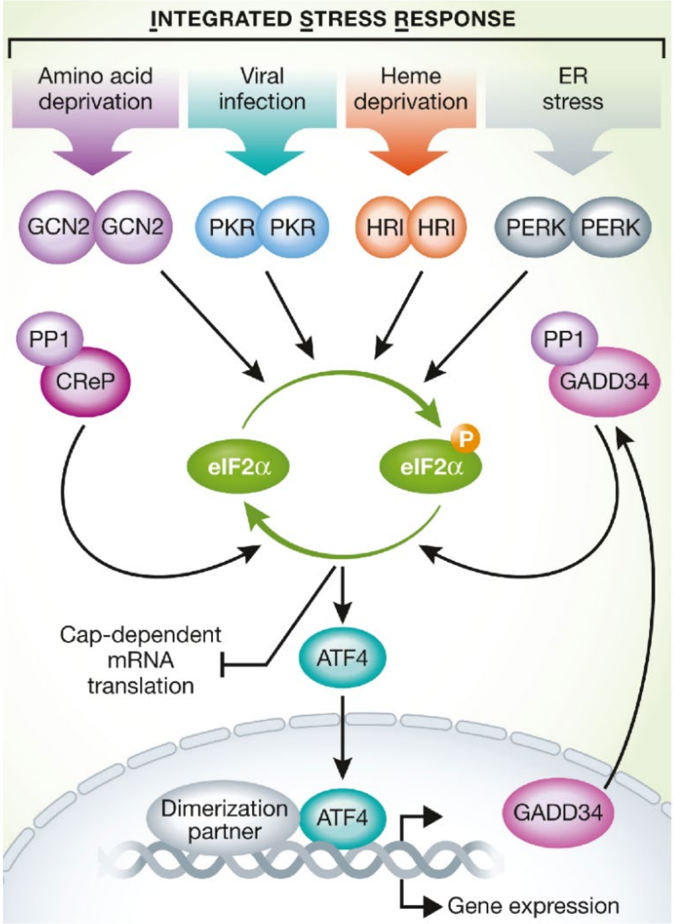

Figure 1.2: The integrated stress response (ISR). Upon reception of cellular stresses like amino acid deprivation, viral infection, heme deprivation, or ER stress, four kinases are activated, resulting in the phosphorylation of eIF2α. Phosphorylated eIF2α prevents cap-dependent translation, while certain stress related genes are upregulated through the transcription factor ATF4. Among the induced stress genes, GADD34 binds to its interaction partner PP1, forming an active holophosphatase. In this conformation, PP1 facilitates eIF2α dephosphorylation and a termination of the ISR (Pakos-Zebrucka et al., 2016).

Activation of any of the four kinases leads to kinase dimerization and phosphorylation of eIF2α. Phosphorylation of eIF2α inhibits the formation of the eIF2-GTP-tRNAiMet ternary complex, which is required for translation initiation, thereby reducing overall cap-dependent protein synthesis rates (Sonenberg & Hinnebusch, 2009). Inhibition of protein synthesis relieves the stress on the ER, by reducing the amount of incoming proteins (Ron, 2002). Similarly, the need for amino acids as protein building blocks is reduced, relieving stress caused by amino acid deprivation (Vazquez de Aldana et al., 1994). Viral mRNA cannot be translated during global protein synthesis inhibition, alleviating the stress caused by viral infection (Garcia et al., 2007). Finally, as a consequence of low translation, globin production is reduced, decreasing the need for heme (Han et al., 2001).

While global protein synthesis is attenuated, translation of specific mRNAs is selectively enhanced during the ISR. The mRNA of activating transcription factor 4

(ATF4) possesses an upstream open reading frame (uORF) in its 5' untranslated region (UTR) that is resistant to eIF2α phosphorylation by providing alternative translation initiation sites (Andreev et al., 2015). Upon entering the nucleus, ATF4 triggers the selective activation of survival genes associated with the unfolded protein response (UPR), including those involved in autophagy, antioxidant response, amino acid biosynthesis and transport, ER-associated degradation (ERAD), and protein chaperones, to restore cellular homeostasis (Neill & Masson, 2023). Notably, ATF4 also promotes the transcription of GADD34. GADD34 is a PP1 regulatory subunit and the PP1:GADD34 complex is among the PP1 holoenzymes whose substrate, eIF2α, is identified.

The dephosphorylation activity of the GADD34:PP1 complex has been demonstrated both *in vitro* and *in vivo* (Connor *et al*, 2001; Novoa *et al*, 2001; Carrara *et al*, 2017; Chen *et al*, 2015). Further, mediating the dephosphorylation of eIF2α through PP1 is the primary and essential function of GADD34 and its paralogue CReP in mammalian development (Harding et al., 2009). Mammalian GADD34 is a large protein (674 aa) with a conserved region near its C-terminus, sufficient for eIF2α dephosphorylation (Novoa et al., 2001). This region is shared with the constitutively expressed CReP, which dephosphorylates basal levels of phospho-eIF2α and also contributes to eIF2α dephosphorylation after ISR induction (Jousse et al., 2003). eIF2α (585 aa) was shown to form a complex with globular actin in order to stably position itself for dephosphorylation by GADD34 and PP1, though the function of this interaction is yet to be elucidated (Chen et al., 2015; Yan et al., 2021). The expression of GADD34 and subsequent complex formation of GADD34:PP1:actin finally culminates in the dephosphorylation of eIF2α, switching off phospho-eIF2α signaling and restoring regular protein synthesis.

While eIF2α phosphorylation relieves stress by down-regulating general protein synthesis and thereby fulfilling a pro-survival function, prolonged elevation of phospho-eIF2α is not tolerated. It was shown that chronic activation of the ISR can lead to cell death by apoptosis (Scheuner et al., 2006). This dual role in cellular homeostasis together with the potential specific targeting of a known PP1 holoenzyme, makes the ISR an interesting candidate for therapeutic intervention. Several small molecules have been identified to date, with functions either in prolonging the ISR, or to inhibit phospho-eIF2α signaling. An example is Sephin1, which selectively inhibits the interaction between GADD34 and PP1, extending the duration of eIF2α phosphorylation. Sephin1 is able to avert the phenotypical and molecular abnormalities found in mice as a consequence of the myelination impairment disorder Charcot-Marie-Tooth 1B and the neurodegenerative disease SOD1-mediated amyotrophic lateral sclerosis (ALS) (Pennuto et al., 2008; Wang et al., 2014). Sephin1 successfully guarded against these protein-misfolding diseases in mice, demonstrating no observable side effects in the process (Das et al., 2015). In contrast to the disruption of the PP1-GADD34 interaction, which prevents phospho-eIF2α dephosphorylation and ISR termination, another strategy for therapeutic intervention is the inhibition of the ISR. The chemical compound ISRIB (small-molecule ISR inhibitor) binds the regulatory site of the eIF2α guanidine-exchange factor (GEF) eIF2B. ISRIB binding promotes eIF2B dimerization and activation, thereby maintaining eIF2B functionality and general protein translation even in the presence of phosphorylated eIF2α (Sidrauski et al., 2015; Zyryanova et al., 2021). As an ISR inhibitor, ISRIB was able to increase memory development in mice (Sidrauski et al., 2013), alleviate the hippocampal-dependent cognitive impairments caused by traumatic brain injury (TBI) in mice (Chou et al., 2017), and ISRIB exhibits positive effects in mice afflicted with prion diseases, notably without off-target effects, which are observed when inhibiting the ISR through direct targeting of eIF2α kinases *in vivo* (Halliday et al., 2015). As a consequence of the contrasting data showing positive effects on disease phenotypes, inhibiting, or extending the ISR could potentially lead to either protective or detrimental effects on diseases, depending on the particular pathology. The precise molecular mechanisms driving these divergent outcomes require further investigation.

1.2 PP1 interactors SDS22 and Inhibitor-3

SDS22 and I3 are the evolutionarily oldest known interactors of PP1, present in animals, plants, and fungi, and conserved from yeast to humans. Together with I2 and NIPP1 they are referred to as ancient interactors of PP1, as they evolved before all other known PIPs. Interactors that evolved later like RepoMan and KNL1, also involved in mitosis, are only present in the animal kingdom (**Figure 1.3**) (Cao et al., 2022; Ceulemans, Stalmans, et al., 2002). The preservation of SDS22 and I3 across extensive evolutionary spans strongly suggests that these proteins serve a crucial function in one or more fundamental cellular processes.

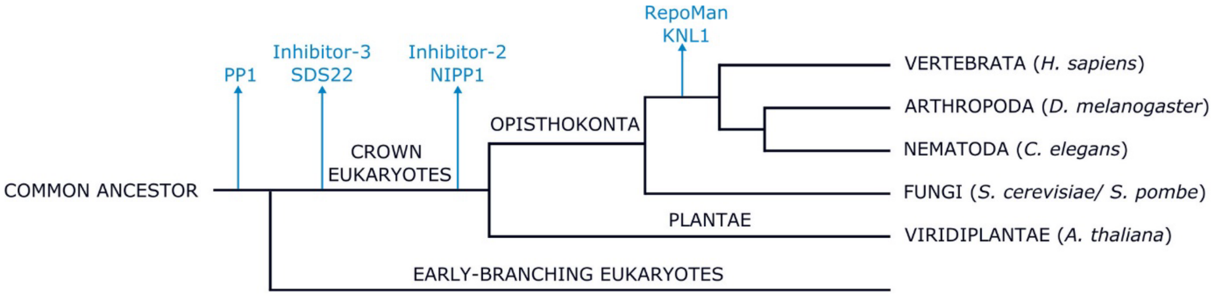

Figure 1.3: Evolutionary emergence of PP1 and its earliest interactors in eukaryotic evolution. Earliest known interactors of PP1 are Inhibitor-3 and SDS22, followed by I2 and NIPP1, all present in the crown eukaryotes. Other interactors like RepoMan and KNL1 evolved only in the animal kingdom (Cao et al., 2022).

I3, also known as Ypi1 (yeast phosphatase inhibitor 1) in yeast, was first discovered as a PP1 inhibitor (Garcia-Gimeno et al., 2003). Like its human counterpart, yeast PP1 (Glc7) is involved in the control of numerous cellular functions, including glycogen metabolism, mitosis, meiosis, sporulation, ion homeostasis, and endocytosis (Cannon et al., 1994; Chang et al., 2002; Francisco et al., 1994; Hisamoto et al., 1994; Ramaswamy et al., 1998; Williams-Hart et al., 2002). In partially defective Glc7 mutants (deletion of GLC7 is lethal), cellular glycogen levels are reduced (Ramaswamy et al., 1998). It was observed that cells overexpressing Ypi1 exhibited decreased glycogen levels compared to cells with an empty plasmid, indicating potential *in vivo* inhibition of Glc7 phosphatase activity by Ypi1 (Garcia-Gimeno et al., 2003). The same study also found that this function was dependent on the RVXF motif in Ypi1, and therefore a direct interaction between PP1 and I3 was necessary for the inhibition. PP1 inhibition was further tested *in vitro*, where recombinant Ypi1 was able to inhibit PP1 with an IC_{50} of ~1 nM (Zhang et al., 1998). Additionally, Ypi1 deletion resulted in lethality in budding yeast, highlighting its essential cellular role (Garcia-Gimeno et al., 2003).

Biochemical analysis identified SDS22, or its yeast counterpart sds22, as an inhibitor of PP1 (Dinischiotu et al., 1997). However, SDS22 is best known for its role in mitosis, functioning by binding to its interaction partner PP1. As such, SDS22 is localized both in the cytoplasm and nucleus, with increased nuclear concentration during mitosis (Posch et al., 2010). A temperature-sensitive mutation causing the loss of sds22 function, results in cell cycle arrest during mid-mitosis and several studies showed that this is due to a direct interaction with PP1 (Posch et al., 2010; Stone et al., 1993; Wurzenberger et al., 2012). In particular, the role of SDS22 and PP1 in chromosome alignment and cell cycle progression was shown to be caused by effects on the nuclear kinase Aurora B and its downstream targets. Aurora B is involved in error correction during the spindle assembly checkpoint (SAC), weakening kinetochore-microtubule bonds when there is low mechanical tension (Hauf et al., 2003; Musacchio & Salmon, 2007). The disruption of the interaction occurs through the phosphorylation of outer kinetochore components, like the PP1-interacting protein KNL1 (Welburn et al., 2010). PP1 is known to oppose the actions of Aurora B, both dephosphorylating Aurora B substrates, and the enzyme itself (Eiteneuer et al., 2014; Murnion et al., 2001). Necessary for this function were both SDS22 and the PP1 substrate targeting subunit RepoMan (Wurzenberger et al., 2012). Specifically, the depletion of SDS22 lead to failed accumulation of PP1 at the kinetochore and therefore a reduced ability of PP1 to counteract Aurora B, leading to cell cycle progression without proper chromosome alignment (Posch et al., 2010). The seemingly paradoxical description of SDS22 as both an inhibitor and activator of PP1 has been starting to unravel by studying the complex formed by PP1 together with SDS22 and the third interaction partner, I3.

Similar to SDS22, I3 also localizes within the nucleus and nucleoli of mammalian cells during interphase (Huang et al., 2005; Trinkle-Mulcahy et al., 2003). Insights from yeast-3-hybrid studies revealed the formation of a ternary complex involving Sds22, Ypi1, and Glc7 (Pedelini et al., 2007). This complex also forms in human cells and within the complex, PP1 remains inactive (Lesage et al., 2007). Both Sds22 and Ypi1 exhibit an inhibitory effect on Glc7 phosphatase activity towards the synthetic substrate para-nitrophenyl phosphate (pNPP). In addition, the formation of the complex with Sds22 further enhances the ability of Ypi1 to inhibit Glc7 activity *in vitro* (Pedelini et al., 2007). In addition to the formation of a ternary complex involving SDS22 and I3, analysis using a conditionally expressed construct indicates that Ypi1 depletion results in a mitotic arrest with a similar phenotype as caused by the loss of Sds22 (Pedelini et al., 2007; Stone et al., 1993). Notably, the deletion of Ypi1 also leads to diminished nuclear localization of PP1, as well as Sds22 (Bharucha et al., 2008). These findings indicate a collaborative role of I3 with SDS22 as positive regulators of nuclear PP1 activity, ultimately exerting an inhibitory influence on Aurora B kinase.

Further investigation into the interplay of SDS22 and I3 revealed possible mechanisms underlying the positive influence of the inhibitors on PP1 activity. While I3 was shown to be necessary for PP1 and SDS22 localization in the nucleus, I3 depletion did not lead to lower amounts of PP1 at the kinetochore. Instead, it was shown that a lack of I3 lead to accumulation of SDS22-bound PP1 at the kinetochore (Eiteneuer et al., 2014). While SDS22 is bound to PP1, PP1 is unable to dephosphorylate substrates to balance Aurora B activity, leading to chromosome segregation defects (Eiteneuer et al., 2014). Based on these findings it was proposed that I3 has a function in SDS22 dissociation from PP1 resulting in PP1 activity (Eiteneuer et al., 2014). In addition to their proposed roles as PP1 regulators, SDS22 and I3 were also discovered to stabilize newly synthesized PP1, with their depletion causing the formation of PP1 aggregates in yeast (Cheng & Chen, 2015) and co-expression resulting in PP1 stabilization (Choy et al., 2019). These results collaboratively indicate that SDS22 and I3 are neither purely inhibitors or substrate specifiers of PP1, but rather likely to transiently associate with PP1, keeping it stable and inactive until their dissociation can lead the release of active PP1.

The mechanism of I3-dependent dissociation of SDS22 from PP1 was further elucidated by researching the connection of the SDS22:PP1:I3 complex (SPI complex) with its interaction partners Shp1 and Cdc48 (Cell division control protein 48). Shp1 (suppressor of high copy protein phosphatase 1) was initially identified to counteract toxicity of Glc7 overexpression. Additionally, mutants of Shp1 exhibited a lack of PP1 catalytic activity in yeast (Zhang et al., 1995). Shp1, as well as p47, one of its homologues in mammals, interacts with the AAA-ATPase family member Cdc48 in yeast, or p97 in mammals. As such Shp1 was shown to act as a cofactor of Cdc48/p97, regulating ER and Golgi membrane fusion as well as ubiquitin-dependent protein degradation (Hartmann-Petersen et al., 2004; Kondo et al., 1997; Meyer et al., 2002). The same study that described SDS22 and I3 as chaperone-like proteins, ensuring PP1 stability, also showed that the SPI complex in yeast associates with Cdc48:Shp1. The interaction was characterized as transient, owing to the fact that only cells expressing a Cdc48 substrate trapping mutant showed pulldowns of all components (Cheng & Chen, 2015). Further studies in human cells confirmed that the SPI complex forms transiently during PP1 biogenesis (Weith et al., 2018). Notably, it could be shown that the SPI complex was disassembled dependent on p97 activity, leading to formation of new holoenzyme complexes. Further, the complex disassembly was reconstituted *in vitro* and was shown to be dependent on the Shp1 homologue p37 (Weith et al., 2018). These results are an important puzzle piece in the explanation of the inhibitory and activational properties of I3 and SDS22 in PP1 regulation: I3 and SDS22 build a stable, ternary complex with PP1, shown to be inactive. Through the disassembly of the complex by p97 and p37, PP1 can form other holoenzymes and potentially perform cellular functions. It is yet to be elucidated what the exact role of the SPI complex and its individual components is in cells, and which pathways it is connected to. Structural data can help to understand the mechanisms of PP1 inhibition and SPI recognition and disassembly.

1.2.1 Structure of PP1:I3

I3 consists of 126 amino acids, which are predicted to be almost entirely unstructured. Conserved regions of I3 comprise the SLiMs, which interact with PP1 (Cao et al., 2022). Like most PIPs, I3 interacts with PP1 opposite of the PP1 active site through its RVXF motif, which for I3 consists of the residues KVEW at positions 40-43 (Zhang et al., 2008). The glutamate residue could lead to a weakening of the I3 interaction compared with other RVXF motifs, due to the bulky, negatively charged properties of the amino acid (Fontanillo et al., 2022). However, a disruption of the RVXF interaction with PP1 through phosphorylation is excluded, as this would require a serine or threonine residue at the same position (Nasa et al., 2018). Another interaction site for PP1 was found at positions 65-77 of I3, which was observed to interact with, or in close proximity to the PP1 active site. This discovery was made evident by observing that deletions within this site resulted in the loss of PP1 inhibition by I3 (Zhang et al., 2008).

Resolution of the PP1α:I3 (PI) complex crystal structure, combined with biophysical analysis revealed additional interaction sites with PP1 and further defined the inhibitory interaction of I3 with the PP1 active site (Srivastava et al., 2023). The PP1α$_{7\text{-}300}$:I3$_{27\text{-}68}$ complex was co-expressed and purified from human Expi293F cells. The crystal structure confirms that I3 interacts with the PP1 RVXF binding pocket (**Figure 1.4**). The RVXF binding pocket is highlighted in light turquoise including the PP1α residues Ile169, Leu243, Phe257, Arg261, Val264, Leu266, Met283, Leu289, Cys291, Phe293, and Tyr255 based on interactions with I2 and PNUTS (Choy et al., 2014; Egloff et al., 1995; Hurley et al., 2007). The I3 RVXF motif (teal) binds within the pocket, forming a β-sheet structure, demonstrating that the naturally intrinsically disordered protein (IDP) I3 gains structure upon binding to PP1. Additionally, a previously unknown interaction with the PP1 SILK binding pocket was discovered. The SILK binding pocket of PP1 is highlighted in light blue and includes the PP1 residues Leu53, Glu54, Leu55 Glu56, Ala57, Pro 58, Leu59, Asp86, Leu88, Glu116 Asn117, Phe119, Asp166, and Glu167 based on interactions with KNL1 and I2 (Bajaj et al., 2018; Chen et al., 2016). The I3 residues contributing to the interaction are SLTIK at positions 27-31 (blue). In addition to RVXF and SILK, two additional interaction sites of I3 were revealed. Between the RVXF motif and the CCC motif I3 forms another rigid β-sheet secondary structure, interacting with the acidic substrate binding groove on the PP1 surface (not highlighted). Conversely, the stretch of amino acids connecting the I3 SILK and RVXF motifs could not be modeled, due to high flexibility of the region. The I3 residues in this region comprise LRKRKP at positions 32-37 and are known as the I3 nuclear localization signal, leading to the import of I3 into the nucleus (Huang et al., 2005). The solvent accessible surface area between the SILK and RVXF binding pockets are predominantly acidic (not highlighted), likely interacting with the largely basic patch of I3 at residues 32-37 in a flexible manner.

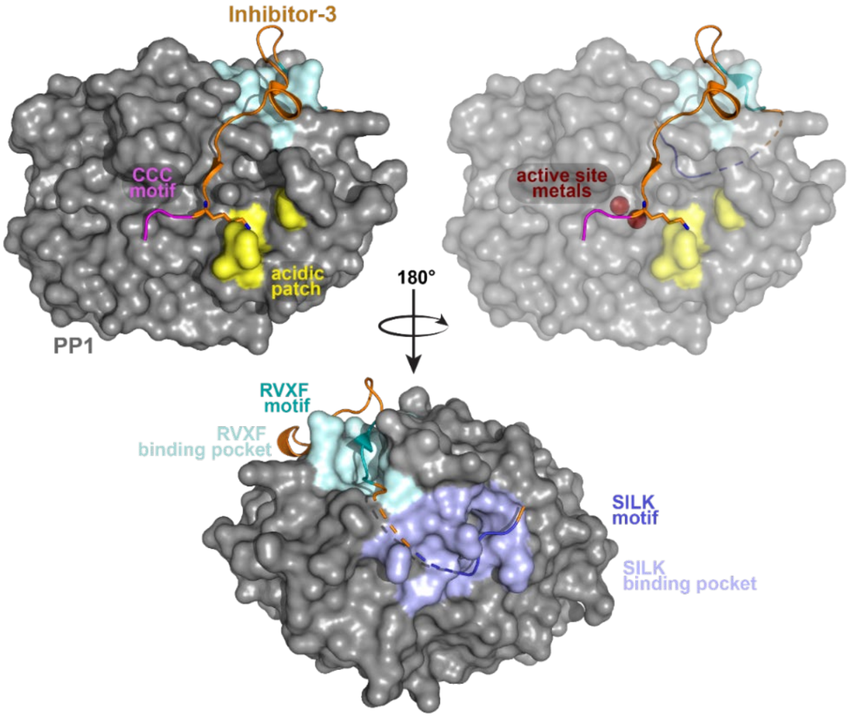

Figure 1.4: Crystal structure of the PP1α$_{7\text{-}300}$:I3$_{27\text{-}68}$-complex. PP1 surface is shown (gray) and I3 is shown as a cartoon (orange). Highlighted are the CCC motif of I3 (magenta), the acidic patch that binds I3 Lys59 (yellow), the PP1 active site metals (red), the RVXF binding pocket of PP1 (light turquoise), the RVXF motif of I3 (teal), the SILK binding pocket of PP1 (light blue) and the SILK motif of I3 (blue). Dashed lines represent I3 residues that were unable to be modeled due to the low resolution of electron density. The figure was designed based on the pdb entry 8DWL.

The PP1:I3 structure contains both active site metal ions, indicating that PP1 could be active in this conformation. However, I3 has been shown to inhibit PP1 both *in vitro* and *in vivo* and deletion of the I3 amino acid residues 65-77 resulted in a loss of PP1 inhibition. While the PI crystal structure was only resolved until I3 residue 62, it could be shown that Lys59 in I3 interacts with an acidic patch in PP1 consisting of Asp208, Asp210, Asn219, and Asp220 (**Figure 1.4**). This interaction is relevant, because it positions three cysteine residues of I3 (CCC motif) directly in front of the PP1 active site. Deletion and surface plasmon resonance (SPR) experiments showed that the CCC motif is essential for both PP1 binding and inhibition (Srivastava et al., 2023).

Individual, double, and full substitution experiments of the three cysteines showed that the CCC motif binds the active site in a dynamic manner, where single and double mutations were tolerated concerning binding affinity and inhibition. The inhibition of PP1 by I3 is likely caused by blocking of the active site through flexible binding of the I3 region comprising the three sequential cysteines. The mechanism of inhibition of occluding the active site was also observed for I2, which in contrast to I3 binds PP1 at the acidic and hydrophobic grooves, blocking the active site through an extended α-helix (Hurley et al., 2007). Therefore, the CCC-motif interaction presents a novel inhibition mechanism for PP1.

1.2.2 Structure of SDS22:PP1

SDS22 consists of 360 amino acid residues which, in contrast to other PIPs, form a distinct structure. Studies have revealed that SDS22 interacts with all PP1 isoforms both *in vivo* and *in vitro* (Ceulemans, Vulsteke, et al., 2002; Peggie et al., 2002; Posch et al., 2010). SDS22 lacks the RVXF motif, which is commonly present in the majority of known PP1-interacting proteins. Instead, SDS22 consists of leucine-rich repeats (LRRs), which are known to mediate protein-protein interactions (Kobe & Kajava, 2001). The SDS22 crystal structure reveals that residues 78-333 form 11 and a half LRRs, which adopt a curved hairpin structure, bending at a conserved asparagine residue (Heroes et al., 2019) (**Figure 1.5**).

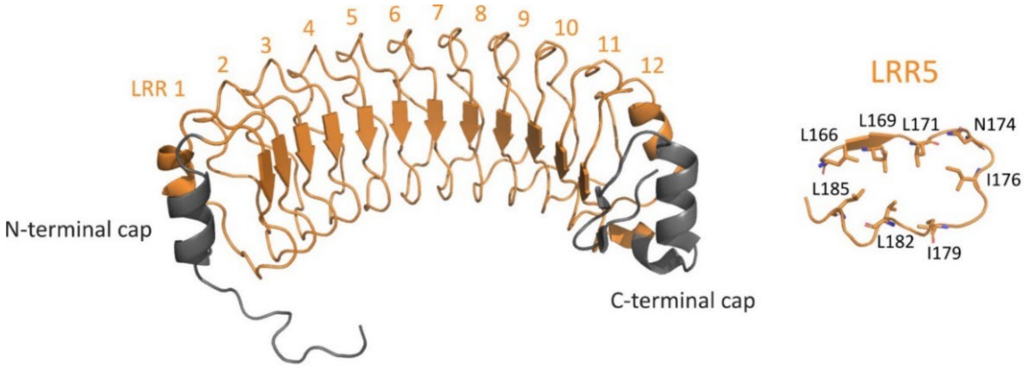

Figure 1.5: Crystal structure of SDS22. SDS22 is presented as a cartoon. LRRs 1-12 are shown (orange), as well as the N- and C-terminal caps (gray). LRR5 is exemplarily represented as a cartoon with conserved amino acid residues shown as sticks (Cao et al., 2022). Based on pdb: 6HKW.

Each full LRR consists of 22 amino acids, including conserved leucine, asparagine, and isoleucine residues. Together the repeats form a curved structure with a concave and convex side through β-sheet interactions among the LRRs. In addition to the hydrophobic core, SDS22 contains an N- and C-terminal cap. Residues 69-75 in the N-terminal cap form an α-helix. The first 54 residues of SDS22 were not resolved in the crystal structure, but there is evidence that the N-cap's shielding of the hydrophobic core from surrounding solvent contributes to SDS22 stability (Stone et al., 1993). The C-terminal cap comprises residues 339-354, which also form an α-helix and has been shown to form an interaction with the p97 N-terminal domain, likely aiding in the recruitment of the SDS22:PP1:I3 complex (van den Boom et al., 2023).

Resolution of the SDS22:PP1 crystal structure revealed, that SDS22 interacts with PP1 through an extensive surface, burying a 3084 Å^2 surface area previously exposed to solvent (Choy et al., 2019) (**Figure 1.6**). The interface comprises 26 residues within the SDS22 LRR concave side and 31 residues of PP1, extending from the C-terminal to the hydrophobic substrate binding groove. Most of the interactions observed are either of an electrostatic or polar nature, which is in line with the presence of a significant amount of charged amino acids at the interface. The N-terminal residues of SDS22 were not resolved in the structure, but interactions with the N-terminus do not seem to contribute to PP1 binding. SDS22 binds close to the active site of PP1, but even though SDS22 is a potent inhibitor of PP1 activity, a direct occlusion of the active site of PP1 does not occur. However, in the SDS22:PP1 crystal structure, only one of the required metal ions for PP1 activity, Fe^{2+} at position M2, was found.

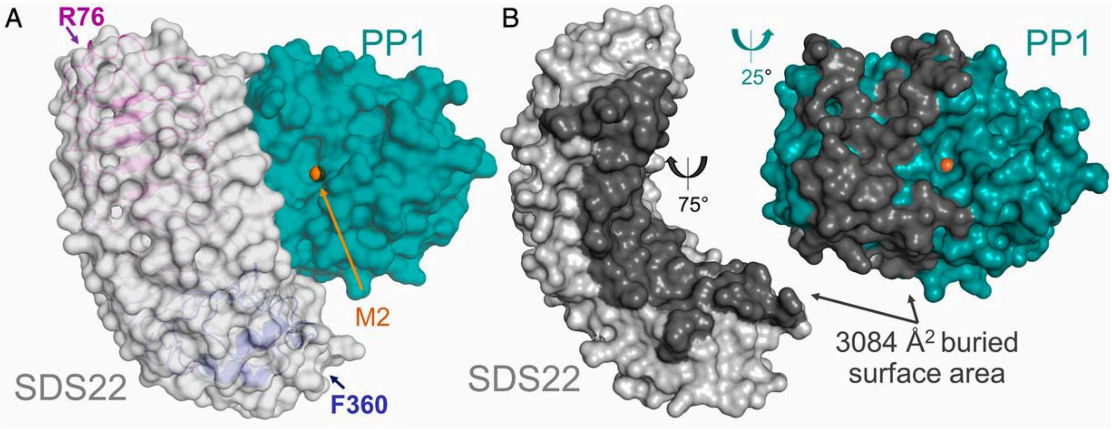

Figure 1.6: Crystal structure of the SDS22$_{56\text{-}360}$:PP1α$_{1\text{-}300}$ complex. A) SDS22 (gray) and PP1 (teal) are shown as a transparent surface. SDS22 residues 76-360 were resolved. Within the SDS22 structure, LRRs are shown as a cartoon (gradient magenta-blue from LRR1-LRR12). Indicated is also the active site M2 metal (orange) **B)** SDS22 (gray) and PP1 (teal) surfaces separated and rotated. Indicated is the extensive interaction interface of both proteins (dark gray) (Choy et al., 2019). Based on pdb: 8OBN.

A closer look at the structural differences between free and SDS22-bound PP1 shows that a shift of several PP1 residues blocks the M1 metal from entering the PP1 hydrophobic groove (Choy et al., 2019). This suggests either that SDS22 binding leads to conformational changes within PP1 resulting in a loss of the M1 metal ion, implying that the SDS22 inhibitory mechanism is ejecting the M1 metal from PP1. Another possibility is that SDS22 exclusively binds PP1, which has already undergone conformational changes and lost the M1 metal. In this scenario, SDS22 might stabilize the metal-deficient PP1 specifically. SPR experiments were employed to test the two hypotheses. For that purpose, SDS22 and PP1 were individually expressed and incubated in metal-rich and metal-poor buffers (Choy et al., 2019). Notably, SDS22 did not bind to PP1 in the presence of 1 mM $MnCl_2$ or $ZnCl_2$. However, equilibration of PP1 in metal-poor buffer resulted in SDS22 binding, suggesting that SDS22 specifically binds metal-deficient PP1. To confirm the preferential binding of PP1 lacking the M1 metal, the experiment was repeated with the mutant $PP1^{H66K}$, which is incapable of binding the M1 metal, and is therefore largely catalytically inactive. Mimicking PP1 that has lost its M1 metal, $PP1^{H66K}$ bound SDS22 with a strong affinity, verifying the previous experiments. While I3 and SDS22 both contribute to PP1 inhibition and stability, as both properties are enhanced in the ternary SDS22:PP1:I3 complex (Choy et al., 2019; Pedelini et al., 2007), structural insights into I3 and SDS22 binding of PP1 revealed that I3 primarily inhibits PP1 by occluding the active site, whereas SDS22 could have a function in keeping metal-deficient PP1 stable within the cell.

1.2.3 The SDS22:PP1:I3 complex

PP1 is known to form ternary complexes, interacting with two PIPs simultaneously. Most of these complexes, like PP1:spinophilin:I2 or PP1:GADD34:I1 (Inhibitor-1), contain proteins which compete for the RVXF binding pocket (Connor et al., 2001; Dancheck et al., 2011; Terry-Lorenzo et al., 2002). SDS22 lacks the RVXF motif and structure determination of SDS22:PP1 and PP1:I3 showed that, indeed, their binding sites do not overlap (Choy et al., 2019; Srivastava et al., 2023). Structure determination of the SDS22:PP1:I3 complex (SPI) revealed that PP1 adopts the SDS22-bound conformation in the ternary complex, lacking the M1 metal ion, while the M2 metal ion is present (Choy et al., 2024) (**Figure 1.7A**). An overlay of SDS22 in SP and SPI showed that SDS22 was found in the same conformation in both complexes (**Figure 1.7B**). Likewise, I3 showed a similar conformation in PI and SPI. I3 residues 39-60 bound in an identical way to PP1 in both complexes, including the Lys59 interaction with the PP1 acidic binding groove, which stabilizes the CCC motif in front of the PP1 active site (Choy et al., 2024). However, I3 residues 27-31, comprising the SILK motif, could not be resolved in the SPI complex, indicating that the SILK motif is not necessary for PP1 interaction (**Figure 1.7C**). This is consistent with the finding that I3 residues 28-31 are necessary for recognition of the SPI complex by the AAA-ATPase p97 and its adapter protein p37 (van den Boom et al., 2021). These I3 residues form an internal recognition site (IRS), which needs to be available for protein-protein interaction and therefore cannot be constantly bound to PP1.

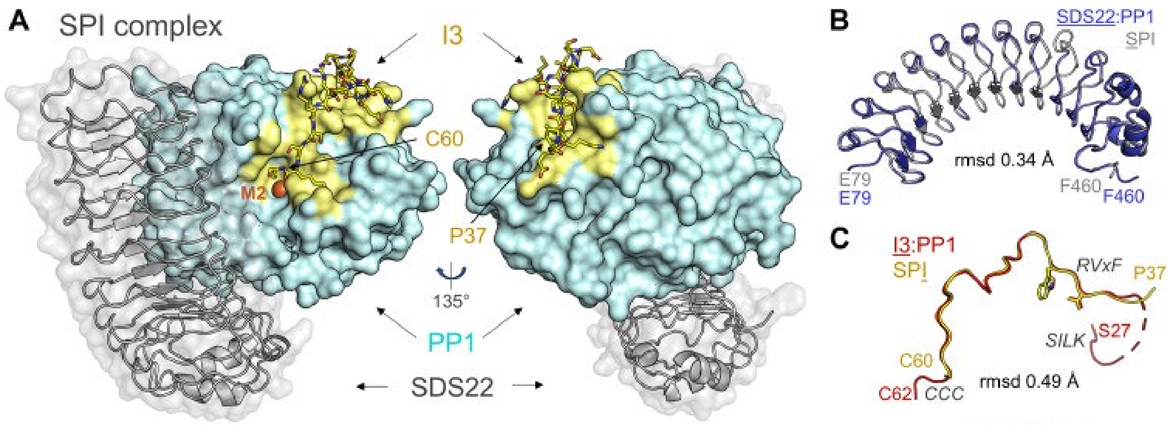

Figure 1.7: Crystal structure of the SDS22$_{56-360}$:PP1α$_{1-330}$:I3$_{1-126}$ complex. A) Structure of SPI with SDS22 shown as a transparent surface and cartoon (gray), PP1 shown as a surface (light cyan), and I3 residues 37-60 as sticks (yellow). I3 interacting surface on PP1 (yellow) and the M2 metal (orange) are highlighted. **B)** Overlay of SDS22 from SPI (gray) and SP (blue, pdb:6OBN). **C)** Overlay of I3 from SPI (yellow) and PI (red, pdb:8DWL) (Choy et al., 2024). Based on pdb: 8U5G.

A structure of SPI bound in complex with p97 and p37 was determined though cryogenic electron microscopy (cryo-EM) and showed SDS22 and PP1 in a similar conformation as in the SPI complex alone, though the metal ion in PP1 was not resolved (van den Boom et al., 2023). Further, a density adjacent to the PP1 active site and near the RVXF binding pocket was detected, which was confirmed to be located exactly where I3 residues 37-60 bind the SPI complex (Choy et al., 2024; van den Boom et al., 2023). These I3 residues, as in all structures that include PP1 and I3, are thought to render PP1 inactive. Since the SPI complex crystal structure was determined with truncated I3 and the cryo-EM structure did not resolve all I3 residues it is still unclear whether SDS22 and I3 interact directly. A synergistic inhibition and stabilization of PP1 through both proteins indicates that such an interaction may exists. Additionally, the SPI complex is disassembled during PP1 biogenesis through p97 and the adapter protein p37, with I3 being translocated through the p97 pore (Weith et al., 2018). In this process, SDS22 also dissociates through an unknown mechanism, suggesting that I3 and SDS22 may interact directly, or that I3 dissociation leads to a conformational change in PP1, promoting SDS22 dissociation, potentially leading to the release of active PP1. To appreciate the unique place that the SPI complex holds as a substrate for p97, it is important to understand p97 and its adapter proteins acting upon ubiquitinated substrates.

1.3 The AAA-ATPase p97

AAA-ATPases (ATPases associated with diverse cellular activities), are a highly conserved family of proteins, which use the energy released by ATP hydrolysis to undergo conformational changes leading to an exertion of mechanical force. This force can be used to act on substrate proteins, leading to protein unfolding, disaggregation, and protein translocation, among others. Present in all AAA-ATPases is at least one common AAA domain which contains the Walker A and Walker B motifs (Neuwald et al., 1999; Walker et al., 1982). Walker A is the primary binding site of ATP, while the Walker B motif coordinates water and a Mg^{2+} ion, facilitating ATP hydrolysis (Story & Steitz, 1992). Some AAA-ATPases are further characterized by another conserved region, the second region of homology (SRH). This region includes an arginine residue, known as the "arginine finger", which participates in interactions between subunits, contributing to the formation of multimeric enzymes as well as concerted nucleotide hydrolysis within the subunits (Karata et al., 1999; Lupas & Martin, 2002; Wang et al., 2005). The formation of these quaternary structures and coordinated action is essential for the sophisticated functions of many AAA-ATPases.

p97, also VCP (valosin-containing protein) in mammals and Cdc48 in yeast, is a homo-hexameric AAA-ATPase. It is primarily known as a ubiquitin-dependent unfoldase, recognizing and unfolding proteins that have undergone modification with the small protein ubiquitin (ubiquitination). Remodeling of p97 substrates has a myriad of cellular functions, such as protein quality control and degradation, membrane fusion, response to cellular stresses, and cell cycle regulation (van den Boom & Meyer, 2018; Wang et al., 2004; Woodman, 2003). The six subunits of p97, each comprising two AAA domains (D1 and D2) and regulatory N- and C-terminal domains, assemble into a barrel-shaped structure with a central pore through which a substrate can be translocated, leading to its unfolding (Olszewski et al., 2019; Zhang et al., 2000). Recognition of substrates is regulated through diverse p97 adapter proteins (Braxton & Southworth, 2023). In cooperation with the ubiquitin adapters Ufd1 (ubiquitin fusion degradation protein 1) and Npl4 (nuclear protein localization 4) for example, ubiquitinated proteins are recognized, unfolded, and thus prepared for degradation in the 26S proteasome (Bodnar et al., 2018; Meyer et al., 2000; Olszewski et al., 2019). While most known p97 substrates have ubiquitin or chains of several ubiquitin moieties attached to them, a ubiquitin-independent pathway is also known. Recognition of the

SDS22:PP1:I3 complex by p97 and the adapter protein p37 leads to I3 unfolding, without a requirement of I3 ubiquitination (Weith et al., 2018).

As one of the most abundant proteins in eukaryotic cells, with diverse substrates and regulatory functions, p97 is an essential player in protein homeostasis within the cell. Over 50 missense mutations in p97 are known to cause an autosomal dominant disorder called multisystem proteinopathy-1 (MSP-1) or VCP disease (Korb et al., 2021; Watts et al., 2004). Some mutations exhibit a toxic gain-of-function phenotype with increased ATPase and unfoldase rates, while others result in a loss-of-function phenotype, impairing the ability of p97 to clear protein aggregates (Blythe et al., 2019; Blythe et al., 2017; Johnson et al., 2010; Tang & Xia, 2016). Common pathological features are the accumulation of ubiquitinated proteins or intranuclear TDP-43 (TAR DNA-binding protein 43) positive inclusions (Kimonis, Mehta, et al., 2008). Symptoms of the disease include phenotypes of Paget’s disease of bone (PDB), familial amyotrophic lateral sclerosis (ALS), Parkinson’s disease (PD), inclusion body myopathy (IBM), Charcot -Marie-Tooth Type-2B (CMT2B), and frontotemporal dementia (FTD) (Kimonis, Fulchiero, et al., 2008). Further, an increased expression of p97 was observed in many cancers and clinical trials with p97 inhibitors have been conducted, currently facing challenges with off-target effect and the emergence of resistance mutations (Anderson et al., 2015; Bastola et al., 2019; Cheng et al., 2022; Roux et al., 2021). Other studies suggest that the p97 inhibitor CB-5083 may alleviate cellular defects associated with p97 mutations, offering potential therapeutic avenues for p97-associated myopathy (Cheng et al., 2022; Wang et al., 2022). However, due to the complexity of diseases linked to p97 mutations, the effectiveness of current inhibitors in mitigating disease phenotypes remains uncertain. Nevertheless, ongoing research aims to develop next-generation inhibitors with improved efficacy.

1.3.1 Cellular functions of p97

Protein unfolding by p97 is an essential step in many different cellular pathways and requires specific adapter proteins (**Figure 1.8**). Some of these pathways are coupled to the proteasomal degradation of the unfolded protein substrate and therefore, in many cases, contribute to maintaining protein homeostasis. Other pathways have a more regulatory role in cell signaling or cellular remodeling and organization. The complexity of the p97 system further illustrates the necessity for proper p97 functionality in maintaining cellular health.

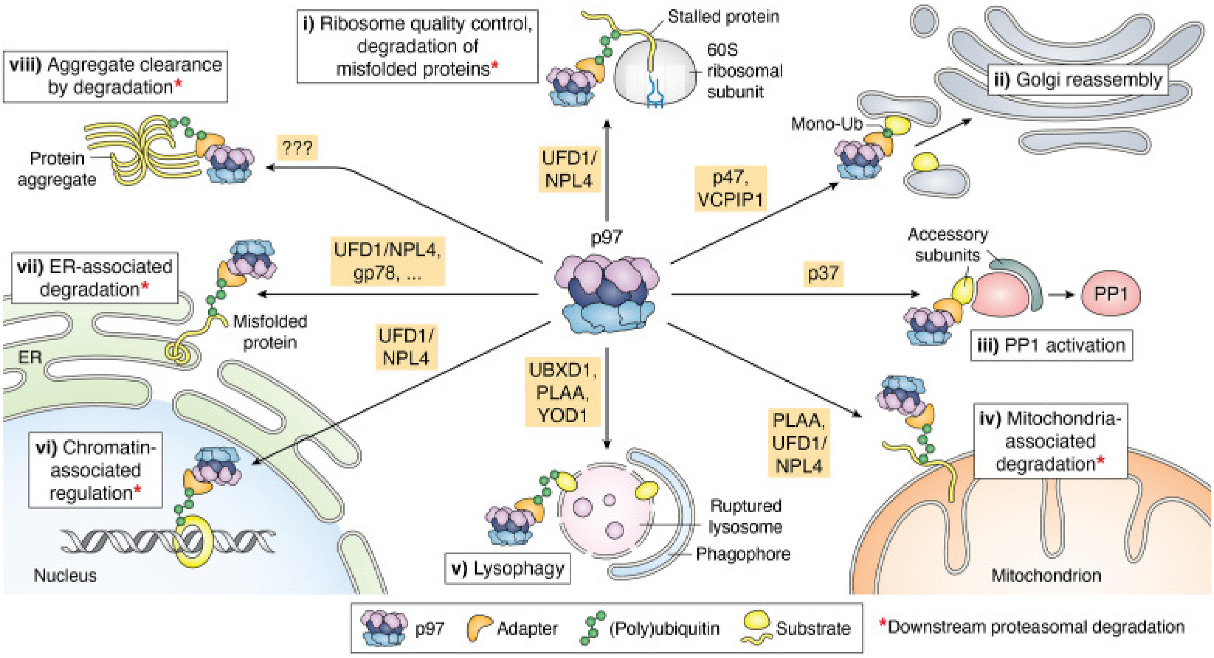

Figure 1.8: p97-dependent pathways and associated adapter proteins. Adapter proteins are highlighted in orange, substrate proteins as spherical shapes or strands representing natively folded or un-/misfolded forms, respectively (yellow), and mono- and poly-ubiquitin represented as a single or chains of small spheres (green). p97-regulated pathways are indicated as follows: **i)** ribosomal quality control, **ii)** Golgi reassembly, **iii)** PP1 activation, **iv)** Mitochondria-associated degradation, **v)** Lysophagy, **vi)** Chromatin-associated regulation, **vii)** ER-associated degradation, and **viii)** Aggregate clearance by degradation. Pathways which result in the proteasomal degradation of the substrate proteins are indicated (*) (Braxton & Southworth, 2023).

Ribosome quality control is a degradative p97-dependet pathway to maintain protein homeostasis. Translation of a nascent polypeptide can be stalled when, for example, the protein is being translated from a faulty mRNAs lacking a STOP codon. In these cases, it was discovered that the ribosome subunits split and the polypeptide chain remains bound to the 60S subunit (Brandman & Hegde, 2016). Subsequently, an E3 ubiquitin ligase, a protein which can attach ubiquitin moieties to other proteins, is recruited and ubiquitinates the nascent polypeptide (Brandman & Hegde, 2016). Together with its adapter proteins Ufd1 and Npl4, p97 recognizes the poly-ubiquitinated polypeptide and, through mechanical force, removes the polypeptide chain from the ribosome, leading to its degradation by the proteasome and thus preventing possible aggregation of the misfolded protein, as well as recycling the ribosome to proper function (Defenouillere et al., 2013; Verma et al., 2013).

An example of a regulatory rather than protein quality control pathway depending on p97 is Golgi reassembly after cell division. In eukaryotic cells, organelles like the ER and Golgi apparatus fragment during mitosis to ensure proper distribution into daughter cells. This fragmentation process guarantees that each new cell receives the necessary cellular components for proper function and integrity. At the end of mitosis, these fragments fuse back together through specific molecular mechanisms. For the Golgi apparatus, these mechanisms involve p97 and its cofactors p47 and VCIP135 (gene name VCPIP1) (Kondo et al., 1997; Uchiyama et al., 2002). The p97:adapter complex interacts with syntaxin-5, a membrane-localized receptor belonging to the t-SNARE family (Soluble N-ethylmaleimide-sensitive factor Attachment Protein Receptors) (Rabouille et al., 1998). Syntaxin-5 is monoubiquitinated during early mitosis, which prevents premature membrane fusion (Huang et al., 2016). The mono-ubiquitination recruits p97:p47:VCIP135 (Meyer et al., 2002). Upon binding, the deubiquitinating enzyme (DUB) VCIP135 removes the syntaxin-5 ubiquitination, allowing restored membrane fusion facilitated by p97:p47 (Huang et al., 2016). The exact mechanism of membrane fusion has not yet been fully elucidated. The p97 adapter p37 was also shown to mediate Golgi reassembly through a slightly different mechanism (Uchiyama et al., 2006) and similar pathways for p97-dependent ER reassembly have been described (Uchiyama et al., 2002).

A signaling related role of p97 is the disassembly of an inactive PP1 complex during PP1 biogenesis via a unique mechanism. The complex consisting of SDS22:PP1:I3 (SPI) is recognized by p97 and its adapter protein p37, leading to I3 unfolding and the disassembly of the whole complex. This process is ubiquitin-independent and allows PP1 to form new complexes with other regulatory subunits (Weith et al., 2018). Although it has not yet been directly shown, it is reasonable to hypothesize that the dissociation of the inhibitory proteins from PP1 leads to PP1 activity, in so far that PP1 can form holoenzymes with activating subunits after SPI disassembly, to dephosphorylate specific substrates. This p97-dependent pathway connects two major protein regulators, p97 and PP1, responsible for a large number of cellular pathways. It will be intriguing to discover which pathways are regulated in this manner to understand the significance of the convergence of these two evolutionarily conserved regulators.

Other p97-mediated pathways include the degradation of proteins associated with the mitochondrion. p97 together with Ufd1:Npl4 and another adapter protein, called PLAA in humans, extracts misfolded proteins from the outer mitochondrial membrane, preparing them for proteasomal degradation (Wu et al., 2016). Further, through a process called lysophagy, damaged lysosomes are removed from the cytosol through autophagy. Autophagy is a cellular mechanism in which a double membrane, the phagophore, forms around cellular cargo. The cargo is often specifically recognized by autophagy receptors, ultimately leading to the degradation of the enclosed cargo by fusion of the phagophore with the lysosome. The clearance of damaged lysosomes themselves is promoted by p97 and the adapter proteins YOD1, UBXD1 and PLAA, by removing specific substrates like calponin-2 from the lysosomal membrane. (Kravic et al., 2022; Papadopoulos et al., 2017). Calponin-2 is a factor, necessary for phagophore formation during autophagy and needs to be removed during later stages for efficient lysophagy to progress (Kravic et al., 2022). Another regulatory pathway of p97, chromatin-associated degradation, combines regulatory p97 functions with substrate degradation. In the process of DNA double-strand break (DSB) repair, the ring-shaped Ku70:Ku80 (Ku) complex becomes trapped on DNA and requires active extraction (Postow et al., 2008). In cooperation with Ufd1:Npl4, p97 removes Ku from repaired DNA, leading to proteasomal degradation of Ku (Postow et al., 2008; van den Boom et al., 2016). Lastly, a well-studied mechanism of p97-dependent protein quality control is the ER-associated degradation (ERAD) of proteins. In this process, proteins that did not properly fold, while going through cycles of quality control on the ER lumen, are ubiquitinated, translocated across the ER membrane through mechanical force of p97 in cooperation with several adapter proteins, and subsequently transferred to the proteasome for degradation (Stein et al., 2014; Wu et al., 2016). This pathway can relive ER-stress caused by the accumulation of misfolded proteins. Similarly, it has also been shown that ubiquitinated aggregates of microtubule-associated protein tau, which are known to cause neurodegeneration, can be targeted by p97 to relive the cell of stress caused by misfolded proteins, though the exact mechanism remains to be elucidated (Saha et al., 2023). Many more p97 substrates and p97-dependent pathways are known and more are likely to emerge in the future. Further research will be necessary to understand these processes in molecular detail.

1.3.2 p97 structure and mechanism

p97 is an 806 aa protein and consists of three domains, which fold into distinct structures, the regulatory N-terminal domain and the two ATPase domains D1 and D2 (**Figure 1.9A**). Six subunits composed of these domains arrange into a homo-hexameric quaternary structure, where the six D1 and D2 domains form two stacked rings with a central pore, and the N-domains arrange on the periphery of the D1 ring (**Figure 1.9B**). Cryo-EM structures of Cdc48 and p97 revealed that the subunits adopt a staircase-like conformation when the ATPase is engaged with a substrate (Cooney et al., 2019; Twomey et al., 2019; van den Boom et al., 2023). To further understand the mechanism of substrate translocation, separate structures were determined with either ADP, or the ATP mimic ADP-BeF (ADP and beryllium fluoride), which traps p97 in an ATP-bound conformation (Twomey et al., 2019). In these conformations it could be observed that hydrophobic residues in pore loops in D1 and D2 can make contact with the client protein backbone. The residues in the pore loops of D2 (W561 and Y562) are aromatic and bulkier than in D1 (M288 and A289), consistent with the observation that the D2 ring is more important than the D1 ring for substrate translocation (Blythe et al., 2017; Bodnar & Rapoport, 2017). ATP hydrolysis in the sixth subunit in both rings results in retraction of the pore loops and a disengagement of the whole subunit. Facilitated by binding of a new ATP molecule, the subunit then re-engages, replacing the first subunit. Following that, the subunits undergo a downward movement, exerting a force that drags the polypeptide chain along in tandem (**Figure 1.9C**). Through this hand-over-hand mechanism, driven by ATP binding and hydrolysis, the substrate is translocated 2 amino acid residues per ATP hydrolysis through the central channel of p97, resulting in protein unfolding (Twomey et al., 2019). p97/Cdc48 have this mechanism in common with other hexameric AAA-ATPases (Gates et al., 2017; Puchades et al., 2017; Rizo et al., 2019).

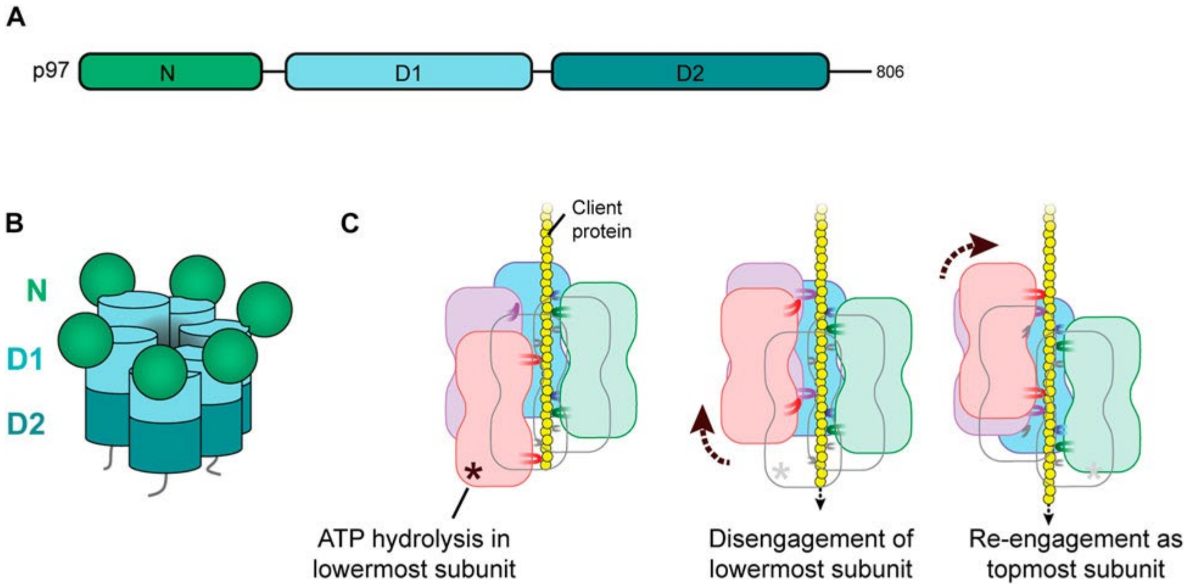

Figure 1.9: Domain arrangement and substrate translocation mechanism of p97. A) Domain structure of p97 with N-terminal domain (green), first AAA-ATPase domain D1 (light blue), and second AAA-ATPase domain D2 (dark green). **B)** Cartoon representation of the staircase arrangement of p97 subunits and domains in the hexameric structure. **C)** Cartoon of the process of p97-mediated client protein (yellow) processing. Hydrophobic pore loops in the ATPase domains interact with the substrate backbone. ATP hydrolysis in the lowermost subunit (red) results in pore loop disengagement, ADP release and new ATP-binding allows re-engagement as the now topmost subunit. Through successive cycles of ATP hydrolysis and binding, the substrate is translocated through the p97 channel (Meyer & van den Boom, 2023).

In many of the p97-dependent processes, p97 unfolds diverse ubiquitinated proteins, which leads to their degradation of the substrate protein by the proteasome. The purpose of p97 in this process was confirmed in a study which showed that a ubiquitinated substrate lacking any flexible linker regions could not be processed by the 26S proteasome alone (Olszewski et al., 2019). Only upon adding a C-terminal extension to the substrate, or p97 to the reaction, could the substrate be processed by the proteasome, confirming that p97 prepares tightly folded substrates without flexible segments for proteasomal degradation (Olszewski et al., 2019). For this indirect process of substrate recognition through ubiquitin chains, p97 requires the adapter proteins Ufd1:Npl4. These two adapter proteins form a heterodimeric complex and elaborate interactions with p97 and the ubiquitinated substrates, facilitated by their many subdomains (**Figure 1.10A**).

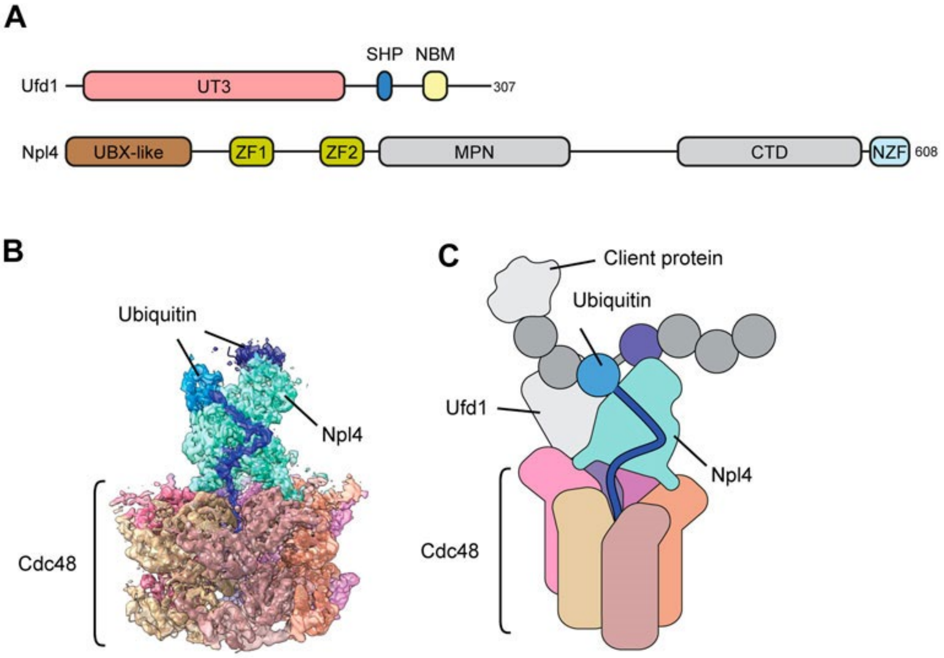

Figure 1.10: Targeting of a ubiquitinated substrate for unfolding by Cdc48:Ufd1:Npl4. A) Domain structures of Ufd1 and Npl4 including the Ufd1 ubiquitin-binding domain UT3, p97-binding SHP and Npl4-binding NBM, as well as the Npl4 ubiquitin-binding domains MPN, CTD and NZF, and p97-binding UBX-like domain and ZF1 and 2. **B)** Cryo-EM structure of Cdc48:Ufd1:Npl4 (pdb: 6OA9). Resolved was an unfolded ubiquitin initiator moiety (dark blue) along the Npl4 (teal) groove, two distal ubiquitins (blue, purple) and all six p97 subunits **C)** Cartoon representation of B), further including the unresolved Ufd1, ubiquitin-chain moieties and substrate protein (gray).

The Ufd1:Npl4 heterodimer associates with p97/Cdc48 via the Ufd1 SHP box and the Npl4 UBX-like domain (Bruderer et al., 2004). These regions interact with the respective opposite p97 N-domains. Additionally, the Npl4 zinc fingers ZF1 and ZF2 establish contact with the p97 D1 ring. (Pan et al., 2021; Twomey et al., 2019). The Npl4 MPN and CTD domains, as well as the N-terminal zinc finger NZF, specific to metazoans, interact with K48-linked ubiquitin chains (Meyer et al., 2002; Twomey et al., 2019). Together with the Ufd1 UT3, these domains stabilize the ubiquitin chain on top of the p97 hexamer (Bodnar et al., 2018; Twomey et al., 2019). Through this interaction between Ufd1:Npl4 and the ubiquitin chain, one ubiquitin moiety unfolds as it extends into a groove within Npl4. This directs the elongated peptide stretch towards the p97 D1 pore, where it is inserted into the p97 channel (**Figure 1.10B** and **C**) (Twomey et al., 2019). Thus, ubiquitin unfolding is initiated by Ufd1:Npl4, leading to further processing by p97. For this, a direct interaction between Ufd1 and Npl1 is necessary (Meyer et al., 2000). Additionally, Ufd1:Npl4 can interact with further accessory adapters aiding in the targeting to specific cellular substrates (Meyer & van den Boom, 2023).

The kinetics of the individual steps in Cdc48:Ufd1:Npl4 processing was determined using a fluorescent unfolding substrate carrying a ubiquitin chain with five ubiquitin moieties (Ub_5), including a fluorescently labeled moiety (Williams et al., 2023). Specifically, it was shown that the initiator ubiquitin is bound and unfolded in 2.3 ± 0.2 s. Secondly, insertion of the unfolded ubiquitin into the Cdc48 pore was within 3.2 ± 0.1 s and did not require ATP hydrolysis. Unfolding of four further, distal ubiquitins and the substrate was achieved within 4.9 ± 1.2 s. Under multiple turnover conditions however, processing of the distal ubiquitins took 125 ± 4 s indicating that, for Ub_5, substrate release is the rate-limiting step of the whole reaction. In contrast to rapid initiation and unfolding, slow substrate release leaves Cdc48 unable to rapidly process a new substrate. This time line was further consistent with the observation that proteasomal degradation of the Ub_5 substrate, combined with Cdc48 processing, took 162 ± 18 s (Williams et al., 2023). In cells this process might be sped up by deubiquitinating enzymes cleaving the ubiquitin chain after processing by Cdc48, or other shuttling factors (Ernst et al., 2009; Li et al., 2024). For a substrate carrying only two instead of five ubiquitin moieties (Ub_2), the initiation was the rate-limiting step, likely because Ufd1:Npl4 could not properly engage with the substrate (Bodnar & Rapoport, 2017; Williams et al., 2023). Consistent with that notion, the Michaelis-Menten constant (K_M) for Ub_2, with 4.1 ± 0.7 µM, was determined to be 10x higher than for Ub_4, highlighting that Ub_2 bound less effectively to Cdc48:Ufd1:Npl4 (Williams et al., 2023). Further, the Ub_2 K_M was similar to a different substrate carrying several K48-linked branched ubiquitin chains, which was determined to be 4.4 µM (Olszewski et al., 2019). Overall, substrates carrying at least two ubiquitin moieties are effectively processed by Cdc48:Ufd1:Npl4, with differences in initiation and substrate release rates.

1.3.3 SEP-domain adapters

Interacting with the p97 N-domain or unstructured C-terminus, at least 30 known cofactor proteins, usually possessing p97- and ubiquitin-binding motifs, assist p97 in its cellular tasks (Buchberger et al., 2015; Ye, 2006). Some of these cofactors possess catalytic activities of their own and can direct p97 to certain cellular processes (Hanzelmann & Schindelin, 2017; Stach & Freemont, 2017). A family of p97 cofactors, the SEP-domain adapters (**S**hp1, **e**yes-closed, **p**47), can target p97 to specific target proteins, similar to Ufd1:Npl4. The human genome encodes four SEP-domain adapters, p47, p37, UBXN2A and UBXN11, compared with the yeast *S. cerevisiae*, which only has one version, called Shp1. In contrast to Ufd1:Npl4, the SEP-domain adapters have a more simplified domain structure (**Figure 1.11**).

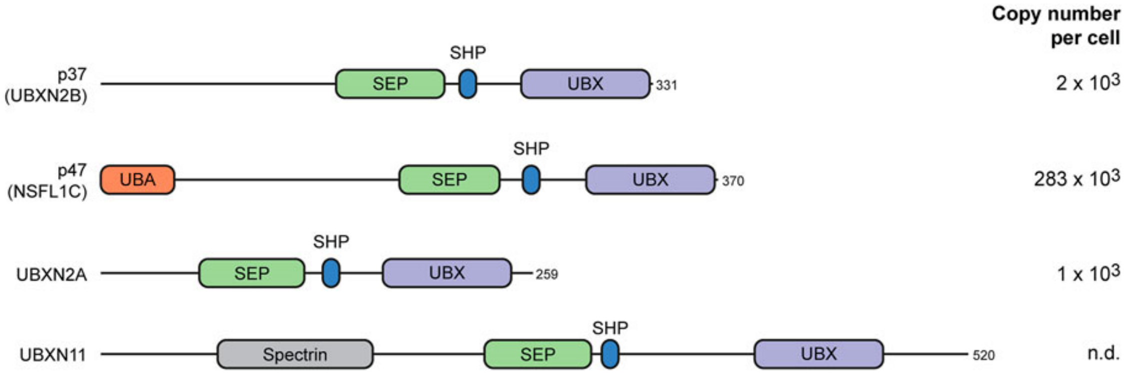

Figure 1.11: Domain strucutres of all four human SEP-domain adapters. UBX domains, SHP boxes and SEP domains interact with p97. UBA domain binds ubiquitin. Spectrin domain interacts with the cytopsceleton. Copy numbers per cell from (Beck et al., 2011) (Meyer & van den Boom, 2023).

With ~283.000 copies per cell, determined by mass spectrometry of human U2OS osteosarcoma cell lysates, p47 stands out as the most abundant adapter of p97 (Beck et al., 2011). Notably, of all four human SEP-domain adapters only p47 possesses a ubiquitin-binding domain (UBA). Unlike Ufd1:Npl4, which recognizes substrates carrying ubiquitin chains, the UBA domain of p47 exhibits a preference for binding mono-ubiquitinated substrates (Meyer et al., 2002). This mono-ubiquitination is necessary for Golgi reassembly after cell division, facilitated by p97:p47 and the deubiquitinating enzyme VCIP135 (Huang et al., 2016; Kondo et al., 1997; Uchiyama et al., 2002). The comparatively less abundant p37 was also shown to be necessary for Golgi biogenesis during mitosis, however this process only required VCIP135 interaction and not activity, suggesting a ubiquitin-independent pathway, in line with the lack of a ubiquitin-interacting domain in p37 (Uchiyama et al., 2006). UBXN2A (UBXD4) and UBXN11 (UBXD5) are less abundant and not well studied in the context of p97-dependent processes. Even though the SEP-domain adapters are each linked to several cellular pathways, a direct p97:SEP domain adapter substrate was only discovered after Shp1 in yeast was shown to interact with Cdc48/p97 and also sustain Glc7/PP1 function (Zhang et al., 1995). Further, a trimeric complex of Glc7 and its two interactors Sds22/SDS22 and Ypi1/Inhibitor-3 was discovered to interact with Cdc48:Shp1 (Cheng & Chen, 2015). A study conducted with the human proteins, including all four SEP-domain adapters, was able to confirm that the SDS22:PP1:I3 complex (SPI) is a substrate of p97 and further that binding of SPI to p97 leads to SPI complex disassembly, dependent on SEP-domain adapters (Weith et al., 2018). Specifically, p37 and UBXN2A interacted strongly and p47 weakly in co-immunoprecipitations with SPI. Those three adapters were then shown to contribute to SDS22-p97 interaction in cells in a triple KO/KD experiment. In single KD experiments, p37 had the biggest effect on SDS22-p97 interaction. A subsequent study showed that p37 and UBXN2A, but not p47 mediate the unfolding of a fluorescently labeled I3 unfolding substrate by p97 (Kracht et al., 2020). *In vitro*, the SPI complex disassembly could be reconstituted with a reaction including p37, p97, SPI and the PP1-interacting protein NIPP1, which bound PP1 after SPI disassembly (Weith et al., 2018). Notably, no ubiquitination of any of the components was necessary for this process.

1.4 Ubiquitin-independent disassembly of SPI by p97:p37

The SEP-domain adapter p37 can target the client protein complex SDS22:PP1:I3 directly to p97, in a ubiquitin-independent manner. Dissecting this process further, it was found that during SPI disassembly I3 serves as the direct substrate of p97, being pulled into the central channel of the AAA-ATPase. This was verified by crosslinks, which formed between I3 and pore residues of p97 (Weith et al., 2018). Additionally, I3 was tagged with a fluorescent protein incapable of refolding after p97 processing, and fluorescence was lost during SPI disassembly, confirming I3 as an unfolding substrate of p97 (Kracht et al., 2020; Weith et al., 2018). The translocation of I3 through the p97 channel suggests that a similar mechanism of action as for ubiquitinated substrate proteins is used for I3 unfolding by p97. However, how the process of I3 unfolding leads to dissociation of SDS22 is unclear.

It was shown that SDS22 dissociates along with I3 and this process was delayed when I3 was depleted in cells (Weith et al., 2018). It could therefore be hypothesized that SDS22 gets destabilized through a loss of interaction between SDS22 and I3 directly, or that I3 extraction leads to conformational changes in PP1, leading to SDS22 dissociation. A direct interaction between I3 and SDS22 could not be shown so far, however, critical I3 residues were not resolved in available crystal structures (Choy et al., 2024; van den Boom et al., 2023). Since SDS22 was show to interact with metal-deficient PP1, it can also be proposed that the dissociation mechanism involves a metal-loading step in the PP1 active site, weakening the affinity of SDS22 (Choy et al., 2019). This metal loading would have to be either a passive process after I3 extraction, or facilitated by p97, p37, I3, NIPP1 or other buffer components, as the process of SPI disassembly was reconstituted with only these proteins present (Weith et al., 2018). Another hypothesis is that NIPP1, another PP1-interacting protein, competes for PP1 binding sites and therefore displaces SDS22 from the complex. Further studies are necessary to confirm either of these hypotheses.

A Cryo-EM structure of p97 and p37 in complex with SPI was solved in the presence of ADP-beryllium fluoride (**Figure 1.12**) (van den Boom et al., 2023). The structure resolved a peptide strand identifiable as I3 inside the pore of p97, as the peptide is positioned in a way that fits with the other resolved I3 residues on PP1. Another study found that I3 is recognized by p97:p37 through an essential internal recognition site (IRS) at residues 28-31, which suggests that I3 could be translocated from the middle, rather than starting with one of the termini (van den Boom *et al*, 2021). This theory was confirmed by using an SPI complex with a circularized I3 as a substrate. This substrate, where both termini were blocked, was effectively translocated by p97:p37 (van den Boom et al., 2021). This finding also highlights that the p97 pore can accommodate at least two peptide strands at the same time.

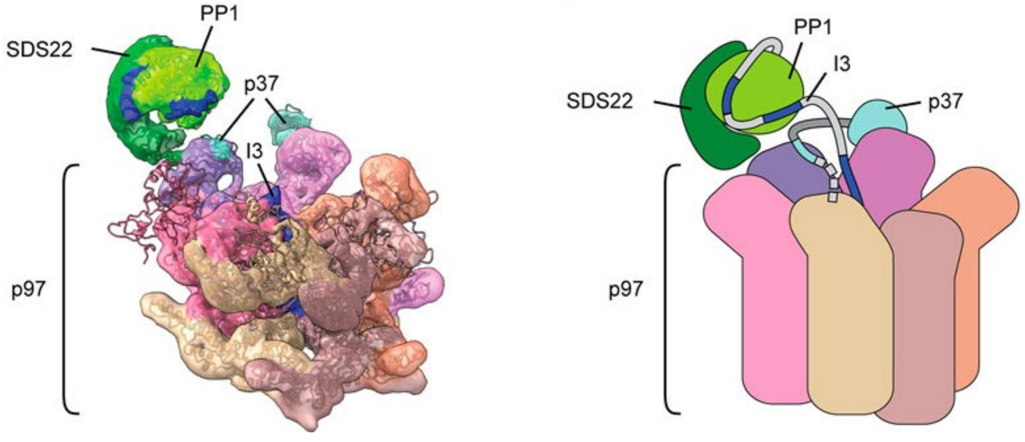

Figure 1.12: Cryo-EM structure of p97:p37:SDS22:PP1:I3. SDS22 (dark green) makes direct contact with one of the p97 N-domains (purple), while bound to PP1 (light green). Resolved residues belonging to I3 on PP1 and inside the p97 pore are highlighted (dark blue), missing residues were added in the cartoon depiction (light gray). p37 binds on top of two adjacent N-domains (teal), unresolved linker region shown in cartoon (dark gray).

Interestingly, an SDS22 helical segment makes direct contact with one of the p97 N-domains, positioning the SPI complex on top of p97 (van den Boom et al., 2023). A crosslink between SDS22 and the N-domain was present even when ATP was added to the reaction, highlighting that the interaction is stable when p97 is active and suggesting a mechanism where SDS22 holds PP1 stable, while I3 is stripped off the complex (van den Boom et al., 2023). How the force exerted on I3 is transferred to SDS22 dissociation remains elusive. p37 binds beneath PP1 to the same N-domain as SDS22 via its SHP box and to the adjacent N-domain via its UBX domain, consistent with earlier crosslink mass spectrometry data (Kracht et al., 2020; van den Boom et al., 2023). While p37 is necessary for the recruitment of SPI, a direct interaction between p37 and the SPI complex could not be observed in the Cryo-EM structure. However, a direct interaction with I3 and the p37 SEP domain and N-terminal region was shown through cross-linking experiments (Kracht et al., 2020; Weith et al., 2018). Additionally, the linker region between SHP box and UBX in p37 conferred substrate specificity upon SPI, distinguishing it further from the highly abundant p47 (Kracht et al., 2020).

How the whole SPI complex disassembles and which cellular functions are connected to this process is still unknown. Protein numbers of PP1, SDS22 and I3 relative to each other differ among cell types. It is therefore difficult to predict how much of PP1 is usually in complex with I3 and SDS22 and which processes are regulated through SPI formation and disassembly. With overlapping functions in mitosis of all three proteins, it could be hypothesized that I3 and SDS22 keep PP1 stable and inactive, until needed at the kinetochores. Freeing PP1 from SDS22 and I3 could therefore lead to PP1 activity, however the formation of a functional PP1 holoenzyme after SPI disassembly it yet to be observed. Since all three proteins are also present in the cytoplasm, similar functions for the SPI complex could be imagined in other cellular pathways beyond mitosis. The defining feature of PP1 is its ability to form different holoenzymes with regulatory and inhibitory subunits throughout its life cycle. SPI formation was thus far only shown during PP1 biogenesis; however, it could be possible that SPI can reassembles after initial disassembly, displacing other regulatory subunits to further keep PP1 stable and unable to indiscriminately dephosphorylate substrates. In that case, PP1 holoenzyme formation could be controlled by SDS22, I3 and p97:p37, with p97 potentially establishing a specific directionality in the assembly of holoenzymes.

1.5 Aims of the thesis

The catalytic subunit of PP1 is a highly conserved protein with many cellular dephosphorylation targets, which link PP1 to numerous regulatory mechanisms like the integrated stress response, apoptosis, and memory formation. PP1 interacts with hundreds of regulatory proteins to achieve substrate dephosphorylation specificity. When the catalytic subunit is free, PP1 targeting of phosphorylated substrates is widely unspecific. Therefore, PP1 activity must be tightly controlled to prevent promiscuous dephosphorylation. Conversely, active PP1 must constantly be available for proper cellular function. SDS22 and I3, two ancient interactors of PP1, are known to both inhibit and stabilize PP1 and play a role in its activity during mitosis. It was shown that PP1, SDS22 and I3 form an inactive trimeric complex during PP1 biogenesis, which can be disassembled by the AAA-ATPase p97 and the adapter protein p37 in a ubiquitin-independent manner. PP1 is then free to bind other interaction partners, however it is so far unknown whether SPI disassembly results in the formation of an active PP1 holophosphatase. Further, it is unclear whether SPI only forms during PP1 biogenesis or also reassembles later in the PP1 life cycle, potentially contributing to general regulation of PP1 holoenzyme formation together with p97:p37. Moreover, it is uncertain why both SDS22 and I3 are needed for this process, and how SDS22 dissociates from PP1, even though I3 is the direct p97 substrate. Aims of this study are to establish Förster resonance energy transfer (FRET)-based assays with the goal to elucidate details of the SPI disassembly mechanism, specifically how I3 and SDS22 dissociation are linked, and how the kinetics of the ubiquitin-independent pathway compare to the ubiquitin-dependent unfolding of substrate proteins by p97. Further, it will be investigated whether SPI formation and disassembly also occur post PP1 biogenesis, and whether PP1 forms an active holoenzyme after SPI disassembly, capable of dephosphorylating an endogenous substrate.

The first aim of this thesis is the establishment of a robust FRET-based assay for the determination of kinetic parameters of the SPI disassembly reaction catalyzed by p97:p37 with purified components. The question to be answered is how the SPI disassembly process compares to the ubiquitin-dependent pathway and whether SPI is effectively targeted by p97. This will be achieved by fluorescent tagging of proteins and their deployment in a FRET-based assay that monitors the association of an alternative PP1 binding partner after SPI disassembly. FRET signals can be monitored in real time and therefore allow a time-resolution of the reaction seconds after it started, which is necessary for accurate determination of kinetic reaction parameters. These parameters can then be compared with other published values, for example Cdc48 processing of a poly-ubiquitinated substrate.

Secondly, upon having established FRET-based assay conditions, additional substrates with FRET labels on I3 and SDS22 instead of on an alternative PP1 binding partner will be produced. These FRET-based assays will individually monitor the dissociation of SDS22 and I3 from PP1 during SPI disassembly. The individual dissociation rates will contribute to further elucidating how SDS22 dissociation is linked to I3 unfolding and dissociation from PP1. Additionally, dimeric complexes of SDS22:PP1 (SP) and PP1:I3 (PI) will be deployed to ask whether both proteins are necessary for efficient complex disassembly. This experiment could contribute to understanding why a trimeric SPI complex forms, even though SDS22 and I3 have overlapping functions in both PP1 inhibition and stabilization.

The third aim is to elucidate whether the SPI complex reassembles after initial SPI disassembly, and whether SDS22 and I3 can displace a different PP1-binding subunit. To accomplish this, FRET-based assay reactions of the SPI disassembly, including a third PP1-binding protein, will be monitored after the addition of a p97-inhibitor. Inhibition of p97 at the end of the disassembly reaction will make it possible to observe whether the SPI complex can re-form and displace a different PP1-interacting protein. SPI forms during PP1 biogenesis, but it is so far uncertain what the purpose of the SPI complex is in cells. Re-association of the complex components could indicate that SPI formation, as well as p97:p37-mediated disassembly is important in later stages of PP1 regulation, possibly even contributing to PP1 holoenzyme exchange.

The final aim of the thesis is the characterization of PP1 activity after SPI disassembly with purified proteins. To find out, whether PP1 is active after having been released from SDS22 and I3, the synthetic PP1 substrate 3-O-methylfluorescein phosphate (OMFP) will be added to the SPI disassembly reaction. OMFP is fluorogenic and thus begins to emit light after dephosphorylation, allowing the detection of PP1 activity. Further, PP1 dephosphorylation of an endogenous substrate after SPI disassembly will be tested by adding the substrate specifier GADD34, the co-factor G-actin, and the endogenous substrate, phosphorylated eIF2α (eIF2α-P), to the reaction. eIF2α-P dephosphorylation will be monitored by Phos-Tag gel analysis. PP1 activity after SPI disassembly by p97:p37 would link p97 to an activational pathway, suggesting that it may partake in more diverse cellular regulation than so far know, possibly regulated by SEP-domain adapters. Moreover, showing eIF2α-P dephosphorylation after SPI disassembly could be a first step of linking SPI to the integrated stress response, suggesting SPI might play a role in diverse cellular pathways in addition to PP1 biogenesis and mitosis.

PP1 is involved in a wide spectrum of cellular processes, which it is targeted to by its many regulatory subunits. This property makes PP1 an interesting drug target, as has been shown for the integrated stress response. The endeavor of developing drugs which interact with PP1 in specific pathways would benefit from further understanding of how PP1 activity, as well as holoenzyme formation and exchange is regulated. PP1, SDS22, I3 and p97 are all preserved across extensive evolutionary time spans. It would therefore be interesting to find out how these proteins converge to regulate potentially fundamental and conserved cellular pathways. p97 itself is also a regulator of a myriad of pathways. Understanding p97 processing of its diverse substrates will further contribute to unraveling the underlying dysfunctions in diverse disease phenotypes caused by p97 mutations.

2. Results

It is so far unclear what the purpose of the SPI complex is in cells and why both SDS22 and I3 are necessary for PP1 regulation. Further, kinetic details of SPI disassembly by p97 and p37 have not been investigating. To achieve the time resolution necessary for kinetic data analysis, fluorescently labeled proteins were created to be used in FRET-based assays. For the first experiments presented here, an indirect method was used to detect the disassembly of SPI by p97:p37, which involved observation of the binding between PP1 and the alternative PP1 interaction partner NIPP1. To achieve this, FRET labels were placed both on PP1 and NIPP1. This indirect method of monitoring SPI disassembly served as an approach to overcome FRET signal limitations, necessary for data input to determine kinetic parameters of the SPI disassembly reaction. FRET-based assays to observe dissociation of SDS22 and I3 directly, were subsequently employed to investigate how SDS22 and I3 dissociation from PP1 is coupled, whether both are necessary for efficient disassembly, and if the SPI complex re-forms after initial disassembly. For these approaches SPI versions were produced where the FRET donor label was placed on PP1 and the acceptor on either I3 or SDS22.

2.1 A FRET-based assay to determine SPI disassembly kinetics

A unique feature of SPI recognition and disassembly by p97 is that it is independent from the small protein modifier ubiquitin, which is usually necessary for p97 substrate binding and processing (Weith et al., 2018). So far, it is unknown how exactly the mechanism of SPI disassembly differs from that of other p97 substrates. To address this question, an *in vitro* FRET-based assay was set up, which allowed the indirect detection of SPI disassembly by monitoring the binding of the alternative PP1-interacting protein NIPP1. SPI disassembly catalyzed by p97:p37 leads to the dissociation of SDS22 and I3 from PP1. Consequently, an alternative PP1 interaction partner, NIPP1, can associate to form a complex with PP1. To track the process of NIPP1 binding, following SPI disassembly, FRET donor and acceptor labels were attached to PP1 and NIPP1, respectively. Binding of fluorescently tagged proteins allows the occurrence of FRET over time. Förster resonance energy transfer (FRET) is a non-radiative energy transfer from an excited donor chromophore to an acceptor chromophore. The energy transfer relies on the principles of dipole-dipole interactions and can occur when the emssion spectrum of the donor overlaps with the excitation spectrum of the acceptor, while both molecules are in close proximity (~1-10 nm). The probability of FRET diminishes rapidly as the distance between fluorophores increases, given that the efficiency of energy transfer is inversely proportional to the sixth power of the distance between them. This property makes FRET a useful tool for studying protein-protein interactions. Additionally, FRET has several advantages over the otherwise commonly used co-immunoprecipitation (CoIP), such as an increased reproducibility and higher time resolution. Higher time resolution is achieved particularly in the first few minutes of the reaction, due to the possibility of real time data collection and higher signal sensitivity.

The FRET donor chromophore used in this study is the fluorescent protein Clover. Clover is a variant of the green fluorescent protein (GFP) and has its excitation and emission maxima at 505 nm and 518 nm, respectively (Lam et al., 2012). The FRET acceptor used in this study is the fluorescent dye TAMRA (5-Carboxytetramethyl-rhodamine). The excitation spectrum of TAMRA overlaps with the Clover emission spectrum, with a maximum at 544 nm. These properties make TAMRA and Clover effective FRET partners for biochemical experiments, as Clover can absorb photons of a wavelength that do not induce TAMRA fluorescence, and their spectral overlaps fulfill the FRET requirement.

For this part of the study TAMRA was enzymatically attached to the PP1-interacting protein NIPP1, using Sortase A (**Figure 2.1a**). To accomplish this, NIPP1 was C-terminally tagged with the sortase recognition amino acid sequence LPETGGG. Sortase A recognizes and cleaves the recognition sequence between the threonine and glycine residue via its active site cysteine. The cleavage results in the formation of an acyl intermediate with the now C-terminal threonine of NIPP1. The three C-terminal glycine residues are subsequently released. Sortase A then catalyzes the transfer of the LPETGGG-tagged protein to a nucleophile containing at least one N-terminal glycine residue. In this case, the nucleophile was a peptide with the N-terminal amino acid sequence GGG, followed by a strep-tag for subsequent use in Strep-affinity purification. The peptide was chemically labeled with the FRET acceptor TAMRA. Through nucleophilic attack of the acyl intermediate of NIPP1 and Sortase A, a covalent bond is created between the C-terminal threonine of NIPP1 and the N-terminal glycine residue of the TAMRA-labeled peptide. In this process the active site cysteine of Sortase A is regenerated. As a consequence, the protein NIPP1 is covalently labeled with a strep-tag, and the fluorescent dye TAMRA for use in FRET-based experiments.

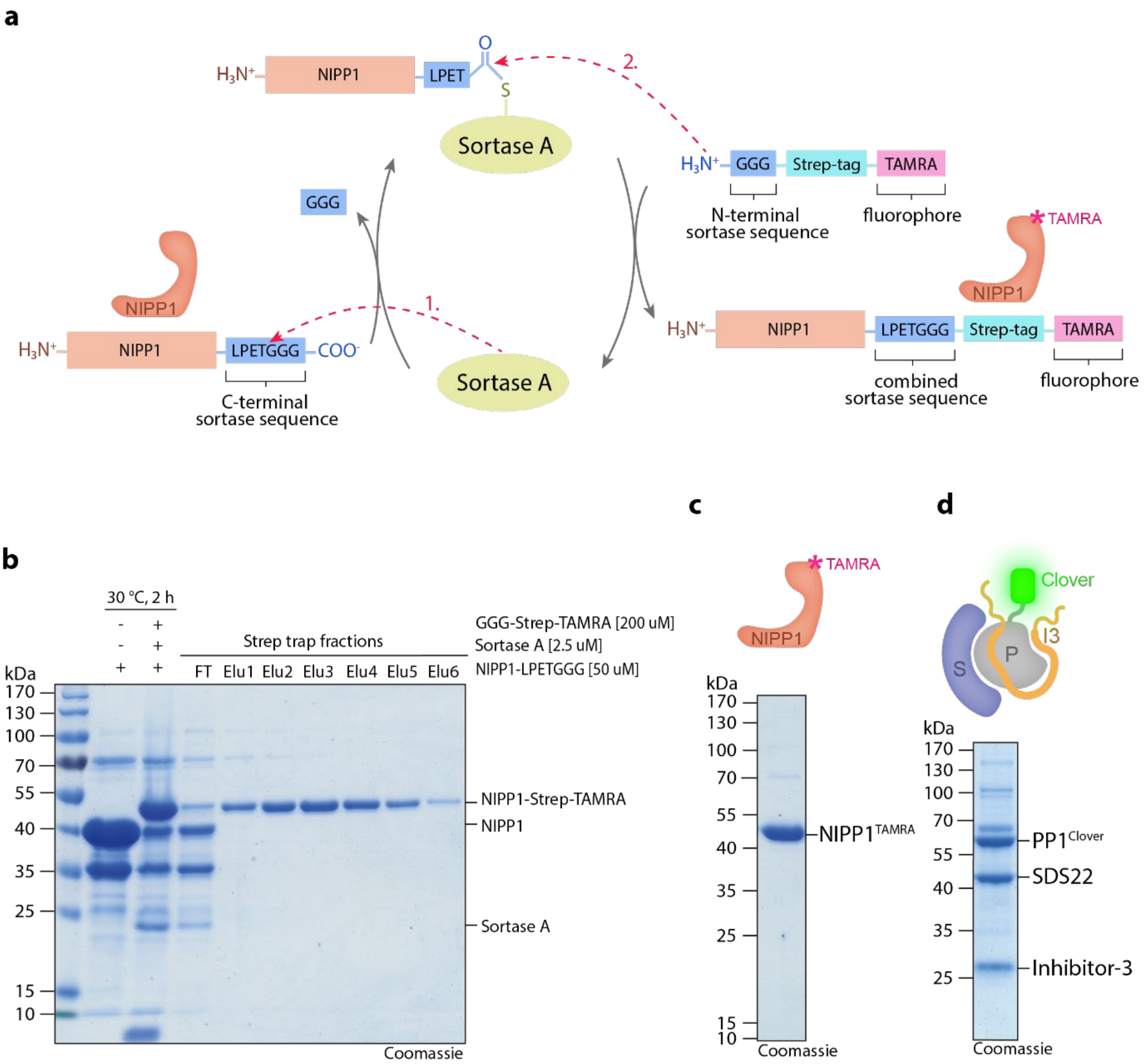

Figure 2.1: Tagging strategy for the creation of FRET substrates to monitor SPI complex disassembly coupled to binding of the alternative PP1 interaction partner NIPP1. a) A schematic representation delineating the enzymatic reaction catalyzed by Sortase A. The protein NIPP1 contains the C-terminal sortase recognition peptide sequence LPETGGG. 1.) Sortase A cleaves between the threonine and glycine residues, forming a thioester intermediate with NIPP1. The three C-terminal glycines are cleaved off. 2. The peptide comprised of a strep-tag fused to the fluorescent dye TAMRA contains the N-terminal sortase peptide sequence GGG. The N-terminally tagged peptide undergoes a nucleophilic attack of the NIPP1-Sortase intermediate, creating a covalent bond between the peptide and NIPP1, while Sortase A is regenerated. **b)** Coomassie-stained protein gel of the Sortase A catalyzed reaction of NIPP1-LPETGGG and GGG-Strep-TAMRA, followed by subsequent protein purification through affinity chromatography. The reaction mixture containing 50 µM NIPP1-LPETGGG, 2.5 µM Sortase A and 200 µM GGG-Strep-TAMRA was incubated for 2 h at 30 °C in a total volume of 2.5 mL. The first lane served as a control containing only NIPP1-LPETGGG. Post sortase reaction, the protein mixture was subjected to a streptavidin affinity chromatography with the pooled flow through and individual elution fractions loaded for analysis. **c)** Coomassie-stained protein gel of NIPP1^{TAMRA} after further purification through size exclusion chromatography. **d)** Coomassie-stained protein gel visualizing the SDS22:PP1^{Clover}:I3 complex. In this study, PP1 was produced as a recombinant protein, with Clover attached to its C-terminus. The complex was co-purified by Ni-NTA affinity chromatography, followed by size exclusion chromatography.

The sortase reaction for labeling NIPP1 contained 50 µM NIPP1-LPETGGG and 2.5 µM calcium-independent Sortase A, both purified from *E. coli* BL12 (DE3), as well as 200 µM GGG-Strep-TAMRA synthesized by Caslo ApS. The reaction was incubated for 2 hours at 30 °C. SDS-PAGE revealed that the reaction containing all three reaction components lead to an upward shift of the band at 40 kDa corresponding to NIPP1-

LPETGGG, compared with the sample containing only NIPP1 (**Figure 2.1b**). To remove remaining unlabeled protein, a Strep-affinity purification was performed. Analysis by SDS-PAGE showed a band corresponding to unlabeled NIPP1 protein in the column flow-through (FT), as unlabeled NIPP1 did not contain a strep-tag. The elution fractions contained TAMRA-labeled NIPP1 protein, as well as residual TAMRA peptide, which had been added in excess. To remove the remaining peptide from NIPP1$^{\mathrm{TAMRA}}$, a size exclusion chromatography was performed, yielding pure NIPP1$^{\mathrm{TAMRA}}$ with only minimal contaminations of higher molecular weight proteins (**Figure 2.1c**).

To create a FRET donor for NIPP1$^{\mathrm{TAMRA}}$, PP1 was expressed as a recombinant protein with the fluorescent protein Clover attached to the PP1 C-terminus. PP1$^{\mathrm{Clover}}$ was purified in a complex together with SDS22 and His-tagged I3. All three proteins were expressed in insect cells and subsequently purified through Ni-NTA-affinity chromatography, followed by size exclusion chromatography. SDS-PAGE analysis shows distinct bands corresponding to all three proteins after size exclusion chromatography (**Figure 2.1d**). The complex was largely free of contaminating insect lysate proteins. Both NIPP1$^{\mathrm{TAMRA}}$ and SDS22:PP1$^{\mathrm{Clover}}$:I3 were deployed for FRET-based analysis of the SPI disassembly reaction.

2.1.1 Establishing a FRET-based assay to monitor SPI disassembly through binding of NIPP1

p97:p37 catalyze the unfolding of I3, followed by the disassembly of the SPI complex, which allows binding of the alternative PP1 interaction partner NIPP1. To monitor this process via FRET, the fluorescent tags Clover and TAMRA were attached to PP1 and NIPP1, respectively. After SPI disassembly, PP1$^{\mathrm{Clover}}$ can bind NIPP1$^{\mathrm{TAMRA}}$, bringing the FRET labels into proximity. The proximity of the FRET partners allows the occurrence of FRET, leading to a reduction in FRET donor emission (Clover) and an increase in FRET acceptor emission (TAMRA) (**Figure 2.2a**). The change in fluorescence can be detected with a fluorescence spectrophotometer by exciting the donor fluorophore at a specific excitation wavelength and recording emission spectra around the donor and acceptor emission maxima.

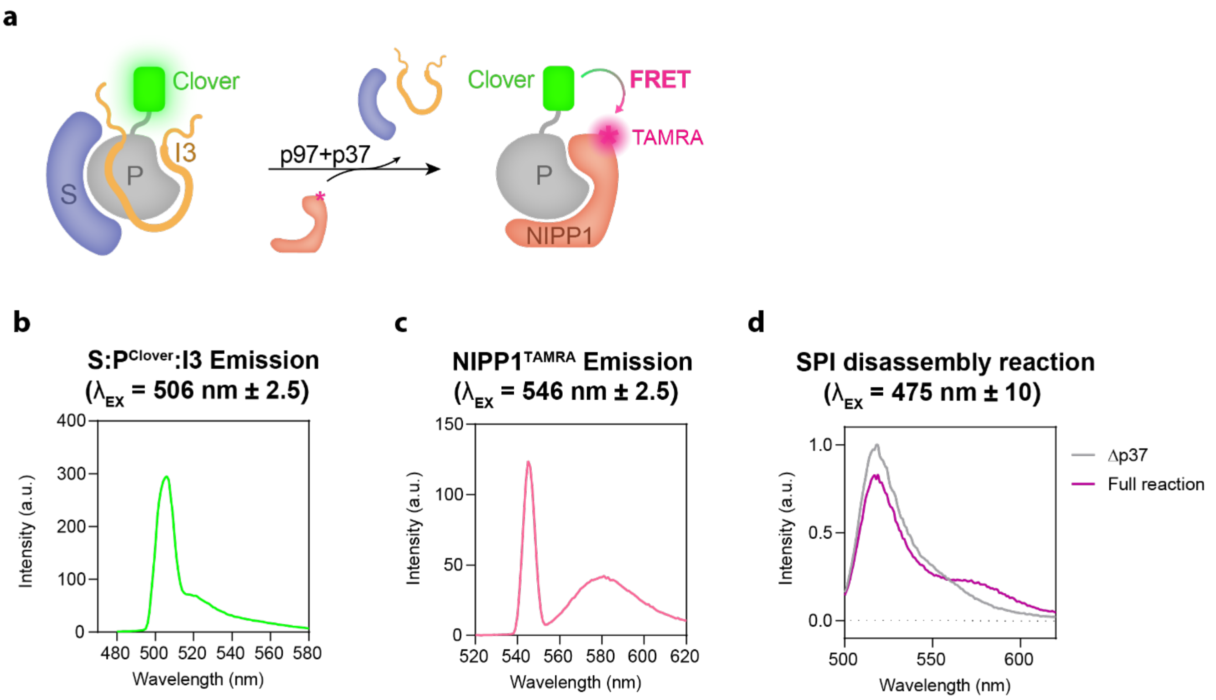

Figure 2.2: Monitoring the development of FRET upon NIPP1$^{\text{TAMRA}}$ binding to PP1$^{\text{Clover}}$ after SPI disassembly. **a)** Schematic illustrating a FRET-based disassembly assay. In this setup, PP1 is linked to the fluorescent protein Clover and purified in complex with SDS22 and I3. In parallel, the alternative PP1-interacting protein NIPP1 is conjugated to the fluorescent dye TAMRA. Following the dissociation of I3 and SDS22 from PP1, mediated by p97:p37, PP1$^{\text{Clover}}$ can then associate with NIPP1$^{\text{TAMRA}}$. The disassembly of the complex and binding of NIPP1$^{\text{TAMRA}}$ triggers FRET between Clover and TAMRA, allowing for detection. **b)** Emission spectrum of Clover as a fusion protein of PP1 in complex with SDS22 and I3 (80 nM). Clover excitation wavelength λ_{EX} was 506 ± 2.5 nm and fluorescence emission were detected between 480-580 nm. **c)** Emission spectrum of TAMRA attached to NIPP1 (80 nM). TAMRA excitation wavelength λ_{EX} was 546 ± 2.5 nm, and fluorescence emission was detected between 520-620 nm. **d)** Fluorescence emission spectra of the full SPI disassembly reaction containing SDS22:PP1$^{\text{Clover}}$:I3 (80 nM), NIPP1$^{\text{TAMRA}}$ (80 nM), p97 (35 nM), p37 (50 nM) and ATP (2 mM) (purple), compared with the same reaction excluding p37 (Δp37, gray). Reactions were incubated at 30 °C for 30 min in a total volume of 60 µL. Excitation was performed at 475 ± 10 nm. Fluorescence emission was recorded between 500 and 620 nm. Data points were normalized between 0 and 1.

To determine suitable excitation and emission wavelengths, fluorescence spectra of the fluorescently labeled proteins SDS22:PP1$^{\text{Clover}}$:I3 and NIPP1$^{\text{TAMRA}}$ were detected individually, and as a mixture of all reaction components. A spectrum captured of SDS22:PP1$^{\text{Clover}}$:I3 alone, with an excitation wavelength of 506 ± 2.5 nm, yielded a peak emission around 518 nm, consistent with the published values (Lam et al., 2012) (**Figure 2.2b**). NIPP1$^{\text{TAMRA}}$ was excited at 546 ± 2.5 nm and showed a maximal emission around 580 nm, disregarding the peak produced by the excitation light around 546 nm (**Figure 2.2c**). Clover and TAMRA emissions were measured at 518 nm and 580 nm in following experiments, respectively.

To exclusively detect TAMRA fluorescence induced by FRET at 580 nm, it was necessary to excite Clover at a wavelength outside the TAMRA excitation spectrum. A fluorescence emission spectrum recorded of the SPI disassembly reaction lacking p37, shows the conditions at the start of the reaction, before SPI was disassembled (**Figure**

2.2d, gray curve). Here, an excitation wavelength of 475 nm was identified to produce the intended emission spectrum, revealing a peak solely at the Clover maximum of 518 nm and not at 580 nm for TAMRA. Conversely, the full reaction, containing p37 and all other reaction components, shows a decrease in fluorescence emission at 518 nm, as well as an increase at 580 nm, corresponding to Clover and TAMRA, respectively. This change in fluorescence emission is representative of FRET occurring between the two chromophores upon binding of NIPP1 to PP1 (**Figure 2.2d**, purple curve). An excitation wavelength of 475 nm was used for all following FRET-based experiments.

FRET-based assays provide the advantage of collecting real-time data points, enabling the resolution of the complete process of catalyzed dissociation or association of interaction partners within seconds. Raw data of the SPI disassembly reaction, followed by NIPP1 binding was acquired by measuring fluorescence emission at 518 nm and 580 nm, corresponding to Clover and TAMRA emission maxima, over a time course of 20 min. For initial data analysis, two reactions were recorded, a full reaction containing NIPP1^{TAMRA}, SDS22:PP1^{Clover}:I3, p97, p37 and ATP, as well as a control reaction lacking p37 (Δp37) (**Figure 2.3a**). For both reactions, a baseline was recorded during the first three minutes of data compiling. A visible drop in fluorescence can be observed when the cuvette containing the reactions was removed from the fluorescence spectrophotometer to start the reaction by adding ATP. In accordance with expectations, the curve of the Δp37 reaction showed no change in fluorescence after ATP addition, for either fluorophore. This stable baseline in reactions lacking p37 indicated that the SPI complex did not disassemble under these conditions and PP1 and NIPP1 were not able to bind, consistent with CoIP experiments performed in previous studies (Weith et al., 2018). Conversely, the full reaction showed a decrease in Clover fluorescence and an increase in TAMRA fluorescence over time, demonstrating that FRET was induced. The development of the FRET signal indicates that PP1 and NIPP1 associated, following SPI disassembly by p97:p37. Combined with the Δp37 control, which showed no development of FRET under conditions in which SPI cannot be recruited to p97, the development of FRET in the full reaction over time shows the implementation of a functional FRET-based assay. Following the successful fluorescent tagging of PP1 and NIPP1, this assay effectively monitors SPI disassembly through NIPP1 binding.

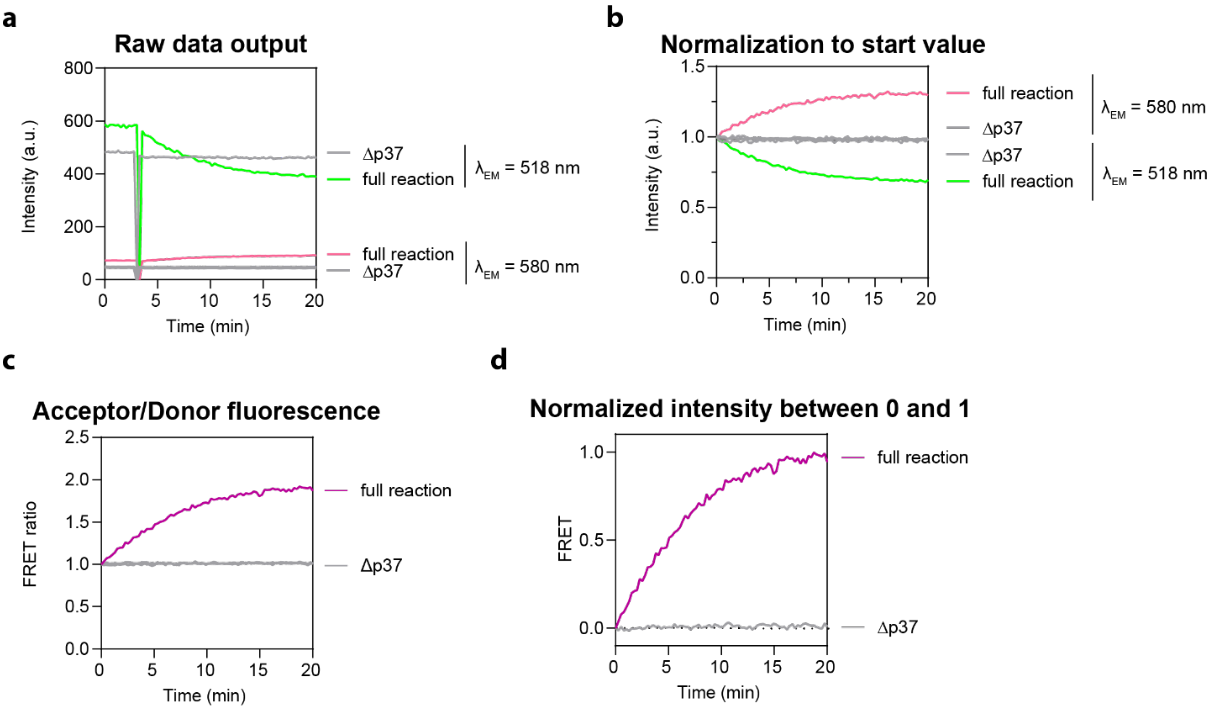

Figure 2.3: Example of FRET-based assay data analysis of an SPI disassembly reaction with subsequent binding of NIPP1. **a)** Raw data output of the fluorescence kinetics recorded over 20 min. Reactions contained SDS22:PP1$^{\mathrm{Clover}}$:I3 (80 nM), NIPP1$^{\mathrm{TAMRA}}$ (80 nM), p97 (35 nM), p37 (50 nM) and ATP (2 mM), compared with the same reaction that excluded p37 (Δp37). ATP was added 3 min after the start of the recording. Excitation wavelength λ_{EX} was 575 ± 10 nm, and emissions were recorded at 518 and 580 nm, corresponding to Clover and TAMRA excitation maxima. **b)** Taking the raw data from a) as input, all values were divided by the average of the last 10 data points recorded before the addition of ATP. Subsequently, all data points after the addition of ATP were excluded. **c)** The recorded TAMRA fluorescence (FRET acceptor, λ_{EM} = 580 ± 2.5 nm, pink and gray) for each of the two reactions shown in b) were divided by the respective Clover fluorescence ((FRET donor, λ_{EM} = 518 ± 2.5 nm, green and gray), resulting in two curves representing the FRET ratio of the previously recorded reactions, namely the full reaction (purple) and the reaction where p37 was omitted (gray). **d)** Final representation of the FRET data, with the curves normalized between 0 and 1.

As a first step in data analysis, the first value after adding ATP was set as the starting point of the reaction (0 min). Subsequently, all curves were divided by the average of the last 10 values before addition of ATP. Dividing by the baseline normalizes the initial intensities and removes the dilution effect of ATP (**Figure 2.3b**). Next, the recorded fluorescence at 580 nm (acceptor) was divided by the fluorescence recorded at 518 nm (donor) within the same sample. Dividing the two fluorescence intensities yielded a single FRET curve per reaction, integrating the data gathered for both fluorophores. Additionally, unspecific, non-FRET effects that affected fluorescence during the measurement are eliminated (**Figure 2.3c**). The last step in data analysis was to normalize the signal between 0 and 1. For this, the initial values of each curve were subtracted from all other values of the same curve. Subsequently, all curves were divided by the average around the plateau of the highest curve (**Figure 2.3d**). This FRET analysis yielded single curves per sample with a high signal/noise ratio, and was applied to all further FRET-based experiments, unless mentioned otherwise.

2.1.2 Optimization and validation of FRET-based assay conditions

To identify optimal assay conditions, ensuring that the SPI reaction rate is not restricted by dissociation constants (K_D) of all complexes formed during the assay, titration experiments with all protein components were conducted. These experiments aimed to pinpoint conditions where the concentration of each protein no longer posed a limitation on the reaction rate.

To determine the optimal p97 concentration, time-course FRET measurements monitoring SPI disassembly reactions with varying levels of p97 were performed. p97 titration reactions comprised 160 nM SDS22:PP1$^{\text{Clover}}$:I3 as the p97 substrate, 480 nM NIPP1$^{\text{TAMRA}}$, and 10-320 nM p97 (**Figure 2.4a**). To mitigate a possible impact of the K_D between p97 and p37, particularly at elevated p97 concentrations, an excess amount of p37 (4µM) was used. As expected, the p97 titration experiments reveled that the reaction speed increased with higher enzyme concentration, as more enzyme can generally catalyze more substrate per minute. The maximal speed reached a limit at 160 nM p97, which also corresponded to the SPI concentration used in this experiment. Doubling the p97 concentration to 320 nM resulted in no further reaction speed increase. The maximal reaction speed at equimolar concentrations of p97 and SPI indicates that one SPI molecule is bound per p97. Additional increase in enzyme concentration has therefore no effect on the reaction speed. A concentration of 160 nM p97 and SPI were used in following experiments.

The p37 titration was performed in a similar manner containing 160 nM p97, 160 nM SDS22:PP1$^{\text{Clover}}$:I3, 480 nM NIPP1$^{\text{TAMRA}}$, and 0-960 nM p37 (**Figure 2.4b**). As also evident from the other titration experiments, omitting the adapter protein p37 resulted in a complete loss of a ΔFRET signal, signifying that the SPI complex does not spontaneously disassembly over the time course of 30 min, but requires enzymatic catalysis by p97:p37. The full reaction speed was achieved at a p37 concentration of 480 nM. At 960 nM p37, no additional acceleration occurred. Based on an available crystal structure of p97:p37 and SPI, it is assumed that only one p37 molecule binds per p97 hexamer (van den Boom et al., 2023). It can therefore be hypothesized that the higher concentration of p37 needed for maximal reaction speeds, relative to p97, is due to a high K_D between p97 and p37. 480 nM p37 were used in further FRET experiments.

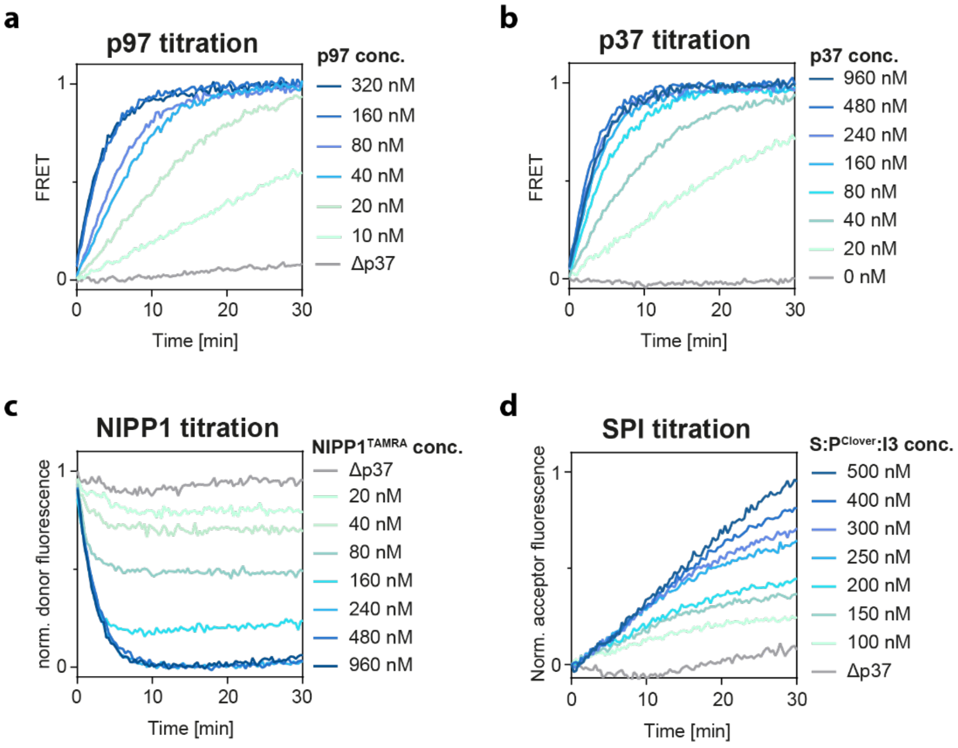

Figure 2.4: Titration of all assay components to determine optimal assay conditions. a) FRET time course measurements of SPI disassembly reactions containing p37 (4 µM), SDS22:PP1^{Clover}:I3 (160 nM), and NIPP1^{TAMRA} (480 nM) with indicated concentrations of p97. Shown are normalized ratios of acceptor and donor fluorescence. Δp37, p37 was omitted. **b)** FRET time course measurements of SPI disassembly reactions containing p97 (160 nM), SDS22:PP1^{Clover}:I3 (160 nM), and NIPP1^{TAMRA} (480 nM) at indicated time points after addition of ATP (2 mM) with indicated concentrations of p37. Shown are normalized ratios of acceptor and donor fluorescence. **c)** FRET time course measurements of SPI disassembly reactions containing p97 (160 nM), p37 (480 nM), and SDS22:PP1^{Clover}:I3 (160 nM) with indicated concentrations of NIPP1^{TAMRA}. Shown is the normalized donor fluorescence (Clover). Δp37, p37 was omitted. **d)** FRET time course measurements of SPI disassembly reactions containing p97 (20 nM), p37 (480 nM), and NIPP1^{TAMRA} (640 nM) after addition of ATP (2 mM) with indicated concentrations of SDS22:PP1^{Clover}:I3. Shown is the normalized acceptor fluorescence (TAMRA). Δp37, p37 was omitted.

In the specific case of NIPP1^{TAMRA}, a concentration was selected to ensure that additional increases of NIPP1^{TAMRA} did not result in further quenching of Clover fluorescence at the end of the reaction. For NIPP1^{TAMRA} titrations, only the change in FRET donor fluorescence was analyzed, as titrating the acceptor lead to fluorescence increase due to higher fluorophore concentrations. The resulting change in acceptor fluorescence, but not donor fluorescence interfered with the reliable detection of the FRET ratio (acceptor/donor fluorescence). Reaching minimal Clover florescence implies that under these conditions, the maximal amount of NIPP1^{TAMRA} was bound by PP1^{Clover} and therefore the upper limit of SPI disassembly was reached. NIPP1^{TAMRA} titration reactions contained 160 nM p97 and SDS22:PP1^{Clover}:I3, 480 nM p37 and 20-960 nM NIPP1^{TAMRA} (**Figure 2.4c**). The highest plateau at the end of the reaction was reached with a NIPP1^{TAMRA} concentration of 240 nM, which was used for following FRET experiments.

The SDS22:PP1^{Clover}:I3 titration curves were examined in a manner similar to NIPP1^{TAMRA}, using the FRET acceptor fluorescence instead of the FRET ratio. The experiment was conducted with concentrations of 100-500 nM SDS22:PP1^{Clover}:I3, 20 nM p97, 480 nM p37, and 640 nM NIPP1^{TAMRA}, to account for the increased SPI concentration (**Figure 2.4d**). The maximum initial rate was already reached at 100 nM SPI, confirming that the 160 nM SPI used as the optimal assay conditions, along with 160 nM p97, 480 nM p37, and 240 nM NIPP1, were enough for ensuring that dissociation constants did not limit the reaction rate.

To further validate that the SPI disassembly reaction worked under the determined optimal conditions, FRET was monitored by recording the entire emission spectrum of Clover and TAMRA over the course of the reaction, under optimal conditions. The recorded spectrum changed over time after addition of ATP, as the Clover fluorescence decreased and the TAMRA fluorescence increased, as indicated for the Clover and TAMRA emission maxima, which is representative of FRET occurring between the fluorophores (**Figure 2.5a**). Secondly, it was verified that the recorded SPI disassembly reactions were dependent on p97 activity. No ΔFRET signal could be observed in the absence of ATP, resembling SPI reactions containing all components except p37. Likewise, the addition of the competitive p97 inhibitor CB-5083 before the start of the reaction lead the absence of FRET development due to the lack of interaction between PP1^{Clover} and NIPP1^{TAMRA} (**Figure 2.5b**). Together, the experiments confirmed that p97 catalytic activity and the adapter protein p37 are necessary for efficient SPI disassembly.

Monitoring SPI disassembly and NIPP1 binding in a co-immunoprecipitation (CoIP) confirmed that I3 and SDS22 almost completely dissociated from PP1^{Clover}, while NIPP1^{TAMRA} bound PP1 stoichiometrically (**Figure 2.5c**). To obtain this result, a PP1γ CoIP was performed containing 160 nM SDS22:PP1^{Clover}:I3, 160 nM p97, 480 nM p37, 240 nM NIPP1^{TAMRA}, and 2 mM ATP. To start the reaction, ATP was added and reactions were incubated at 30 °C. At indicated time points, 1-30 min after the start of the incubation, reactions were stopped by adding ice cold IP buffer containing 1 % Triton X-100. CoIPs were performed with a PP1γ antibody and samples were analyzed by SDS-PAGE, followed by western-blotting and immunodetection with the indicated antibodies.

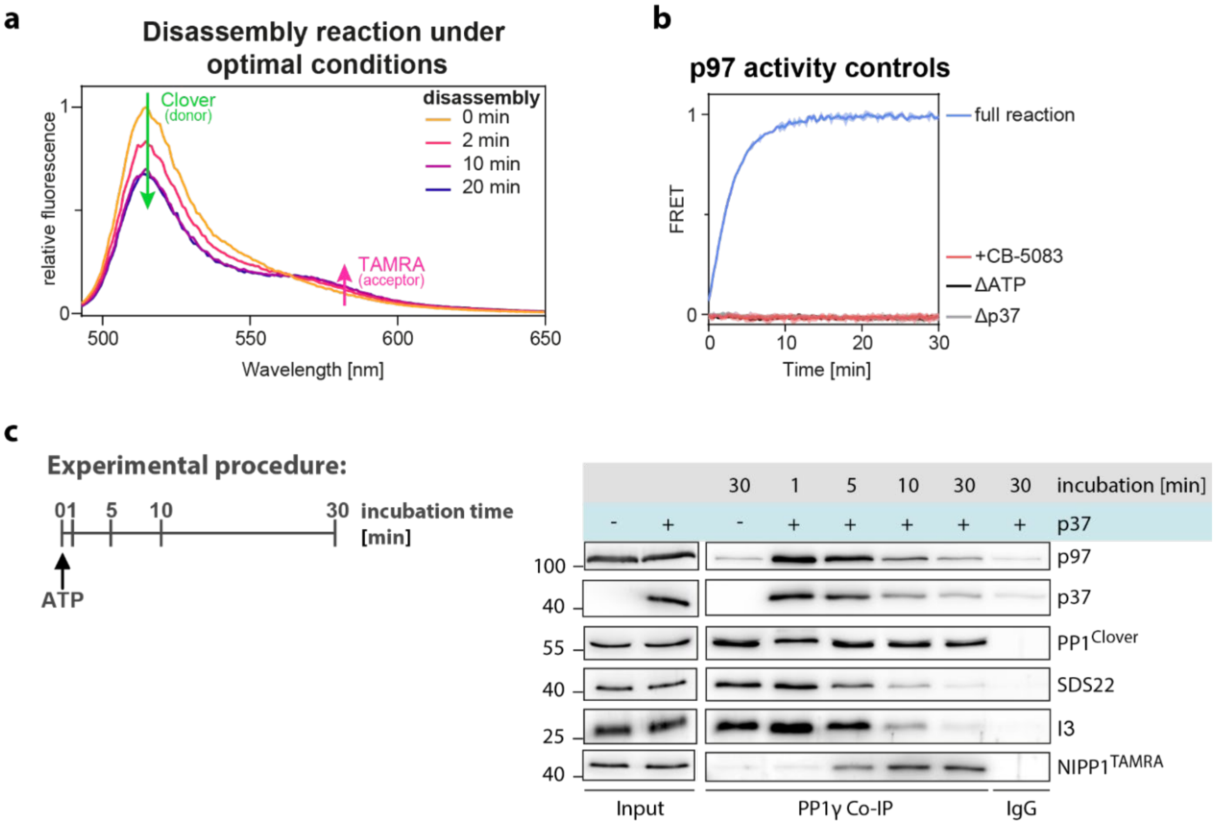

Figure 2.5: Validation of FRET-based assay, which monitors NIPP1$^{\text{TAMRA}}$ binding to PP1$^{\text{Clover}}$ after SPI disassembly. a) Fluorescence spectra of the disassembly reaction containing p97 (160 nM), p37 (4 µM), SDS22:PP1$^{\text{Clover}}$:I3 (160 nM), and NIPP1$^{\text{TAMRA}}$ (480 nM) at indicated time points after addition of ATP (2 mM). Spectra were normalized to the maximum fluorescence at 0 min. Emission maxima of Clover and TAMRA are indicated. **b)** FRET time course measurements of the SPI disassembly reaction and NIPP1 binding, containing p97 (160 nM), p37 (480 µM), SDS22:PP1$^{\text{Clover}}$:I3 (160 nM), NIPP1$^{\text{TAMRA}}$ (240 nM) , and ATP (2 mM), as indicated in the presence of p97 inhibitor CB-5083 (10 µM), or absence of ATP (ΔATP) or p37 (Δp37). Measurements were conducted at 30 °C. Shown are the means of the normalized ratios of acceptor and donor fluorescence ± SD, n=3. **c)** Co-immunoprecipitation time course experiment of the SPI disassembly reaction, after addition of ATP. Reactions contained p97 (160 nM), p37 (480 µM), SDS22:PP1$^{\text{Clover}}$:I3 (160 nM), NIPP1$^{\text{TAMRA}}$ (240 nM) , and ATP (2 mM) as indicated. PP1$^{\text{Clover}}$ was immuno-isolated at specified time points and associated proteins detected by Western blot analysis with indicated antibodies.

Analysis of western blot signals revealed that PP1$^{\text{Clover}}$ was pulled down equally in all CoIP samples. Further, no unspecific binding could be detected in the IgG control, confirming that the changes in signals observed for the PP1 interaction partners correspond to a direct or indirect change in PP1 association, rather than unspecific binding or technical errors. Over the course of the reaction, both SDS22 and I3 signals became weaker, indicating that the proteins were no longer bound to PP1. The majority of the complex was disassembled after 10 min. Similarly, p97 and p37 signals decrease over the course of the reaction as the SPI components are released after complex disassembly. NIPP1$^{\text{TAMRA}}$ binding to PP1$^{\text{Clover}}$ increased over the progression of the reaction, with the majority of NIPP1 bound after 10 min. The observation that NIPP1 association reaches a maximum around 10 min after the start of the reaction is congruent with curves recorded using the FRET-based assay monitoring NIPP1$^{\text{TAMRA}}$

binding under the same conditions (**Figure 2.5b**). Further, FRET labels did not interfere with SPI disassembly and NIPP1 assembly, and determined optimal conditions for FRET-based assays lead to efficient disassembly of SPI by p97:p37.

2.1.3 Determination of kinetic parameters of the SPI disassembly reaction

The time resolution achievable with FRET-based assays allows the determination of kinetic reaction parameters. Commonly, initial velocity rates of an enzymatic reaction under varying substrate concentrations have been used for the estimation of the Michaelis-Menten constant (K_M), defined as the amount of substrate necessary to allow an enzyme to function at half its maximal velocity, and the catalytic constant (k_{cat}), a factor defining the number of substrate molecules turned over per enzyme molecule per second. For initial velocity rate determination of K_M and k_{cat}, it is necessary to record a reaction during its linear range, meaning below saturating conditions with low enzyme and substrate concentrations. As evident from the SDS22:PP1^{Clover}:I3 titration curves discussed before, the FRET detection limit allowed the detection of curves only in the mid to low nanomolar substrate concentration range (**Figure 2.4d**). Additionally, the initial velocity rates were only linear for the first few data point, which did not allow accurate assessment of enzymatic parameters.

To overcome the limitation of using initial velocity rates, we employed a previously described analysis of progress curves to determine K_M and k_{cat}. Progress curve analysis was done through computational analysis instead of a linear transform of initial velocity rates, leading to more unbiased results (Choi et al., 2017). For computational analysis of progress curves, as is also common for Michaelis-Menten equation-based evaluation, quasi-steady-state conditions are assumed. In an enzymatic reaction, substrates bind to an enzyme to form enzyme-substrate complexes, which then undergo sterical or chemical transformations to yield products. The Quasi-Steady-State Approximation (QSSA) assumes that the concentration of the enzyme-substrate complex changes rapidly at the beginning of the reaction and quickly reaches a quasi-steady state. Hence, the rate of change of the concentration of the intermediate becomes negligible, simplifying the equation that describes the system. The Total Quasi-Steady-State Approximation (tQSSA or tQ model) extends the QSSA to more complex enzymatic reactions with several possible intermediate states. Providing two reaction curves with different enzyme and substrate concentrations as input for the computational analysis proves to yield a more accurate representation of complex enzyme kinetics than the standard QSSA, across a wide range of substrate and enzyme concentrations (Choi et al., 2017).

In this study, the tQ model was used to assess SPI disassembly kinetics. Additionally, an indirect detection of SPI disassembly by p97:p37 was employed, monitoring the binding of the alternative PP1 interaction partner NIPP1, instead of labeling either SDS22 or I3 directly. Labeling NIPP1 had the advantage that only one of the FRET fluorophores had to be used at low concentrations, which increased FRET-sensitivity. For one analysis, two distinct data sets were obtained under different experimental conditions. The first data set was generated with low concentrations of total enzyme (ET) and substrate (ST) relative to the assumed Michaelis-Menten constant (K_M), denoted as ET $\ll$ K_M and ST $\ll$ K_M. The second data set was acquired under conditions where the substrate concentration exceeded the expected K_M, or ST $\gg$ K_M. Specifically, input curves for kinetics measured at 30 °C contained 40 nM SDS22:PP1^{Clover}:I3, 20 nM p97, 480 nM p37, and 240 nM NIPP1^{TAMRA} for ET $\ll$ K_M and ST $\ll$ K_M, or 1150 nM SDS22:PP1^{Clover}:I3, 80 nM p97, 480 nM p37, and 9 µM NIPP1^{TAMRA}, for ST $\gg$ K_M conditions, respectively. Reactions were started with 2 mM ATP and incubated at 30 °C for 35 min (**Figure 2.6a**, panel 1). With the two condition, SPI disassembly and NIPP1-PP1 binding could be observed under contrasting circumstances, yielding curves that provided the input for further analysis.

Using RStudio and the EKMCMC script provided by Choi et al., the two input curves served as the experimental data to simultaneously determine both k_{cat} and K_M. The script uses Bayesian inference as a method to determine output data. Bayesian statistics involves updating probability distributions based on new data, allowing for the incorporation of prior knowledge and continuous refinement of parameter estimates. Including new data and prior knowledge required that the input for analysis contained both, the two recorded input curves, as well as a rough guess of possible values for K_M and k_{cat} based on knowledge derived from the titration experiments (**Figure 2.4**). For analysis of the input curves recorded at 30 °C, the initial values for K_M = 80 nM, and k_{cat} = 1 min^{-1} were used as estimations. The number of repeats of the Bayesian inference calculations for refinement was set at 100,000. The analysis yielded a distribution of 100,000 probable combinations of K_M and k_{cat} (**Figure 2.6a**, panel 2). A quality control for the output data points created by the EKMCMC script is a visual analysis of the scatter plot. The plots should yield distributions which are not strictly horizontal or vertical, as this would indicate that the input curves did not contain enough information to accurately determine one of the kinetic parameters. The values determined for the input curves recorded at 30 °C formed a diagonal distribution, suggesting that the input data met the requirements for accurate estimation of both kinetic parameters.

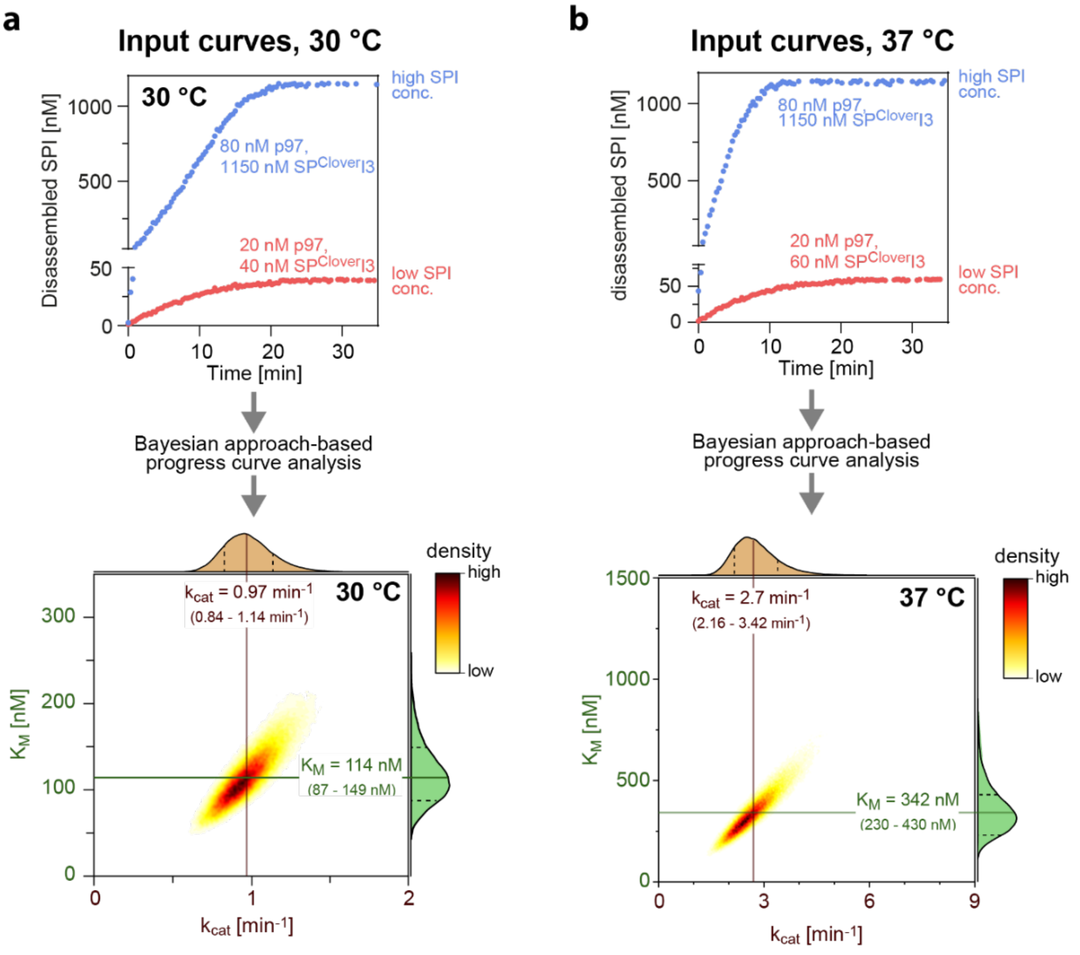

Figure 2.6: Determination of kinetic parameters of NIPP1 binding to PP1 upon SPI disassembly. **a)** Determination of kinetic parameters for SDS22:PP1^{Clover}:I3 disassembly followed by NIPP1^{TAMRA} association at 30 °C, by employing a Bayesian approach-based analysis of progress curves and considering low and high substrate (SPI) concentrations. The upper panel displays FRET input data of reactions containing p97 (low conc.: 20 nM; high conc.: 80 nM), SDS22:PP1^{Clover}:I3 (low conc.: 40 nM; high conc.: 1150 nM), p37 (480 nM), NIPP1^{TAMRA} (low conc.: 240 nM; high conc.: 9 µM) and ATP (2 mM). The lower panel presents the output of the kinetics analysis, with a 2D-kernel plot illustrating the point density function of 100,000 calculated combinations of probable K_M and k_{cat} values. Geometric means (solid lines) and geometric standard deviations (dashed lines) for K_M and k_{cat} are shown. **b)** Determination of kinetic parameters as in a) at 37 °C. Reactions contained p97 (low conc.: 20 nM; high conc.: 80 nM), SDS22:PP1^{Clover}:I3 (low conc.: 60 nM; high conc.: 1150 nM), p37 (480 nM), NIPP1^{TAMRA} (low conc.: 240 nM; high conc.: 2.5 µM) and ATP (2 mM).

To estimate the kinetic parameters, the probability distribution was presented as a 2D-kernel plot and geometric means and standard deviations for all K_M and k_{cat} values were calculated. For lognormal distributions, as presented here, the geometric mean provides a more accurate estimation than the arithmetic mean. The geometric mean of the K_M describing the SPI disassembly reaction at 30 °C, was 114 *÷ 1.31. The k_{cat}

determined under the same conditions was 0.97 min^{-1} *÷ 1.17 (**Figure 2.6a**). In conclusion, a concentration of 114 nM SDS22:$\text{PP1}^{\text{Clover}}$:I3 lead to the reaction speed of half the maximal velocity where ~1 SPI molecule per p97 molecule per minute was catalyzed.

The same experiment was repeated at 37 °C, a temperature that more closely corresponds to the conditions under which protein catalysis would occur in human cells. Input curves measured at 37 °C contained 60 nM or 1150 nM SDS22:$\text{PP1}^{\text{Clover}}$:I3, 20 nM or 80 nM p97, 480 nM p37, and 240 nM or 2.5 µM $\text{NIPP1}^{\text{TAMRA}}$. Reactions were started by the addition of 2 mM ATP and recorded over 35 min. The initial values used as input for Bayesian inference were K_M = 300 nM and k_{cat} = 2.5 s^{-1}. The calculations yielded a diagonal scatter plot with 100,000 probable combinations of K_M and k_{cat}. The geometric means and standard deviation of the kinetic parameters of the SPI disassembly reaction, indirectly measured through NIPP1 binding, were K_M = 342 *÷ 1.37 nM, and k_{cat} = 2.70 *÷ 1.25 min^{-1}, indicating that the reaction reached half its maximal velocity at 342 nM SPI and ~2.7 SPI molecules per p97 molecule per minute were catalyzed under these conditions (**Figure 2.6b**).

2.2 Characterization of SDS22 and I3 interplay during SPI complex disassembly

SDS22 and I3 are ancient interactors of PP1. Both proteins have been shown to inhibit PP1 individually (Dinischiotu et al., 1997; Garcia-Gimeno et al., 2003). At the same time, both are necessary for cellular functions of PP1 like the chromosome segregation during mitosis (Eiteneuer et al., 2014). The SPI complex is recognized by p97:p37, followed by the energy-dependent translocation of I3 through the p97 central pore. The process also leads to the dissociation of SDS22 and PP1 (Weith et al., 2018). It is so far unclear what the purpose of the SPI complex is in cells and why both proteins are necessary for PP1 regulation. To approach these questions, FRET-based assays, tracking the dissociation of SDS22 and I3 from PP1 directly, were established. To achieve this, SPI complexes with two fluorescent labels, $\text{PP1}^{\text{Clover}}$ and either $^{\text{TAMRA}}\text{SDS22}$ or I3^{TAMRA} were created. Resulting assays were used to address how the disassembly of SDS22 and I3 is coupled and whether both are necessary for efficient SPI disassembly by p97:p37.

2.2.1 Establishing FRET-based assays to monitor SDS22 and I3 interactions with PP1

Creating FRET substrates for monitoring the dissociation of SDS22 and I3 from PP1 directly was done in a similar manner as described before. PP1 was C-terminally attached to the fluorescent protein Clover. A published crystal structure of the SPI complex shows that the PP1 C-terminus is sterically close to the SDS22 N-terminus and the I3 C-terminus (Choy et al., 2024) (**Figure 2.7a**). The exact locations of N- or C-terminal amino acids were not resolved, due to high flexibility of these regions. Emphasized is also the RVXF interaction motif in I3, which binds to PP1.

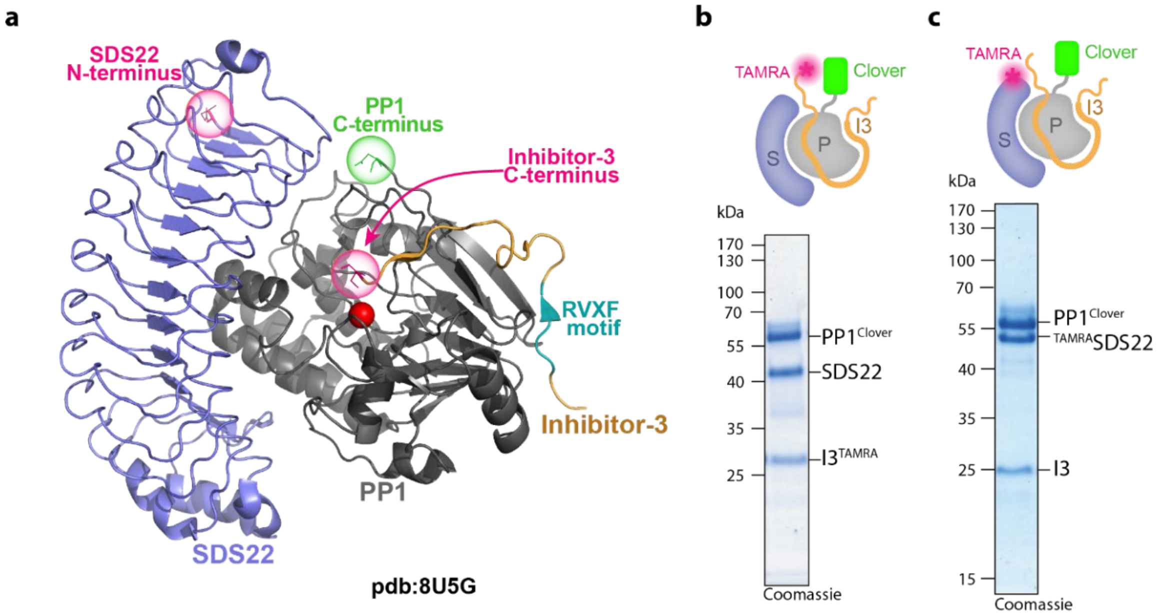

Figure 2.7: Creating FRET substrates with two fluorescently labeled SPI components. a) Available x-ray crystal structure of the SDS22:PP1:I3 complex (pdb: 8U5G) with the resolved residues SDS22$_{79\text{-}360}$ (blue), PP1α$_{7\text{-}300}$ (gray), and Inhibitor-3$_{37\text{-}60}$ (yellow). Highlighted are amino acids resolved around the protein termini. Specifically, the PP1 C-terminal aspartate (green) as well as the SDS22 N-terminal glutamate and the I3 C-terminal cysteine (pink). Highlighted is also the Fe^{2+} ion bound in the PP1 active site (red) and the RVXF motif of I3 (teal). **b)** Coomassie-stained protein gel visualizing the purified SDS22:PP1^{Clover}:I3^{TAMRA} complex after Strep affinity and size exclusion chromatography. Clover was recombinantly attached to the PP1 C-terminus and I3-labeled with TAMRA at its C-terminus with Sortase A. **c)** Coomassie-stained protein gel visualizing the purified ^{TAMRA}SDS22:PP1^{Clover}:I3 complex after Strep affinity and size exclusion chromatography. Clover was recombinantly attached to the PP1 C-terminus and SDS22 labeled with TAMRA at its N-terminus with Sortase A.

A requirement for FRET is the proximity of FRET partners. As the distance between the donor and acceptor molecules increases, the efficiency of FRET decays, following a sixth-power dependence on the separation distance. For that reason, the TAMRA label was attached to the C-terminus of I3-LPETGGG as described for NIPP1^{TAMRA}, through a Sortase A-dependent reaction (**Figure 2.1a**). Similarly, the SDS22 N-terminus was labeled by using a peptide containing the TAMRA dye followed by a strep tag and the sortase recognition amino acid sequence LPETGGG. SDS22 itself was expressed with the N-terminal amino acid tag GGG, necessary for binding the Sortase A active site and subsequent covalent attachment to the TAMRA-Strep-LPETGGG peptide.

The SPI complexes with PP1^{Clover} and sortase tags on SDS22 or I3 were co-expressed and purified from insect cells. I3 was additionally N-terminally tagged with a His-tag for Ni-NTA-affinity chromatography. Insect cell lysates were filtered and subjected to Ni-NTA and size-exclusion chromatography. After successful purification the protein complexes were labeled with TAMRA through incubation with Sortase A and the respective TAMRA-strep peptide. After labeling, the complexes were further purified by Strep-affinity chromatography to remove unlabeled SPI. Strep-affinity purification was followed by another size-exclusion chromatography to separate the labeled SPI complex from free remaining TAMRA-Strep peptide. SDS-PAGE analysis of SDS22:PP1^{Clover}:I3^{TAMRA} showed an upward shift of I3 from 25 kDa to ~27 after conjugation to the TAMRA-Strep peptide (**Figure 2.7b**). The second complex ^{TAMRA}SDS22:PP1^{Clover}:I3 showed a shift of the SDS22 band from ~42 kDa to just below 55 kDa, indicating successful labeling (**Figure 2.7c**). Both purified protein complexes were largely free of lysate contamination and were used for FRET-based assays to explore how the disassembly of SDS22 and I3 is coupled.

Resembling the FRET-based assay designed for observing the interaction between PP1^{Clover} and NIPP1^{TAMRA} after SPI disassembly, the SDS22 and I3-labeled FRET substrates serve to track the occurrence of FRET over the course of the SPI disassembly reaction catalyzed by p97:p37. The disassembly of the SPI complex and binding of NIPP1^{TAMRA} leads to an increase of FRET over the course of the reaction. Conversely, SPI complexes, which initially have the FRET labels in close proximity, exhibit a maximal FRET signal at the start. Clover at the PP1 C-terminus and TAMRA at the I3 C-terminus in the SDS22:PP1^{Clover}:I3^{TAMRA} complex interact to create FRET. The fluorescently labeled SPI complex is recognized and disassembled by p97:p37 leading to SDS22 and I3 dissociation and making PP1 available to bind other interaction partners. Adding NIPP1 in surplus to the reaction serves to bind PP1^{Clover} after the disassembly reaction. Upon binding of NIPP1, I3^{TAMRA} is no longer able to interact with PP1^{Clover} and the FRET signal decays over the course of the reaction (**Figure 2.8a**).

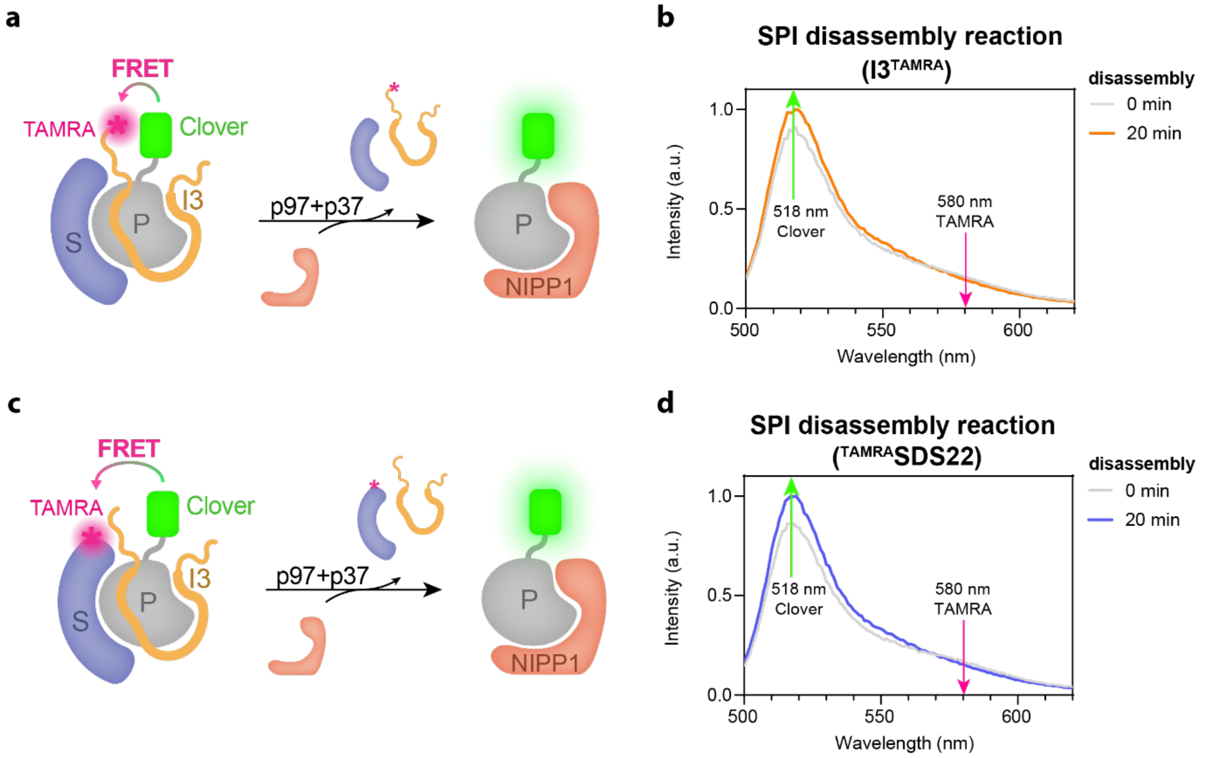

Figure 2.8: Two different FRET assays monitoring the disassembly of either SDS22 or I3 from PP1 through p97:p37. a) A schematic illustrating a FRET-based disassembly assay. PP1 is linked to the fluorescent protein Clover and purified in complex with SDS22 and I3. Additionally, I3 is conjugated to the fluorescent dye TAMRA. Following the disassembly of I3 and SDS22 from PP1, facilitated by p97:p37, PP1 can associate with NIPP1, leading to FRET decay. **b)** Fluorescence spectra of the disassembly reaction containing p97 (160 nM), p37 (480 µM), SDS22:PP1$^{\text{Clover}}$:I3$^{\text{TAMRA}}$ (160 nM), and NIPP1 (240 nM) at indicated time points after addition of ATP (2 mM). Spectra were normalized to the maximum fluorescence at 0 min. Emission maxima of Clover and TAMRA are indicated. **c)** As in a), but with $^{\text{TAMRA}}$SDS22:PP1$^{\text{Clover}}$:I3. **d)** Fluorescence spectra of the disassembly reaction containing p97 (160 nM), p37 (480 µM), $^{\text{TAMRA}}$SDS22:PP1$^{\text{Clover}}$:I3 (160 nM), and NIPP1 (240 nM) at indicated time points after addition of ATP (2 mM). Spectra were normalized to the maximum fluorescence at 0 min. Emission maxima of Clover and TAMRA are indicated.

FRET decay during SPI disassembly can be observed by tracking the reaction through a fluorescence spectrum covering the Clover and TAMRA emission wavelengths. Two spectra of catalyzed SDS22:PP1$^{\text{Clover}}$:I3$^{\text{TAMRA}}$ disassembly were recorded. One at the start (0 min) and one at the end of the reaction (20 min) (**Figure 2.8b**). Excitation of Clover was performed at 475 nm. The peak around the Clover emission maximum at 518 nm shifted to a higher intensity throughout the reaction, while the fluorescence around the TAMRA emission maximum at 580 nm decreased. The observed spectral fluorescence change signifies a reduction in FRET, since the FRET donor Clover increased in fluorescence, and the fluorescence of FRET acceptor TAMRA weakened, while excitation occurred steadily at 475 nm. The experimental data show that the decrease in FRET, and therefore dissociation of I3$^{\text{TAMRA}}$ from PP1$^{\text{Clover}}$, could be successfully followed under these conditions. Similarly, labeling of SDS22 with TAMRA and co-expression with I3 and PP1$^{\text{Clover}}$ is designed to show the full FRET signal at the beginning of the SPI disassembly reaction. Throughout the course of the disassembly reaction of ^{TAMRA}SDS22:PP1^{Clover}:I3 by p97:p37, in the presence of NIPP1, SDS22 dissociated from PP1 leading to a decrease in FRET (**Figure 2.8c**). The spectra recorded at the beginning and end of the reaction showed an increase in Clover fluorescence and a reduction in TAMRA fluorescence, indicating FRET decay over the course of the reaction (**Figure 2.8d**). Developing assays to independently monitor the interactions of both SDS22 and I3 with PP1 enables a more nuanced exploration of their distinct behaviors during the disassembly reaction. Tracking the binding dynamics of both proteins allows the identification of differences and similarities, offering insights into potential interconnections governing their disassembly processes.

2.2.2 Validation of FRET-based assay conditions monitoring SDS22 and I3 interactions with PP1

With the aim of verifying the assay conditions, during which none of the protein components act as rate-limiting factors, titrations were conducted similarly to the FRET assay for monitoring NIPP1^{TAMRA} and PP1^{Clover} binding. Notably, FRET time-course measurements to monitor SDS22:PP1^{Clover}:I3^{TAMRA} disassembly reactions with varying concentrations of p97 showed that the maximal reaction speed was reached at a concentration of 80 nM p97 and above, in reactions containing 160 nM SPI (**Figure 2.9a**). The same could be observed for the p97 titration experiment with ^{TAMRA}SDS22:PP1^{Clover}:I3 (**Figure 2.9b**). In following experiments, 160 nM p97 and 160 nM of SPI variants were used, to stay consistent with conditions previously determined with the NIPP1^{TAMRA} binding assay.

Titrations of the adapter protein p37 were conducted from 0-960 nM p37. SDS22:PP1^{Clover}:I3^{TAMRA} and all other SPI disassembly components were present in previously determined optimal concentrations (**Figure 2.9c**). Omitting the adapter resulted in no change in FRET over the course of the reaction. In line with previous experiments, the stable FRET signal indicates that the SDS22:PP1^{Clover}:I3^{TAMRA} complex did not undergo disassembly under these conditions. The maximal reaction velocity and plateau was reached at a concentration of 240 nM p37 and above. The same could be observed for disassembly reactions performed with ^{TAMRA}SDS22:PP1^{Clover}:I3 at otherwise identical conditions (**Figure 2.9d**). A concentration of 480 nM p37 was used in following experiments, to remain consistent with previous conditions.

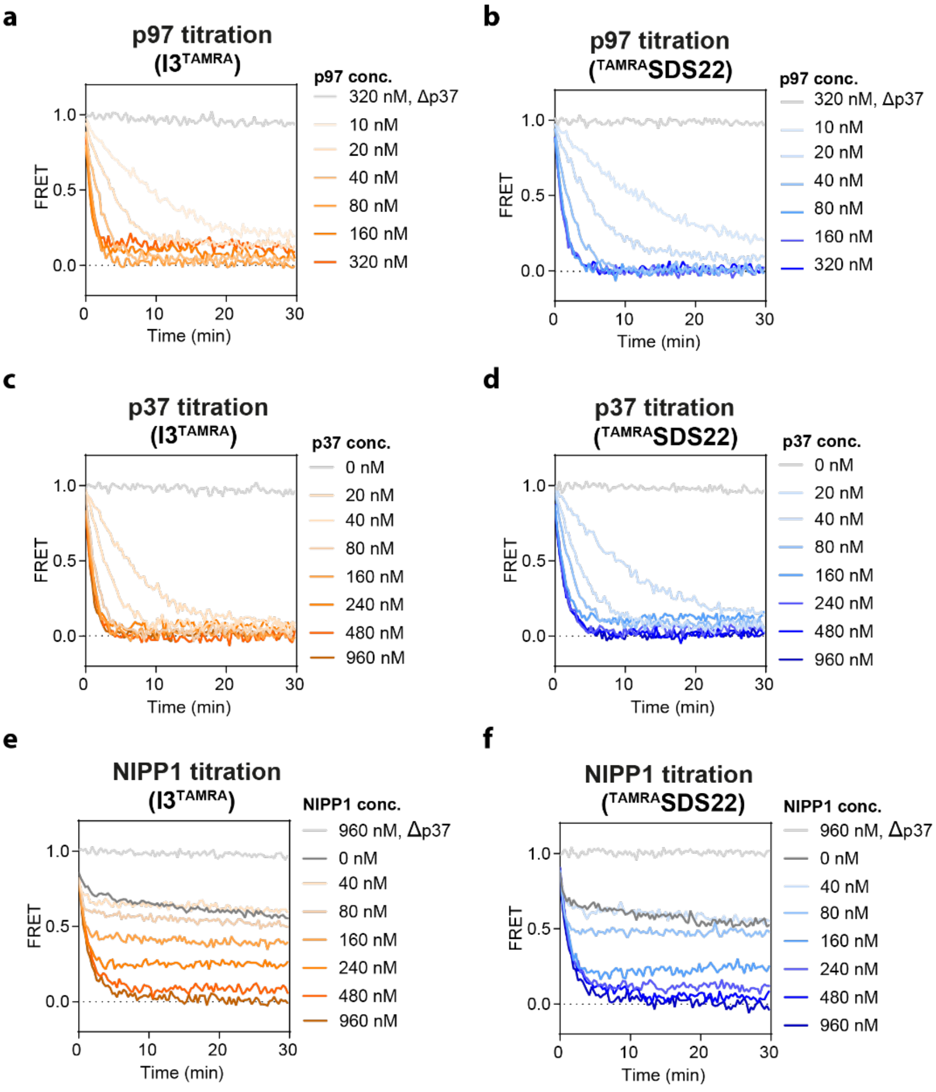

Figure 2.9: Titrations of FRET-based assay components for monitoring the disassembly of SDS22 and I3 from PP1 through p97:p37. a) FRET time course measurements of SPI disassembly reactions containing p37 (4 µM), SDS22:PP1^{Clover}:I3^{TAMRA} (160 nM), NIPP1 (480 nM) and ATP (2 mM), with indicated concentrations of p97. Shown are normalized ratios of acceptor and donor fluorescence. Δp37, p37 was omitted. **b)** As in a) but with ^{TAMRA}SDS22:PP1^{Clover}:I3. **c)** FRET time course measurements of SPI disassembly reactions containing p97 (160 nM), SDS22:PP1^{Clover}:I3^{TAMRA} (160 nM), NIPP1 (480 nM) and ATP (2 mM), with indicated concentrations of p37. Shown are normalized ratios of acceptor and donor fluorescence. **d)** As in c) but with ^{TAMRA}SDS22:PP1^{Clover}. **e)** FRET time course measurements of SPI disassembly reactions containing p97 (160 nM) p37 (480 µnM), SDS22:PP1^{Clover}:I3^{TAMRA} (160 nM), and ATP (2 mM), with indicated concentrations of NIPP1. Shown are normalized ratios of acceptor and donor fluorescence. Δp37, p37 was omitted. **f)** As in e) but with ^{TAMRA}SDS22:PP1^{Clover}

NIPP1 titrations were performed with 0-960 nM NIPP1. For SDS22:PP1^{Clover}:I3^{TAMRA} complex disassembly the control curve excluding NIPP1 demonstrated that disassembly of I3^{TAMRA} from PP1^{Clover} could still be observed without the presence of an alternative binding partner (**Figure 2.9e**). With increasing concentrations of NIPP1, the amount of I3^{TAMRA} dissociation increased as well, up to 960 nM NIPP1. The continued I3 dissociation could mean, that even at high NIPP1 concentrations, I3 is not fully disassembled from PP1. Together with the fact that we can observe net I3 disassembly without the addition of NIPP1 suggests that the SPI complex can re-form after disassembly by p97:p37. In that case, the plateau at the end of the reaction shows the equilibrium that the reaction reached between I3 and NIPP1 binding under the respective conditions.

I3 and NIPP1 share the RVXF PP1-interaction motif. Therefore, both interaction partners cannot bind at the same time. SDS22 binds PP1 at a different location, however the disassembly reaction containing the SDS22 TAMRA-labeled complex ^{TAMRA}SDS22:PP1^{Clover}:I3 showed a similar disassembly pattern as the equivalent I3-labled version, under varying concentrations of NIPP1 (**Figure 2.9f**). ^{TAMRA}SDS22 was disassembled from PP1^{Clover} in the control experiment which omitted NIPP1. Addition of increasing concentrations of NIPP1 lead to further dissociation of ^{TAMRA}SDS22, implying that NIPP1 displaces SDS22 in a concentration-dependent manner. However, the increased dissociation of SDS22 with increasing NIPP1 concentrations could indicate either a direct displacement through an overlapping binding site other than RVXF, or that I3 dissociation triggers SDS22 to also dissociate from PP1. Similar to I3, the NIPP1 titration suggests that SDS22 dissociates during SPI disassembly and can re-associate, resulting in an equilibrium dependent on respective assay conditions. A concentration of 240 nM NIPP1 was employed in further FRET-based assays monitoring I3^{TAMRA} and ^{TAMRA}SDS22 disassembly from PP1^{Clover}.

Titrations with SPI were not performed, because decreasing FRET label concentrations lead to a loss of signal. Both double labeled SPI complexes were efficiently disassembled by p97:p37 under conditions previously determined for NIPP1^{TAMRA} association, confirming that FRET labels on I3 and SDS22 in combination with PP1^{Clover} did not disturb SPI recognition and disassembly. Additionally, the optimal conditions for NIPP1^{TAMRA} assay were confirmed to lead to maximal reaction rates.

To investigate how much of the SPI complex is disassembled under the previously determined protein concentrations, double labeled SPI FRET substrates were created containing a TEV-protease cleavage site between the TAMRA label and SDS22 or I3. TEV-protease cleaves proteins at a specific TEV-protease cleavage sequence (TEVc). Upon incubation of TEV-protease with the TEVc-containing protein complexes, the TAMRA fluorophore undergoes cleavage from the SPI complex, causing a full loss of the FRET signal. Through the TEV-protease assay, true upper and lower FRET levels could be determined. The Δp37 curves correspond to the maximal FRET level where

SPI is fully assembled, while the TEV-protease treated reactions represent the lowest level of FRET, where no Clover and TAMRA are in proximity.

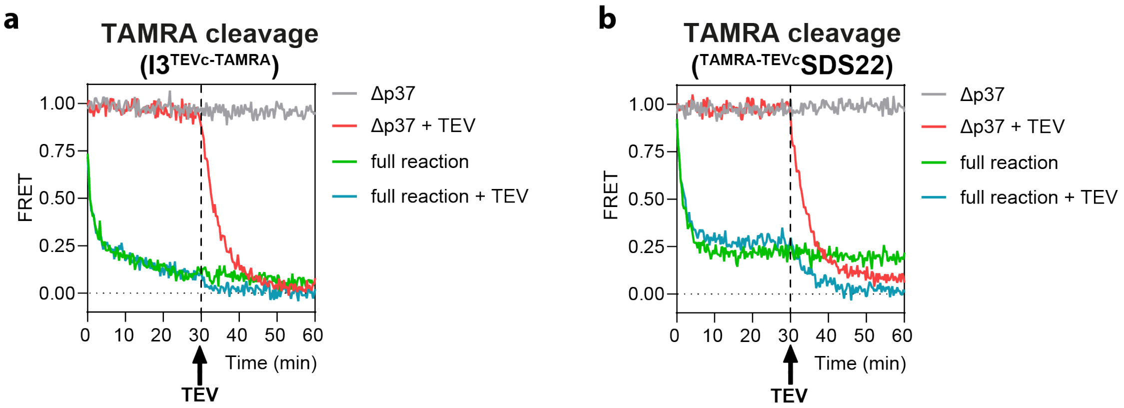

Figure 2.10: TEV-protease experiments with TEVc-FRET substrates to determine full SPI disassembly levels. a) FRET time course measurements of SPI disassembly reactions with 300 µM TEV-protease (TEV) added after 30 min. Full reactions contained p97 (160 nM), p37 (480 nM), SDS22:PP1^{Clover}:I3$^{TEVc-TAMRA}$ (160 nM) containing a TEV-protease cleavage site (TEVc) between I3 and TAMRA, NIPP1 (480 nM) and ATP (2 mM). Shown are normalized ratios of acceptor and donor fluorescence of representatives of 3 independent experiments. Δp37, p37 was omitted. **b)** as in a) except reactions contained $^{TAMRA-TEVc}$SDS22:PP1^{Clover}:I3 (160 nM) including a TEV-protease cleavage site (TEVc) between TAMRA and SDS22.

For analysis of the complexes containing TEV-cleavage sites, SDS22:PP1^{Clover}:I3$^{TEVc-TAMRA}$ was incubated with p97, p37, and NIPP1. Following the addition of ATP, a reduction in FRET over the next 30 min could be observed as expected, signifying the disassembly of the SPI complex with I3$^{TEVc-TAMRA}$ dissociating from PP1^{Clover} (**Figure 2.10a**, green curve). After 30 min, 300 µM TEV-protease was added to the reaction (blue curve). After addition of TEV-protease, the FRET signal showed a further decline of ~5-10 %. The same lower level of FRET could be observed for a reaction where p37 was omitted and TEV-protease added after 30 min (red curve). Further reduction of the FRET signal between PP1^{Clover} and I3^{TAMRA} indicates that under optimal assay conditions I3 is 90-95 % dissociated. The remaining 5-10 % percent could be due to I3 re-associating with PP1.

For the SDS22 TAMRA-labeled construct, equivalent experiments were performed. Incubating $^{TAMRA-TEVc}$SDS22:PP1^{Clover}:I3 with p97, p37 and NIPP1 lead to an expected decay in FRET over the following 30 min (**Figure 2.10b**, green curve). Adding TEV-protease after 30 min lead to a further FRET decrease of ~20-25 % (blue curve). A similar level could be observed for a reaction lacking p37, which was incubated with the same amount of TEV-protease (red curve). Further reduction of the FRET signal demonstrates that, at the end of the SPI disassembly reaction, 75-80 % of SDS22 is dissociated from PP1. The lack of total dissociation could suggest that SDS22 reassociates with PP1 after initial disassembly. Another possibility is that 20-25 % SDS22 remain bound to PP1, which would conflict with the almost full dissociation of SDS22 from PP1 observed in CoIP experiments (**Figure 2.5c**). The differences in total disassembly between I3^{TAMRA} and ^{TAMRA}SDS22 could mean that during constant p97 activity, SDS22 binds back to PP1 more quickly than I3. SDS22 binding back more quickly could be due to I3 getting unfolded and threaded through p97 during SPI disassembly, whereas the dissociation mechanism of SDS22 is unknown. The ability of I3 and SDS22 to potentially re-associate with PP1 after initial disassembly needs to be further investigated.

2.2.3 SDS22 and I3 disassembly occurs simultaneously

While I3 is translocated through the p97 pore during SPI disassembly, SDS22 dissociation has not been characterized. Possibilities include that SDS22 is competed off PP1 by an additional binding subunit, in this case NIPP1, that a direct interaction between I3 and SDS22 causes a weakening of SDS22 affinity to PP1 upon I3 dissociation, or that I3 dissociation causes a conformational change in PP1, like the loading of a metal ion, which ultimately leads to SDS22 dissociation. To further elucidate how SDS22 and I3 disassembly from the SPI complex is coupled, all three FRET-based assays were employed, containing one of the three FRET substrates each, with TAMRA labels on either SDS22, I3, or NIPP1.

The previously determined optimal FRET conditions were employed for all three different FRET-based assays to accurately determine relative dissociation and association speeds of the individual proteins at maximum reaction velocity. To reliably compare reaction speeds between the different assays, the reactions were recorded in triplicate. The I3-labeled version SDS22:PP1^{Clover}:I3^{TAMRA} was incubated with all assay components for 30 min (**Figure 2.11a**). Experimental data show a fast decay in FRET, reaching a plateau at 5-10 min. Omitting the adapter p37 results in a stable baseline representing no SPI disassembly. The SDS22-labeled version ^{TAMRA}SDS22:PP1^{Clover}:I3 was disassembled under equivalent conditions. The curve representing the full reaction shows a similar drop in FRET signal between 0 and 10 min, whereas the reaction excepting p37 remained at the same FRET level for the whole reaction time (**Figure 2.11b**). The association of NIPP1 after SPI disassembly was measured by tracking SDS22:PP1^{Clover}:I3 disassembly, followed by NIPP1^{TAMRA} binding. Same assay conditions as before were applied. The full reaction reached a plateau ~15 min after the start of the reaction, while the Δp37 curve remained at base levels (**Figure 2.11c**). To draw further conclusions about relative dissociation and association speeds, curves were analyzed in the same graph.

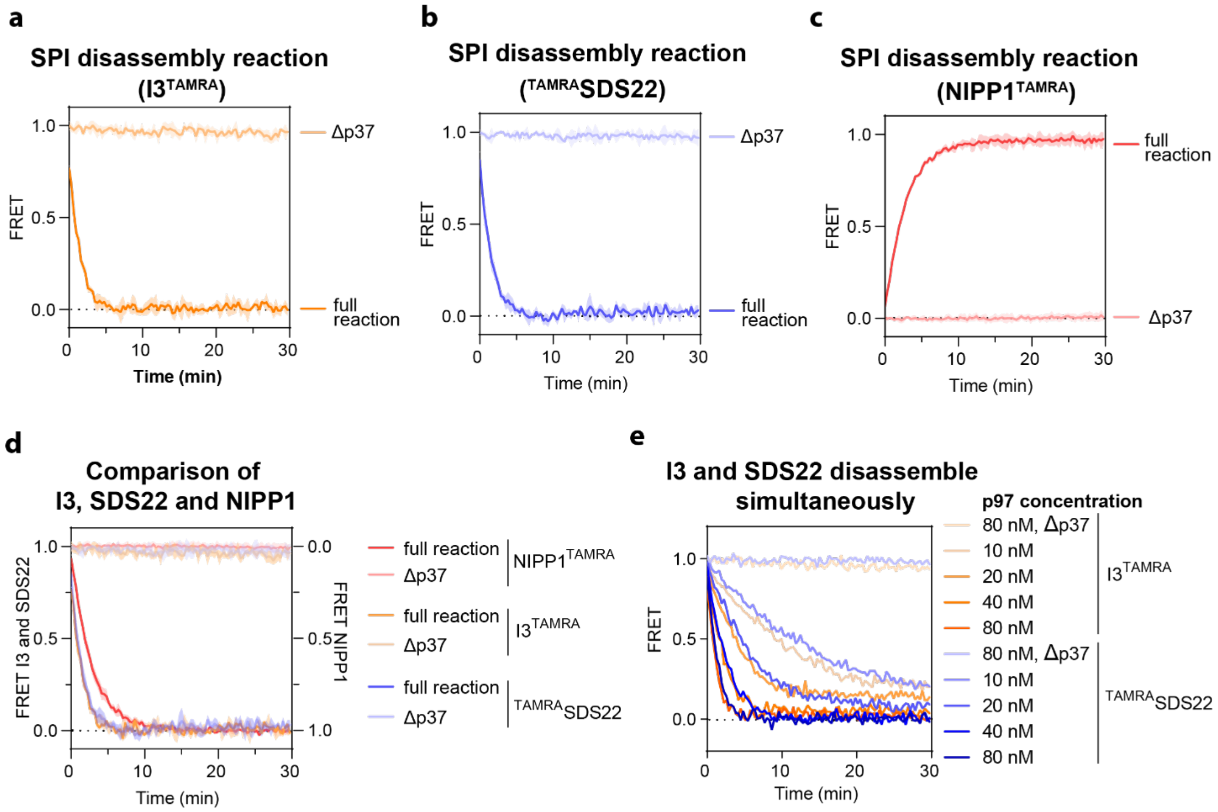

Figure 2.11: FRET assays show simultaneous disassembly of SDS22 and I3. a) FRET time course measurements of SPI disassembly reactions. Full reactions contained p97 (160 nM) p37 (480 µnM), SDS22:PP1^{Clover}:I3^{TAMRA} (160 nM), NIPP1 (240 nM), and ATP (2 mM). Curves were recorded at 30 °C. Shown are the means of the normalized ratios of acceptor and donor fluorescence ± SD, n=3. Δp37, p37 was omitted. **b)** as in a) but with ^{TAMRA}SDS22:PP1^{Clover}:I3. **c)** as in a) but with SDS22:PP1^{Clover}:I3 and NIPP1^{TAMRA}. **d)** Reactions from a), b) and c) overlaid. Note separate y-axis for NIPP1^{TAMRA} fluorescence. **e)** Overlay of FRET time course measurements of SPI disassembly reactions with the TAMRA fluorophore attached to either I3 or SDS22. Reactions contained p37 (4 µM), SDS22:PP1^{Clover}:I3^{TAMRA} (160 nM) or ^{TAMRA}SDS22:PP1^{Clover}:I3 (160 nM), NIPP1 (240 nM), and ATP (2 mM), with indicated concentrations of p97. Shown are normalized ratios of acceptor and donor fluorescence. Δp37, p37 was omitted.

An overlay of all three reactions, with an inverted curve of NIPP1, reveals that SDS22 and I3 dissociated from PP1 at the same time. The alternative PP1 binding partner NIPP1 then associated with PP1 with a slight delay, indicating that SDS22 is not displaced by NIPP1, but dissociates in reaction to I3 dissociation (**Figure 2.11d**). To verify the observation that SDS22 and I3 disassembly is coupled, a p97 titration experiment was performed and overlain graphs created for both SDS22:PP1^{Clover}:I3^{TAMRA} and ^{TAMRA}SDS22:PP1^{Clover}:I3. To obtain data with varying amounts of p97, concentrations of p97 were varied between 10-80 nM, while all other assay conditions remained constant. The experiments revealed that at all four different p97 concentration, and therefore different reactions velocities, ^{TAMRA}SDS22 and

I3^{TAMRA} and SDS22:PP1^{Clover}:I3^{TAMRA} curves show the same decrease in FRET over time, confirming that both SPI components disassemble simultaneously (**Figure 2.11e**).

2.2.4 SDS22 and I3 are both necessary for efficient SPI disassembly

I3 is the direct substrate of p97-mediated unfolding, while SDS22 binds a p97 N-terminal domain and therefore likely contributes to SPI complex recognition by p97:p37 (van den Boom et al., 2023; Weith et al., 2018). To explore whether both proteins are necessary for recognition and disassembly of the SPI complex, FRET substrate complexes lacking either I3 or SDS22 were created. Additionally, rescue experiments with individually purified I3 or SDS22 were performed.

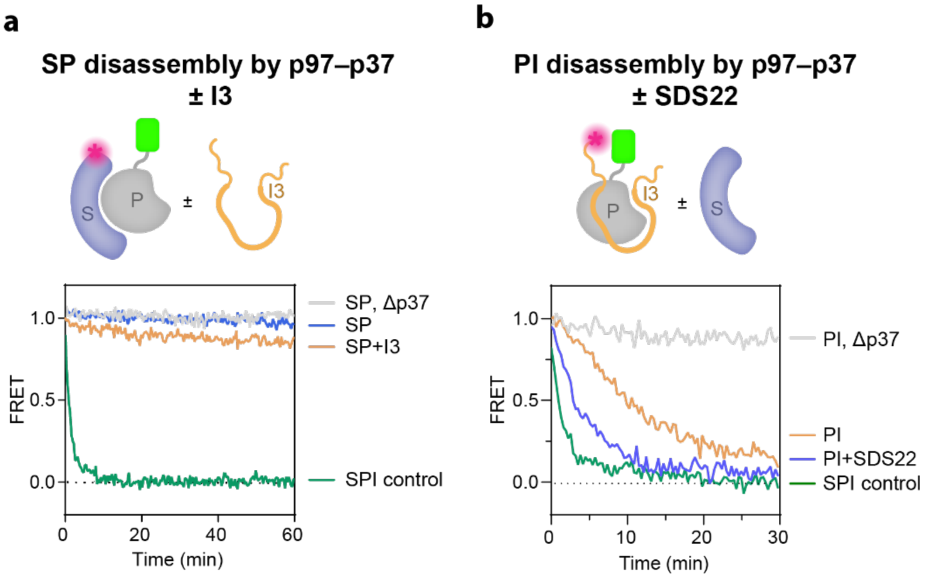

Figure 2.12: SDS22 and I3 are both necessary for efficient SPI disassembly by p97:p37. a) FRET time course measurements of the ^{TAMRA}SDS22:PP1^{Clover} complex (SP) incubated with p97:p37. The full ^{TAMRA}SDS22:PP1^{Clover}:I3 complex (SPI) served as a control. Reactions contained p97 (160 nM), p37 (480 nM), ^{TAMRA}SDS22:PP1^{Clover} (160 nM) or ^{TAMRA}SDS22:PP1^{Clover}:I3 (160 nM), NIPP1 (240 nM), and ATP (2 mM). Curves were recorded at 30 °C. Shown are the representative normalized ratios of acceptor and donor fluorescence of 3 independent experiments. Δp37, p37 was omitted. **b)** FRET time course measurements of the PP1^{Clover}:I3^{TAMRA} complex (PI) incubated with p97:p37 and individually purified SDS22. The full SDS22:PP1^{Clover}:I3^{TAMRA} complex (SPI) served as a control. Reactions contained p97 (160 nM), p37 (480 nM), PP1^{Clover}:I3^{TAMRA} (160 nM) or SDS22:PP1^{Clover}:I3^{TAMRA} (160 nM), NIPP1 (240 nM), and ATP (2 mM). Curves were recorded at 30 °C. Shown are the representative normalized ratios of acceptor and donor fluorescence of 3 independent experiments. Δp37, p37 was omitted.

^{TAMRA}SDS22:PP1^{Clover} (SP) was incubated with p97, p37, NIPP1 and ATP to discover whether the SP complex without I3 is a substrate for p97. Similar to a control lacking p37, no decrease in FRET could be detected over 60 min for the full reaction containing SP (**Figure 2.11a**, blue curve). The steady FRET signal suggests that SP alone cannot be disassembled by p97:p37, and I3 is necessary for efficient SPI disassembly. To mitigate the effect of I3 missing from the SP complex, I3 expressed individually in insect cells was incubated with SP for 2 hours before the start of the reaction. Compared with a control containing the full co-purified ^{TAMRA}SDS22:PP1^{Clover}:I3 complex, only a small decrease in FRET over the course of the reaction could be detected with SP + I3 (yellow curve). The decrease indicates that adding I3 to the SP complex, in the presence of p97:p37 and NIPP1, leads to a small amount of SDS22 disassembly. However, the full disassembly rate of the co-purified SPI complex could not be rescued. I3 is an intrinsically disordered protein, which only folds into a secondary structure by binding to PP1. It is possible that the isolated expression and purification of I3 produced a protein unable to properly fold and bind PP1. It is also possible that SPI complex formation requires the aid of eukaryotic chaperones, present in insect cell lysate, but not the *in vitro* disassembly assays.

Corresponding to the SP disassembly assay, co-purified PP1^{Clover}:I3^{TAMRA} (PI) complex lacking SDS22 was subjected to disassembly by p97:p37. The reaction started with FRET labels of I3 and PP1 in close vicinity. Over the course of a reaction containing PI, p97, p37, NIPP1 and ATP, the FRET signal decreased slowly, compared with a reaction containing the full SPI complex (**Figure 2.11b**, yellow curve). The decrease in FRET of the curve containing the PI reaction indicates that PI is a substrate for p97:p37, however the efficiency of disassembly with the complex devoid of SDS22 is greatly diminished. Adding individually expressed SDS22 purified from insect cells to the PI disassembly reaction resulted in an increase in reaction speed of >50 % compared to the PI reaction (blue curve). The increase suggests that SDS22 aids in SPI disassembly, possibly through the interaction between SDS22 and p97. The full reaction speed of the co-purified SPI complex could not be reached through the addition of SDS22, once again indicating that SPI folds differently in cells than *in vitro*. Combined, the SP and PI disassembly assays show that I3 is strictly necessary for SPI disassembly *in vitro*, and both SDS22 and I3 are necessary for efficient SPI disassembly, suggesting that the full SPI complex is likely the relevant substrate of p97 in cells.

2.2.5 SDS22 and PP1 interaction is improved by the presence of I3

Through FRET-based assays performed with SP and PI complexes, it was observed that by adding the missing SPI component, disassembly speeds increased (**Figure 2.12**). To explore whether the enhanced velocities were partially due to the SPI complex forming more stably with all components present, an association experiment with PP1^{Clover} and ^{TAMRA}SDS22 was conducted. PP1^{Clover} and ^{TAMRA}SDS22 were expressed independently in bacterial and insect cells, respectively, and mixed with varying concentrations of I3 and SDS22.

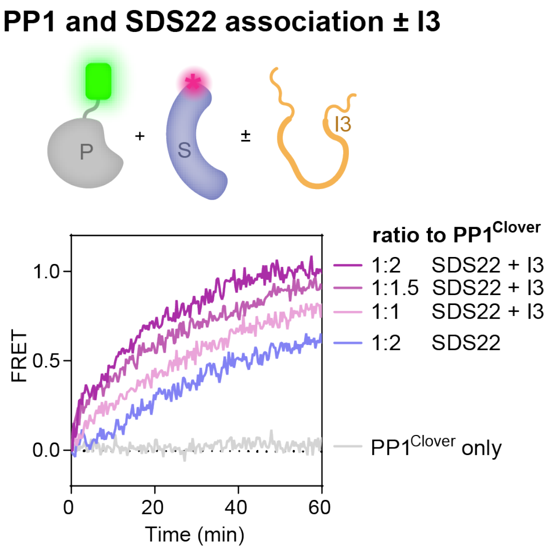

Figure 2.13: Association experiment with PP1 and SDS22 in the presence or absence of I3. FRET time course measurements of the association of individually purified PP1^{Clover} and ^{TAMRA}SDS22 in the presence and absence of I3. Reactions contained PP1^{Clover} (500 nM), ^{TAMRA}SDS22 (500-1000 nM), and I3 (500-1000 nM). Indicated are the ratios of SDS22 and I3 to PP1 that are contained in the respective reaction. Curves were recorded at 30 °C. Shown are the normalized ratios of acceptor and donor fluorescence.

To conduct the association experiment, ^{TAMRA}SDS22 was added to PP1^{Clover} at a ratio of 1:2. Compared to a control curve recorded with only PP1^{Clover}, an increase in FRET is observable over a time course of 60 min, indicating association of SDS22 and PP1. (**Figure 2.13**, blue curve). To test whether SDS22 binding to PP1 increases in the presence of I3, a titration experiment was performed. ^{TAMRA}SDS22 and I3 were introduced at varying concentrations into a sample containing only PP1^{Clover}. Data analysis revealed that adding ^{TAMRA}SDS22 and I3 to PP1^{Clover} (ratio 1:1), resulted in an increase in FRET compared to the control containing only PP1^{Clover} and ^{TAMRA}SDS22 (ratio 1:2). The FRET increase signifies that more SDS22 associated with PP1 in the presence of I3 even at a lower concentration of SDS22. Increasing concentrations of SDS22 and I3 in relation to PP1 resulted in further FRET increase. At a ratio of 1:2, of SDS22 and I3 to PP1, the FRET signal increased by ~50 % compared with the control containing the same protein concentrations, but lacking I3. Increased FRET in the presence of I3 suggests a cooperative binding of SDS22 and I3, where I3 aids the association of SDS22 to PP1.

For technical reasons the same experiment was not conducted with TAMRA-labeled I3, because the individually purified protein was not stable enough in liquid buffer solution to be subjected to Sortase A catalyzed labeling at 30 °C for 2 h. Consequently, it is uncertain whether the improvement in association between I3 and PP1 occurs similarly in the presence of SDS22, as in the reverse situation.

2.3 Exploring SPI complex reassembly and stability

The PP1 catalytic subunit (PP1) is largely indiscriminate and highly reactive towards various phosphorylated substrates (Bertolotti, 2018; Pinna & Donella-Deana, 1994). Since SDS22 and I3 bind PP1 during PP1 biosynthesis, it could be suggested that the SPI complex forms to keep PP1 stable and inactive during translation and after PP1 is released from the ribosome. Another possibility is that the SPI complex also forms in between cycles of p97:p37 mediated disassembly, to ensure PP1 sequestration and therefore limit excess dephosphorylation in the cell, or even regulate PP1 holoenzyme exchange. The FRET assays monitoring binding of SDS22 and I3 to PP1 were used to investigate if SPI reassembles in the absence of p97 activity, to observe displacement of other PP1-binding subunits by SDS22 and I3, as well as to analyze SPI complex stability in presence of a PP1-binding competitor.

2.3.1 The SPI complex reassembles upon inhibition of p97 activity

Previous experiments showed that p97:p37 mediated SPI disassembly did not lead to full dissociation of SDS22 or I3 from PP1. Specifically, increasing NIPP1 concentrations lead to further disassembly of the SPI complex, suggesting that the plateau at the end of the reaction represents an equilibrium state between NIPP1 binding and SDS22 and I3 re-association. (**Figure 2.9**). Additionally, employing TEV-protease cleavage of the TAMRA fluorophore on SDS22 and I3, and conditions at which maximal reaction velocities were reached, demonstrated that SDS22 and I3 are not fully disassembled from PP1 at the end of the reaction (**Figure 2.10**). Both findings hint at the SPI complex re-forming after initial disassembly by p97:p37. Applying a more direct approach to test this hypothesis, a FRET-based assay was set up where p97 activity was inhibited at the end of the SPI disassembly reaction. Incubation of SPI, p97, p37 and NIPP1 leads to SDS22 and I3 dissociation from PP1 and NIPP1 binding. After the conclusion of the disassembly reaction, the small molecule p97-inhibitor CB-5083 is added to the reaction. p97 inhibition causes SPI disassembly to halt. If the SPI complex can reassemble after initial disassembly, this should result in the development of a FRET signal signifying reassembly of the SPI complex under dissociation of NIPP1 (**Figure 2.14a**).

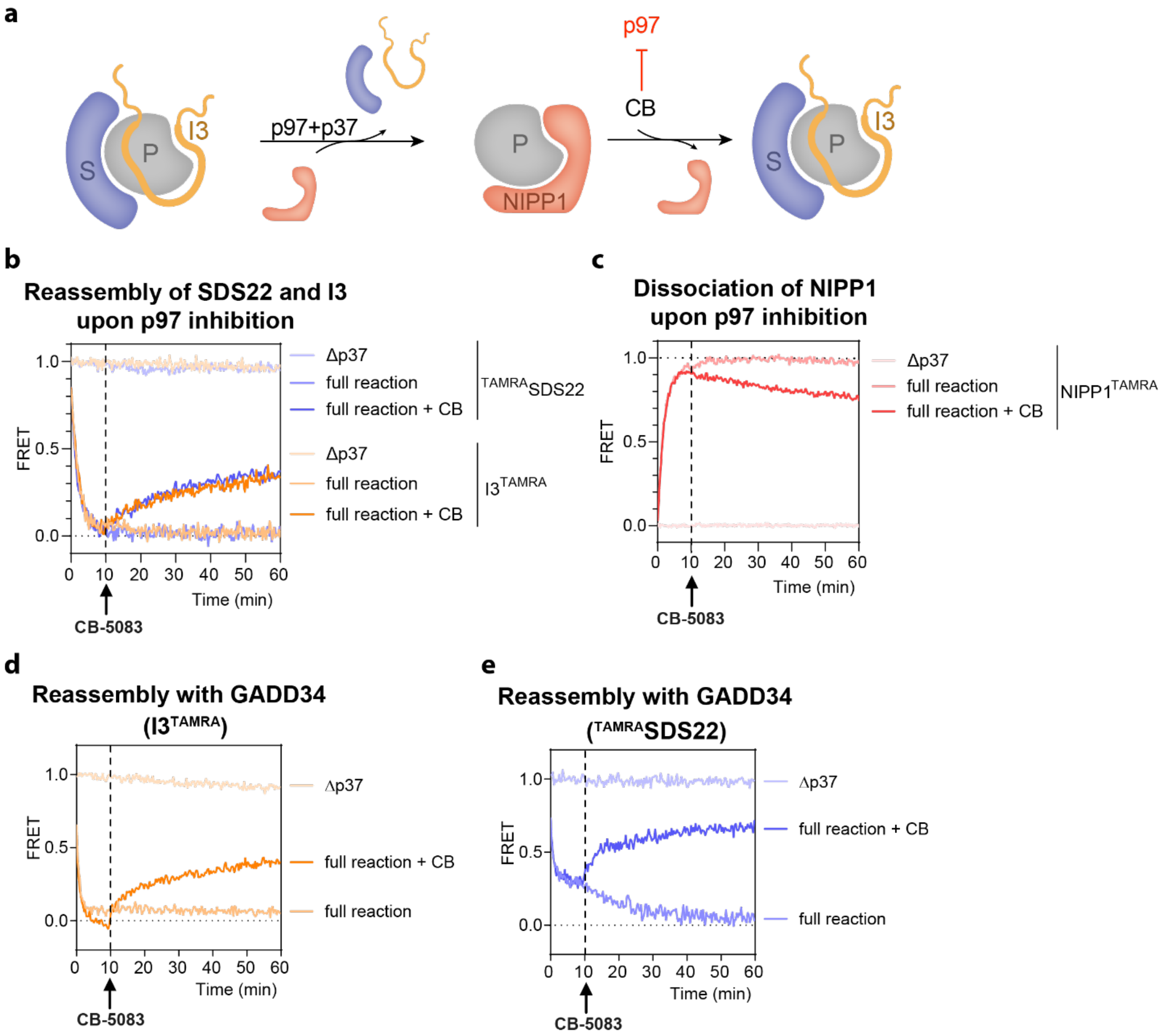

Figure 2.14: SPI reassembles upon p97 inhibition, after initial disassembly by p97:p37. a) Schematic illustration of the SPI disassembly and reassembly reaction. Following the disassembly of I3 and SDS22 from PP1, facilitated by p97:p37, PP1 can associate with NIPP1. Upon inhibition of p97 through the small molecule inhibitor CB-5083, SDS22 and I3 displace NIPP1. Representation of FRET labels was omitted. **b)** FRET time course measurements of SPI disassembly and reassembly reactions. After 10 min of disassembly CB-5083 (10 µM) or DMSO as a control were added to the indicated reactions. Full reactions contained p97 (160 nM) p37 (480 µnM), $^{\text{TAMRA}}$SDS22:PP1$^{\text{Clover}}$:I3 (160 nM) or SDS22:PP1$^{\text{Clover}}$:I3$^{\text{TAMRA}}$ (160 nM), NIPP1 (240 nM) and ATP (2 mM). Shown are the representative normalized ratios of acceptor and donor fluorescence of 3 independent experiments. Δp37, p37 was omitted. **c)** as in b), but reactions contained SDS22:PP1$^{\text{Clover}}$:I3 (160 nM) and NIPP1$^{\text{TAMRA}}$ (240 nM). Shown are the representative normalized ratios of acceptor and donor fluorescence of 3 independent experiments. **d)** FRET time course measurements of SPI disassembly and reassembly reactions with conditions as before, but with GADD34 as an alternative PP1 binding partner. After 10 min of disassembly CB-5083 (10 µM) or DMSO was added to the indicated reactions. Full reactions contained p97 (160 nM) p37 (480 µnM), SDS22:PP1$^{\text{Clover}}$:I3$^{\text{TAMRA}}$ (160 nM), MBP-GADD34$^{513\text{-}636}$ (240 nM) and ATP (2 mM). **e)** as in d) but with $^{\text{TAMRA}}$SDS22:PP1$^{\text{Clover}}$:I3.

To observe, whether the SPI complex re-forms after inhibition of p97, FRET-based assays containing either the I3 or SDS22 TAMRA-labeled SPI versions were employed. Full reactions contained optimal concentrations of p97, p37, NIPP1 and the respective SPI version. Following addition of ATP, a decay of FRET for the full 70 min of the recording could be observed, with a minimum reached after approximately 10 min (**Figure 2.14b**). The controls excluding p37 showed no change in FRET over the course of the reaction, as the SPI complex could not be recognized by p97. A separate reaction was treated with 10 µM CB-5083 dissolved in DMSO. CB-5083 is a small molecule inhibitor of p97, which binds to p97 at the nucleotide binding pockets, resulting in competitive inhibition of the ATPase (Tang et al., 2019). Following p97 inhibition, curves depicting reactions with either SDS22:PP1$^{\text{Clover}}$:I3$^{\text{TAMRA}}$ or $^{\text{TAMRA}}$SDS22:PP1$^{\text{Clover}}$:I3 exhibit an approximately 40 % increase in FRET signal compared to the full reactions treated with an equivalent amount of DMSO. These results demonstrate that both SDS22 and I3 re-associate with PP1, when p97 activity is inhibited.

Conversely, the same experiment with NIPP1$^{\text{TAMRA}}$ and SDS22:PP1$^{\text{Clover}}$:I3 shows an increase in FRET over the course of the full reaction supplemented with DMSO after 10 min, signifying that NIPP1 associated with PP1 (**Figure 2.14c**). The reaction complemented with CB-5083 10 min after the start of SPI disassembly, exhibits a decrease in FRET of ~25 % over the time course of 60 min. A decrease in FRET indicates NIPP1 dissociation from PP1, upon the inhibition of p97 activity. Together the experiments performed under addition of CB-5083 confirm that SDS22 and I3 displace NIPP1 from PP1, and the SPI complex reassembles in the absence of p97 activity. Full reassembly of SPI or dissociation of NIPP1 could not be observed with this experiment.

It is unclear why only ~40 % of SPI reassembled under the given conditions. One potential interpretation is that the proteins may undergo damage due to exposure to recurrent cycles of p97-mediated disassembly. It is also possible that the reassembly of the SPI complex requires the help of chaperones and is therefore less efficient in biochemical *in vitro* assays. Reassembly of SPI and dissociation of NIPP1 occur at slower kinetic rates than the disassembly reaction. The slower reassembly rate could be explained by the passive nature of the reassembly, dependent on mass action and affinities of the three proteins to PP1, compared to the catalyzed SPI disassembly reaction.

To verify if SDS22 and I3 can also displace another PP1-interacting protein upon p97 inhibition, a truncated version of the PP1 substrate specifier GADD34 was used instead of NIPP1. The same FRET-based fluorescence time measurements were conducted, containing either I3 or SDS22 TAMRA-labeled SPI versions, as well as p97, p37 and MBP-GADD34$^{513\text{-}636}$. For solubility reasons, GADD34 was expressed as a shortened version, including all PP1-interacting motifs, and an MBP (maltose-binding protein)-solubility tag (Crespillo-Casado et al., 2018). Equivalent to the experiment performed with NIPP1, I3^{TAMRA} re-associated with PP1^{Clover}, while displacing GADD34, upon inhibition of p97 with CB-5083 (**Figure 2.14d**). The same experiment performed with ^{TAMRA}SDS22:PP1^{Clover}:I3 showed that SDS22 did not dissociate the same amount after 10 min as it did with NIPP1 present. The reduced dissociation suggests, that SDS22 and MBP-GADD34$^{513\text{-}636}$ can bind PP1 simultaneously. However, upon the addition of CB-5083, SDS22 re-associated with PP1 over the course of 60 min (**Figure 2.14e**). Combined these results show that the SPI complex re-forms in the presence of p97-inhibitor, displacing the alternative subunits NIPP1 and MBP-GADD34$^{513\text{-}636}$.

To confirm the observation that the SPI complex reassembles after initial disassembly by p97:p37, a PP1γ CoIP experiment with purified components and treatment with the ATP-hydrolyzing enzyme apyrase was performed. Apyrase catalyzes the hydrolysis of ATP and ADP into AMP and inorganic phosphate. Similar to CB-5083, ATP hydrolysis causes the inhibition of p97 activity, which requires ATP for its catalytic function. p97, SDS22:PP1^{Clover}:I3, p37, and NIPP1 were incubated at optimal concentrations with 2 mM ATP, for indicated time points from 1 to 70 min. Apyrase was incubated with specified samples for indicated time points to observe SPI reassembly (**Figure 2.15**).

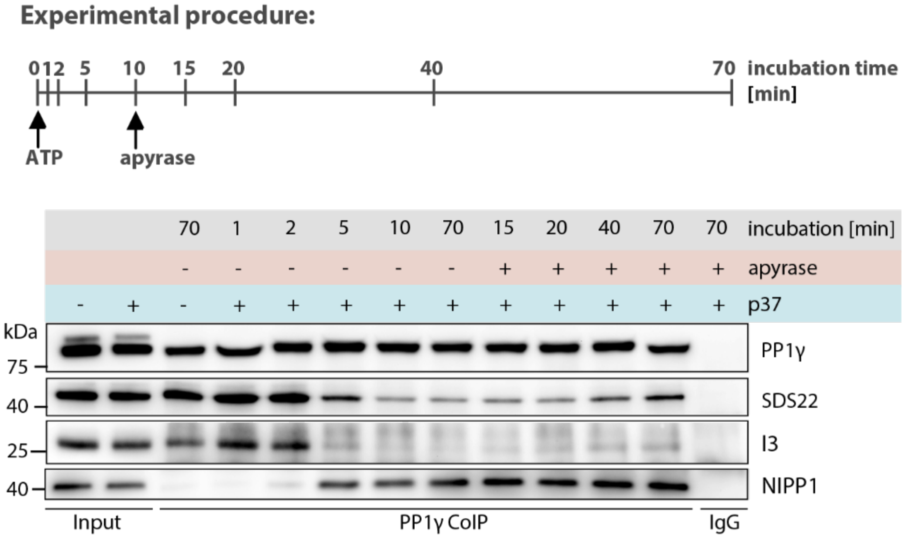

Figure 2.15: CoIP experiment of SPI reassembly induced by the addition of ATP hydrolyzing enzyme apyrase. Co-immunoprecipitation time course experiment of the SPI disassembly and reassembly reaction, through addition of ATP or apyrase and stopping the reaction at specified time points. Reactions contained p97 (160 nM), p37 (480 µM), SDS22:PP1^{Clover}:I3 (160 nM), NIPP1 (240 nM), ATP (2 mM), and apyrase (0.5 U), as indicated. PP1^{Clover} was immuno-isolated at specified time points and associated proteins detected by Western blot analysis with indicated antibodies.

Over the time course of 10 min after addition of ATP, SDS22 and I3 signals became weaker, while the NIPP1 signal increased, demonstrating the disassembly by SPI with subsequent binding of NIPP1. The sample containing no p37 served as a control for how much SDS22 and I3 were co-isolated with PP1γ at the beginning of the reaction.

Comparison with the sample treated for 70 min with ATP shows that the disassembly reaction was largely completed after 10 min. Apyrase was added as indicated after 10 min treatment with ATP. Over the course of 60 min after apyrase addition, increases in SDS22 and I3 signals could be observed. Increased co-immunoprecipitation of SDS22 and I3 confirmed the reassembly of the SPI complex upon p97 inhibition, previously detected via FRET. Similar to the FRET-based assays, only partial reassembly of SDS22 and I3 were observed in the CoIP experiment. Dissociation of NIPP1 after p97-inhibition could not be detected by CoIP and Western-blotting. One of the reasons for utilizing FRET-based assays instead of CoIPs was the higher sensitivity and reliability of FRET. It can be assumed that the lack of changing NIPP1 levels following apyrase addition are due to low assay sensitivity.

2.3.1.1 SDS22 re-binds PP1 upon p97 inhibition in the presence of Mn^{2+} ions

The association of SDS22 and PP1 has been shown before to depend on the metal loading state of PP1. Necessary for its catalytic activity, PP1 has two metal ions bound in its active site. The crystal structure of SDS22 and PP1 reveals that only one metal ion is bound under these circumstances. Further, surface plasmon resonance (SPR) showed that SDS22 exclusively bound metal-deficient PP1, equilibrated in metal ion poor buffer (Choy et al., 2019). FRET-based assay buffer used in this study contained 5 mM $MgCl_2$ for ATP complexation. While PP1 was shown to be active with a variety of two-valent ions bound in its catalytic center, distinct ions are present upon PP1 isolation from certain tissues. PP1 expressed in bacterial cells contains Mn^{2+} ions in both metal-binding sites. To make sure both metal binding sites were occupied with ions during the following experiments, an additional 1 mM of $MnCl_2$ was added to the buffer. To test whether SDS22 could re-associate with PP1 after SPI disassembly, even in the presence of high concentration of Mn^{2+} ions, an SPI reassembly experiment was performed with buffer containing or lacking 1 mM $MnCl_2$.

The SPI dis- and reassembly reaction was performed as before, but in the presence of 1 mM $MnCl_2$. The disassembly of SDS22 from PP1 was observed over a time course of 30 min. As detected before, a minimum of FRET signal was reached after approximately 10 min. The addition of 10 µM CB-5083 caused an increase in FRET signal of ~40 % for both samples, containing or lacking $MnCl_2$ (**Figure 2.16**). Since SDS22 re-associated the same under both conditions, it can be excluded that the presence of metal ions impedes SDS22 re-binding of PP1 following SPI disassembly.

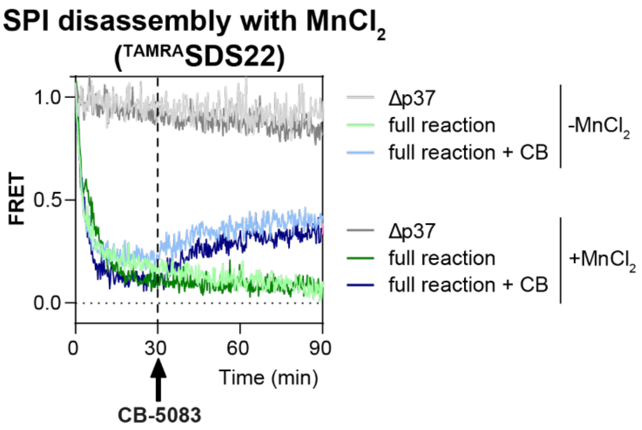

Figure 2.16: SDS22 association with PP1 upon p97 inhibition with CB-5083 in the presence of an excess amount of Mn^{2+} ions. FRET time course measurements of SPI disassembly and reassembly reactions in the presence or absence of $MnCl_2$ (1 mM). After 30 min of disassembly, CB-5083 (10 µM) was added to the indicated reactions. Full reactions contained p97 (160 nM) p37 (480 µnM), ^{TAMRA}SDS22:PP1^{Clover}:I3 (160 nM), NIPP1 (240 nM) and ATP (2 mM). Shown are the representative normalized ratios of acceptor and donor fluorescence of 3 independent experiments. Δp37, p37 was omitted.

2.3.2 The SPI complex is stable in the presence of a PP1-binding competitor

FRET-based assays showed that SPI was able to re-form, displacing other PP1-interacting proteins during inhibition of p97 activity. To test the stability of SPI in the absence of catalyzed disassembly, dissociation experiments were performed. To accomplish this, SPI complex variants carrying TAMRA labels either on SDS22 or I3 were incubated over 18 hours with varying concentrations of the PP1-binding competitor NIPP1. Observed were changes in FRET, signifying dissociation of SPI complex components ^{TAMRA}SDS22 and I3^{TAMRA} from PP1^{Clover}.

To monitor I3 dissociation from PP1 over 18 hours, 160 nM SDS22:PP1^{Clover}:I3^{TAMRA} and 0-960 nM NIPP1 were incubated at 30 °C. Compared to a control additionally containing the full SPI disassembly reaction (+ 160 nM p97, 480 nM p37 and 2 mM ATP), only a small amount of FRET decay and therefore I3 dissociation can be observed, even at high concentrations of NIPP1 (**Figure 2.17a**). After 60 min, a NIPP1 concentration corresponding to a 6x surplus relative to SPI resulted in a 10 % decrease in FRET. At the end of the recording after 18 hours, the FRET signal was reduced by a maximum of 20 %, with the full disassembly reaction serving as a control. The low change of FRET signal indicates that after 18 hours, ~80 % of I3 remained bound to PP1, even in the presence of a vast excess of NIPP1, highlighting the stability of the SPI complex, compared with other PP1-interacting proteins.

The same experiment was conducted with the SDS22 TAMRA-labeled FRET substrate ^{TAMRA}SDS22:PP1^{Clover}:I3. 60 min after the start of the incubation, ~10 % of SDS22 had dissociated from PP1 in the sample containing the highest NIPP1 concentration. The 10 % were calculated relative to the full reaction containing p97:p37. A total FRET-decrease of ~20 % was observed after 18 hours at a 6x surplus of NIPP1 (**Figure 2.17b**). Consequently, ~80 % of SDS22 were bound to PP1 at the end of the incubation with NIPP1. In conclusion, both I3 and SDS22 were not proficiently displaced from PP1 by NIPP1, highlighting the stability of SPI in the presence of a PP1-binding competitor over time. Compared to reactions additionally containing p97, p37 and ATP, the SPI dissociation experiments with NIPP1 show that efficient dissociation of both I3 and SDS22 from PP1 required p97 activity.

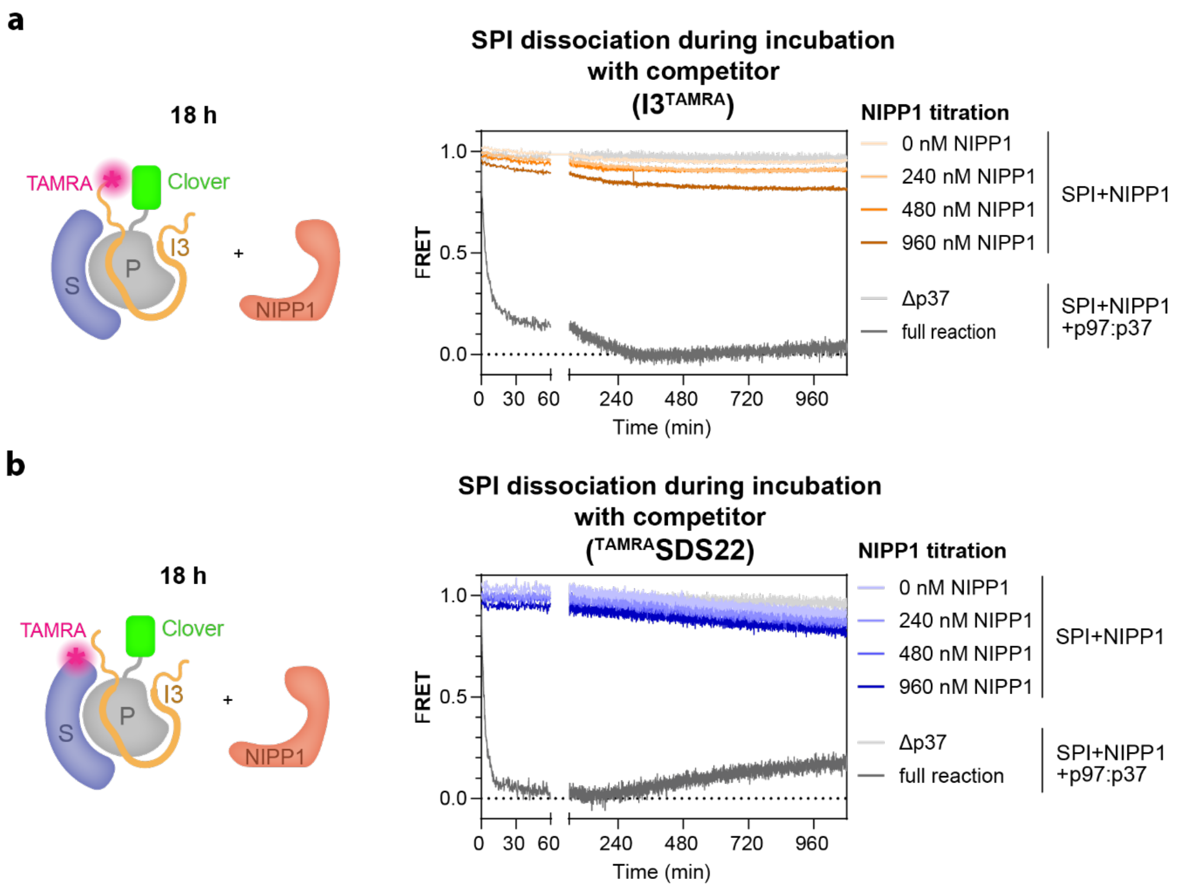

Figure 2.17: The SPI complex is stable in the presence of high concentrations of the competitor NIPP1. a) FRET time course measurements of SPI disassembly with varying concentrations of NIPP1. A full disassembly reaction containing p97 and p37 served as a control. Reactions were incubated for 18 hours and contained SDS22:PP1$^{\text{Clover}}$:I3$^{\text{TAMRA}}$ (160 nM), and NIPP1 (0-960 nM), p97 controls contained NIPP1 (240 nM), ATP (2 mM), p97 (160 nM) as well as p37 (480 nM) as indicated. Shown are normalized ratios of acceptor and donor fluorescence. Δp37, p37 was omitted. **b)** as in a, but with $^{\text{TAMRA}}$SDS22:PP1$^{\text{Clover}}$:I3. Shown are normalized ratios of acceptor and donor fluorescence. Δp37, p37 was omitted.

2.3.3 SDS22 and I3 can displace a PP1-binding competitor

Long incubation with excess levels of NIPP1 lead to only limited dissociation of SDS22 and I3 from PP1. Most of the SPI complex remained bound or reassembled in favor of NIPP1 (**Figure 2.17**). To test whether free SDS22 and I3 can conversely displace

NIPP1 from a NIPP1:PP1 complex (NP), as shown during p97 inhibition after SPI disassembly, dissociation experiments with different concentrations of SDS22 and I3 relative to NP were performed. To achieve this, NIPP1-LPETGGG and PP1$^{\text{Clover}}$ were co-expressed and purified from insect cells. Subsequently, NIPP1 was labeled with TAMRA as described before (**Figure 2.1**).

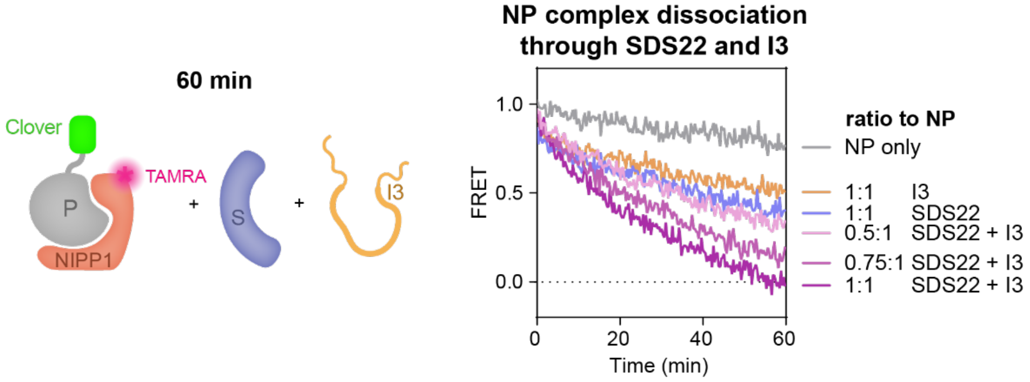

Figure 2.18 SDS22 and I3 displace another PP1 interaction partner. FRET time course measurements of the NIPP1:PP1 complex (NP) dissociation in the presence and absence of SDS22 and I3. Reactions contained NIPP1$^{\text{TAMRA}}$:PP1$^{\text{Clover}}$ (1000 nM), SDS22 (500-1000 nM), and I3 (500-1000 nM). Indicated are the ratios of SDS22 and I3 to NP contained in the respective reaction. Curves were recorded at 30 °C. Shown are the normalized ratios of acceptor and donor fluorescence.

To observe NP dissociation, the NIPP1$^{\text{TAMRA}}$:PP1$^{\text{Clover}}$ complex was incubated with equimolar concentrations of I3 and SDS22, individually. Compared to a control reaction only containing NP, a decrease in FRET signal over the course of 60 min was observed for both samples, implying NP dissociated in the presence of I3, as well as SDS22 (**Figure 2.18**). The addition of SDS22 and I3 together resulted in further, concentration-dependent FRET decay. The experimental results suggest that I3 and SDS22 both displace NIPP1 from PP1 at equimolar concentrations. Of note, the presence of both SDS22 and I3 simultaneously led to further increase of NP dissociation, indicating that both proteins together displace NIPP1 even more effectively. This result is consistent with the observation that SDS22 association is aided by the presence of I3 (**Figure 2.13**). A limitation of this assay is the lack of a positive NP dissociation control that shows the state of full NP disassembly, as was shown for the full SPI disassembly reaction in the reverse experiment (**Figure 2.17**). However, it can be concluded that free SDS22 and I3 can displace NIPP1 from PP1, while free NIPP1 is unable to effectively displace SDS22 and I3 from PP1, which strictly requires p97 activity.

2.4 Investigation of PP1 activity after SPI disassembly by p97:p37

SDS22 and I3 are known to form an inactive complex with PP1 during PP1 biogenesis, but has also been implicated in PP1 function during mitosis. To explore whether SPI disassembly can result in the release of active PP1, dephosphorylation of the synthetic PP1 substrate 3-O-methylfluorescein phosphate (OMFP) was measured during SPI disassembly. To further investigate whether PP1 forms an active holoenzyme complex, association of the substrate specifying PP1 subunit GADD34 was tracked, followed by dephosphorylation of the endogenous PP1 substrate eIF2α.

2.4.1 PP1 dephosphorylates a synthetic substrate after SPI disassembly

OMFP is a synthetic substrate of PP1. Structurally, OMFP consists of a methylated fluorescein molecule, carrying a phosphate group. In this form, fluorescein does not emit visible light. OMFP can interact with the PP1 active site, resulting in OMFP catalysis to OMF and inorganic phosphate (Swingle & Honkanen, 2014). OMF emits light at a wavelength of 515 nm, which can be tracked using a fluorescence spectrophotometer. To investigate PP1 activity after SPI disassembly, an OMFP dephosphorylation assay was set up (**Figure 2.19a**). The inactive SPI complex requires disassembly by p97:p37, to make PP1 available for interaction. After SPI disassembly, the SPI complex can re-form (**Figure 2.14**). Reassembly of the SPI complex results in restored inhibition of PP1. To prevent constant re-association of SDS22 and I3, an inactive mutant of PP1, PP1^{H66K}, was employed, to serve as an SDS22- and I3-binding "sponge". Upon addition of the inactive PP1^{H66K} mutant, PP1 becomes free to associate with, and dephosphorylate OMFP. The release of active PP1 can be observed by the increased production of fluorescent OMF.

Measurements of OMF fluorescence were conducted with samples containing 100 µM OMFP and p97, p37 and SPI at optimal concentrations determined by FRET. A reaction containing only OMFP and free PP1, expressed in bacterial cells, served as a control for how much OMFP is dephosphorylated in the absence of PP1 inhibitors. The exclusion of p37 causes the SPI complex to stay intact, since SPI recognition by p97 is impeded. Under these circumstances, no PP1 activity should be observed. Notably, the full reaction showed no increase in OMF fluorescence compared with the Δp37 control (**Figure 2.19b**). Under both conditions, OMFP was not dephosphorylated by PP1, demonstrating that PP1 was inactive. The observation that PP1 is inactive even during p97 activity suggests that SDS22 and I3 re-associated with PP1, before catalyzed dephosphorylation of OMFP could occur. The inhibition of PP1 activity during SPI disassembly confirms that SPI re-forms constantly, even in the presence of active p97 and p37.

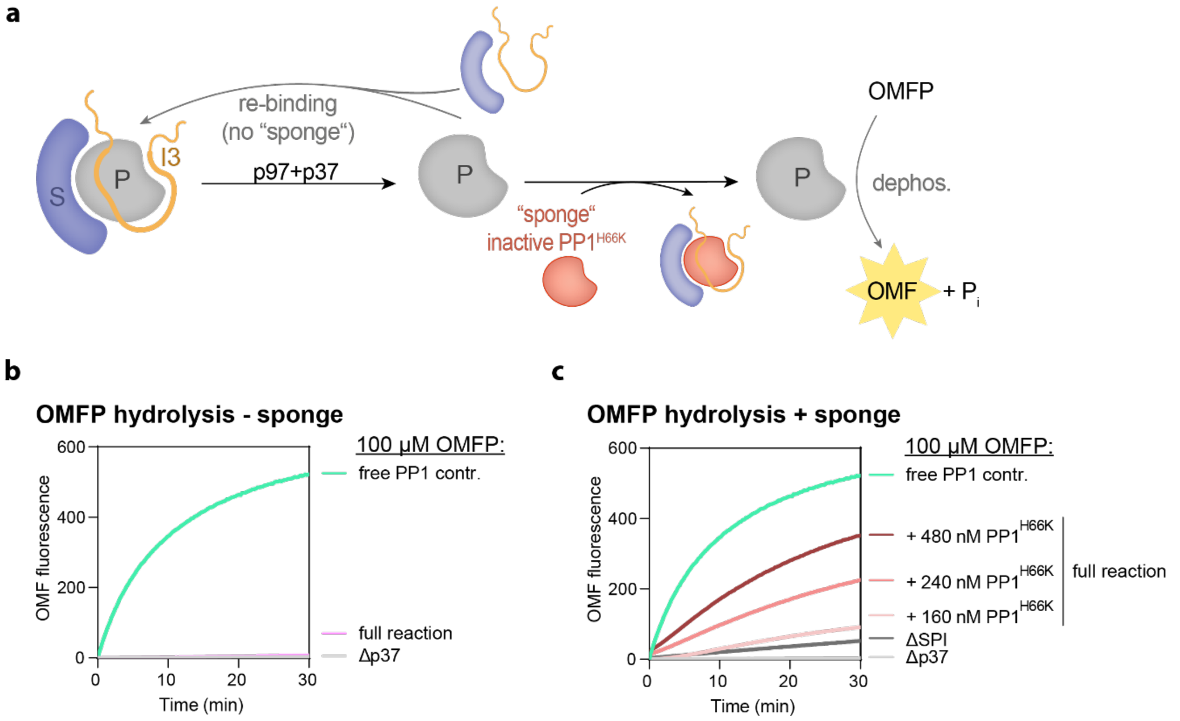

Figure 2.19: PP1 dephosphorylates the synthetic substrate OMFP after SPI disassembly. a) Schematic illustration of the SPI disassembly reaction leading to either reassembly of the SPI complex or dephosphorylation of OMFP by PP1, in the presence of the inactive PP1^{H66K} mutant. Following the disassembly of I3 and SDS22 from PP1, facilitated by p97:p37, PP1 can re-bind SDS22 and I3, remaining inactive. Upon addition of the inactive PP1^{H66K} mutant, which serves as a sponge to bind SDS22 and I3, PP1 is now active and dephosphorylates OMFP to the fluorescent OMF. **b)** Fluorometric measurements tracking the dephosphorylation of OMFP over time with full reactions containing OMFP (100 µM), SDS22:PP1:I3 (160 nM), p97 (160 nM) and p37 (480 nM). A reaction containing only OMFP (100 µM) and apo-PP1 (160 nM) served as a control (green). To account for a low background hydrolysis, OMFP-only curves were subtracted from all curves. Excitation wavelength was set at 475 nm, and emission wavelength at 515 nm. Δp37, p37 was omitted. **c)** Fluorometric measurements tracking the dephosphorylation of OMFP over time with reactions containing OMFP (100 µM), SDS22:PP1:I3 (160 nM), p97 (160 nM) and p37 (480 nM) and indicated concentrations of PP1^{H66K}. A reaction containing only OMFP and apo-PP1 (160 nM, green) served as a control. To account for a low background hydrolysis, OMFP-only curves were subtracted from all curves. Excitation wavelength was set at 475 nm, and emission wavelength at 515 nm. ΔSPI, SDS22:PP1:I3 was omitted. Δp37, p37 was omitted.

To overcome the challenge of observing PP1 activity in the presence of SDS22 and I3, the inactive PP1 mutant PP1^{H66K} was used as “sponge” to bind dissociated SDS22 and I3 and prevent re-binding of the active PP1. Full reactions contained p97, p37, SPI and varying concentrations of PP1^{H66K}. A control lacking SPI showed a low background OMFP dephosphorylation due to low residual activity of PP1^{H66K}. This residual dephosphorylation of OMFP served as a baseline reference for the PP1 activity observed in the full reactions. Of note, the addition of increasing concentrations of PP1^{H66K} resulted in an increase of OMF fluorescence (**Figure 2.19c**). The increase in fluorescence signifies that more OMFP was dephosphorylated with increasing availability of the inactive sponge PP1^{H66K}, which served to capture dissociated SDS22 and I3 after SPI disassembly. Hence, the dephosphorylation of OMFP upon SPI disassembly in the presence of the SDS22 and I3 sponge PP1^{H66K} demonstrates that PP1 is active after its release from the SPI complex, mediated by p97:p37.

2.4.2 PP1 dephosphorylates an endogenous substrate after SPI disassembly

PP1 was shown to dephosphorylate the synthetic substrate OMFP, which requires no additional substrate specifying subunits (**Figure 2.19**). In order to investigate if PP1 forms an active holoenzyme complex post SPI disassembly, which is proficient in substrate dephosphorylation, dephosphorylation assays were conducted using the substrate specifier GADD34 and the endogenous PP1 substrate phosphorylated eIF2α (eIF2α-P), which in cells regulate the integrated stress response.

For the use in biochemical assays, a truncated version of GADD34, attached to maltose-binding protein (MBP) through a poly-asparagine linker was produced in *E. coli*. The MBP tag served as a solubility tag for the protein fragment, which gains most of its structure only after binding to PP1. The truncated GADD34$^{513\text{-}636}$ contained the regions necessary for PP1 binding, as well as G-actin (globular actin) binding, which was shown to be necessary for recruitment and dephosphorylation of eIF2α-P (Chen et al., 2015). The ability to bind both PP1 and G-actin makes GADD34$^{513\text{-}636}$ a proficient substrate specifier for eIF2α.

As a first step towards exploring eIF2α-P dephosphorylation by PP1 after SPI disassembly, the association of MBP-GADD34$^{513\text{-}636}$ and PP1 was explored. An indirect detection of PP1 binding was employed by making use of the FRET-based assay designed to monitor the dissociation of I3$^{\text{TAMRA}}$ from PP1$^{\text{Clover}}$. I3 and GADD34 both share the RVXF-like PP1 interaction motif, which excludes simultaneous interaction with PP1. For FRET-based assay analysis, GADD34 was used instead of NIPP1 as an alternative holoenzyme subunit. Upon incubation of SPI and GADD34 with p97:p37, I3 and SDS22 dissociate and GADD34 associates with PP1. SDS22 is able to re-associate in the presence of GADD34. The FRET labels on I3 and PP1 allow the tracking of I3 dissociation as it is displaced by GADD34 (**Figure 2.20a**).

FRET time-course measurements were conducted with full reactions containing optimal concentrations of p97, p37 and SDS22:PP1$^{\text{Clover}}$:I3$^{\text{TAMRA}}$ over a time course of 30 min. Experimental data show that the full reaction results in a decrease of FRET signal over time (**Figure 2.20b**). This decrease signifies an equilibrium between I3 dissociation and re-binding to PP1 during SPI disassembly. Adding the control protein, which contained only MBP and the linker region produced no further net dissociation of I3, indicating that MBP alone was not able to displace I3. Upon addition of MBP-GADD34$^{513\text{-}636}$, further ~40 % decrease in FRET signal was observed. The loss of

FRET signal shows that I3 was displaced from PP1 upon addition of MBP-GADD34$^{513-636}$, indicating that GADD34 and PP1 can form a holoenzyme after SPI disassembly.

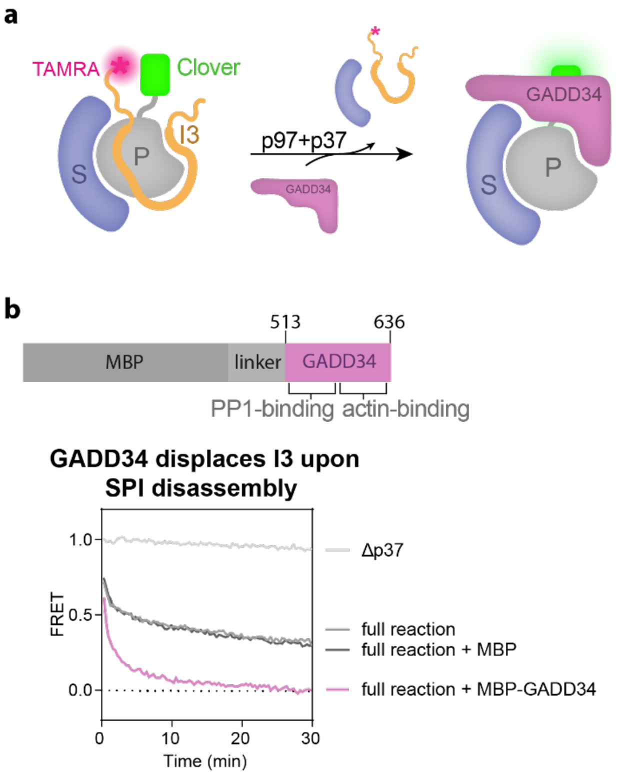

Figure 2.20: MBP-GADD34$^{513-636}$ displaces I3 from PP1 after disassembly by p97:p37. a) Schematic illustration of a subunit exchange from the SPI complex to PP1 bound by GADD34 and SDS22, facilitated by p97:p37. FRET labels are on I3 (TAMRA) and PP1 (Clover) **b)** FRET time course measurements of SPI disassembly reactions, monitoring the dissociation of I3 from PP1 in the absence or presence of MBP-GADD34$^{513-636}$, MBP, or no added potential binding partner. Full reactions contained p97 (160 nM) p37 (480 µnM), SDS22:PP1^{Clover}:I3^{TAMRA} (160 nM), and ATP (2 mM). MBP-GADD34$^{513-636}$ or MBP (240 nM) were added as indicated. Shown are the representative normalized ratios of acceptor and donor fluorescence of 3 independent experiments. Δp37, p37 was omitted. Also shown is an illustration of the GADD34 version used in this assay. Truncated GADD34$^{513-636}$ is attached to MBP.

To elucidate whether the PP1:GADD34 holoenzyme complex can dephosphorylate eIF2α-P after SPI disassembly, protein dephosphorylation assays were established, with subsequent detection via coomassie-stained Phos-tag gels. The assay included a PP1 subunit exchange step, where the SPI complex is disassembled by p97:p37. This is followed by PP1 association with the alternative interaction partners GADD34 and G-actin, building a trimeric complex capable of eIF2α-P dephosphorylation (**Figure 2.21a**). For the eIF2α-P dephosphorylation assay, MBP-GADD34$^{513-636}$ as well as eIF2α$^{2-187}$-P were employed. eIF2α$^{2-187}$ contains all regions necessary to serve as a substrate for PP1:GADD34 (Yan et al., 2021). N-terminally SUMO-tagged eIF2α$^{2-187}$ was generated in *E. coli*. After purification, during which the SUMO-tag was cleaved off, eIF2α$^{2-187}$ was phosphorylated by incubation with GST-PERK and ATP. To remove PERK after the reaction, a reverse GST-purification was performed, yielding pure phosphorylated eIF2α$^{2-187}$ to be used in eIF2α-P dephosphorylation assays.

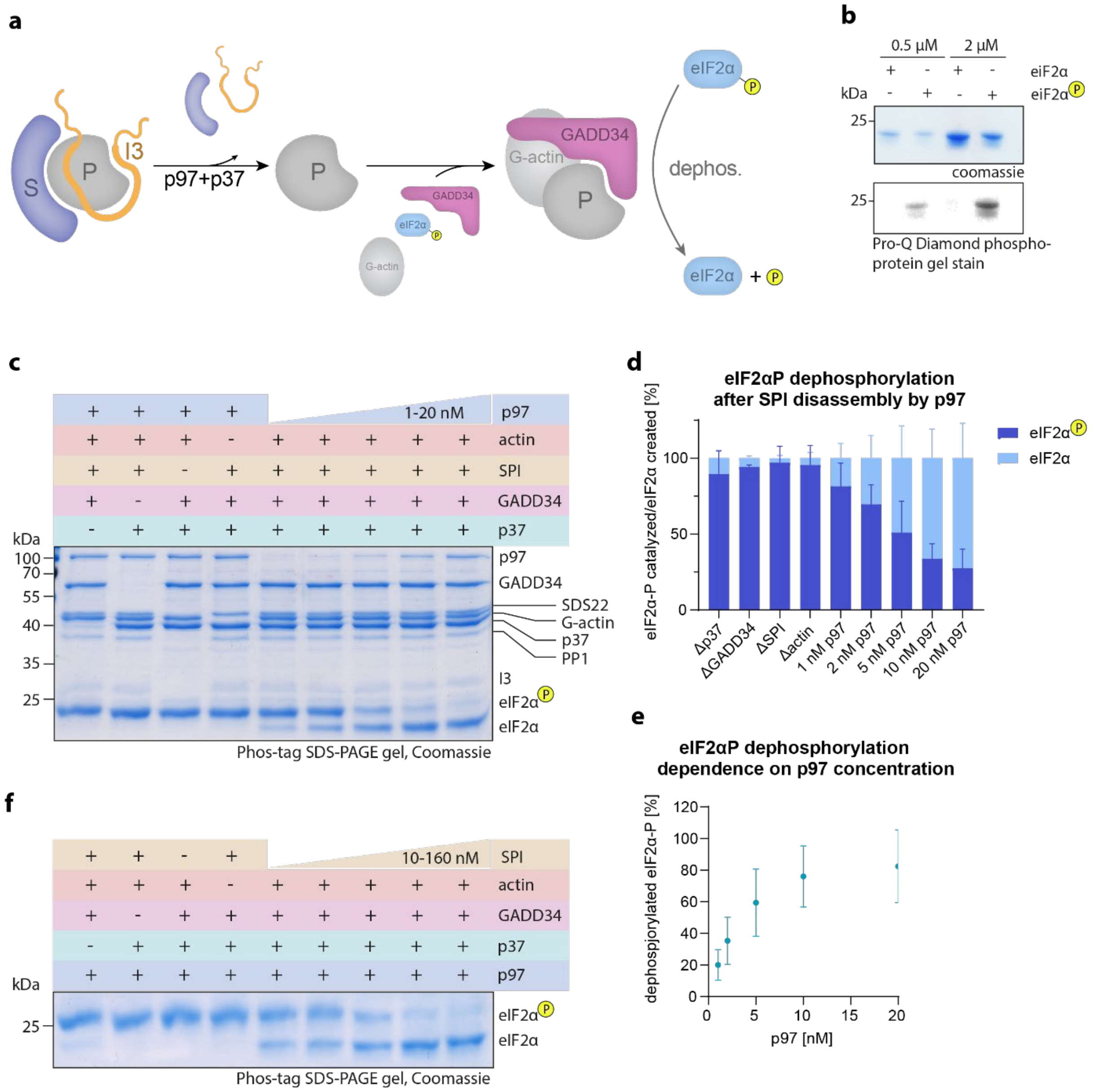

Figure 2.21: PP1 dephosphorylates an endogenous substrate *in vitro* after SPI disassembly, dependent on p97 activity. a) Schematic illustration of the SPI disassembly reaction followed by a PP1 subunit exchange and dephosphorylation of phosphorylated eIF2α-P through the newly built PP1:GADD34:G-actin complex. **b)** Coomassie and Pro-Q Diamond phospho-protein gel stained images of recombinantly expressed and purified eIF2α before and after phosphorylation by GST-PERK, with subsequent reverse GST-affinity purification. Loaded were two different concentrations (0.5 µM, 2 µM) of either eIF2α or phosphorylated eIF2α (eIF2α-P). **c)** Coomassie stained Phos-tag SDS-PAGE gel of an eIF2α-P dephosphorylation experiment. Reactions contained SDS22:PP1:I3 (160 nM), p97 (1, 2, 5, 10, or 20 nM, controls contained 20 nM), p37 (480 nM), MBP-GADD34$^{513-636}$ (400 nM), G-actin (400 nM), eIF2α-P (2 µM), and ATP (2 mM), as indicated. All samples were incubated at 30 °C for 10 min. Reactions were stopped by adding SDS-PAGE loading buffer. **d)** Quantification of three independent eIF2α-P dephosphorylation experiments represented in d). Percentages of eIF2α-P and eIF2α present at the end of the reaction for each experiment were normalized to the ΔGADD34 sample, with eIF2α-P + eIF2α = 100%. Shown are means and standard deviations of the absolute values (n = 3), subjected to fraction of a whole analysis. **e)** Data from e) presented as percentages of dephosphorylated eIF2α-P, dependent on p97 concentration. **f)** Coomassie stained Phos-tag SDS-PAGE gel of an eIF2α-P dephosphorylation experiment with varying concentrations of SPI. Reactions contained SDS22:PP1:I3 (10, 20, 40, 80, 160 nM, controls contained 160 nM), p97 (20 nM), p37 (480 nM), MBP-GADD34$^{513-636}$ (400 nM), G-actin (400 nM), eIF2α-P (2 µM), and ATP (2 mM), as indicated. All samples were incubated at 30 °C for 10 min. Reactions were stopped by adding SDS-PAGE loading buffer.

For quality analysis following eIF2α$^{2-187}$ phosphorylation, protein samples before and after the PERK reaction were loaded on SDS-PAGE gels. Gels were detected by coomassie or Pro-Q Diamond phospho-protein stain. Coomassie stained samples showed a band for both eIF2α and eIF2α-P at two different concentrations (**Figure 2.21b**). The bands confirmed, that protein was loaded in all samples. The gel detected with Pro-Q Diamond phospho-protein stain revealed bands for both concentrations of eIF2α-P, but not eIF2α. The phospho-protein stain selectively stains phosphorylated proteins in acrylamide gels, confirming that eIF2α-P was successfully phosphorylated.

eIF2α-P dephosphorylation experiments were performed with 160 nM SPI, 480 nM p37, 400 nM MBP-GADD34$^{513\text{-}636}$, 400 nM G-actin, 2 µM eIF2α-P, 2 mM ATP, and increasing concentrations of p97. All samples were incubated at 30 °C for 10 min. The coomassie-stained Phos-tag gel showed bands for all included proteins. Importantly, Phos-tag reagent interacts with phosphate groups attached to proteins. During the SDS-PAGE run of the Phos-tag gel, phosphorylated proteins were thus held back and migrated slower than the equivalent non-phosphorylated protein. Consequently, distinct bands for both eIF2α-P and eIF2α were visible, with decreasing amount of eIF2α-P and accumulation of eIF2α signifying the occurrence of eIF2α-P dephosphorylation through PP1:GADD34:G-actin (**Figure 2.21c**).

Phos-tag gel analysis showed that the sample lacking p37 did not lead to eIF2α-P dephosphorylation, which is expected since PP1 remains sequestered in the inactive SPI complex. Additionally, this result shows that GADD34, similar to NPP1, cannot displace SDS22 and I3 as binding partners of PP1. Likewise, a sample containing SPI and p97:p37 was not capable of eIF2α-P dephosphorylation in the absence of GADD34, confirming that the substrate specifier is strictly necessary for the process. An additional control omitting G-actin, confirmed that the trimeric complex of PP1:GADD34:G-actin is necessary for eIF2α-P dephosphorylation.

Notably, in the reactions containing all components, increasing eIF2α-P dephosphorylation was observed with increasing concentrations of p97 from 1-20 nM (**Figure 2.21c**). The increase in eIF2α-P dephosphorylation revealed that p97:p37 mediated disassembly of SPI was necessary for the formation of the PP1:GADD34:G-actin complex, which was subsequently capable of dephosphorylating eIF2α-P. Quantification of both eIF2α versions in all samples of three independent experiments demonstrated that p97-dependent eIF2α-P dephosphorylation after SPI disassembly occurred reproducibly (**Figure 2.21d**). Plotting the percentage of eIF2α dephosphorylation against the p97 concentration illustrates that the rate of dephosphorylation was dependent on the amount of p97, reaching saturating conditions between 10-20 nM p97 (**Figure 2.21e**). An experiment performed under identical conditions, but varying concentrations of SPI instead of p97, confirmed that eIF2α-P dephosphorylation was dependent on the concentration of PP1, as shown before for p97 (**Figure 2.21f**). In conclusion, the dephosphorylation of eIF2α-P after SPI disassembly required the presence of p37, GADD34 and G-actin. eIF2α-P dephosphorylation rates were dependent on concentrations of p97 and SPI. Consequently, p97-mediated disassembly of SPI *in vitro* leads to the formation of an active holoenzyme complex, capable of efficient dephosphorylation of an endogenous PP1 substrate.

3. Discussion

PP1 is a highly conserved protein that plays a crucial role in the majority of serine/threonine dephosphorylation events in eukaryotic cells. The PP1 catalytic subunit is highly active and indiscrimination, a trait it mitigates by forming holoenzymes with regulatory subunits, crucial for ensuring substrate specificity. However, the precise mechanisms governing PP1 activity, holoenzyme formation, and subunit exchange remain not fully understood. SDS22 and I3 form an inactive complex with PP1 (SPI) during PP1 biogenesis. p97 and its adapter protein p37 can mediate disassembly of this SPI complex, allowing the binding of another PP1 regulatory subunit. Further, it was shown that SPI formation contributes to PP1 stability and both SDS22 and I3 are necessary for proper PP1 function.

This study sought to understand the role of p97 and the SPI complex in PP1 activity and holoenzyme formation by elucidating details and kinetics of the SPI disassembly reaction, and uncovering the significance of the process in pathways beyond PP1 biogenesis. The work presented here establishes that SPI disassembly by p97:p37 releases active PP1 capable of dephosphorylating an endogenous substrate. SPI is efficiently targeted by p97, and for this both SDS22 and I3 are necessary. SDS22 and I3 dissociation and association occurs in a cooperative manner, suggesting novel functions for I3. Further, SDS22 and I3 can re-associate with PP1 after SPI disassembly by displacing other regulatory subunits. In contrast, SDS22 and I3 are not displaced from PP1 during incubation with a competitor, strictly requiring p97-catalysis for dissociation. These results suggest that cycles of SPI formation and disassembly control PP1 activity in cells, potentially regulating diverse cellular processes. The main findings of the thesis are summarized in **Figure 3.1**.

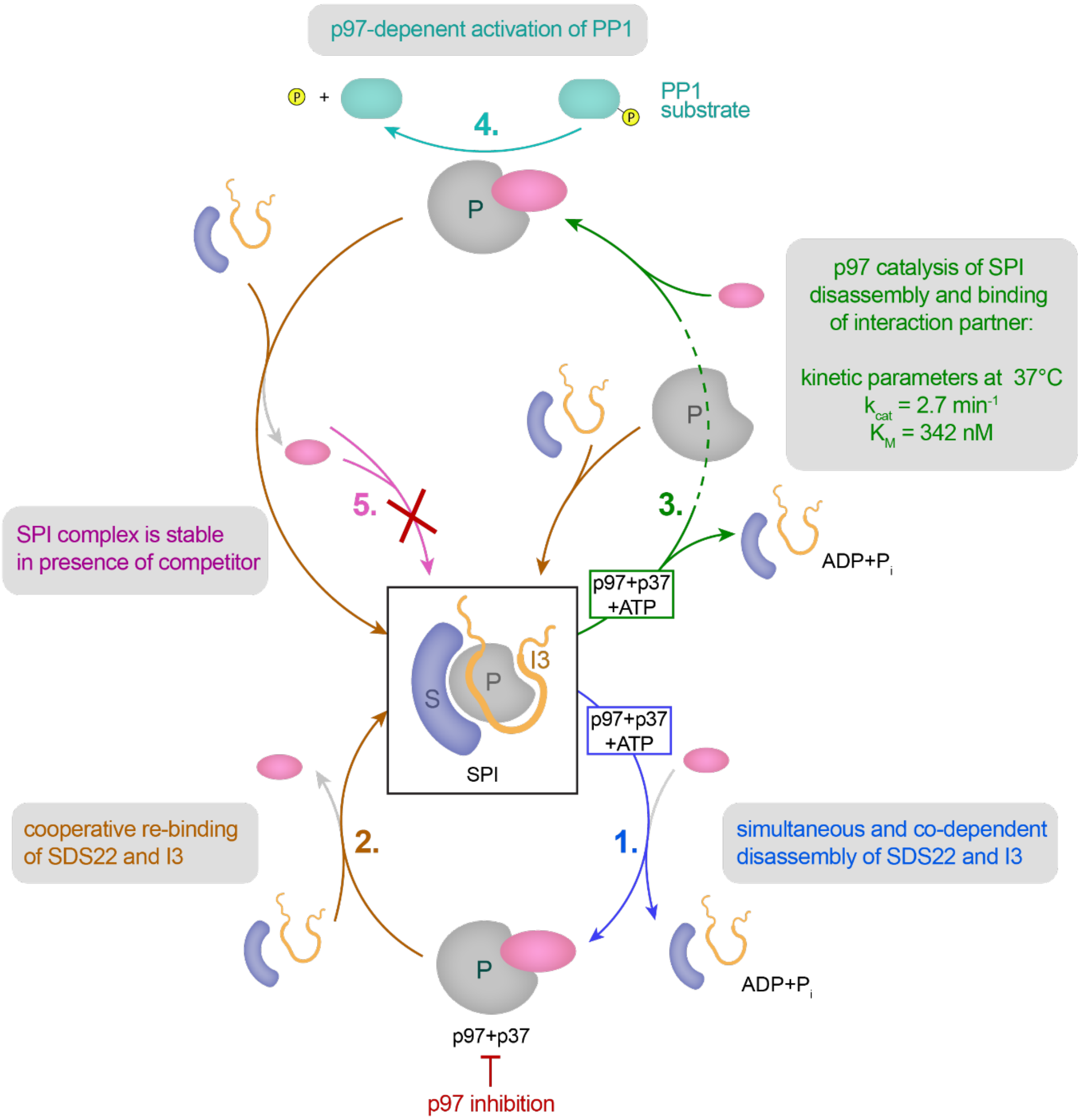

Figure 3.1: Summary of the main results achieved in this thesis. 1) During energy-dependent SPI disassembly by p97:p37, SDS22 and I3 dissociate simultaneously and both proteins are necessary for sufficient disassembly. **2)** Inhibition of p97 at the end of the disassembly reaction allows to monitor the re-association of SDS22 and I3 to PP1, in a cooperative manner. **3)** By monitoring the binding of an alternative PP1 interaction partner (pink) after SPI disassembly, kinetic parameters of the reaction at 37 °C were determined (k_{cat} = 2.7 min^{-1}, K_M = 324 nM). **4)** Binding of an activating subunit during SPI disassembly leads to dephosphorylation of an endogenous PP1 substrate. **5)** While SDS22 and I3 can displace alternative PP1 binding partners, SPI remains stable over long time periods in the presence of a competitor.

3.1 p97 efficiently targets SPI and poly-ubiquitinated substrates

p97-mediated unfolding of ubiquitinated substrates plays a critical role in cellular pathways such as protein quality control and degradation, membrane fusion, response to cellular stresses, and cell cycle regulation (van den Boom & Meyer, 2018; Wang et al., 2004; Woodman, 2003). For these processes to occur, ubiquitinated substrates are efficiently recognized and unfolded by p97 and its adapter proteins. In contrast, recognition of the SPI complex occurs directly, without the need for ubiquitination (Weith et al., 2018). To find out whether SPI is targeted efficiently by p97 and p37, kinetic parameters of the reaction were determined by detecting NIPP1 binding to PP1 after SPI disassembly via FRET. Using two input curves at low and high SPI concentrations and computational Bayesian approach-based analysis of progress curves, a K_M of 342 *÷ 1.37 nM and a k_{cat} of 2.70 *÷ 1.25 min^{-1} were determined for NIPP1 binding after SPI disassembly as 37 °C (**Figure 2.6b**). These parameters show a tight substrate binding with an average of 2.7 SPI complexes disassembled per p97 per minute. At 30 °C the same measurements yielded a K_M of 114 *÷ 1.31, and a k_{cat} of 0.97 min^{-1} *÷ 1.17, highlighting that the reaction still efficiently took place at a lower temperature (**Figure 2.6a**). Titration experiments with p97 and SPI showed that the maximal reaction speed was reached at equimolar concentrations of p97 and SPI indicating that one SPI molecule is processed by p97 at a time (**Figure 2.4**). This means that the kinetic parameters were determined under multiple turnover conditions. A limitation of the assay is the indirect detection of SPI disassembly through NIPP1 binding. SPI double-labeled FRET substrates could not be used, due to the FRET detection limit. NIPP1 binds with a slight delay after dissociation of SDS22 and I3, so that it can be assumed that SPI disassembly actually occurs more quickly (**Figure 2.11c**).

Notably, the K_M of SPI disassembly by p97:p37 was lower compared with poly-ubiquitinated substrates disassembled by Cdc48 and Ufd1:Npl4, indicating more efficient targeting of SPI. Michaelis-Menten analysis of unfolding of a fluorescently tagged substrate carrying four ubiquitin moieties (Ub_4) yielded a K_M of ~410 nM under multiple turnover conditions at 37 °C, slightly higher than for the SPI disassembly reaction (Williams et al., 2023). Further, a substrate that was attached to only two ubiquitin moieties (Ub_2), as well as a poly-ubiquitinated substrate carrying several branched ubiquitin chains, were determined to be processed by p97 with a K_M of 4.1 µM (Williams et al., 2023) or 4.4 µM (Olszewski et al., 2019), respectively, which is more than an order of magnitude higher than SPI targeting determined in this study. Ufd1:Npl4 is known to coordinate with accessory adapters, potentially increasing the targeting efficiency in cells. Titration experiments with p37 showed that a maximal reaction speed was reached at p37 concentrations exceeding p97, suggesting a relatively high dissociation constant (**Figure 2.9**). This could suggest that similar cofactors might also exist for SPI disassembly by p97:p37, however additional accessory adapters have not been identified thus far. Values for the turnover number k_{cat} were not determined in the studies monitoring poly-ubiquitinates substrates, however the comparatively low K_Ms of the SPI disassembly reaction signify that the half maximal speed of the reaction was achieved at lower protein concentrations compared to ubiquitinated substrates, highlighting efficient targeting of the SPI complex by p97 and p37.

3.2 Interplay of SDS22 and I3 in SPI disassembly

The interaction and dissociation of regulatory proteins like SDS22 and I3 significantly influence PP1 activity. Detailed knowledge of these mechanisms can provide insights into how PP1 function is modulated, which is crucial for understanding cellular regulation. SDS22 and I3 have overlapping functions in PP1 regulation with both proteins inhibiting PP1 and contributing to its stability in a chaperone-like manner (Cheng & Chen, 2015; Choy et al., 2019; Dinischiotu et al., 1997; Garcia-Gimeno et al., 2003). During SPI disassembly, I3 is the direct substrate of p97-mediated unfolding (Weith et al., 2018). SDS22 binds to PP1, but the exact mechanism of its disassembly remains unclear. In this study, high resolution FRET-based assays showed that even though I3 and SDS22 have overlapping functions, both proteins are needed for efficient disassembly of the SPI complex. Further, it was found that, SDS22 dissociation is in fact linked to I3 dissociation, and not facilitated by a third PP1-interacting protein.

3.2.1 SDS22 and I3 are both essential for efficient SPI disassembly

SDS22 binds specifically to PP1 that has lost a metal ion, suggesting a primarily stabilizing function (Choy et al., 2019). However, SDS22 has also been shown to inhibit PP1 in vivo and in vitro (Dinischiotu et al., 1997; Pedelini et al., 2007). Similarly, I3 occludes the active site of PP1, providing a clear and direct inhibitory effect, but also contributes to PP1 stability in cells (Cheng & Chen, 2015; Srivastava et al., 2023). Further, both proteins have been shown to be important for PP1 activity during chromosome segregation, suggesting also a shared activating function (Eiteneuer et al., 2014). With these numerous overlapping functions, it is unclear why both SDS22 and I3 are necessary for PP1 regulation.

Deploying dimeric PP1 complexes, SDS22:PP1 (SP) or PP1:I3 (PI), for FRET-based disassembly assays showed that SP cannot be recognized and disassembled by p97:p37 without the presence of I3 (**Figure 2.12a**). In fact, no change in FRET signal could be observed for SP disassembly alone. To address this further, individually expressed I3 was incubated with SP before the reaction. However, incubation with I3 lead to only a small decrease in FRET, indicating minimal SDS22 disassembly compared to the full co-purified SPI complex. Correspondingly, the PI complex lacking SDS22 also showed diminished disassembly efficiency, which improved by over 50 % upon adding purified SDS22, although not to the full extent of the SPI complex (**Figure 2.12b**). This suggests that SDS22 aids in SPI disassembly. Overall, rescue experiments confirmed that both SDS22 and I3 are necessary for efficient SPI disassembly in vitro, indicating that the full SPI complex is the relevant substrate of p97. Further, it was demonstrated that I3 and SDS22 directly contribute to dissociation of the other component from PP1. Limitations of these assays are that other cellular factors, which were not present in the *in vitro* reaction, might contribute to effective SPI complex formation or disassembly.

I3's disordered nature, which requires PP1 binding for proper folding, might explain that the SP complex could not be efficiently disassembled even in the presence of I3. Purification of I3 alone requires the presence of 1 % Triton X-100, which might interfere with proper complex formation. Another possibility is that SPI complex assembly in cells is dependent on certain co-factors, for example dictating the order of I3 and SDS22 binding or regulating assembly and disassembly through post-translational modifications. Factors of that sort have not yet been identified. Moreover, it has been demonstrated that deleting I3 results in a delayed dissociation of SDS22 from PP1 in cells (Weith et al., 2018). The results presented here confirm this finding and show that this effect is due to absence of I3 in the SPI complex. Results showing simultaneous dissociation of SDS22 and I3 further illustrate the coordination of both interaction partners in SPI disassembly (**Figure 2.11 d, e**). Recent studies have demonstrated that SDS22 directly interacts with the N-terminal domain of p97 when complexed with PP1 and I3, indicating that SDS22 is involved in SPI binding to p97 (van den Boom et al., 2023). Contribution to targeting of SPI to p97:p37 could explain the increased PI disassembly observed after addition of purified SDS22. The findings that I3 dissociation from PP1 is greatly increased by the presence of SDS22, and SDS22 dissociation is directly dependent on I3, confirm essential and separate roles of both proteins in SPI disassembly, highlighting the significance of both proteins in the process. Additional distinct roles of both proteins in PP1 regulation may be identified in the future.

3.2.2 SDS22 dissociation is linked to I3 dissociation from PP1

The interaction dynamics between SDS22, I3, and PP1 involve complex structural and binding considerations. SDS22 binds to PP1 at a unique site, lacking the common RVXF binding motif. Conversely, with the RVXF binding pocket, both I3 and NIPP1 share at least one overlapping binding site (O'Connell et al., 2012; Zhang et al., 2008). SDS22 and I3 form a complex with PP1, but a direct interaction could not be shown, since relevant residues of I3 are not resolved in any available structures (Choy et al., 2024; Srivastava et al., 2023; van den Boom et al., 2023). An interesting feature of the SPI structure is that the M1 metal ion is missing from the PP1 active site. It has been shown before that SDS22 binds metal-deficient PP1 with a low off-rate, and further does not associate with PP1 in metal-rich buffer when both PP1 ion binding sites are occupied (Choy et al., 2019). The process of SDS22 dissociation from PP1 during SPI disassembly is elusive. Potential mechanisms include: 1) displacement of SDS22 through the competition of a third PP1-binding protein with overlapping PP1 interaction sites, 2) SDS22 dissociation caused by the loss of a direct interaction between I3 and SDS22, or 3) loss of interaction between PP1 and SDS22 through a conformational change in PP1, like the loading of the second metal ion in the active site.

The role of a third PP1-interacting protein in SPI disassembly was analyzed by comparing disassembly patterns in the presence and absence of NIPP1. In control experiments without NIPP1, $^{\text{TAMRA}}$SDS22 disassembled from PP1$^{\text{Clover}}$. Increasing NIPP1 concentrations led to further dissociation of $^{\text{TAMRA}}$SDS22, suggesting a concentration-dependent effect (**Figure 2.9f**). A similar effect was also observed for the I3 labeled substrate (**Figure 2.9e**). However, this increased dissociation could either indicate a direct displacement of SDS22 by NIPP1 through a non-RVXF binding site or that I3 dissociation prompts SDS22 to dissociate from PP1 and re-binding of SDS22 and I3 is prevented by NIPP1 binding. To further test these hypotheses, SPI disassembly reactions with FRET labels on PP1 and one of the three interaction partners, respectively, were compared. It was shown that SDS22 and I3 dissociate simultaneously, while the alternative PP1 binding partner, NIPP1, associates with PP1 with a slight delay (**Figure 2.11d**). This was verified through a p97 titration experiment, where varying p97 concentrations were used while keeping other assay conditions constant. The resulting overlain graphs for SDS22:PP1$^{\text{Clover}}$:I3$^{\text{TAMRA}}$ and $^{\text{TAMRA}}$SDS22:PP1$^{\text{Clover}}$:I3 showed the same decrease in FRET over time, confirming simultaneous disassembly of both components (**Figure 2.11e**). Simultaneous SDS22 and I3 dissociation and binding of NIPP1 with a delay indicates that SDS22 is not displaced by NIPP1, but dissociates in response to I3 dissociation.

It is evident that I3, but not a third binding partner, is essential for the SDS22-PP1 dissociation. These results are underlined by cellular I3 depletion experiments, which lead to delayed SDS22 dissociation from PP1 (Weith et al., 2018). However, despite extensive analysis, the precise mechanism by which SDS22 disassembles remains unresolved. A possibility is that SDS22 dissociation from PP1 could be facilitated by a direct interaction with I3. In that case, unfolding and dissociation of I3 would weaken the SDS22 interaction with the SPI complex, potentially leading to SDS22 dissociation. The N- and C-termini of I3 were likely too flexible to be resolved in any PP1:I3-containing crystal structures. However, the orientation of the most C-terminally resolved residues of I3 bound to SDS22:PP1 suggest that residues between C62 and H126 could make direct contact with SDS22, but this was thus far not confirmed (Choy et al., 2024).

Another hypothesis is that loading of the second PP1 active site metal results in SDS22 dissociation by reducing binding affinity. The metal-loading process could occur passively, once I3 is pulled off PP1 and the I3 CCC motif no longer binds in front of the PP1 active site. A second possibility is that I3 assists in the loading and stabilization of the metal ion. Though this process is still under investigation, a similar mechanism has been proposed for PTPA in Protein phosphatase 2A (PP2A) regulation (Guo et al., 2014). Both SDS22 and I3 inhibit and stabilize PP1. It is therefore unclear why both proteins are needed for PP1 regulation. If evidence could demonstrate that either a direct interaction between I3 and SDS22 or I3-assisted metal-loading leads to SDS22 dissociation, it could be proposed that the role of I3 within the SPI complex is to facilitate SDS22 dissociation in conjunction with p97:p37, a process that otherwise proceeds inefficiently. Continued research into these mechanisms is essential for a comprehensive understanding of I3 and SDS22 function in PP1 regulation.

3.2.3 A possible role for I3 in PP1 metal ion binding

It has been shown that SDS22 preferentially binds metal-deficient PP1 and does not bind PP1 in metal-rich buffer (Choy et al., 2019). Consequently, PP1 has to undergo metal ion loss, before efficient association with SDS22 can occur. The process and the involvement of other proteins in this ion removal remain unclear. It has been discussed before that I3 may be involved in metal ion loading during SPI disassembly (**Chapter**

3.2.2). Data presented here suggest that I3 is not only linked to SDS22 dissociation, but also helps in the association of SDS22 to PP1, possibly through metal ion ejection from PP1.

In the binding experiments by Choy et al., PP1 purified from bacterial cells contained two manganese ions in its active site. To demonstrate that re-association of SDS22 after SPI disassembly also occurs in metal-rich buffer, p97 inhibition experiments were repeated in the presence of 1 mM $MnCl_2$. Contrary to the binding assays, SDS22 was able to associate with PP1 under p97 inhibition, even in metal-rich buffer (**Figure 2.16**). A possibility is that the components present during SPI disassembly, but not the binding assays, aid in SDS22 binding. As I3 was shown to be essential for SDS22 dissociation from PP1 (**Figure 2.12**a), it could be imagined that I3 is also involved in proper SDS22 binding. To test this hypothesis, an SDS22 association experiment was conducted with $PP1^{Clover}$ and individually purified ^{TAMRA}SDS22 and I3. Incubation of PP1 and SDS22 lead to SP complex formation. Addition of increasing concentrations of I3, along with SDS22, caused a concentration dependent increase of SDS22 association (**Figure 2.13**). Notably, I3 and SDS22 together lead to more SDS22 association than SDS22 alone, highlighting that I3 directly aided SDS22 association to PP1. Further, experiments performed with a co-purified NIPP1:PP1 complex and individually purified SDS22 and I3 confirmed these results. The addition of SDS22 and I3 together resulted in increased and concentration-dependent NIPP1:PP1 dissociation, relative to I3 and SDS22 alone (**Figure 2.18**). These experimental results suggest that I3 and SDS22 both displace NIPP1 from PP1 cooperatively.

The results discussed above indicate a cooperative binding of SDS22 and I3 to PP1. Different studies showed that both yeast-3-hybrid and pulldown experiments, expressing Sds22 and Ypi1/I3 alongside Glc7/PP1 led to more effective interactions than expressing Sds22 or I3 alone, confirming that SPI formation is also cooperative in cells (Lesage et al., 2007; Pedelini et al., 2007). However, this could have been due to a reduced disassembly rate of the dimeric complexes expressed in the yeast cells, because p97 cannot take them apart efficiently, as shown before (**Figure 2.12**). The experiments presented here show that I3 directly increases SDS22:PP1 formation *in vitro*. Direct interactions between SDS22 and I3 could influence the structure or conformation of one of the proteins, but this has not been shown. Since I3 binds in front of the active site metals in PP1, it is conceivable that I3 can mediate the dissociation of a metal ion. The PP1-interacting protein, Inhibitor-2 (I2), binds to PP1 through a kinked α-helix that engages with the hydrophobic and acidic grooves of PP1. This interaction leads to the removal of one of the PP1 active site metals and obstructs the active site, thereby inhibiting PP1 (Hurley et al., 2007). Even though I3 and I2 are not structurally related, they both bind in front of the PP1 active site through different modes of interaction. It is therefore possible that I3 has a similar function in PP1 metal ejection as I2. Combined with results presented here that suggest a role for I3 in SDS22 dissociation from PP1, I3 can be hypothesized to regulate the SDS22-PP1 interaction, possibly through metal ion exchange in the PP1 active site. Monitoring metal association directly with methods like total reflection X-ray fluorescence (TXRF), as well as mutagenesis experiments to explore direct I3 and SDS22 binding could present conclusive evidence about the mechanism of SDS22 dissociation.

3.3 SPI re-forms after initial disassembly

It has previously been shown that SPI forms a complex during PP1 biogenesis (Weith et al., 2018). This complex contributes both to PP1 inhibition and stability, and can be disassembled by p97:p37, freeing PP1 to form holophosphatases. One of the major questions concerning the role of the SPI complex is, whether the complex only forms after PP1 biogenesis, or if SDS22 and I3 re-bind PP1 after initial disassembly. Reassembly of the SPI complex would suggest that SPI formation is a reoccurring step in a cycle where the PP1 catalytic subunit is inhibited and freed to form interactions with other holoenzyme subunits. In that case, PP1 regulation by SDS22 and I3 binding and p97-mediated disassembly might regulate numerous PP1-related pathways beyond PP1 maturation. This study shows that SDS22 and I3 shift back to a PP1-bound state after p97 inhibition.

CB-5083 is a competitive inhibitor of p97, binding to the nucleotide binding sites and preventing ATP binding and hydrolysis (Tang et al., 2019). Upon addition of CB-5083 to SPI disassembly reactions, also containing NIPP1, both SDS22 and I3 re-associated with PP1 as shown in FRET-based and CoIP experiments (**Figure 2.14b, Figure 2.15**). Consistent with that, NIPP1 dissociated from PP1 during p97 inhibition, in a similar time frame (**Figure 2.14c**). Association of SDS22 and I3, as well as concurrent dissociation of NIPP1 shows that SDS22 and I3 displace NIPP1 when p97 is inhibited. SPI reassembly also occurred in the presence of 1 mM $MnCl_2$, even though SDS22 alone was shown to only bind PP1 in metal-poor conditions. Similar effects on SDS22 and I3 re-association with PP1 could be observed using GADD34 instead of NIPP1 as a third interaction partner (**Figure 2.14 d, e**). Inhibition of p97 after SPI disassembly lead to re-association of SDS22 and I3 in the presence of GADD34, suggesting that competitive SPI reassembly is a general mechanism, potentially occurring with numerous PP1-interacting proteins.

Further indications for the occurrence of SPI reassembly after initial disassembly were found in this study. Titrating increasing concentrations of NIPP1 to the SPI disassembly reaction resulted in increasing dissociation of I3 and SDS22 (**Figure 2.9 e, f**). Since it was established that NIPP1 associates after I3 and SDS22 dissociation, the observed increase in dissociation is not due to NIPP1 competition (**Figure 2.11d**). Instead, these results indicate that NIPP1 in high concentrations can partially prevent SPI reassembly. Moreover, FRET assay substrates containing TEV-protease cleavage sites between SDS22 or I3 and their respective FRET label allowed the determination of FRET levels corresponding to full SPI disassembly. Performing experiments for I3 and SDS22 individually revealed that at the end of the SPI disassembly reaction ~5-10 % I3 and ~20-25 % SDS22 is bound to PP1 (**Figure 2.10 a, b**). This could suggest that during SPI disassembly, constant I3 and SDS22 re-association occurs. A possibility is that a certain amount of SPI remains unprocessed and SDS22 and I3 remain bound, however having shown SPI reassembly occurs under p97 inhibition indicates SDS22 and I3 re-associate rapidly, so that some amount is constantly bound. Since I3 is the direct substrate of p97, it is unfolded and translocated through the p97 pore, while SDS22 is not unfolded. This additional step in I3 processing could account for the lower amount of I3-PP1 binding observed in TEV experiments, as I3 may simply be slower to re-associate than SDS22. Thirdly, PP1 activity experiments performed with the small molecule OMFP lead to no activity for the full SPI disassembly reaction (**Figure 2.19b**). However, the supplementation with an SDS22- and I3-binding “sponge” protein resulted in concentration-dependent PP1 activity, indicating that SDS22 and I3 constantly re-associated with PP1 in the absence of a sponge, keeping PP1 inhibited (**Figure 2.19c**).

Reassembly of SPI and NIPP1 dissociation occurs more slowly than p97-mediated disassembly and full SPI reassembly could not be observed. The slower reassembly rate can be attributed to the passive nature of the process, which relies on the mass action and affinities of the three proteins to PP1, in contrast to the catalyzed SPI disassembly reaction. However, it is also possible that *in vitro* reassembly is slower, because certain co-factors for SPI formation are missing. This hypothesis is supported by the observation that the dimeric SP and PI complexes are not effectively disassembled by p97 *in vitro*, even upon addition of individually expressed I3 and SDS22, respectively (**Figure 2.12 a, b**). A third hypothesis is that repeated SPI disassembly causes SDS22, PP1, or I3 to lose structural integrity, which are therefore not able to bind back to their interaction partners. Further evidence for how SPI disassembly is regulated in cells would help clarify the mechanisms underlying these interactions and the stability of the complex *in vivo*.

Unpublished analytical gel filtration experiments of lysates treated with CB-5083 and the translation inhibitor cycloheximide, conducted by Johannes van den Boom, confirmed that PP1, which was not newly synthesized, shifted into the SDS22- and I3-bound form after p97 inhibition. The reassembly occurred within 2 hours in cells and most of the free SDS22 and I3 was found in the SI complex after treatments. These findings highlight that SPI reassembly occurs efficiently in cells after PP1 biogenesis, supporting the hypothesis that SPI formation plays a role in the later stages of the PP1 life cycle, post-maturation.

3.4 Cycles of SDS22 and I3 binding and p97-mediated disassembly regulate PP1 activity

SPI reassembles upon p97-inhibition after initial disassembly by p97:p37 in vitro and in cells, indicating that the formation of the SPI complex has functions outside of PP1 biogenesis (**Chapter 3.3**). A remaining question is the purpose of PP1 regulation beyond maturation by SDS22 and I3 binding, and p97-mediated SPI disassembly. A possibility is that SPI passively serves to store active PP1 in an inhibitory complex to prevent indiscriminate phosphorylation after PP1 dissociation from other regulatory subunits. Another hypothesis is that SDS22 and I3 binding to PP1 and simultaneous displacement of another PP1 subunit contributes to PP1 holoenzyme subunit exchange. The results detailed here suggest that PP1 undergoes cycles of SPI formation and disassembly. Thus, constant SPI disassembly through p97:p37 and SPI reassembly results in the formation of a steady-state where a fraction of PP1 is available to form different holoenzymes and another fraction is kept inactive and stable in the SPI complex.

SDS22 and I3 re-associate with PP1 during SPI disassembly, displacing other PP1 interacting subunits in the process (**Figure 2.14**). The process of displacement was recreated with a pre-formed, co-expressed NIPP1:PP1 (NP) complex and separately purified SDS22 and I3. Incubation of NP with increasing concentration of SDS22 and I3 lead to concentration-dependent NP dissociation, confirming NIPP1 displacement by SDS22 and I3 (**Figure 2.18**). A limitation of this assay is the absence of a positive NP dissociation control, which would demonstrate the condition of complete NP disassembly. In the absence of this control, it can be concluded that SDS22 and I3 displace NIPP1, however full NP dissociation could not be observed. In contrast to NP, the SPI complex remained stable in the presence of high concentrations of NIPP1 over a time course of 18 hours (**Figure 2.17**). Neither SDS22 nor I3 dissociated significantly during the long incubation with NIPP1, highlighting that SPI disassembly is strictly dependent on p97-activity. Similarly, but in a shorter time frame, it was observed that GADD34 does not rapidly displace SDS22 and I3 from PP1. In samples of eIF2α-P dephosphorylation assays during SPI disassembly, which lacked p37, no dephosphorylation was observed, even though both SPI and GADD34 and other necessary components were present (**Figure 2.21c**). Further, the Δp37 control in a I3 displacement assay showed that GADD34 did not passively displace I3 during 30 minutes of incubation with SPI (**Figure 2.20b**). These results demonstrate that p97 activity was strictly necessary for PP1-GADD34 binding.

Previous studies defined SDS22 and I3 as maturation factors, which transiently bind during PP1 biogenesis. This study presents evidence that SDS22 and I3 together with p97:p37 regulate PP1 activity beyond PP1 biogenesis. Combined results suggest that PP1 holoenzyme formation and substrate dephosphorylation are regulated by cycles of p97-mediated SPI disassembly, and mass action directed re-association of SDS22 and I3 (**Figure 3.2**). Specifically, it was shown that SDS22 and I3 readily take apart other holoenzyme complexes, displacing regulatory PP1 subunits. In contrast, for SPI disassembly, p97-activity was strictly necessary, as SPI is stable in the presence of PP1-binding competitors. Further, SPI reassembles during p97 inhibition, which indicates that a steady-state of free PP1, available for holoenzyme formation, and inhibited PP1 complexed in SPI is maintained by SDS22 and I3 binding and p97-dependent SPI disassembly, even in later stages of the PP1 life cycle. This allows the hypothesis that SPI is a thermodynamic sink that sequesters inactive PP1 in cells until active PP1 is liberated by p97-mediated SPI disassembly.

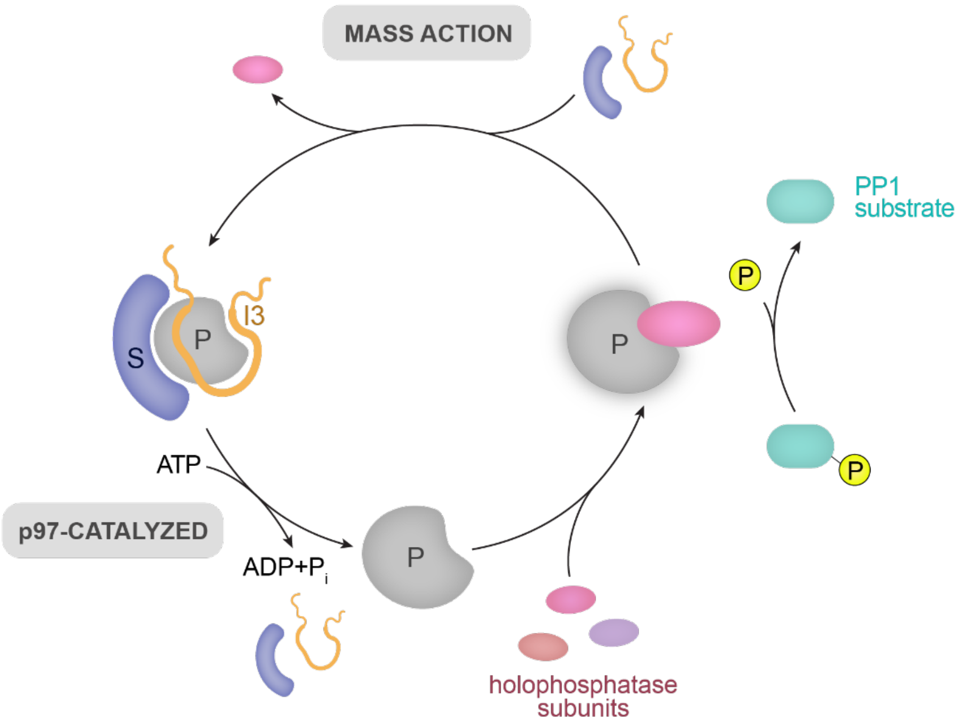

Figure 3.2: Cycles of SDS22 and I3 binding and displacement of PP1 regulatory subunits by mass action, as well as p97-catalyzed disassembly regulate PP1 holophosphatase formation, which can result in PP1 substrate dephosphorylation.

The consequences of unselective PP1-mediated dephosphorylation in cells could include loss of signal transduction during stress (Garcia et al., 2003; Hicks et al., 2023), impairment of cell division (Lesage et al., 2011; Rebelo et al., 2015; Saurin, 2018), and loss of DNA repair control (Kuntziger et al., 2011). Therefore, regulation of PP1 activity in cells is paramount. Consequently, the purpose of SPI and p97 in PP1 regulation might be the prevention of unnecessary dephosphorylation through cycles of SPI formation, while allowing controlled release of PP1 through p97. In that scenario SDS22 and I3 constantly displace activating PP1 subunits, keeping PP1 trapped and inhibited. The SPI complex is highly stable and thus the cell would be kept safe from promiscuous dephosphorylation by PP1. Release of active PP1 is dependent on p97 activity, but how exactly the release of PP1 would be controlled in cells is unclear. The SEP domain adapter p37 shows low expression levels in U2OS cells, compared to other p97 adapters. Another SEP domain adapter, UBXN2A, can also mediate SPI disassembly *in vitro*. Therefore, availability of p37 and UBXN2A might contribute to the control of available PP1 for holoenzyme formation in cells.

An open question in the PP1 field is, how holoenzyme exchange is controlled. While it has been shown that PP1 interactors like GADD34 are subject to transcriptional control, and affinities as well as post-translational modifications of the proteins are important for complex formation and stability, it is unknown whether subunit exchange is an active process. The observation that SDS22 and I3 can displace other PP1 regulatory subunits allows the hypothesis that cycles of PP1 regulation through SDS22 and p97 not only recycle active PP1 between holophosphatases but possibly also accelerate subunit dissociation, resulting in a dynamic exchange of subunits. The holoenzyme exchange function of p97:p37 and SDS22 and I3 can only be hypothesized as current data do not show that this happens in cells, or that SDS22 and I3 accelerate holoenzyme dissociation. Providing evidence for this hypothesis could be challenging as it requires the reconstitution of a complex system involving multiple proteins. Further data that show enhanced rates of subunit exchange are needed to establish a specific directionality in the assembly of PP1 holoenzymes, achieved through p97 and SPI.

3.5 p97-mediated SPI disassembly results in the formation of an active PP1 holoenzyme

In order for SPI formation and p97-mediated disassembly cycles to serve as a regulatory mechanism in cells, it is necessary for PP1 to become active following SPI disassembly. This study establishes that PP1 is active after SPI disassembly *in vitro*, without the need of additional co-factors or substrate specifiers. Further, PP1 readily dephosphorylated the endogenous substrate eIF2α-P, together with its substrate specifier GADD34 after SPI disassembly, dependent of p97 activity.

Observing PP1 activity after SPI disassembly poses the challenge that SDS22 and I3 have been shown to constantly re-associate with PP1 after initial SPI disassembly (**Chapter 3.3**). These results were confirmed by the observation that PP1 was not able to dephosphorylate the synthetic substrate OMFP during SPI disassembly, due to re-association of SDS22 and I3 (**Figure 2.19b**). However, additional incubation of the SPI disassembly reaction with the inactive mutant PP1^{H66K} resulted in concentration-dependent dephosphorylation of OMFP to fluorescent OMF (**Figure 2.19c**). The inactive PP1 served as a “sponge” to bind dissociated SDS22 and I3 and thus prevent reassembly. The subsequent dephosphorylation of OMFP shows that PP1 is active after release from SPI. To explore whether PP1 released from SPI can form a holoenzyme complex capable of dephosphorylation, eIF2α-P dephosphorylation assays were performed in the presence of SPI, p97:p37, substrate specifier GADD34 and co-factor G-actin. eIF2α-P dephosphorylation during SPI disassembly was observed with a concentration dependent effect of p97, as well as SPI (**Figure 2.21**). The formation of a holoenzyme complex between PP1 and GADD34 was confirmed through an I3 displacement assay with GADD34 (**Figure 2.20**). Overall it could be shown that PP1 is active after its release from the SPI complex, mediated by p97:p37. Further, PP1 can form an active holoenzyme after SPI disassembly with GADD34 and eIF2α-P dephosphorylation rates were dependent on concentrations of p97 and SPI.

The reconstitution with purified components showed release of active PP1 after SPI disassembly by p97. It is still to be tested whether the same process also occurs in cells. Unpublished data show that PP1 purified from cell lysates was less active against OMFP when the cells were previously treated with p97 inhibitor CB-5083 (Johannes van den Boom), consistent with the results that p97 inhibition leads to sequestration of PP1 in the SPI complex (**Figure 2.14b**). Together the results indicate that p97-catalyzed SPI disassembly directly leads to PP1 activity in cells. In the OMFP assays performed without the addition of the SDS22- and I3-binding “sponge”, PP1 activity was not observed (**Figure 2.19b**). However, FRET SPI disassembly experiments lacking both PP1^{H66K}, as well as any other PP1-binding subunits, showed that both SDS22 and I3 partially dissociate from PP1 (**Figure 2.9 e, f**). Even though net dissociation was shown, the OMFP experiments show that PP1 is not active directly after SPI disassembly and before I3 and SDS22 can re-associate and inhibit PP1 once more. A hypothesis is that a conformational change in PP1 is needed, before full activity can be observed. Since SDS22-bound PP1 lacks a metal ion necessary for PP1 activity, this conformational change might be a metal loading step (Choy et al., 2019).

As it was shown that PP1 activity after SPI disassembly also occurs in cells, it would be interesting to link p97-catalyzed release of active PP1 to a cellular pathway. Since the dephosphorylation of eIF2α-P after SPI disassembly was shown here, it could be hypothesized that p97 contributes to regulation of the integrated stress response. It has previously been shown that p97 regulates the ISR by facilitating the degradation of the GADD34 paralogue CReP (Hulsmann et al., 2018). Additionally, unpublished data indicate that SPI can serve as a reservoir for the formation of an active PP1:GADD34 complex. Specifically, it was shown that upon p97-inhibition in cells, GADD34 bound to PP1 increases by ~20 % (Sandra Koska). Since eIF2α-P is the cellular substrate of GADD34:PP1, these results indicate that p97-mediated SPI disassembly could participate in the control of the amount of dephosphorylated eIF2a in cells, however the consequences of SPI disassembly for the ISR remains to be fully elucidated. Other PP1-related pathways may be regulated in the same way and the significance of the convergence of these two evolutionarily conserved regulators, PP1 and p97, will be a relevant subject of future studies.

This study provided valuable insights into the regulation of PP1 activity and holoenzyme formation. By elucidating key aspects of this PP1 regulatory mechanism, the groundwork for future research to further confirm and expand upon these findings was laid. Subsequent studies could focus on elaborating the results in a cellular context and investigating additional factors involved in SPI formation and disassembly. Moreover, connecting the detailed mechanism of PP1 regulation to distinct cellular pathways will be crucial for understanding its broader biological significance.

4. Methods

4.1 Molecular Cloning

4.1.1 Polymerase Chain Reaction (PCR)

For Gibson cloning and site-directed mutagenesis, standard PCR conditions for amplification with Phusion High Fidelity Polymerase (NEB) were used. Reactions contained 1x Phusion HF or GC buffer (NEB), 10 mM dNTPs (NEB), 10 µM forward primer, 10 µM reverse primer, 10 ng template DNA, 0.02 U/µL Phusion DNA polymerase, and optionally 2.5-10 % DMSO in a reaction volume of 50 µL. Reactions were incubated in a thermocycler as described in **Table 1**.

Table 1: PCR program used for generation of Gibson fragments and site-directed mutagenesis.

Cycle step	Temperature (°C)	Time	Cycle repetition
Initial Denaturation	98	30 s	1x
Denaturation	98	10 s	5x
Annealing	T_a – 5	30 s	
Extension	72	1 min/kb	
Denaturation	98	10 s	25x
Annealing	T_a	30 s	
Extension	72	1 min/kb	
Final Extension	72	10 min	1x

Annealing temperatures (T_a) were dependent on the primer sequences, and elongation times were calculated based on the length of the PCR product in kb. If necessary a temperature gradient from T_a – 5 to 72 °C was used in the annealing step to ensure successful amplification.

4.1.2 Gibson assembly

The fluorescent protein tag Clover, Sortase sites (LPETGGG, GGG), TEV cleavage sites and full protein sequences were inserted into appropriate vectors using Gibson Primers containing the respective overlapping sequences. For Gibson cloning both vector and insert were amplified by PCR as described before. PCR products were subjected to electrophoresis on 1 % agarose gels in TAE buffer (40 mM Tris pH 8.4, 1 mM Na_2EDTA, 20 mM acetic acid) and subsequently purified from the gel. The amplified vector backbones were incubated with 1 µL of DpnI (NEB) for 1 hour at 37 °C. Following this, 40 fmol of both the insert and vector backbone were subjected to incubation with the Gibson assembly master mix (75 mM Tris-HCl pH 7.5, 3.75 % PEG-8000, 7.5 mM $MgCl_2$, 0.15 mM dNTPs, 7.5 mM DTT, 0.75 mM NAD, 0.004 U/µL T5 Exonuclease, 0.025 U/µL Phusion Polymerase, 4 U/µL Taq DNA Ligase) for 1 hour at 50 °C.

4.1.3 Site-directed mutagenesis

$PP1^{H66K}$ was generated using site-directed mutagenesis following the identical PCR protocol mentioned earlier with primers containing the respective base changes, followed by ligation through incubation with T4 Polynucleotide Kinase (NEB), DpnI (NEB), and T4 DNA Ligase (NEB) in T4 DNA ligase buffer containing 10 mM ATP (NEB) for 1 hour at room temperature.

4.1.4 DNA transformation, isolation, and sequencing

For selection, plasmids were transformed into *Escherichia coli* XL-1 blue competent cells (Agilent). For this, 4 µL ligated DNA was incubated with 50 µL of cell suspension for 10 min, followed by a 45 s heat-shock at 42 °C. After incubating samples for 1 min on ice, cells were recovered in 800 µL SOC medium at 37 °C for 45 min, and streaked onto LB-agar plates containing 50 µg/mL Ampicillin or 25 µg/mL Kanamycin. To isolate plasmid DNA from bacteria, a bacterial clone was inoculated into LB medium supplemented with the relevant antibiotic. The cells were cultured by shaking at 150 rpm and 37 °C overnight. Subsequently, DNA extraction was performed using the NucleoSpin Plasmid Mini kit (Macherey-Nagel). Plasmid DNA sequences were verified using GATC Sanger sequencing services.

4.1.5 Plasmids, Peptides, and Viruses

The following plasmids, peptides and viruses were created, purchased, or received as gifts for this study as specified in **Table 2**.

Table 2: Plasmids, peptides and virus V2-generations used in this study.

Database entry	Name	Source/created by
Plasmids		
2172	pFL-His-PP1-Clover, GGG-SDS22	Anja Kück
2173	pFL-His-PP1-Clover, NIPP1-LPETGGG	Anja Kück
1926	pST44-$PP1^{H66K}$	Anja Kück
1709	pFL-I3-TEVc-His-LPETGGG	Anja Kück
1710	pFL-PP1-Clover, GGG-TEVc-SDS22	Anja Kück

1700	pFL-GGG-His-SDS22	Anja Kück
1699	pST44-PP1-Clover	Anja Kück
1698	pET16b-PP1	Anja Kück
1696	pMal-His-LPETGGG	Anja Kück
1695	pET30b-7M-SortaseA	Addgene #51141
1592	pFL-PP1-Clover, GGG-SDS22	Anja Kück
1589	pMalE-Gadd34$^{513\text{-}636}$-His-LPETGGG	Anja Kück
1574	pET16b-NIPP1-LPETGGG	Anja Kück
1556	pFL-PP1-Clover, SDS22	Anja Kück
1593	pFL-Inhibitor3-His-LPETGGG	Johannes van den Boom
1522	pMal-GADD34$^{513\text{-}636}$-His	David Ron
1523	peCFP-NIPP1	Addgene Plasmid #44226
1524	pCAGGS-Raichu-Rho_CR (Clover)	Addgene Plasmid #40258
1560	pET16b-His-NIPP1	Anja Kück
1736	pFL-His-PP1-Clover	Anja Kück
1944/UK168	pGEX-1-1-PerkKD	David Ron
1945/UK2731	pSUMO3-1-heIF2a$^{2\text{-}187}$	David Ron
1943	pET28a His-SENP2 catalytic domain	Addgene Plasmid #16357
1287	pFL-I3 untagged	Jonas Seiler
Peptides		
	GGGWSHPQFEKK(TAMRA)-NH$_2$	CASLO ApS
	(TAMRA)-AWSHPQFEKLPETGGG	CASLO ApS
Viruses (V2)		
	V2 His-PP1-Clover, GGG-SDS22	Anja Kück
	V2 His-PP1-Clover, NIPP1-LPETGGG	Emilia Chlosta
	V2 I3-TEVc-His-LPETGGG	Anja Kück
	V2 PP1-Clover, GGG-TEVc-SDS22	Anja Kück
	V2 GGG-His-SDS22	Anja Kück
	V2 PP1-Clover, GGG-SDS22	Anja Kück
	V2 PP1-Clover, SDS22	Anja Kück
	V2 Inhibitor3-His-LPETGGG	Anja Kück
	V2 I3 untagged	Johannes van den Boom
	V2 His-PP1-Clover, GGG-SDS22	Emilia Chlosta

pFL-PP1-Clover and related plasmids were created from the plasmid pCAGGS-Raichu-Rho-CR (Lam et al., 2012). pET16b-NIPP1-LPETGGG was created using the NIPP1 sequence from peCFP-NIPP1 (Trinkle-Mulcahy et al., 2001). We received pMAL-hGADD34$^{513\text{-}636}$, pGEX-4T-1-PERK KD, and pSUMO3-1-heIF2α$^{2\text{-}187}$ as kind gifts from D. Ron (Crespillo-Casado et al., 2018; Harding et al., 1999; Yan et al., 2021). The pET30b-7M-SortaseA plasmid and pET28a-SENP2 (catalytic domain) were kind gifts from H. Ploegh (Addgene #51141) and Guy Salvesen (Addgene plasmid #16357).

4.2 Protein expression

4.2.1 Expression in *E. coli* BL21

Recombinant proteins produced in *Escherichia coli* BL21(DE3) competent cells (Agilent) were transformed into the chemically competent cells via heat shock. Plasmid DNA was incubated with 100 µL cell suspension for 10 min. The heat shock was performed at 42 °C for 45 s, after which the samples were incubated on ice for 1 min. Cells were recovered in 800 µL SOC media for 45 min, streaked onto LB-agar plates containing the appropriate antibiotic and grown overnight at 37 °C. Overnight starter cultures were cultivated in 20 mL LB-medium supplemented with 25 µg/mL kanamycin or 50 µg/mL ampicillin, depending on the respective antibiotic resistance. Cells were grown in 1 L LB medium, also containing the respective antibiotic, at 37 °C until the OD_{600} reached 0.6-0-8. Protein expression was induced by adding 0.5 mM IPTG, and cultures were incubated at 18 °C for another 18-20 hours. Cells were then harvested at 4 °C and 4000 rpm for 15 min, and the pellet was resuspended in lysis buffer (50 mM HEPES pH 8, 150 mM KCl, 5 mM $MgCl_2$, 5% glycerol, 25 mM imidazole).

4.2.2 Expression in *E. coli* ArcticExpress

For recombinant proteins produced in *Escherichia coli* ArcticExpress(DE3) competent cells (Agilent) a previously established protocol was used (Kelker et al., 2009). Plasmid DNA was transformed into 100 µL cell suspension. The transformation protocol was the same as described before, except the heat shock was performed at 42 °C for exactly 20 seconds. Overnight starter cultures were cultivated in 20 mL LB medium supplemented with 20 µg/mL gentamycin, 50 µg/mL ampicillin, and 1 mM $MnCl_2$. Cells were grown in 1 L LB medium, containing 1 mM $MnCl_2$ and no antibiotics, at 30 °C for approximately 3 hours or until the OD_{600} reached ~0.6. Subsequently, the temperature was lowered to 10 °C using an ice bath, and expression was induced with 0.2 mM IPTG for 20-24 hours. Following induction and expression, cells were harvested at 4 °C and 4000 rpm for 15 min, and the pellet was resuspended in an equal volume of fresh LB medium, containing 1 mM $MnCl_2$ and 200 µg/mL chloramphenicol to suppress ribosome activity. The suspension was gently agitated (~40 rpm) for 2 hours at 10 °C to facilitate *in vivo* folding of PP1 in the presence of chaperonins. Finally, cell pellets were resuspended in PP1 lysis buffer (50 mM HEPES pH 8.0, 5 mM imidazole, 700 mM KCl, 1 mM $MnCl_2$, 0.1% (v/v) Triton X-100, 1 mM PMSF).

4.2.3 Expression in insect cells (Baculovirus system)

For transformation of pFL vectors into DH10EMBacY competent cells (Thermo) with subsequent bacmid isolation, approximately 2 µg of plasmid DNA was added to 50 µL of cells, followed by a 1-hour incubation on ice. The *E. Coli* strain harbors a baculovirus shuttle vector (bacmid) capable of undergoing recombination with a donor plasmid. Heat shock was performed at 42 °C for 35-45 seconds, and cells were then recovered in 1000 µL LB for around 6 hours at 110 rpm. The cells were plated on LB-agar plates containing 50 µg/ml kanamycin, 10 µg/ml tetracycline, 7 µg/ml gentamycin, 40 µg/ml IPTG, and 100 µg/ml X-Gal. Positive integration of the pFL vector into the bacmid was verified through blue/white selection. After approximately 48 hours of growth to observe white colonies, three clones per construct were streaked on a fresh plate to ensure their purity. Subsequently, 3x 2 mL LB containing all three antibiotics were inoculated with three different clones for bacmid preparation.

Bacmid DNA isolation was performed with the NucleoSpin Plasmid Mini kit until before the step of loading the DNA on the columns. Instead the bacmid DNA in the supernatant was precipitated with isopropanol. Isopropanol (700 µl) was added to the DNA, gently mixed, and left overnight at -20 °C. After a 15-minute centrifugation at maximum speed, a visible pellet was obtained. The pellet was washed with 70% ethanol, spun down, and ethanol was removed under the hood. After allowing for evaporation, the DNA was resuspended in 40 µl of sterile H_2O.

For transfection of Sf9 cells, derived from the parental Spodoptera frugiperda cell line (Thermo), with bacmid DNA for virus production, bacmid DNA from three clones was used to account for potential expression variations. Sf9 cell density, maintained at 27 °C, 115 rpm in SF900 III medium, was determined using a Neubauer chamber. Following cell counting, 1×10^6 cells per clone were taken from the liquid stock and added to a 6-well plate, along with 1 mL media per well. For each clone, 200 µL SF900 III medium with 20 µL Bacmid DNA and 5 µL FuGene HD transfection reagent was incubated for 20 minutes at room temperature and then added to the wells. The incubation of the plate proceeded for 4 days at 27 °C. Transfection was verified under a fluorescence microscope, with GFP serving as the control gene. Only expression-positive clones were further processed.

For the first virus amplification (V0) 8×10^6 cells were extracted per clone from the liquid stock. 10 cm dishes were prepared, each filled with 8 ml SF900 III medium. 8×10^6 Sf9 cells were added to each dish. The complete content (supernatant + cells) from each well of the 6-well plate was transferred to one of the 10 cm dishes. The dishes were incubated for 4 days at 27 °C. Checking under the microscope for GFP expression, the best expressing clone was centrifuged at 1000×g for 5 minutes. The supernatant was transferred to a new sterile 15 ml tube and 5-10 % inactivated FCS was added. The V0 virus generation, was stored at 4 °C.

The V1 amplification was similar to the V0 generation, except that a 50 mL volume was used containing 5×10^7 cells. The Sf9 cells were then infected with the V0 virus supernatant. V0 virus was added to the media at a 1:50 ratio through a 0.2 µm sterile filter. The 50 mL flask was incubated for 4 days at 27 °C and 115 rpm. Expression was examined under a fluorescence microscope before harvesting the V1. The contents of the flasks were centrifuged at 1000×g for 5 minutes. The supernatant was then transferred to a new sterile 50 mL tube and 5-10 % inactivated FCS was added. The V1 virus generation was stored at 4 °C.

The third virus amplification step in Sf9 cells was conducted freshly, and the V2 virus generation was not stored but used entirely for infection. V2 amplification was carried out in a 50 mL volume, following the same protocol as V1. Large scale protein expression was performed in High Five Cells (BTI-TN-5B1-4), a clonal isolate derived from the parental Trichoplusia ni cell line (Thermo). A 5000 mL flask was used to prepare 1000-1400 mL of 1×10^6 High Five cells per mL media. The complete V2 virus (50 mL) was added to the High Five cell suspension. The expression took place at 27 °C and 115 rpm over 4 days. Cells were then centrifuged at 3500 rpm for 15 minutes. The pellets were re-suspended in lysis buffer (50 mM HEPES pH 8, 150 mM KCl, 5 mM $MgCl_2$, 5% glycerol, 25 mM imidazole) and stored at -80 °C.

4.3 Protein purification

His-**NIPP1** versions**,** His-**Sortase A**, and His-**SENP2** were generated in *Escherichia coli* BL21 (DE3). The cleared bacterial lysates were applied to a HisTrap FF 5 mL (Cytiva) column using p97 buffer (50 mM HEPES pH 8, 150 mM KCl, 5 mM $MgCl_2$, 5 % glycerol) containing 25 mM imidazole. Elution was performed with p97 buffer supplemented with 300 mM imidazole, followed by gel filtration on a Superdex 16/600 pg 75 (Cytiva) column in p97 buffer with 1 mM DTT.

His-**I3** was expressed in insect cells and purified in the same manner as described above, with buffers containing 200 mM NaCl, 20 mM Tris pH 7.9 and 1% Triton X-100 His-p97. His wash buffers also included 15 mM imidazole and 0.5 mM TCEP and the protein was eluted with wash buffer complemented with 300 mM imidazole. I3 gel filtration buffer contained 1 mM DTT and gel filtration was performed using a Superdex 16/600 pg 200 (Cytiva), due to the intrinsically disordered structure of I3.

His-**PP1γ** and His-**PP1γ$^{\mathbf{H66K}}$** were produced in *Escherichia coli* ArcticExpress DE3 (Agilent). Cleared lysate was loaded onto a HisTrap 5 mL column and eluted with 10 mL of PP1 elution buffer (50 mM HEPES pH 8.0, 250 mM imidazole, 700 mM KCl, and 1 mM $MnCl_2$) directly onto a gel filtration column Superdex 26/600 pg 200 (Cytiva). Elution from the gel filtration column was with PP1 gel filtration buffer (50 mM HEPES pH 8.0, 500 mM KCl, 1 mM $MnCl_2$, 0.5 mM TCEP). Proteins were concentrated to ~30 µM.

The **PP1γ:I3 (PI)** complex and the **SDS22:PP1γ:I3 (SPI)** complex and all variants thereof (including Clover, sortase sequences and TEV cleavage sites) were generated in insect cells using two viruses and a dual-expression cassette system. For this, I3 was tagged with a 6 histidine-tag (His). The PI and SPI complexes were purified from cleared High Five cell lysates on a HisTrap FF (Cytiva) column in p97 buffer with 25 mM imidazole and eluted directly onto a HiTrap Q HP anion exchange column 5 mL (Cytiva) with p97 buffer containing 300 mM imidazole. After elution from the anion exchange column through p97 buffer containing 1 M KCl, proteins were further purified by gel filtration on a Superdex 16/600 pg 200 (Cytiva) in p97 buffer with 1 mM DTT.

His-**PP1γ:SDS22 (SP)** and His-**PP1γ:NIPP1 (NP)** complexes were expressed and purified with respective labels as described before for the SPI complexes. Same buffers and procedures were used, but the anion exchange chromatography was omitted from the protocol. Of note, PP1 was tagged with a 6-histidine tag in both complexes.

G-SDS22 was generated in insect cells. His-tagged G-SDS22 was purified from cleared High Five cell lysates in SDS22 lysis buffer (50 mM HEPES pH 8.0, 0.5 M KCl, 5 mM imidazole, 0.1% Triton X-100). Lysate was loaded on a HisTrap FF (Cytiva) column in lysis buffer containing 5 mM imidazole and no Triton. Column was washed until a base line was reached, followed by a wash with 8 % SDS22 elution buffer

(50 mM HEPES pH 8.0, 0.5 M KCl, 250 mM imidazole). Subsequently, the column underwent an overnight incubation with SDS22 wash buffer (50 mM HEPES pH 8.0, 0.5 M KCl), containing 1000 U of His-TEV-protease (Sigma-Aldrich) to eliminate the His-tag and expose an N-terminal glycine for sortase-labeling. The protein was then eluted using the wash buffer.

GST-PERK catalytic domain was produced in *Escherichia coli* BL21 DE3 (Agilent). The cleared lysate was applied to a GSTrap HP column (Cytiva) using GST-wash buffer (50 mM HEPES pH 7.5, 150 mM KCl, 1 mM DTT), and elution was carried out with GST-wash buffer supplemented with 20 mM glutathione.

eIF2α$^{2\text{-}187}$ N-terminally tagged with SUMO and His, was generated in *Escherichia coli* BL21 DE3 (Agilent). The cleared lysate was applied to a HisTrap FF column (Cytiva) using eIF2α wash buffer (50 mM HEPES pH 7.5, 500 mM KCl, 10 mM imidazole, 0.5 mM TCEP), and elution was performed with eIF2α wash buffer containing 300 mM imidazole. Subsequently, SUMO-tag cleavage using SENP2 protease was carried out overnight in a 15 mL volume with a protease concentration of 0.01 mg/mL at 4 °C. The protein was then eluted using the wash buffer.

His-**MBP-GADD34$^{513\text{-}636}$** and His-**MBP** (containing the same linker region also present in MBP-GADD34$^{513\text{-}636}$) were produced in *Escherichia coli* BL21 DE3 (Agilent), the cleared bacterial lysate underwent loading on a HisTrap FF column (Cytiva) in GADD34 lysis buffer (50 mM Tris pH 7.4, 500 mM NaCl, 20 mM imidazole, 0.5 mM TCEP). Elution was carried out using GADD34 lysis buffer supplemented with 300 mM imidazole, followed by MBP purification using an MBPTrap HP 5 mL column (Cytiva). For this step, proteins were loaded in GADD34 lysis buffer and eluted with the same buffer containing 10 mM maltose. Subsequent to MBP affinity purification, size exclusion chromatography was performed on a Superdex 26/600 pg 200 column (Cytiva). The protein eluted as both soluble aggregates and soluble protein, with the latter concentrated from the second peak for further use.

Actin from rabbit muscle (Sigma-Aldrich) was diluted to 1 mg/mL in G-buffer (5 mM Tris pH 8.0, 0.2 mM ATP, 0.5 mM DTT and 0.2 mM $CaCl_2$) for use in eIF2α-P dephosphorylation assay.

His-**p97, p37, SDS22:PP1:Inhibitor-3**-His (SPI) without FRET labels were used from lab stocks created by Johannes van-den-Boom.

All proteins were analyzed by SDS-PAGE using mPAGE Bis-Tris 4-20 % polyacrylamide gels (Millipore), Tris-MOPS-SDS running buffer (Genscript). Gels were run at 120 mA for 40 minutes and stained with InstantBlue Coomassie protein stain (Abcam). Proteins were concentrated, snap frozen in liquid nitrogen, and stored at −80 °C.

4.4 Protein labeling

The labeling of sortase site containing proteins with TAMRA (5(6)-Carboxy-tetramethylrhodamin) was carried out using a Ca^{2+}-independent Sortase A. Proteins containing the C-terminal sortase recognition motif (-LPETGGG; 50 µM) were incubated with TAMRA-conjugated Strep-tag peptide GGGWSHPQFEKK-TAMRA peptide (200 µM) and Sortase A (2.5 µM) in p97 buffer with 1 mM DTT at 30 °C for 2 hours. For proteins containing the N-terminal sortase recognition motif (GGG-), the TAMRA-conjugated Strep-tag peptide (TAMRA)-AWSHPQFEKLPETGGG was used instead. Caslo ApS synthesized and labeled the peptides. The Strep-tag in the TAMRA peptide was used for the purification of the labeled protein, by immobilizing it on a StrepTrap HP (Cytiva) column. After elution with p97 buffer containing 2.5 mM desthiobiotin, excess unincorporated peptide was removed through gel filtration using a Superdex 16/600 pg 200 (Cytiva) column or Superdex 16/600 pg 75 (Cytiva) column for NIPP1 and SDS22, in p97 buffer with 1 mM DTT.

4.5 In vitro eIF2α phosphorylation with PERK

For phosphorylation of eIF2α, 50 µM $eIF2\alpha^{2\text{-}187}$ and 100 nM GST-PERK catalytic domain were incubated at 37 °C for 2 hours in a total volume of 4 mL containing 100 mM KCl, 25 mM HEPES pH 7.5, 5 mM $MgCl_2$, 1 mM TCEP and 2.5 mM ATP. To remove GST-PERK, a reverse GST purification on a GSTrap HP column (Cytiva) was performed as described for GST-PERK.

4.6 Fluorescence spectra

Fluorescence was induced and monitored using a Varian Cary Eclipse spectrofluorometer (Thermo). The fluorescence emission spectrum of Clover as a fusion protein of PP1 in complex with SDS22 and I3 contained 80 nM $SDS22:PP1^{Clover}:I3$ complex. Clover fluorescence was excited at 506 ± 2.5 nm and fluorescence emission was detected between 480-580 nm. The TAMRA fluorescence spectrum of $NIPP1^{TAMRA}$ was recorded between 520-620 nm and TAMRA excitation was performed at 546 ± 2.5 nm. Spectra were recorded at 30 °C in a total volume of 60 µL.

Fluorescence emission spectra recorded of the full SPI disassembly reaction and the same reaction omitting p37 contained 80 nM SDS22:PP1^{Clover}:I3, 80 nM NIPP1^{TAMRA}, 35 nM p97, 50 nM p37 2 mM and ATP (2 mM). Reactions were incubated at 30 °C for 30 min in a total volume of 60 µL. Excitation was performed at 475 ± 10 nm. Fluorescence emission was recorded between 500 and 620 nm. Data points were divided by the highest value to yield a normalized spectrum between 0 and 1.

4.7 FRET-based assays

All time course measurement samples (72 µl) were diluted in p97 buffer + 2 % BSA + 1 mM DTT and transferred to fluorescence cuvettes (Hellma) and heated to 30 °C. For kinetics, a baseline was recorded for 3–5 min before the reaction was started by the addition of ATP (2 mM). Samples were excited at a wavelength of 475 ± 10 nm. Donor emission was recorded at 518 nm and acceptor emission at 580 ± 2.5 nm. Data points were measured approximately every 19 seconds using an average time of 1 second. Reactions were recorded over indicated times. For data analysis, we normalized each trace's fluorescence intensity before addition of ATP (8 µl) to remove the dilution effect. The ratio of both emission intensities was calculated by dividing the acceptor intensity by the donor intensity. For NIPP1^{TAMRA} or SDS22-PP1^{Clover}-I3 titrations, only the donor or acceptor emissions were used for data analysis, respectively. Curves were normalized between the FRET signal before the addition of ATP and the lowest (dissociation/disassembly) or the highest plateau (association) at the end of the reaction in the dataset.

4.7.1 Initial conditions for SPI disassembly reaction with NIPP1^{TAMRA}

SPI disassembly initial conditions, as shown in Figure 2.3, were 80 nM SDS22:PP1^{Clover}:I3, 80 nM NIPP1^{TAMRA}, 35 nM p97, 50 nM p37, and 2 mM ATP, compared with the same reaction which excluded p37. ATP was added 3 min after the start of the recording. Reactions were recorded over a time course of 20 min.

4.7.2 Optimal conditions of the SPI disassembly reaction

For the SPI disassembly reaction under optimal conditions as determined in Figure 2.4, 160 nM SPI variant, 240 nM NIPP1 variant, MBP-GADD34$^{513-636}$, or MBP, 160 nM p97, 480 nM p37, and 2 mM ATP were added to reaction buffer (p97 buffer, 2 % BSA, 1 mM DTT). For titrations one component was added at different concentrations as indicated and reactions without p37 were used as a negative control. ATP was added approximately 3 min after the initial recording of a baseline. For fluorescence spectra analysis of the SPI reaction, same concentrations were used as for time course measurements. Reactions were incubated with ATP for indicated times. Fluorescence signals were divided by the highest data point to normalize spectra intensities between 0 and 1.

4.7.3 TEV experiments

Reactions containing SPI variants with a TEV cleavage site (TEVc) between the TAMRA fluorophore and the rest of the protein, 300 µM TEV-protease (TEV) was added after 30 minutes of disassembly. For reassembly, p97 inhibition was induced by adding 10 µM CB-5038 (Selleckchem) or DMSO as a control. Cuvettes were mixed by gently pipetting up and down. Data points collected while adding the inhibitor/DMSO were removed. In the experiment testing the effect of Mn^{2+} ions on the reassembly of SDS22, 1 mM $MnCl_2$ was added to the reaction buffer.

4.7.4 Association experiments

Association of $PP1^{Clover}$ and $SDS22^{TAMRA}$ was measured with 500 nM $PP1^{Clover}$ and different concentrations of $SDS22^{TAMRA}$ and I3 (500 nM, 750, 1000 nM), to achieve a 1:1, 1:1.5 or 1:2 ratio to $PP1^{Clover}$ as indicated. The $PP1^{Clover}$ and $SDS22^{TAMRA}$ only curve was recorded with 1000 nM $SDS22^{TAMRA}$.

4.7.5 Dissociation experiments

To observe the dissociation of the NIPP1–PP1 complex (NP) (1000 nM) was incubated with SDS22 and I3 at different ratios (500, 750 and 1000 nM), together and individually.

SDS22 and I3 dissociation experiments performed with 160 nM SDS22:$PP1^{Clover}$:$I3^{TAMRA}$ or ^{TAMRA}SDS22:$PP1^{Clover}$:I3 and 0-960 nM NIPP1 as a competitive binding partner for PP1, were incubated over 18 hours to follow fluorescence decay. As a control, a full SPI disassembly reaction containing 160 nM SDS22:$PP1^{Clover}$:$I3^{TAMRA}$, 240 nM NIPP1, 160 nM p97, 480 nM p37 and 2 mM ATP, as well as a control lacking p37, was recorded for the same time course.

4.7.6 SP and PI disassembly experiments

For experiments conducted with $PP1^{Clover}$:$I3^{TAMRA}$ (PI) (160 nM) or $^{TAMRA}SDS22$:$PP1^{Clover}$ (SP) (160 nM), reactions contained 160 nM p97, 480 nM p37, 240 nM NIPP1, and 2 mM ATP unless otherwise stated. 160 nM SDS22 was added to a reaction as indicated, to observe changes in PI dissociation.

4.8 Fluorometric OMFP dephosphorylation assay

3-O-Methylfluorescein Phosphate Bis-Cyclohexylammonium Salt (OMFP) (Novachemistry) was preserved as a 100 mM stock solution in DMSO with 100 mM H_2SO_4. The dephosphorylation of OMFP by PP1 was observed using a Varian Cary Eclipse spectrofluorometer (Thermo). Excitation of samples occurred at a wavelength of 485 ± 2.5 nm, and emission was recorded at 525 ± 2.5 nm. Data points were collected at approximately 19-second intervals, averaging over 1 second each. Reactions (120 µL) contained 100 µM OMFP, 160 nM SDS22:PP1:I3, 160 nM p97, 480 nM p37, and 2 mM ATP in p97 buffer wit 1 mM DTT unless otherwise stated. Initially, a baseline was established by recording 3-4 minutes of only OMFP. Subsequently, a master mix containing all additional components was introduced, and the reactions were monitored over a 60-minute time course. Given the low background hydrolysis of OMFP in our buffer, a reaction was documented using 100 µM OMFP in the buffer, and this trace was subtracted from all other recordings. As a positive control, apo-PP1 at a concentration of 160 nM was employed to verify OMFP reactivity with PP1. $PP1^{H66K}$ was titrated to the reactions in concentrations of 160, 240, or 480 nM. $PP1^{H66K}$ only control contained 480 nM $PP1^{H66K}$ in p97 buffer + 1 mM DTT.

4.9 eIF2a-P dephosphorylation assay and PhosTag gel analysis

Actin was pre-incubated with a 10x molar excess of latrunculin B (Sigma-Aldrich) for 1 hour on ice to ensure actin depolymerization. Reactions of 20 µL contained 480 nM p37, 160 nM SPI, 400 nM $MBP\text{-}GADD34^{513\text{-}636}$, 400 nM G-actin, 2000 nM eIF2α-P, 2 mM ATP and p97 (1, 2, 5, 10, 20 nM) in assay buffer (50 mM HEPES pH 8.0, 200 mM KCl, 0.02% Triton, 2 mM $MnCl_2$, 1 mM DTT). Control samples contained 20 nM p97. The reactions were started by adding ATP and then incubated at 30 °C for 10 minutes. To stop the reactions, 5 µL of 6x SDS-loading buffer (0.35 M Tris-HCl pH 6.8, 30 % glycerol, 10 % SDS, 9.3 % DTT, 0.02 % bromophenol blue) was added. Subsequently, the samples were examined using 12 % polyacrylamide gels containing 5 mM PhosTag AAL solution (Fujifilm) and 10 mM $MnCl_2$. The gel preparation followed the instructions provided by the supplier and was subjected to analysis through staining with InstantBlue Coomassie protein stain. For the experiment with varying concentrations of SPI, the same conditions were applied with reactions containing 10, 20, 40, 80, or 160 nM SPI and 20 nM p97. Control samples contained 160 nM SPI.

4.10 Quantification and statistical analysis

The determination of kinetic parameters using the FRET-based disassembly assay followed a previously described method (Choi et al., 2017). FRET curves were recorded and normalized as outlined above, and subsequently, these curves were further normalized to the substrate concentration employed in the assay. The data points used for analysis are depicted in the corresponding figures. For the determination of kinetic parameters, two curves with distinct enzyme and substrate concentrations were used for each temperature (**30 °C:** low conc.: 20 nM p97 and 40 nM $SP^{Clover}I3$, high conc.: 80 nM p97 and 1150 nM $SP^{Clover}I3$; **37 °C:** low conc.: 20 nM p97 and 60 nM $SP^{Clover}I3$, high conc.: 80 nM p97 and 1150 nM $SP^{Clover}I3$). These two respective curves served as input for the Bayesian approach-based analysis script (EKMCMC) using RStudio. The “combined_est” command was used to simultaneously determine both k_{cat} and K_M. The parameters for each temperature were set as follows (**30 °C parameters:** enz1=20, enz2=80, subs1=40, subs2=1150, MM=80, catal=1, tun=2.4, std=1, nrepeat=100000, jump=10, burning=0, catal_m=1, catal_v=10000, MM_m=1, MM_v=10000; **37 °C parameters:** enz1=20, enz2=80, subs1=60, subs2=1150, MM=300, catal=2.5, tun=2.4, std=5, nrepeat=100000, jump=10, burning=0, catal_m=1, catal_v=10000, MM_m=1, MM_v=10000). The output of these calculations consisted of 100,000 probable combinations of k_{cat} and K_M, represented as a 2D-kernel plot. Given the lognormal distribution of the output data, the geometric mean and geometric standard deviation were calculated for each parameter.

Image J software was used to determine gel band intensities of Coomassie stained PhosTag gels. Bands pertaining to eIF2α and eIF2α-P were subjected to the plot lanes analysis. Output integrals of three independent experiments were normalized to one ΔGADD34 sample, with eIF2α-P + eIF2α = 100 %, yielding percentages of eIF2α-P + eIF2α for each sample. Percentages of eIF2α-P and eIF2α present at the end of the reaction for each experiment were subjected to fraction of a whole analysis and standard deviations of the absolute values (n = 3) were calculated.

4.11 *In vitro* co-immunoprecipitations

SPI disassembly reactions with purified components and co-immunoprecipitation (CoIP) analysis were performed using 160 nM p97, 480 nM p37, 160 nM SDS22:PP1γ^{Clover}:I3, and 480 nM NIPP1^{TAMRA}. Proteins were incubated in p97 buffer supplemented with 1 mM DTT and 2 % BSA. Disassembly was initiated by addition of 2 mM ATP and incubation at 30 °C for indicated time points from 1-30 min. For experiments monitoring SPI reassembly, 0.5 U apyrase (NEB) or apyrase buffer as a control were added after 30 minutes. Reaction were incubated for further 10-60 min. At indicated time points, reactions were stopped by tenfold dilution in ice-cold p97 buffer containing 1 % Triton and 2 % BSA. For PP1γ CoIPs, samples were incubated with PP1γ antibody (Santa Cruz C-19, or goat IgG as control) and GammaBind G-Sepharose (Cytiva) for 1 hour at 4 °C. Beads were washed three times in p97 buffer containing 1 % Triton and eluted by boiling in SDS-loading buffer. Samples were analyzed by Western blotting and probed with indicated antibodies.

4.12 Immunoblotting

Protein bands were transferred to nitrocellulose membranes using a wet Western blotting system with Millipore mPAGE Transfer buffer supplemented with 10 % ethanol. The blotting process was conducted for 3 hours at 600 mA. Subsequently, the membranes were blocked using 5 % milk in TBS-T. Detection was carried out with the following antibodies. Western blot signals were visualized with secondary antibodies against the respective primary antibody species, carrying the HRP (horseradish peroxidase) reporter protein.

Table 3: Primary and secondary antibodies used for western blot signal detection.

Description	Species	Dilution	Source/created by
Primary antibodies			
polyclonal anti-NIPP1	rabbit	1:500	Sigma, no. HPA027452
polyclonal anti-PP1γ	goat	1:500	Santa Cruz C-19, no. sc-6108
polyclonal anti-SDS22	goat	1:1000	Santa Cruz E-20, no. sc-162164
polyclonal anti-Inhibitor-3	rabbit	1:1000	Eiteneuer et al., 2014
Secondary antibodies			
rabbit IgG HRP	goat	1:10000	Bio-Rad, no. 160-6515
goat IgG HRP	mouse	1:10000	Santa Cruz, no. sc-2354

5. References

Anderson, D. J., Le Moigne, R., Djakovic, S., Kumar, B., Rice, J., Wong, S., Wang, J., Yao, B., Valle, E., Kiss von Soly, S., Madriaga, A., Soriano, F., Menon, M. K., Wu, Z. Y., Kampmann, M., Chen, Y., Weissman, J. S., Aftab, B. T., Yakes, F. M., . . . Rolfe, M. (2015). Targeting the AAA ATPase p97 as an Approach to Treat Cancer through Disruption of Protein Homeostasis. *Cancer Cell*, *28*(5), 653-665. https://doi.org/10.1016/j.ccell.2015.10.002

Andreev, D. E., O'Connor, P. B., Fahey, C., Kenny, E. M., Terenin, I. M., Dmitriev, S. E., Cormican, P., Morris, D. W., Shatsky, I. N., & Baranov, P. V. (2015). Translation of 5' leaders is pervasive in genes resistant to eIF2 repression. *Elife*, *4*, e03971. https://doi.org/10.7554/eLife.03971

Bajaj, R., Bollen, M., Peti, W., & Page, R. (2018). KNL1 Binding to PP1 and Microtubules Is Mutually Exclusive. *Structure*, *26*(10), 1327-1336 e1324. https://doi.org/10.1016/j.str.2018.06.013

Bastola, P., Bilkis, R., De Souza, C., Minn, K., & Chien, J. (2019). Heterozygous mutations in valosin-containing protein (VCP) and resistance to VCP inhibitors. *Sci Rep*, *9*(1), 11002. https://doi.org/10.1038/s41598-019-47085-9

Beck, M., Schmidt, A., Malmstroem, J., Claassen, M., Ori, A., Szymborska, A., Herzog, F., Rinner, O., Ellenberg, J., & Aebersold, R. (2011). The quantitative proteome of a human cell line. *Mol Syst Biol*, *7*, 549. https://doi.org/10.1038/msb.2011.82

Bertolotti, A. (2018). The split protein phosphatase system. *Biochem J*, *475*(23), 3707-3723. https://doi.org/10.1042/BCJ20170726

Beullens, M., Van Eynde, A., Vulsteke, V., Connor, J., Shenolikar, S., Stalmans, W., & Bollen, M. (1999). Molecular determinants of nuclear protein phosphatase-1 regulation by NIPP-1. *J Biol Chem*, *274*(20), 14053-14061. https://doi.org/10.1074/jbc.274.20.14053

Bharucha, J. P., Larson, J. R., Gao, L., Daves, L. K., & Tatchell, K. (2008). Ypi1, a positive regulator of nuclear protein phosphatase type 1 activity in Saccharomyces cerevisiae. *Mol Biol Cell*, *19*(3), 1032-1045. https://doi.org/10.1091/mbc.e07-05-0499

Blythe, E. E., Gates, S. N., Deshaies, R. J., & Martin, A. (2019). Multisystem Proteinopathy Mutations in VCP/p97 Increase NPLOC4.UFD1L Binding and Substrate Processing. *Structure*, *27*(12), 1820-1829 e1824. https://doi.org/10.1016/j.str.2019.09.011

Blythe, E. E., Olson, K. C., Chau, V., & Deshaies, R. J. (2017). Ubiquitin- and ATP-dependent unfoldase activity of P97/VCP*NPLOC4*UFD1L is enhanced by a mutation that causes multisystem proteinopathy. *Proc Natl Acad Sci U S A*, *114*(22), E4380-E4388. https://doi.org/10.1073/pnas.1706205114

Bodnar, N. O., Kim, K. H., Ji, Z., Wales, T. E., Svetlov, V., Nudler, E., Engen, J. R., Walz, T., & Rapoport, T. A. (2018). Structure of the Cdc48 ATPase with its ubiquitin-binding cofactor Ufd1-Npl4. *Nat Struct Mol Biol*, *25*(7), 616-622. https://doi.org/10.1038/s41594-018-0085-x

Bodnar, N. O., & Rapoport, T. A. (2017). Molecular Mechanism of Substrate Processing by the Cdc48 ATPase Complex. *Cell*, *169*(4), 722-735 e729. https://doi.org/10.1016/j.cell.2017.04.020

Bollen, M., Peti, W., Ragusa, M. J., & Beullens, M. (2010). The extended PP1 toolkit: designed to create specificity. *Trends Biochem Sci*, *35*(8), 450-458. https://doi.org/10.1016/j.tibs.2010.03.002

Bononi, A., Agnoletto, C., De Marchi, E., Marchi, S., Patergnani, S., Bonora, M., Giorgi, C., Missiroli, S., Poletti, F., Rimessi, A., & Pinton, P. (2011). Protein kinases and phosphatases in the control of cell fate. *Enzyme Res*, *2011*, 329098. https://doi.org/10.4061/2011/329098

Brady, M. J., & Saltiel, A. R. (2001). The role of protein phosphatase-1 in insulin action. *Recent Prog Horm Res*, *56*, 157-173. https://doi.org/10.1210/rp.56.1.157

Brandman, O., & Hegde, R. S. (2016). Ribosome-associated protein quality control. *Nat Struct Mol Biol*, *23*(1), 7-15. https://doi.org/10.1038/nsmb.3147

Braxton, J. R., & Southworth, D. R. (2023). Structural insights of the p97/VCP AAA+ ATPase: How adapter interactions coordinate diverse cellular functionality. *J Biol Chem*, *299*(11), 105182. https://doi.org/10.1016/j.jbc.2023.105182

Bruderer, R. M., Brasseur, C., & Meyer, H. H. (2004). The AAA ATPase p97/VCP interacts with its alternative co-factors, Ufd1-Npl4 and p47, through a common bipartite binding mechanism. *J Biol Chem*, *279*(48), 49609-49616. https://doi.org/10.1074/jbc.M408695200

Brush, M. H., & Shenolikar, S. (2008). Control of cellular GADD34 levels by the 26S proteasome. *Mol Cell Biol*, *28*(23), 6989-7000. https://doi.org/10.1128/MCB.00724-08

Buchberger, A., Schindelin, H., & Hanzelmann, P. (2015). Control of p97 function by cofactor binding. *FEBS Lett*, *589*(19 Pt A), 2578-2589. https://doi.org/10.1016/j.febslet.2015.08.028

Cannon, J. F., Pringle, J. R., Fiechter, A., & Khalil, M. (1994). Characterization of glycogen-deficient glc mutants of Saccharomyces cerevisiae. *Genetics*, *136*(2), 485-503. https://doi.org/10.1093/genetics/136.2.485

Cao, X., Lemaire, S., & Bollen, M. (2022). Protein phosphatase 1: life-course regulation by SDS22 and Inhibitor-3. *FEBS J*, *289*(11), 3072-3085. https://doi.org/10.1111/febs.16029

Carrara, M., Sigurdardottir, A., & Bertolotti, A. (2017). Decoding the selectivity of eIF2alpha holophosphatases and PPP1R15A inhibitors. *Nat Struct Mol Biol*, *24*(9), 708-716. https://doi.org/10.1038/nsmb.3443

Casamayor, A., & Arino, J. (2020). Controlling Ser/Thr protein phosphatase PP1 activity and function through interaction with regulatory subunits. *Adv Protein Chem Struct Biol*, *122*, 231-288. https://doi.org/10.1016/bs.apcsb.2020.06.004

Ceulemans, H., & Bollen, M. (2004). Functional diversity of protein phosphatase-1, a cellular economizer and reset button. *Physiol Rev*, *84*(1), 1-39. https://doi.org/10.1152/physrev.00013.2003

Ceulemans, H., Stalmans, W., & Bollen, M. (2002). Regulator-driven functional diversification of protein phosphatase-1 in eukaryotic evolution. *Bioessays*, *24*(4), 371-381. https://doi.org/10.1002/bies.10069

Ceulemans, H., Vulsteke, V., De Maeyer, M., Tatchell, K., Stalmans, W., & Bollen, M. (2002). Binding of the concave surface of the Sds22 superhelix to the alpha 4/alpha 5/alpha 6-triangle of protein phosphatase-1. *J Biol Chem*, *277*(49), 47331-47337. https://doi.org/10.1074/jbc.M206838200

Chang, J. S., Henry, K., Wolf, B. L., Geli, M., & Lemmon, S. K. (2002). Protein phosphatase-1 binding to scd5p is important for regulation of actin organization and endocytosis in yeast. *J Biol Chem*, *277*(50), 48002-48008. https://doi.org/10.1074/jbc.M208471200

Chatterjee, J., Beullens, M., Sukackaite, R., Qian, J., Lesage, B., Hart, D. J., Bollen, M., & Kohn, M. (2012). Development of a peptide that selectively activates protein phosphatase-1 in living cells. *Angew Chem Int Ed Engl*, *51*(40), 10054-10059. https://doi.org/10.1002/anie.201204308

Chen, E., Choy, M. S., Petrenyi, K., Konya, Z., Erdodi, F., Dombradi, V., Peti, W., & Page, R. (2016). Molecular Insights into the Fungus-Specific Serine/Threonine

Protein Phosphatase Z1 in Candida albicans. *mBio*, *7*(4). https://doi.org/10.1128/mBio.00872-16

Chen, J. J. (2007). Regulation of protein synthesis by the heme-regulated eIF2alpha kinase: relevance to anemias. *Blood*, *109*(7), 2693-2699. https://doi.org/10.1182/blood-2006-08-041830

Chen, M. J., Dixon, J. E., & Manning, G. (2017). Genomics and evolution of protein phosphatases. *Sci Signal*, *10*(474). https://doi.org/10.1126/scisignal.aag1796

Chen, R., Rato, C., Yan, Y., Crespillo-Casado, A., Clarke, H. J., Harding, H. P., Marciniak, S. J., Read, R. J., & Ron, D. (2015). G-actin provides substrate-specificity to eukaryotic initiation factor 2alpha holophosphatases. *Elife*, *4*. https://doi.org/10.7554/eLife.04871

Cheng, C., Weiss, L., Leinonen, H., Shmara, A., Yin, H. Z., Ton, T., Do, A., Lee, J., Ta, L., Mohanty, E., Vargas, J., Weiss, J., Palczewski, K., & Kimonis, V. (2022). VCP/p97 inhibitor CB-5083 modulates muscle pathology in a mouse model of VCP inclusion body myopathy. *J Transl Med*, *20*(1), 21. https://doi.org/10.1186/s12967-021-03186-6

Cheng, Y. L., & Chen, R. H. (2015). Assembly and quality control of the protein phosphatase 1 holoenzyme involves the Cdc48-Shp1 chaperone. *J Cell Sci*, *128*(6), 1180-1192. https://doi.org/10.1242/jcs.165159

Choi, B., Rempala, G. A., & Kim, J. K. (2017). Beyond the Michaelis-Menten equation: Accurate and efficient estimation of enzyme kinetic parameters. *Sci Rep*, *7*(1), 17018. https://doi.org/10.1038/s41598-017-17072-z

Chou, A., Krukowski, K., Jopson, T., Zhu, P. J., Costa-Mattioli, M., Walter, P., & Rosi, S. (2017). Inhibition of the integrated stress response reverses cognitive deficits after traumatic brain injury. *Proc Natl Acad Sci U S A*, *114*(31), E6420-E6426. https://doi.org/10.1073/pnas.1707661114

Choy, M. S., Hieke, M., Kumar, G. S., Lewis, G. R., Gonzalez-DeWhitt, K. R., Kessler, R. P., Stein, B. J., Hessenberger, M., Nairn, A. C., Peti, W., & Page, R. (2014). Understanding the antagonism of retinoblastoma protein dephosphorylation by PNUTS provides insights into the PP1 regulatory code. *Proc Natl Acad Sci U S A*, *111*(11), 4097-4102. https://doi.org/10.1073/pnas.1317395111

Choy, M. S., Moon, T. M., Ravindran, R., Bray, J. A., Robinson, L. C., Archuleta, T. L., Shi, W., Peti, W., Tatchell, K., & Page, R. (2019). SDS22 selectively recognizes and traps metal-deficient inactive PP1. *Proc Natl Acad Sci U S A*, *116*(41), 20472-20481. https://doi.org/10.1073/pnas.1908718116

Choy, M. S., Srivastava, G., Robinson, L. C., Tatchell, K., Page, R., & Peti, W. (2024). The SDS22:PP1:I3 complex: SDS22 binding to PP1 loosens the active site metal to prime metal exchange. *J Biol Chem*, *300*(1), 105515. https://doi.org/10.1016/j.jbc.2023.105515

Choy, M. S., Yusoff, P., Lee, I. C., Newton, J. C., Goh, C. W., Page, R., Shenolikar, S., & Peti, W. (2015). Structural and Functional Analysis of the GADD34:PP1 eIF2alpha Phosphatase. *Cell Rep*, *11*(12), 1885-1891. https://doi.org/10.1016/j.celrep.2015.05.043

Cohen, P. (2002). The origins of protein phosphorylation. *Nat Cell Biol*, *4*(5), E127-130. https://doi.org/10.1038/ncb0502-e127

Connor, J. H., Weiser, D. C., Li, S., Hallenbeck, J. M., & Shenolikar, S. (2001). Growth arrest and DNA damage-inducible protein GADD34 assembles a novel signaling complex containing protein phosphatase 1 and inhibitor 1. *Mol Cell Biol*, *21*(20), 6841-6850. https://doi.org/10.1128/MCB.21.20.6841-6850.2001

Cooney, I., Han, H., Stewart, M. G., Carson, R. H., Hansen, D. T., Iwasa, J. H., Price, J. C., Hill, C. P., & Shen, P. S. (2019). Structure of the Cdc48 segregase in the act of unfolding an authentic substrate. *Science*, *365*(6452), 502-505. https://doi.org/10.1126/science.aax0486

Corda, P. O., Bollen, M., Ribeiro, D., & Fardilha, M. (2024). Emerging roles of the Protein Phosphatase 1 (PP1) in the context of viral infections. *Cell Commun Signal*, *22*(1), 65. https://doi.org/10.1186/s12964-023-01468-8

Crespillo-Casado, A., Claes, Z., Choy, M. S., Peti, W., Bollen, M., & Ron, D. (2018). A Sephin1-insensitive tripartite holophosphatase dephosphorylates translation initiation factor 2alpha. *J Biol Chem*, *293*(20), 7766-7776. https://doi.org/10.1074/jbc.RA118.002325

Dancheck, B., Ragusa, M. J., Allaire, M., Nairn, A. C., Page, R., & Peti, W. (2011). Molecular investigations of the structure and function of the protein phosphatase 1-spinophilin-inhibitor 2 heterotrimeric complex. *Biochemistry*, *50*(7), 1238-1246. https://doi.org/10.1021/bi101774g

Das, I., Krzyzosiak, A., Schneider, K., Wrabetz, L., D'Antonio, M., Barry, N., Sigurdardottir, A., & Bertolotti, A. (2015). Preventing proteostasis diseases by selective inhibition of a phosphatase regulatory subunit. *Science*, *348*(6231), 239-242. https://doi.org/10.1126/science.aaa4484

Defenouillere, Q., Yao, Y., Mouaikel, J., Namane, A., Galopier, A., Decourty, L., Doyen, A., Malabat, C., Saveanu, C., Jacquier, A., & Fromont-Racine, M. (2013). Cdc48-associated complex bound to 60S particles is required for the clearance of aberrant translation products. *Proc Natl Acad Sci U S A*, *110*(13), 5046-5051. https://doi.org/10.1073/pnas.1221724110

Dinischiotu, A., Beullens, M., Stalmans, W., & Bollen, M. (1997). Identification of sds22 as an inhibitory subunit of protein phosphatase-1 in rat liver nuclei. *FEBS Lett*, *402*(2-3), 141-144. https://doi.org/10.1016/s0014-5793(96)01514-1

Egloff, M. P., Cohen, P. T., Reinemer, P., & Barford, D. (1995). Crystal structure of the catalytic subunit of human protein phosphatase 1 and its complex with tungstate. *J Mol Biol*, *254*(5), 942-959. https://doi.org/10.1006/jmbi.1995.0667

Eiteneuer, A., Seiler, J., Weith, M., Beullens, M., Lesage, B., Krenn, V., Musacchio, A., Bollen, M., & Meyer, H. (2014). Inhibitor-3 ensures bipolar mitotic spindle attachment by limiting association of SDS22 with kinetochore-bound protein phosphatase-1. *EMBO J*, *33*(22), 2704-2720. https://doi.org/10.15252/embj.201489054

Ernst, R., Mueller, B., Ploegh, H. L., & Schlieker, C. (2009). The otubain YOD1 is a deubiquitinating enzyme that associates with p97 to facilitate protein dislocation from the ER. *Mol Cell*, *36*(1), 28-38. https://doi.org/10.1016/j.molcel.2009.09.016

Eto, M. (2009). Regulation of cellular protein phosphatase-1 (PP1) by phosphorylation of the CPI-17 family, C-kinase-activated PP1 inhibitors. *J Biol Chem*, *284*(51), 35273-35277. https://doi.org/10.1074/jbc.R109.059972

Foley, K., McKee, C., Nairn, A. C., & Xia, H. (2021). Regulation of Synaptic Transmission and Plasticity by Protein Phosphatase 1. *J Neurosci*, *41*(14), 3040-3050. https://doi.org/10.1523/JNEUROSCI.2026-20.2021

Fontanillo, M., Trebacz, M., Reinkemeier, C. D., Aviles Huerta, D., Uhrig, U., Sehr, P., & Kohn, M. (2022). Short peptide pharmacophores developed from protein phosphatase-1 disrupting peptides (PDPs). *Bioorg Med Chem*, *65*, 116785. https://doi.org/10.1016/j.bmc.2022.116785

Francisco, L., Wang, W., & Chan, C. S. (1994). Type 1 protein phosphatase acts in opposition to IpL1 protein kinase in regulating yeast chromosome segregation. *Mol Cell Biol*, *14*(7), 4731-4740. https://doi.org/10.1128/mcb.14.7.4731-4740.1994

Garcia-Gimeno, M. A., Munoz, I., Arino, J., & Sanz, P. (2003). Molecular characterization of Ypi1, a novel Saccharomyces cerevisiae type 1 protein phosphatase inhibitor. *J Biol Chem*, *278*(48), 47744-47752. https://doi.org/10.1074/jbc.M306157200

Garcia, A., Cayla, X., Guergnon, J., Dessauge, F., Hospital, V., Rebollo, M. P., Fleischer, A., & Rebollo, A. (2003). Serine/threonine protein phosphatases PP1 and PP2A are key players in apoptosis. *Biochimie*, *85*(8), 721-726. https://doi.org/10.1016/j.biochi.2003.09.004

Garcia, M. A., Meurs, E. F., & Esteban, M. (2007). The dsRNA protein kinase PKR: virus and cell control. *Biochimie*, *89*(6-7), 799-811. https://doi.org/10.1016/j.biochi.2007.03.001

Gates, S. N., Yokom, A. L., Lin, J., Jackrel, M. E., Rizo, A. N., Kendsersky, N. M., Buell, C. E., Sweeny, E. A., Mack, K. L., Chuang, E., Torrente, M. P., Su, M., Shorter, J., & Southworth, D. R. (2017). Ratchet-like polypeptide translocation mechanism of the AAA+ disaggregase Hsp104. *Science*, *357*(6348), 273-279. https://doi.org/10.1126/science.aan1052

Genoux, D., Haditsch, U., Knobloch, M., Michalon, A., Storm, D., & Mansuy, I. M. (2002). Protein phosphatase 1 is a molecular constraint on learning and memory. *Nature*, *418*(6901), 970-975. https://doi.org/10.1038/nature00928

Gibbons, J. A., Kozubowski, L., Tatchell, K., & Shenolikar, S. (2007). Expression of human protein phosphatase-1 in Saccharomyces cerevisiae highlights the role of phosphatase isoforms in regulating eukaryotic functions. *J Biol Chem*, *282*(30), 21838-21847. https://doi.org/10.1074/jbc.M701272200

Goldberg, J., Huang, H. B., Kwon, Y. G., Greengard, P., Nairn, A. C., & Kuriyan, J. (1995). Three-dimensional structure of the catalytic subunit of protein serine/threonine phosphatase-1. *Nature*, *376*(6543), 745-753. https://doi.org/10.1038/376745a0

Guo, F., Stanevich, V., Wlodarchak, N., Sengupta, R., Jiang, L., Satyshur, K. A., & Xing, Y. (2014). Structural basis of PP2A activation by PTPA, an ATP-dependent activation chaperone. *Cell Res*, *24*(2), 190-203. https://doi.org/10.1038/cr.2013.138

Halliday, M., Radford, H., Sekine, Y., Moreno, J., Verity, N., le Quesne, J., Ortori, C. A., Barrett, D. A., Fromont, C., Fischer, P. M., Harding, H. P., Ron, D., & Mallucci, G. R. (2015). Partial restoration of protein synthesis rates by the small molecule ISRIB prevents neurodegeneration without pancreatic toxicity. *Cell Death Dis*, *6*(3), e1672. https://doi.org/10.1038/cddis.2015.49

Han, A. P., Yu, C., Lu, L., Fujiwara, Y., Browne, C., Chin, G., Fleming, M., Leboulch, P., Orkin, S. H., & Chen, J. J. (2001). Heme-regulated eIF2alpha kinase (HRI) is required for translational regulation and survival of erythroid precursors in iron deficiency. *EMBO J*, *20*(23), 6909-6918. https://doi.org/10.1093/emboj/20.23.6909

Hanzelmann, P., & Schindelin, H. (2017). The Interplay of Cofactor Interactions and Post-translational Modifications in the Regulation of the AAA+ ATPase p97. *Front Mol Biosci*, *4*, 21. https://doi.org/10.3389/fmolb.2017.00021

Harding, H. P., Zhang, Y., & Ron, D. (1999). Protein translation and folding are coupled by an endoplasmic-reticulum-resident kinase. *Nature*, *397*(6716), 271-274. https://doi.org/10.1038/16729

Harding, H. P., Zhang, Y., Scheuner, D., Chen, J. J., Kaufman, R. J., & Ron, D. (2009). Ppp1r15 gene knockout reveals an essential role for translation initiation factor 2 alpha (eIF2alpha) dephosphorylation in mammalian development. *Proc Natl Acad Sci U S A*, *106*(6), 1832-1837. https://doi.org/10.1073/pnas.0809632106

Hartmann-Petersen, R., Wallace, M., Hofmann, K., Koch, G., Johnsen, A. H., Hendil, K. B., & Gordon, C. (2004). The Ubx2 and Ubx3 cofactors direct Cdc48 activity to proteolytic and nonproteolytic ubiquitin-dependent processes. *Curr Biol*, *14*(9), 824-828. https://doi.org/10.1016/j.cub.2004.04.029

Hauf, S., Cole, R. W., LaTerra, S., Zimmer, C., Schnapp, G., Walter, R., Heckel, A., van Meel, J., Rieder, C. L., & Peters, J. M. (2003). The small molecule Hesperadin reveals a role for Aurora B in correcting kinetochore-microtubule attachment and in maintaining the spindle assembly checkpoint. *J Cell Biol*, *161*(2), 281-294. https://doi.org/10.1083/jcb.200208092

Helps, N. R., Luo, X., Barker, H. M., & Cohen, P. T. (2000). NIMA-related kinase 2 (Nek2), a cell-cycle-regulated protein kinase localized to centrosomes, is complexed to protein phosphatase 1. *Biochem J*, *349*(Pt 2), 509-518. https://doi.org/10.1042/0264-6021:3490509

Hendrickx, A., Beullens, M., Ceulemans, H., Den Abt, T., Van Eynde, A., Nicolaescu, E., Lesage, B., & Bollen, M. (2009). Docking motif-guided mapping of the interactome of protein phosphatase-1. *Chem Biol*, *16*(4), 365-371. https://doi.org/10.1016/j.chembiol.2009.02.012

Heroes, E., Lesage, B., Gornemann, J., Beullens, M., Van Meervelt, L., & Bollen, M. (2013). The PP1 binding code: a molecular-lego strategy that governs specificity. *FEBS J*, *280*(2), 584-595. https://doi.org/10.1111/j.1742-4658.2012.08547.x

Heroes, E., Rip, J., Beullens, M., Van Meervelt, L., De Gendt, S., & Bollen, M. (2015). Metals in the active site of native protein phosphatase-1. *J Inorg Biochem*, *149*, 1-5. https://doi.org/10.1016/j.jinorgbio.2015.03.012

Heroes, E., Van der Hoeven, G., Choy, M. S., Garcia, J. D. P., Ferreira, M., Nys, M., Derua, R., Beullens, M., Ulens, C., Peti, W., Van Meervelt, L., Page, R., & Bollen, M. (2019). Structure-Guided Exploration of SDS22 Interactions with Protein Phosphatase PP1 and the Splicing Factor BCLAF1. *Structure*, *27*(3), 507-518 e505. https://doi.org/10.1016/j.str.2018.12.002

Hicks, D., Giresh, K., Wrischnik, L. A., & Weiser, D. C. (2023). The PPP1R15 Family of eIF2-alpha Phosphatase Targeting Subunits (GADD34 and CReP). *Int J Mol Sci*, *24*(24). https://doi.org/10.3390/ijms242417321

Hisamoto, N., Sugimoto, K., & Matsumoto, K. (1994). The Glc7 type 1 protein phosphatase of Saccharomyces cerevisiae is required for cell cycle progression in G2/M. *Mol Cell Biol*, *14*(5), 3158-3165. https://doi.org/10.1128/mcb.14.5.3158-3165.1994

Huang, H. S., Pozarowski, P., Gao, Y., Darzynkiewicz, Z., & Lee, E. Y. (2005). Protein phosphatase-1 inhibitor-3 is co-localized to the nucleoli and centrosomes with PP1gamma1 and PP1alpha, respectively. *Arch Biochem Biophys*, *443*(1-2), 33-44. https://doi.org/10.1016/j.abb.2005.08.021

Huang, S., Tang, D., & Wang, Y. (2016). Monoubiquitination of Syntaxin 5 Regulates Golgi Membrane Dynamics during the Cell Cycle. *Dev Cell*, *38*(1), 73-85. https://doi.org/10.1016/j.devcel.2016.06.001

Hulsmann, J., Kravic, B., Weith, M., Gstaiger, M., Aebersold, R., Collins, B. C., & Meyer, H. (2018). AP-SWATH Reveals Direct Involvement of VCP/p97 in Integrated Stress Response Signaling Through Facilitating CReP/PPP1R15B Degradation. *Mol Cell Proteomics*, *17*(7), 1295-1307. https://doi.org/10.1074/mcp.RA117.000471

Hurley, T. D., Yang, J., Zhang, L., Goodwin, K. D., Zou, Q., Cortese, M., Dunker, A. K., & DePaoli-Roach, A. A. (2007). Structural basis for regulation of protein phosphatase 1 by inhibitor-2. *J Biol Chem*, *282*(39), 28874-28883. https://doi.org/10.1074/jbc.M703472200

Ito, M., Nakano, T., Erdodi, F., & Hartshorne, D. J. (2004). Myosin phosphatase: structure, regulation and function. *Mol Cell Biochem*, *259*(1-2), 197-209. https://doi.org/10.1023/b:mcbi.0000021373.14288.00

Jin, H., Sperka, T., Herrlich, P., & Morrison, H. (2006). Tumorigenic transformation by CPI-17 through inhibition of a merlin phosphatase. *Nature*, *442*(7102), 576-579. https://doi.org/10.1038/nature04856

Johnson, J. O., Mandrioli, J., Benatar, M., Abramzon, Y., Van Deerlin, V. M., Trojanowski, J. Q., Gibbs, J. R., Brunetti, M., Gronka, S., Wuu, J., Ding, J., McCluskey, L., Martinez-Lage, M., Falcone, D., Hernandez, D. G., Arepalli, S., Chong, S., Schymick, J. C., Rothstein, J., . . . Traynor, B. J. (2010). Exome sequencing reveals VCP mutations as a cause of familial ALS. *Neuron*, *68*(5), 857-864. https://doi.org/10.1016/j.neuron.2010.11.036

Jousse, C., Oyadomari, S., Novoa, I., Lu, P., Zhang, Y., Harding, H. P., & Ron, D. (2003). Inhibition of a constitutive translation initiation factor 2alpha phosphatase, CReP, promotes survival of stressed cells. *J Cell Biol*, *163*(4), 767-775. https://doi.org/10.1083/jcb.200308075

Karata, K., Inagawa, T., Wilkinson, A. J., Tatsuta, T., & Ogura, T. (1999). Dissecting the role of a conserved motif (the second region of homology) in the AAA family of ATPases. Site-directed mutagenesis of the ATP-dependent protease FtsH. *J Biol Chem*, *274*(37), 26225-26232. https://doi.org/10.1074/jbc.274.37.26225

Katayose, Y., Li, M., Al-Murrani, S. W., Shenolikar, S., & Damuni, Z. (2000). Protein phosphatase 2A inhibitors, I(1)(PP2A) and I(2)(PP2A), associate with and modify the substrate specificity of protein phosphatase 1. *J Biol Chem*, *275*(13), 9209-9214. https://doi.org/10.1074/jbc.275.13.9209

Kaufman, R. J. (2002). Orchestrating the unfolded protein response in health and disease. *J Clin Invest*, *110*(10), 1389-1398. https://doi.org/10.1172/JCI16886

Kelker, M. S., Page, R., & Peti, W. (2009). Crystal structures of protein phosphatase-1 bound to nodularin-R and tautomycin: a novel scaffold for structure-based drug design of serine/threonine phosphatase inhibitors. *J Mol Biol*, *385*(1), 11-21. https://doi.org/10.1016/j.jmb.2008.10.053

Kelsall, I. R., Rosenzweig, D., & Cohen, P. T. (2009). Disruption of the allosteric phosphorylase a regulation of the hepatic glycogen-targeted protein phosphatase 1 improves glucose tolerance in vivo. *Cell Signal*, *21*(7), 1123-1134. https://doi.org/10.1016/j.cellsig.2009.03.001

Kilberg, M. S., Pan, Y. X., Chen, H., & Leung-Pineda, V. (2005). Nutritional control of gene expression: how mammalian cells respond to amino acid limitation. *Annu Rev Nutr*, *25*, 59-85. https://doi.org/10.1146/annurev.nutr.24.012003.132145

Kimonis, V. E., Fulchiero, E., Vesa, J., & Watts, G. (2008). VCP disease associated with myopathy, Paget disease of bone and frontotemporal dementia: review of a unique disorder. *Biochim Biophys Acta*, *1782*(12), 744-748. https://doi.org/10.1016/j.bbadis.2008.09.003

Kimonis, V. E., Mehta, S. G., Fulchiero, E. C., Thomasova, D., Pasquali, M., Boycott, K., Neilan, E. G., Kartashov, A., Forman, M. S., Tucker, S., Kimonis, K., Mumm, S., Whyte, M. P., Smith, C. D., & Watts, G. D. (2008). Clinical studies in familial VCP myopathy associated with Paget disease of bone and frontotemporal dementia. *Am J Med Genet A*, *146A*(6), 745-757. https://doi.org/10.1002/ajmg.a.31862

Kobe, B., & Kajava, A. V. (2001). The leucine-rich repeat as a protein recognition motif. *Curr Opin Struct Biol*, *11*(6), 725-732. https://doi.org/10.1016/s0959-440x(01)00266-4

Kondo, H., Rabouille, C., Newman, R., Levine, T. P., Pappin, D., Freemont, P., & Warren, G. (1997). p47 is a cofactor for p97-mediated membrane fusion. *Nature*, *388*(6637), 75-78. https://doi.org/10.1038/40411

Korb, M. K., Kimonis, V. E., & Mozaffar, T. (2021). Multisystem proteinopathy: Where myopathy and motor neuron disease converge. *Muscle Nerve*, *63*(4), 442-454. https://doi.org/10.1002/mus.27097

Kracht, M., van den Boom, J., Seiler, J., Kroning, A., Kaschani, F., Kaiser, M., & Meyer, H. (2020). Protein Phosphatase-1 Complex Disassembly by p97 is Initiated through Multivalent Recognition of Catalytic and Regulatory Subunits by the p97 SEP-domain Adapters. *J Mol Biol*, *432*(23), 6061-6074. https://doi.org/10.1016/j.jmb.2020.10.001

Kravic, B., Bionda, T., Siebert, A., Gahlot, P., Levantovsky, S., Behrends, C., & Meyer, H. (2022). Ubiquitin profiling of lysophagy identifies actin stabilizer CNN2 as a target of VCP/p97 and uncovers a link to HSPB1. *Mol Cell*, *82*(14), 2633-2649 e2637. https://doi.org/10.1016/j.molcel.2022.06.012

Kumar, G. S., Gokhan, E., De Munter, S., Bollen, M., Vagnarelli, P., Peti, W., & Page, R. (2016). The Ki-67 and RepoMan mitotic phosphatases assemble via an identical, yet novel mechanism. *Elife*, *5*. https://doi.org/10.7554/eLife.16539

Kuntziger, T., Landsverk, H. B., Collas, P., & Syljuasen, R. G. (2011). Protein phosphatase 1 regulators in DNA damage signaling. *Cell Cycle*, *10*(9), 1356-1362. https://doi.org/10.4161/cc.10.9.15442

Lam, A. J., St-Pierre, F., Gong, Y., Marshall, J. D., Cranfill, P. J., Baird, M. A., McKeown, M. R., Wiedenmann, J., Davidson, M. W., Schnitzer, M. J., Tsien, R. Y., & Lin, M. Z. (2012). Improving FRET dynamic range with bright green and red fluorescent proteins. *Nat Methods*, *9*(10), 1005-1012. https://doi.org/10.1038/nmeth.2171

Lesage, B., Beullens, M., Pedelini, L., Garcia-Gimeno, M. A., Waelkens, E., Sanz, P., & Bollen, M. (2007). A complex of catalytically inactive protein phosphatase-1 sandwiched between Sds22 and inhibitor-3. *Biochemistry*, *46*(31), 8909-8919. https://doi.org/10.1021/bi7003119

Lesage, B., Qian, J., & Bollen, M. (2011). Spindle checkpoint silencing: PP1 tips the balance. *Curr Biol*, *21*(21), R898-903. https://doi.org/10.1016/j.cub.2011.08.063

Li, H., Ji, Z., Paulo, J. A., Gygi, S. P., & Rapoport, T. A. (2024). Bidirectional substrate shuttling between the 26S proteasome and the Cdc48 ATPase promotes protein degradation. *Mol Cell*, *84*(7), 1290-1303 e1297. https://doi.org/10.1016/j.molcel.2024.01.029

Liu, H., Krizek, J., & Bretscher, A. (1992). Construction of a GAL1-regulated yeast cDNA expression library and its application to the identification of genes whose overexpression causes lethality in yeast. *Genetics*, *132*(3), 665-673. https://doi.org/10.1093/genetics/132.3.665

Liu, J., & Brautigan, D. L. (2000). Glycogen synthase association with the striated muscle glycogen-targeting subunit of protein phosphatase-1. Synthase activation involves scaffolding regulated by beta-adrenergic signaling. *J Biol Chem*, *275*(34), 26074-26081. https://doi.org/10.1074/jbc.M003843200

Lundberg, E., Fagerberg, L., Klevebring, D., Matic, I., Geiger, T., Cox, J., Algenas, C., Lundeberg, J., Mann, M., & Uhlen, M. (2010). Defining the transcriptome and proteome in three functionally different human cell lines. *Mol Syst Biol*, *6*, 450. https://doi.org/10.1038/msb.2010.106

Lupas, A. N., & Martin, J. (2002). AAA proteins. *Curr Opin Struct Biol*, *12*(6), 746-753. https://doi.org/10.1016/s0959-440x(02)00388-3

Manning, G., Whyte, D. B., Martinez, R., Hunter, T., & Sudarsanam, S. (2002). The protein kinase complement of the human genome. *Science*, *298*(5600), 1912-1934. https://doi.org/10.1126/science.1075762

Meyer, H., & van den Boom, J. (2023). Targeting of client proteins to the VCP/p97/Cdc48 unfolding machine. *Front Mol Biosci*, *10*, 1142989. https://doi.org/10.3389/fmolb.2023.1142989

Meyer, H. H., Shorter, J. G., Seemann, J., Pappin, D., & Warren, G. (2000). A complex of mammalian ufd1 and npl4 links the AAA-ATPase, p97, to ubiquitin and nuclear transport pathways. *EMBO J*, *19*(10), 2181-2192. https://doi.org/10.1093/emboj/19.10.2181

Meyer, H. H., Wang, Y., & Warren, G. (2002). Direct binding of ubiquitin conjugates by the mammalian p97 adaptor complexes, p47 and Ufd1-Npl4. *EMBO J*, *21*(21), 5645-5652. https://doi.org/10.1093/emboj/cdf579

Moorhead, G. B., Trinkle-Mulcahy, L., & Ulke-Lemee, A. (2007). Emerging roles of nuclear protein phosphatases. *Nat Rev Mol Cell Biol*, *8*(3), 234-244. https://doi.org/10.1038/nrm2126

Moremen, K. W., Tiemeyer, M., & Nairn, A. V. (2012). Vertebrate protein glycosylation: diversity, synthesis and function. *Nat Rev Mol Cell Biol*, *13*(7), 448-462. https://doi.org/10.1038/nrm3383

Murnion, M. E., Adams, R. R., Callister, D. M., Allis, C. D., Earnshaw, W. C., & Swedlow, J. R. (2001). Chromatin-associated protein phosphatase 1 regulates aurora-B and histone H3 phosphorylation. *J Biol Chem*, *276*(28), 26656-26665. https://doi.org/10.1074/jbc.M102288200

Musacchio, A., & Salmon, E. D. (2007). The spindle-assembly checkpoint in space and time. *Nat Rev Mol Cell Biol*, *8*(5), 379-393. https://doi.org/10.1038/nrm2163

Nagaraj, N., Wisniewski, J. R., Geiger, T., Cox, J., Kircher, M., Kelso, J., Paabo, S., & Mann, M. (2011). Deep proteome and transcriptome mapping of a human cancer cell line. *Mol Syst Biol*, *7*, 548. https://doi.org/10.1038/msb.2011.81

Nasa, I., Rusin, S. F., Kettenbach, A. N., & Moorhead, G. B. (2018). Aurora B opposes PP1 function in mitosis by phosphorylating the conserved PP1-binding RVxF motif in PP1 regulatory proteins. *Sci Signal*, *11*(530). https://doi.org/10.1126/scisignal.aai8669

Neill, G., & Masson, G. R. (2023). A stay of execution: ATF4 regulation and potential outcomes for the integrated stress response. *Front Mol Neurosci*, *16*, 1112253. https://doi.org/10.3389/fnmol.2023.1112253

Neuwald, A. F., Aravind, L., Spouge, J. L., & Koonin, E. V. (1999). AAA+: A class of chaperone-like ATPases associated with the assembly, operation, and disassembly of protein complexes. *Genome Res*, *9*(1), 27-43. https://www.ncbi.nlm.nih.gov/pubmed/9927482

Novoa, I., Zeng, H., Harding, H. P., & Ron, D. (2001). Feedback inhibition of the unfolded protein response by GADD34-mediated dephosphorylation of eIF2alpha. *J Cell Biol*, *153*(5), 1011-1022. https://doi.org/10.1083/jcb.153.5.1011

Nuytten, M., Beke, L., Van Eynde, A., Ceulemans, H., Beullens, M., Van Hummelen, P., Fuks, F., & Bollen, M. (2008). The transcriptional repressor NIPP1 is an essential player in EZH2-mediated gene silencing. *Oncogene*, *27*(10), 1449-1460. https://doi.org/10.1038/sj.onc.1210774

O'Connell, N., Nichols, S. R., Heroes, E., Beullens, M., Bollen, M., Peti, W., & Page, R. (2012). The molecular basis for substrate specificity of the nuclear NIPP1:PP1 holoenzyme. *Structure*, *20*(10), 1746-1756. https://doi.org/10.1016/j.str.2012.08.003

Olszewski, M. M., Williams, C., Dong, K. C., & Martin, A. (2019). The Cdc48 unfoldase prepares well-folded protein substrates for degradation by the 26S proteasome. *Commun Biol*, *2*, 29. https://doi.org/10.1038/s42003-019-0283-z

Pakos-Zebrucka, K., Koryga, I., Mnich, K., Ljujic, M., Samali, A., & Gorman, A. M. (2016). The integrated stress response. *EMBO Rep*, *17*(10), 1374-1395. https://doi.org/10.15252/embr.201642195

Pan, M., Zheng, Q., Yu, Y., Ai, H., Xie, Y., Zeng, X., Wang, C., Liu, L., & Zhao, M. (2021). Seesaw conformations of Npl4 in the human p97 complex and the inhibitory mechanism of a disulfiram derivative. *Nat Commun*, *12*(1), 121. https://doi.org/10.1038/s41467-020-20359-x

Papadopoulos, C., Kirchner, P., Bug, M., Grum, D., Koerver, L., Schulze, N., Poehler, R., Dressler, A., Fengler, S., Arhzaouy, K., Lux, V., Ehrmann, M., Weihl, C. C., & Meyer, H. (2017). VCP/p97 cooperates with YOD1, UBXD1 and PLAA to drive clearance of ruptured lysosomes by autophagy. *EMBO J*, *36*(2), 135-150. https://doi.org/10.15252/embj.201695148

Pedelini, L., Marquina, M., Arino, J., Casamayor, A., Sanz, L., Bollen, M., Sanz, P., & Garcia-Gimeno, M. A. (2007). YPI1 and SDS22 proteins regulate the nuclear localization and function of yeast type 1 phosphatase Glc7. *J Biol Chem*, *282*(5), 3282-3292. https://doi.org/10.1074/jbc.M607171200

Peggie, M. W., MacKelvie, S. H., Bloecher, A., Knatko, E. V., Tatchell, K., & Stark, M. J. (2002). Essential functions of Sds22p in chromosome stability and nuclear localization of PP1. *J Cell Sci*, *115*(Pt 1), 195-206. https://doi.org/10.1242/jcs.115.1.195

Pennuto, M., Tinelli, E., Malaguti, M., Del Carro, U., D'Antonio, M., Ron, D., Quattrini, A., Feltri, M. L., & Wrabetz, L. (2008). Ablation of the UPR-mediator CHOP restores motor function and reduces demyelination in Charcot-Marie-Tooth 1B mice. *Neuron*, *57*(3), 393-405. https://doi.org/10.1016/j.neuron.2007.12.021

Pinna, L. A., & Donella-Deana, A. (1994). Phosphorylated synthetic peptides as tools for studying protein phosphatases. *Biochim Biophys Acta*, *1222*(3), 415-431. https://doi.org/10.1016/0167-4889(94)90050-7

Posch, M., Khoudoli, G. A., Swift, S., King, E. M., Deluca, J. G., & Swedlow, J. R. (2010). Sds22 regulates aurora B activity and microtubule-kinetochore interactions at mitosis. *J Cell Biol*, *191*(1), 61-74. https://doi.org/10.1083/jcb.200912046

Postow, L., Ghenoiu, C., Woo, E. M., Krutchinsky, A. N., Chait, B. T., & Funabiki, H. (2008). Ku80 removal from DNA through double strand break-induced ubiquitylation. *J Cell Biol*, *182*(3), 467-479. https://doi.org/10.1083/jcb.200802146

Puchades, C., Rampello, A. J., Shin, M., Giuliano, C. J., Wiseman, R. L., Glynn, S. E., & Lander, G. C. (2017). Structure of the mitochondrial inner membrane AAA+ protease YME1 gives insight into substrate processing. *Science*, *358*(6363). https://doi.org/10.1126/science.aao0464

Rabouille, C., Kondo, H., Newman, R., Hui, N., Freemont, P., & Warren, G. (1998). Syntaxin 5 is a common component of the NSF- and p97-mediated reassembly pathways of Golgi cisternae from mitotic Golgi fragments in vitro. *Cell*, *92*(5), 603-610. https://doi.org/10.1016/s0092-8674(00)81128-9

Ragusa, M. J., Dancheck, B., Critton, D. A., Nairn, A. C., Page, R., & Peti, W. (2010). Spinophilin directs protein phosphatase 1 specificity by blocking substrate binding sites. *Nat Struct Mol Biol*, *17*(4), 459-464. https://doi.org/10.1038/nsmb.1786

Ramaswamy, N. T., Li, L., Khalil, M., & Cannon, J. F. (1998). Regulation of yeast glycogen metabolism and sporulation by Glc7p protein phosphatase. *Genetics*, *149*(1), 57-72. https://doi.org/10.1093/genetics/149.1.57

Rebelo, S., Santos, M., Martins, F., da Cruz e Silva, E. F., & da Cruz e Silva, O. A. (2015). Protein phosphatase 1 is a key player in nuclear events. *Cell Signal*, *27*(12), 2589-2598. https://doi.org/10.1016/j.cellsig.2015.08.007

Resh, M. D. (2012). Targeting protein lipidation in disease. *Trends Mol Med*, *18*(4), 206-214. https://doi.org/10.1016/j.molmed.2012.01.007

Rizo, A. N., Lin, J., Gates, S. N., Tse, E., Bart, S. M., Castellano, L. M., DiMaio, F., Shorter, J., & Southworth, D. R. (2019). Structural basis for substrate gripping and translocation by the ClpB AAA+ disaggregase. *Nat Commun*, *10*(1), 2393. https://doi.org/10.1038/s41467-019-10150-y

Ron, D. (2002). Translational control in the endoplasmic reticulum stress response. *J Clin Invest*, *110*(10), 1383-1388. https://doi.org/10.1172/JCI16784

Roux, B., Vaganay, C., Vargas, J. D., Alexe, G., Benaksas, C., Pardieu, B., Fenouille, N., Ellegast, J. M., Malolepsza, E., Ling, F., Sodaro, G., Ross, L., Pikman, Y., Conway, A. S., Tang, Y., Wu, T., Anderson, D. J., Le Moigne, R., Zhou, H. J., . . . Benajiba, L. (2021). Targeting acute myeloid leukemia dependency on VCP-mediated DNA repair through a selective second-generation small-molecule inhibitor. *Sci Transl Med*, *13*(587). https://doi.org/10.1126/scitranslmed.abg1168

Sadler, A. J., & Williams, B. R. (2007). Structure and function of the protein kinase R. *Curr Top Microbiol Immunol*, *316*, 253-292. https://doi.org/10.1007/978-3-540-71329-6_13

Saha, I., Yuste-Checa, P., Da Silva Padilha, M., Guo, Q., Korner, R., Holthusen, H., Trinkaus, V. A., Dudanova, I., Fernandez-Busnadiego, R., Baumeister, W., Sanders, D. W., Gautam, S., Diamond, M. I., Hartl, F. U., & Hipp, M. S. (2023). The AAA+ chaperone VCP disaggregates Tau fibrils and generates aggregate seeds in a cellular system. *Nat Commun*, *14*(1), 560. https://doi.org/10.1038/s41467-023-36058-2

Saurin, A. T. (2018). Kinase and Phosphatase Cross-Talk at the Kinetochore. *Front Cell Dev Biol*, *6*, 62. https://doi.org/10.3389/fcell.2018.00062

Scheuner, D., Patel, R., Wang, F., Lee, K., Kumar, K., Wu, J., Nilsson, A., Karin, M., & Kaufman, R. J. (2006). Double-stranded RNA-dependent protein kinase phosphorylation of the alpha-subunit of eukaryotic translation initiation factor 2 mediates apoptosis. *J Biol Chem*, *281*(30), 21458-21468. https://doi.org/10.1074/jbc.M603784200

Sharma, K., D'Souza, R. C., Tyanova, S., Schaab, C., Wisniewski, J. R., Cox, J., & Mann, M. (2014). Ultradeep human phosphoproteome reveals a distinct regulatory nature of Tyr and Ser/Thr-based signaling. *Cell Rep*, *8*(5), 1583-1594. https://doi.org/10.1016/j.celrep.2014.07.036

Shi, Y. (2009). Serine/threonine phosphatases: mechanism through structure. *Cell*, *139*(3), 468-484. https://doi.org/10.1016/j.cell.2009.10.006

Sidrauski, C., Acosta-Alvear, D., Khoutorsky, A., Vedantham, P., Hearn, B. R., Li, H., Gamache, K., Gallagher, C. M., Ang, K. K., Wilson, C., Okreglak, V., Ashkenazi, A., Hann, B., Nader, K., Arkin, M. R., Renslo, A. R., Sonenberg, N., & Walter, P. (2013). Pharmacological brake-release of mRNA translation enhances cognitive memory. *Elife*, *2*, e00498. https://doi.org/10.7554/eLife.00498

Sidrauski, C., Tsai, J. C., Kampmann, M., Hearn, B. R., Vedantham, P., Jaishankar, P., Sokabe, M., Mendez, A. S., Newton, B. W., Tang, E. L., Verschueren, E., Johnson, J. R., Krogan, N. J., Fraser, C. S., Weissman, J. S., Renslo, A. R., &

Walter, P. (2015). Pharmacological dimerization and activation of the exchange factor eIF2B antagonizes the integrated stress response. *Elife*, *4*, e07314. https://doi.org/10.7554/eLife.07314

Sonenberg, N., & Hinnebusch, A. G. (2009). Regulation of translation initiation in eukaryotes: mechanisms and biological targets. *Cell*, *136*(4), 731-745. https://doi.org/10.1016/j.cell.2009.01.042

Srivastava, G., Choy, M. S., Bolik-Coulon, N., Page, R., & Peti, W. (2023). Inhibitor-3 inhibits Protein Phosphatase 1 via a metal binding dynamic protein-protein interaction. *Nat Commun*, *14*(1), 1798. https://doi.org/10.1038/s41467-023-37372-5

Stach, L., & Freemont, P. S. (2017). The AAA+ ATPase p97, a cellular multitool. *Biochem J*, *474*(17), 2953-2976. https://doi.org/10.1042/BCJ20160783

Stein, A., Ruggiano, A., Carvalho, P., & Rapoport, T. A. (2014). Key steps in ERAD of luminal ER proteins reconstituted with purified components. *Cell*, *158*(6), 1375-1388. https://doi.org/10.1016/j.cell.2014.07.050

Stone, E. M., Yamano, H., Kinoshita, N., & Yanagida, M. (1993). Mitotic regulation of protein phosphatases by the fission yeast sds22 protein. *Curr Biol*, *3*(1), 13-26. https://doi.org/10.1016/0960-9822(93)90140-j

Story, R. M., & Steitz, T. A. (1992). Structure of the recA protein-ADP complex. *Nature*, *355*(6358), 374-376. https://doi.org/10.1038/355374a0

Swingle, M. R., & Honkanen, R. E. (2014). Development and validation of a robust and sensitive assay for the discovery of selective inhibitors for serine/threonine protein phosphatases PP1alpha (PPP1C) and PP5 (PPP5C). *Assay Drug Dev Technol*, *12*(8), 481-496. https://doi.org/10.1089/adt.2014.603

Tang, W. K., Odzorig, T., Jin, W., & Xia, D. (2019). Structural Basis of p97 Inhibition by the Site-Selective Anticancer Compound CB-5083. *Mol Pharmacol*, *95*(3), 286-293. https://doi.org/10.1124/mol.118.114256

Tang, W. K., & Xia, D. (2016). Mutations in the Human AAA(+) Chaperone p97 and Related Diseases. *Front Mol Biosci*, *3*, 79. https://doi.org/10.3389/fmolb.2016.00079

Tang, X., Hui, Z. G., Cui, X. L., Garg, R., Kastan, M. B., & Xu, B. (2008). A novel ATM-dependent pathway regulates protein phosphatase 1 in response to DNA damage. *Mol Cell Biol*, *28*(8), 2559-2566. https://doi.org/10.1128/MCB.01711-07

Tanuma, N., Kim, S. E., Beullens, M., Tsubaki, Y., Mitsuhashi, S., Nomura, M., Kawamura, T., Isono, K., Koseki, H., Sato, M., Bollen, M., Kikuchi, K., & Shima, H. (2008). Nuclear inhibitor of protein phosphatase-1 (NIPP1) directs protein phosphatase-1 (PP1) to dephosphorylate the U2 small nuclear ribonucleoprotein particle (snRNP) component, spliceosome-associated protein 155 (Sap155). *J Biol Chem*, *283*(51), 35805-35814. https://doi.org/10.1074/jbc.M805468200

Terrak, M., Kerff, F., Langsetmo, K., Tao, T., & Dominguez, R. (2004). Structural basis of protein phosphatase 1 regulation. *Nature*, *429*(6993), 780-784. https://doi.org/10.1038/nature02582

Terry-Lorenzo, R. T., Elliot, E., Weiser, D. C., Prickett, T. D., Brautigan, D. L., & Shenolikar, S. (2002). Neurabins recruit protein phosphatase-1 and inhibitor-2 to the actin cytoskeleton. *J Biol Chem*, *277*(48), 46535-46543. https://doi.org/10.1074/jbc.M206960200

Trinkle-Mulcahy, L., Andrews, P. D., Wickramasinghe, S., Sleeman, J., Prescott, A., Lam, Y. W., Lyon, C., Swedlow, J. R., & Lamond, A. I. (2003). Time-lapse imaging reveals dynamic relocalization of PP1gamma throughout the mammalian cell cycle. *Mol Biol Cell*, *14*(1), 107-117. https://doi.org/10.1091/mbc.e02-07-0376

Trinkle-Mulcahy, L., Sleeman, J. E., & Lamond, A. I. (2001). Dynamic targeting of protein phosphatase 1 within the nuclei of living mammalian cells. *J Cell Sci*, *114*(Pt 23), 4219-4228. https://doi.org/10.1242/jcs.114.23.4219

Tsaytler, P., & Bertolotti, A. (2013). Exploiting the selectivity of protein phosphatase 1 for pharmacological intervention. *FEBS J*, *280*(2), 766-770. https://doi.org/10.1111/j.1742-4658.2012.08535.x

Tsaytler, P., Harding, H. P., Ron, D., & Bertolotti, A. (2011). Selective inhibition of a regulatory subunit of protein phosphatase 1 restores proteostasis. *Science*, *332*(6025), 91-94. https://doi.org/10.1126/science.1201396

Twomey, E., Li, Y., Lei, J., Sodja, C., Ribecco-Lutkiewicz, M., Smith, B., Fang, H., Bani-Yaghoub, M., McKinnell, I., & Sikorska, M. (2010). Regulation of MYPT1 stability by the E3 ubiquitin ligase SIAH2. *Exp Cell Res*, *316*(1), 68-77. https://doi.org/10.1016/j.yexcr.2009.09.001

Twomey, E. C., Ji, Z., Wales, T. E., Bodnar, N. O., Ficarro, S. B., Marto, J. A., Engen, J. R., & Rapoport, T. A. (2019). Substrate processing by the Cdc48 ATPase complex is initiated by ubiquitin unfolding. *Science*, *365*(6452). https://doi.org/10.1126/science.aax1033

Uchiyama, K., Jokitalo, E., Kano, F., Murata, M., Zhang, X., Canas, B., Newman, R., Rabouille, C., Pappin, D., Freemont, P., & Kondo, H. (2002). VCIP135, a novel essential factor for p97/p47-mediated membrane fusion, is required for Golgi and ER assembly in vivo. *J Cell Biol*, *159*(5), 855-866. https://doi.org/10.1083/jcb.200208112

Uchiyama, K., Totsukawa, G., Puhka, M., Kaneko, Y., Jokitalo, E., Dreveny, I., Beuron, F., Zhang, X., Freemont, P., & Kondo, H. (2006). p37 is a p97 adaptor required for Golgi and ER biogenesis in interphase and at the end of mitosis. *Dev Cell*, *11*(6), 803-816. https://doi.org/10.1016/j.devcel.2006.10.016

van den Boom, J., Kueck, A. F., Kravic, B., Muschenborn, H., Giesing, M., Pan, D., Kaschani, F., Kaiser, M., Musacchio, A., & Meyer, H. (2021). Targeted substrate loop insertion by VCP/p97 during PP1 complex disassembly. *Nat Struct Mol Biol*, *28*(12), 964-971. https://doi.org/10.1038/s41594-021-00684-5

van den Boom, J., Marini, G., Meyer, H., & Saibil, H. R. (2023). Structural basis of ubiquitin-independent PP1 complex disassembly by p97. *EMBO J*, *42*(14), e113110. https://doi.org/10.15252/embj.2022113110

van den Boom, J., & Meyer, H. (2018). VCP/p97-Mediated Unfolding as a Principle in Protein Homeostasis and Signaling. *Mol Cell*, *69*(2), 182-194. https://doi.org/10.1016/j.molcel.2017.10.028

van den Boom, J., Wolf, M., Weimann, L., Schulze, N., Li, F., Kaschani, F., Riemer, A., Zierhut, C., Kaiser, M., Iliakis, G., Funabiki, H., & Meyer, H. (2016). VCP/p97 Extracts Sterically Trapped Ku70/80 Rings from DNA in Double-Strand Break Repair. *Mol Cell*, *64*(1), 189-198. https://doi.org/10.1016/j.molcel.2016.08.037

Vazquez de Aldana, C. R., Wek, R. C., Segundo, P. S., Truesdell, A. G., & Hinnebusch, A. G. (1994). Multicopy tRNA genes functionally suppress mutations in yeast eIF-2 alpha kinase GCN2: evidence for separate pathways coupling GCN4 expression to unchanged tRNA. *Mol Cell Biol*, *14*(12), 7920-7932. https://doi.org/10.1128/mcb.14.12.7920-7932.1994

Verbinnen, I., Ferreira, M., & Bollen, M. (2017). Biogenesis and activity regulation of protein phosphatase 1. *Biochem Soc Trans*, *45*(1), 89-99. https://doi.org/10.1042/BST20160154

Verma, R., Oania, R. S., Kolawa, N. J., & Deshaies, R. J. (2013). Cdc48/p97 promotes degradation of aberrant nascent polypeptides bound to the ribosome. *Elife*, *2*, e00308. https://doi.org/10.7554/eLife.00308

Wakula, P., Beullens, M., Ceulemans, H., Stalmans, W., & Bollen, M. (2003). Degeneracy and function of the ubiquitous RVXF motif that mediates binding to protein phosphatase-1. *J Biol Chem*, *278*(21), 18817-18823. https://doi.org/10.1074/jbc.M300175200

Walker, J. E., Saraste, M., Runswick, M. J., & Gay, N. J. (1982). Distantly related sequences in the alpha- and beta-subunits of ATP synthase, myosin, kinases and other ATP-requiring enzymes and a common nucleotide binding fold. *EMBO J*, *1*(8), 945-951. https://doi.org/10.1002/j.1460-2075.1982.tb01276.x

Wang, F., Li, S., Wang, T. Y., Lopez, G. A., Antoshechkin, I., & Chou, T. F. (2022). P97/VCP ATPase inhibitors can rescue p97 mutation-linked motor neuron degeneration. *Brain Commun*, *4*(4), fcac176. https://doi.org/10.1093/braincomms/fcac176

Wang, L., Popko, B., & Roos, R. P. (2014). An enhanced integrated stress response ameliorates mutant SOD1-induced ALS. *Hum Mol Genet*, *23*(10), 2629-2638. https://doi.org/10.1093/hmg/ddt658

Wang, Q., Song, C., Irizarry, L., Dai, R., Zhang, X., & Li, C. C. (2005). Multifunctional roles of the conserved Arg residues in the second region of homology of p97/valosin-containing protein. *J Biol Chem*, *280*(49), 40515-40523. https://doi.org/10.1074/jbc.M509636200

Wang, Q., Song, C., & Li, C. C. (2004). Molecular perspectives on p97-VCP: progress in understanding its structure and diverse biological functions. *J Struct Biol*, *146*(1-2), 44-57. https://doi.org/10.1016/j.jsb.2003.11.014

Watts, G. D., Wymer, J., Kovach, M. J., Mehta, S. G., Mumm, S., Darvish, D., Pestronk, A., Whyte, M. P., & Kimonis, V. E. (2004). Inclusion body myopathy associated with Paget disease of bone and frontotemporal dementia is caused by mutant valosin-containing protein. *Nat Genet*, *36*(4), 377-381. https://doi.org/10.1038/ng1332

Weith, M., Seiler, J., van den Boom, J., Kracht, M., Hulsmann, J., Primorac, I., Del Pino Garcia, J., Kaschani, F., Kaiser, M., Musacchio, A., Bollen, M., & Meyer, H. (2018). Ubiquitin-Independent Disassembly by a p97 AAA-ATPase Complex Drives PP1 Holoenzyme Formation. *Mol Cell*, *72*(4), 766-777 e766. https://doi.org/10.1016/j.molcel.2018.09.020

Welburn, J. P., Vleugel, M., Liu, D., Yates, J. R., 3rd, Lampson, M. A., Fukagawa, T., & Cheeseman, I. M. (2010). Aurora B phosphorylates spatially distinct targets to differentially regulate the kinetochore-microtubule interface. *Mol Cell*, *38*(3), 383-392. https://doi.org/10.1016/j.molcel.2010.02.034

Williams-Hart, T., Wu, X., & Tatchell, K. (2002). Protein phosphatase type 1 regulates ion homeostasis in Saccharomyces cerevisiae. *Genetics*, *160*(4), 1423-1437. https://doi.org/10.1093/genetics/160.4.1423

Williams, C., Dong, K. C., Arkinson, C., & Martin, A. (2023). The Ufd1 cofactor determines the linkage specificity of polyubiquitin chain engagement by the AAA+ ATPase Cdc48. *Mol Cell*, *83*(5), 759-769 e757. https://doi.org/10.1016/j.molcel.2023.01.016

Woodman, P. G. (2003). p97, a protein coping with multiple identities. *J Cell Sci*, *116*(Pt 21), 4283-4290. https://doi.org/10.1242/jcs.00817

Wu, J. Q., Guo, J. Y., Tang, W., Yang, C. S., Freel, C. D., Chen, C., Nairn, A. C., & Kornbluth, S. (2009). PP1-mediated dephosphorylation of phosphoproteins at mitotic exit is controlled by inhibitor-1 and PP1 phosphorylation. *Nat Cell Biol*, *11*(5), 644-651. https://doi.org/10.1038/ncb1871

Wu, X., Li, L., & Jiang, H. (2016). Doa1 targets ubiquitinated substrates for mitochondria-associated degradation. *J Cell Biol*, *213*(1), 49-63. https://doi.org/10.1083/jcb.201510098

Wurzenberger, C., Held, M., Lampson, M. A., Poser, I., Hyman, A. A., & Gerlich, D. W. (2012). Sds22 and Repo-Man stabilize chromosome segregation by counteracting Aurora B on anaphase kinetochores. *J Cell Biol*, *198*(2), 173-183. https://doi.org/10.1083/jcb.201112112

Yadav, L., Tamene, F., Goos, H., van Drogen, A., Katainen, R., Aebersold, R., Gstaiger, M., & Varjosalo, M. (2017). Systematic Analysis of Human Protein Phosphatase Interactions and Dynamics. *Cell Syst*, *4*(4), 430-444 e435. https://doi.org/10.1016/j.cels.2017.02.011

Yamashiro, S., Yamakita, Y., Totsukawa, G., Goto, H., Kaibuchi, K., Ito, M., Hartshorne, D. J., & Matsumura, F. (2008). Myosin phosphatase-targeting subunit 1 regulates mitosis by antagonizing polo-like kinase 1. *Dev Cell*, *14*(5), 787-797. https://doi.org/10.1016/j.devcel.2008.02.013

Yan, Y., Harding, H. P., & Ron, D. (2021). Higher-order phosphatase-substrate contacts terminate the integrated stress response. *Nat Struct Mol Biol*, *28*(10), 835-846. https://doi.org/10.1038/s41594-021-00666-7

Yang, H., Hou, H., Pahng, A., Gu, H., Nairn, A. C., Tang, Y. P., Colombo, P. J., & Xia, H. (2015). Protein Phosphatase-1 Inhibitor-2 Is a Novel Memory Suppressor. *J Neurosci*, *35*(45), 15082-15087. https://doi.org/10.1523/JNEUROSCI.1865-15.2015

Ye, Y. (2006). Diverse functions with a common regulator: ubiquitin takes command of an AAA ATPase. *J Struct Biol*, *156*(1), 29-40. https://doi.org/10.1016/j.jsb.2006.01.005

Zeke, A., Lukacs, M., Lim, W. A., & Remenyi, A. (2009). Scaffolds: interaction platforms for cellular signalling circuits. *Trends Cell Biol*, *19*(8), 364-374. https://doi.org/10.1016/j.tcb.2009.05.007

Zhang, J., Zhang, L., Zhao, S., & Lee, E. Y. (1998). Identification and characterization of the human HCG V gene product as a novel inhibitor of protein phosphatase-1. *Biochemistry*, *37*(47), 16728-16734. https://doi.org/10.1021/bi981169g

Zhang, L., Qi, Z., Gao, Y., & Lee, E. Y. C. (2008). Identification of the interaction sites of Inhibitor-3 for protein phosphatase-1. *Biochem Biophys Res Commun*, *377*(2), 710-713. https://doi.org/10.1016/j.bbrc.2008.10.062

Zhang, S., Guha, S., & Volkert, F. C. (1995). The Saccharomyces SHP1 gene, which encodes a regulator of phosphoprotein phosphatase 1 with differential effects on glycogen metabolism, meiotic differentiation, and mitotic cell cycle progression. *Mol Cell Biol*, *15*(4), 2037-2050. https://doi.org/10.1128/MCB.15.4.2037

Zhang, X., Shaw, A., Bates, P. A., Newman, R. H., Gowen, B., Orlova, E., Gorman, M. A., Kondo, H., Dokurno, P., Lally, J., Leonard, G., Meyer, H., van Heel, M., & Freemont, P. S. (2000). Structure of the AAA ATPase p97. *Mol Cell*, *6*(6), 1473-1484. https://doi.org/10.1016/s1097-2765(00)00143-x

Zyryanova, A. F., Kashiwagi, K., Rato, C., Harding, H. P., Crespillo-Casado, A., Perera, L. A., Sakamoto, A., Nishimoto, M., Yonemochi, M., Shirouzu, M., Ito, T., & Ron, D. (2021). ISRIB Blunts the Integrated Stress Response by Allosterically Antagonising the Inhibitory Effect of Phosphorylated eIF2 on eIF2B. *Mol Cell*, *81*(1), 88-103 e106. https://doi.org/10.1016/j.molcel.2020.10.031

Abbreviations

AAA-ATPase	ATPases associated with diverse cellular activities
aa	Amino acid
ALS	Amyotrophic lateral sclerosis
ATF4	Activating transcription factor 4
ATP	Adenosine triphosphate
AMP	Adenosine monophosphate
ADP	Adenosine diphosphate
BSA	Bovine serum albumin
CB-5083	p97-inhibitor CB-5083
Cdc48	Cell division control protein 48
CoIP	Co-Immunoprecipitation
CMT2B	Charcot -Marie-Tooth Type-2B
CPI-17	Protein kinase-C potentiated inhibitor
CReP	Constitutive repressor of eIF2α phosphorylation
Cryo-EM	Cryogenic electron microscopy
DMSO	Dimethyl sulfoxide
DNA	Deoxyribonucleic acid
DSB	DNA double-strand break
DUB	Deubiquitinating enzyme
E. coli	Escherichia coli
EDTA	Ethylenediaminetetraacetic acid
heIF2α	Human eukaryotic translation initiation factor 2A
eIF2α-P	Phosphorylated eukaryotic translation initiation factor 2A
Elu	Elution
ER	Endoplasmic reticulum
ERAD	ER-associated degradation
FCS	Fetal calf serum
FRET	Förster resonance energy transfer
FT	Flow through
G-actin	Globular actin
GADD34	Growth arrest and DNA damage-inducible protein
GCN1	General control nonderepressible 2
GEF	Guanidine-exchange factor

GFP	Green fluorescent protein
GST	Glutathione S-transferase
GTP	Guanosine triphosphate
dNTP	Deoxynucleotide triphosphate
DTT	Dithiothreitol
FTD	Frontotemporal dementia
HRI	Heme-regulated eIF2α kinase
His	6 histidine tag
HRP	Horseradish peroxidase
I1	Inhibitor-1
I2	Inhibitor-2
I3	Inhibitor-3
IBM	Inclusion body myopathy
IDP	Intrinsically disordered protein
iMet	Initiation methionine
IPTG	Isopropyl ß-D-1-thiogalactopyranoside
IRS	Internal recognition site
ISR	Integrated stress response
ISRIB	Small-molecule ISR inhibitor
kb	Kilo base
kDa	Kilo Dalton
k_{cat}	Catalytic constant
K_M	Michaelis-Menten constant
Ku	Complex containing Ku70 and Ku80
λ_{EM}	Emission wavelength
λ_{EX}	Excitation wavelength
LB	Lysogeny broth
MBP	Maltose-binding protein
MOPS	3-(N-morpholino)propane sulfonic acid
mRNA	Messenger ribonucleic acid
MSP-1	Multisystem proteinopathy-1
MYPT1	Myosin phosphatase target subunit 1
NAD	Nicotinamide adenine dinucleotide
NEB	New England Biolabs
NIPP1	Nuclear inhibitor of PP1

NP	NIPP1:PP1 complex
Npl4	Nuclear protein localization 4
OD_{600}	Optical density at 600 nm
OMF	3-O-methylfluorescein
OMFP	3-O-methylfluorescein phosphate
PAGE	Polyacrylamide gel electrophoresis
PCR	Polymerase chain reaction
PD	Parkinson’s disease
PDB	Paget’s disease of bone
pdb	Protein database
PEG	Polyethylene glycol
PERK	Protein kinase RNA-like endoplasmic reticulum kinase
PI	PP1:Inhibitor-3 complex
PIP	PP1-interacting protein
PKR	Double-stranded RNA-dependent protein kinase
PMSF	Phenylmethylsulfonyl fluoride
PP1	Protein-phosphatase-1
PPP	Phosphoprotein phosphatase
S	Sedimentation coefficient
SAC	Spindle assembly checkpoint
SDS	Sodium dodecyl sulfate
SDS22	Protein phosphatase 1 regulatory subunit 7
SENP2	SUMO/sentrin specific peptidase 2
SEP	Shp1, eyes-closed, p47
Shp1	Suppressor of high copy protein phosphatase 1
SNARE	Soluble N-ethylmaleimide-sensitive factor attachment protein receptor
SOC	Super optimal broth
SP	SDS22:PP1 complex
SPI	SDS22:PP1:Inhibitor-3 complex
SPR	Surface plasmon resonance
SRH	Second region of homology
SUMO	Small ubiquitin-like modifier
T_a	Annealing temperature

TAMRA	5(6)-Carboxy-tetramethylrhodamin
TBS-T	Tris-buffered saline + tween
TCEP	Tris(2-carboxyethyl)phosphine
TDP-43	TAR DNA-binding protein 43
TEV	Tobacco etch virus protease
TEVc	TEV cleavage site
TBI	Traumatic brain injury
tRNA	Transfer ribonucleic acid
U	Units (µmol/min)
Ufd1	Ubiquitin fusion degradation protein 1
UPR	Unfolded protein response
UTR	5' untranslated region
VCP	Valosin-containing protein
ZF	Zinc finger

Amino acids are abbreviated using the common one and three letter codes.

Declarations

Declaration:

In accordance with § 6 (para. 2, clause g) of the Regulations Governing the Doctoral Proceedings of the Faculty of Biology for awarding the doctoral degree Dr. rer. nat., I hereby declare that I represent the field to which the topic “*Regulation of PP1 activity by binding and p97-mediated dissociation of SDS22 and Inhibitor-3”* is assigned in research and teaching and that I support the application of Anja Kück.

Name of the scientific supervisor

Essen, date

Signature of the scientific supervisor

Declaration:

In accordance with § 7 (para. 2, clause d and f) of the Regulations Governing the Doctoral Proceedings of the Faculty of Biology for awarding the doctoral degree Dr. rer. nat., I hereby declare that I have written the herewith submitted dissertation independently using only the materials listed, and have cited all sources taken over verbatim or in content as such.

Essen, date

Signature of the doctoral candidate

Declaration:

In accordance with § 7 (para. 2, clause e and g) of the Regulations Governing the Doctoral Proceedings of the Faculty of Biology for awarding the doctoral degree Dr. rer. nat., I hereby declare that I have undertaken no previous attempts to attain a doctoral degree, that the current work has not been rejected by any other faculty, and that I am submitting the dissertation only in this procedure.

Essen, date

Signature of the doctoral candidate